Integrity and Fracture Response of Offshore Pipelines Subject to Large Plastic Strains

by
Nikzad Nourpanah

Submitted in partial fulfillment of the requirements
for the degree of Doctor of Philosophy

at

Dalhousie University
Halifax, Nova Scotia
March 2011

DALHOUSIE UNIVERSITY

DEPARTMENT OF DEPARTMENT OF CIVIL AND RESOURCE ENGINEERING

The undersigned hereby certify that they have read and recommend to the Faculty of Graduate Studies for acceptance a thesis entitled "Integrity and Fracture Response of Offshore Pipelines Subject to Large Plastic Strains" by Nikzad Nourpanah in partial fulfillment of the requirements for the degree of Doctor of Philosophy.

Dated: 11 March, 2011

External Examiner: _____
Dr. Kamran Nikbin

Research Supervisor: _____
Dr. Farid Taheri

Examining Committee: _____
Dr. Tamunoiyala Koko

_____
Dr. Jiunn-Ming Chuang

DALHOUSIE UNIVERSITY

Date: 11 March, 2011

Author: Nikzad Nourpanah

Title: Integrity and Fracture Response of Offshore Pipelines Subject to Large Plastic Strains

Department: Department of Civil and Resource Engineering

Degree: Ph.D. Convocation: May Year: 2011

Signature of Author

To my dear parents,

Parviz Nourpanah & Fatemeh Zibakalam

and also to my beloved wife,

Zahra Torbatian

&

To the fine brave people of Iran; freedom is near.

Contents

List of Tables

List of Figures

Abstract

Steel pipelines are widely used in offshore oil/gas facilities. To achieve economically feasible designs, regulatory codes permit utilization of the pipelines well past their elastic response limit. This requires thorough integrity check of the pipeline subject to large scale yielding (LSY). Engineering criticality assessments (ECA) are used to justify the integrity of a cracked pipeline against fracture failure. The currently used ECA crack driving force equation was developed for load-controlled components subject to very limited crack-tip plasticity. Moreover, fracture toughness data are extracted from deeply-cracked laboratory specimens that produce the lowest margin of toughness values. Therefore, the current framework can be overly conservative (or include non-uniform inaccuracies) for ECA of modern pipelines that undergo LSY and ductile crack growth prior to failure. The two main goals of this thesis are: (i) Development of an alternative crack driving force estimation scheme, (ii) Justification of the use of use of shallow-cracked single edge notch tensile (SENT) specimens for the ECA. Strain concentration in concrete coated pipelines, and effect of Lüders plateau on the fracture response are also investigated.

A new reference strain J-estimation scheme is proposed and calibrated to 300 nonlinear parametric FE models, which takes advantage of the linear evolution of the J with LSY bending strains. The scheme is hence strain-based and needless of limit load solutions, providing additional accuracy and robustness.

The near-tip stress and strain fields of cracked pipelines were also investigated and compared to those obtained from a K-T type formulation. It is shown that the J-Q constraint theory can satisfactorily characterize these fields up to extreme plastic bending levels. Similar J-Q trajectories were also observed in the SENT and pipeline models. Subsequently, FE models utilizing a voided plasticity material were used to parametrically investigate ductile crack growth and subsequent failure of pipelines subject to a biaxial stress state. Plastic strain and stress triaxiality fields ahead of the propagating crack, along with R-curves, were compared among SENT and pipeline models. It is concluded that the SENT specimen could be a viable option for ECA of such pipes based on the observed crack tip constraint similarity.

List of Abbreviations and Symbols Used

Greeks

α	Ramberg-Osgood fitting parameter
β, γ	power-law fitting coefficients in Equation (6.10)
β_i	($i = 1 \sim 7$, fitting coefficients in Equation (4.8)
$\Delta\varepsilon_L$	$= \varepsilon_L - \varepsilon_y$, width of Lüders plateau
Δa	crack growth
Δt_c	critical stable time increment
Δ	confidence level
δ_t	crack tip opening displacement
δ_{ij}	Kronecker's delta
η	design confidence factor in Equation (4.12)
κ	curvature
κ_{crit}	critical curvature, denoting failure of the pipeline
λ	coating parameter
ν	Poisson's ratio
Φ_D, $\Phi_{D,c}$	damage integral and its critical value
σ_f	current flow stress
σ_h	hoop stress caused by the internal pressure in the pipeline
σ_m	$= \frac{1}{3}\sigma_{kk}$, mean (hydrostatic) stress (first invariant of the stress tensor)
σ_y	yield stress, or an *effective* yield stress in a Ramberg-Osgood material
σ_{11}	crack opening stress
σ_e	$= \left(\frac{3}{2}S_{ij}S_{ij}\right)^{1/2}$, equivalent Mises stress (second invariant of the stress tensor)
σ_{ij}	the Cauchy (true) stress tensor
σ_{nom}	nominal stress (excluding all concentration causes)
σ_{ref}	reference stress
σ_{unc}	uncracked stress (including all other concentration causes except that of the crack)
σ_u	ultimate tensile strength

τ_y	shear strength of anti-corrosion layer
ε_{ij}^p	plastic strain tensor
ε_0	concrete crushing strain
ε_g	global bending strain at the outermost pipe fiber
ε_L	Lüders termination strain
ε_p	equivalent plastic strain
ε_y	$= \sigma_y/E$, yield strain
ε_{11}	axial strain along the tensile chord of steel pipe
$\varepsilon_{\mathrm{FJ}}$	axial strain in the field joint
$\varepsilon_{\mathrm{max,FJ}}$	axial strain in the field joint
ε_{ave}	axial strain averaged along the tensile chord of steel pipe
ε_{crit}	critical (local) buckling strain of pipeline under bending
ε_{ij}	strain tensor
ε_{nom}	nominal strain (excluding all concentration causes)
ε_{pH}	plastic part of the principal circumferential (hoop) strain
ε_{pL}	plastic part of the principal longitudinal strain
ε_{pR}	plastic part of the principal radial strain
ε_{ref}	reference strain
ε_{unc}	uncracked strain (including all other concentration causes except that of the crack)
ξ	confidence level parameter

Romans

a	crack depth
a_e	effective crack depth, modified for small scale yielding correction
b_1	intercept in the constraint estimation Equation (7.9)
B	width of SENT or SENB specimen
c	half of the crack length ($2c$ is the full crack length)
$CTOD$	crack tip opening displacement
$CTOD_c$	fracture toughness in terms of $CTOD$ at initiation of crack growth

D	Diameter of pipeline
d	$= \delta_t/(J/\sigma_y)$, crack tip opening parameter
$\mathrm{d}f$	void volume increase rate
$\mathrm{d}f_{gr}$	void volume increase rate due to to growth of existing voids
$\mathrm{d}f_{nucl}$	void volume increase rate due to to nucleation of new voids
$\mathrm{d}(.)$	derivative of (.) with respect to time; rate of change
D_0	size of the GTN elements ahead of the crack tip ($^1/_2 D_0$ in symmetric models)
E	modulus of elasticity
$E^{'}$	$= E$ in plane stress, and $= E/(1-\nu^2)$ in plane strain
E_c	modulus of elasticity of concrete
f	void volume fraction in the GTN material
f^*	modified void volume fraction
$f_c^{'}$	compressive strength of concrete
f_0	initial void volume fraction
f_1, f_2	plasticity functions in the reference strain method Equation (5.9)
f_c	critical void volume fraction
$f_{_F}$	critical void volume fraction
f_{con}	compressive stress in concrete
h_1	fully plastic non-dimensional function in the EPRI scheme
I_c	second moment of area of concrete coating
I_s	second moment of area of steel pipe
J	the J-integral in Mode-I
J_0	fracture toughness of a material with no Lüders plateau
J_c	fracture toughness in terms of J at initiation of crack growth
J_e	$= K^2/E^{'}$, J-integral for an elastic material
J_p	fully plastic J-integral, for a material following Equation (5.5)
J_R	fracture toughness in terms of J as a function of crack growth
J_{ave}	spatial average of $J(s)$ along the crack front (s-coordinate)
J_{crit}	fracture toughness of a material with a Lüders plateau
K, K_I	Mode-I stress intensity factor

l_1	a characteristic dimension of a cracked body
L	length of pipeline, SENT or SENB specimens in a symmetric FE model
L_t	length of concrete coated pipeline symmetric model (see Figure 3.4)
L_{F}	length of field joint (see Figure 3.1)
M	bending moment
M_p	$= \sigma_y D^2 t$, fully plastic moment capacity of an uncracked pipe
n	strain hardening index
N	tensile load applied to concrete coated pipe end
N_y	fully plastic axial capacity of steel pipe
p	internal pressure in pipeline
P	applied load on the structure
$P(.)$	probablity of event (.)
P_y	a limit load of the structure
q_i	modification factors for the GTN yield potential ($i = 1, 2, 3$)
Q	constraint parameter
Q_{ave}	spatial average of $Q(s)$ along the crack front (s-coordinate)
r, θ	polar coordinates based at the crack tip (r emanates from the initial crack tip towards the uncracked ligament)
r_m	mean radius of the pipeline
$\bar{R}$	mean radius of deformed void
R_0	radius of an initially spherical void
R_x, R_z	X and Z rotations applied to the pipeline end
R_{hub}	radius of hub for reeling
s	coordinate emanating from the initial crack center running along the crack front length, $0 < s < c$
S_{ij}	$= \sigma_{ij} - {}^1\!/_3 \sigma_{kk}\delta_{ij}$, deviator stress tensor
$\hat{\text{SCF}}$	strain concentration factor predicted by Equation (4.8)
SCF	strain concentration factor
SCF_{des}	strain concentration factor recommended for design
SCF_{FE}	exact strain concentration factor from FE analysis

SCF_{UL}	upper limit of strain concentration factor predicted by Equation (4.14)
t	pipe wall thickness
t_c	concrete coating thickness
t_{ACL}	thickness of anti-corrosion layer
u_x, u_y	Displacement components applied at the MBL model boundary
W	thickness of SENT or SENB specimen
W_s	strain energy density function

Abbreviations

2PFM	two parameter fracture mechanics
HRR	Hutchinson-Rice-Rosengren singularity field
ACL	anti-corrosion layer
API	American Petroleum Institute
DNV	Det Norske Veritas
ECA	engineering criticality assessment
EPFM	elastic-plastic fracture mechanics
EPRI	electric power research institute
FE	finite element
FJ	field joint
GTN	Gurson-Tvergaard-Needleman voided plasticity material model
LEFM	linear elastic fracture mechanics
LGC	large geometry change
MBL	modified boundary layer
NLG	nonlinear geometry
SBD	strain based design
SGC	small geometry change
SPFM	single parameter fracture mechanics

Acknowledgements

First of all, I would like to thank my parents, Parviz and Zohreh, and my younger sister and brother, Golnoosh and Behnood, all of whom are back home in Iran. Just at the time when I could have been there for them, I rather selfishly left the country to pursue my PhD studies in Canada. Never, for even a second, did they stop supporting me emotionally, and never have I managed to stop missing them. I cannot imagine having been able to finish my studies and pursue a happy life, without their unreserved love and constant encouragement.

I've long joked that "healthy competition" with my long-time girlfriend, and now wife, shoved me into graduate studies. It is not a joke; she has long been my inspiration and motivation. I've lived some of the best years of my life with Zahra. She has been by my side through all the crazy ups and downs, with love, caring and sympathy. She was joy and light in the never-ending winters of Halifax. She was there when no one else was, and no one else could be. She trusted in me and never ceased to do so during the past years. My deepest gratitude goes to my beloved Zahra.

I was lucky enough to have Shiva, my older sister, and her two lovely kids, Sheida and Yousef, in Halifax. I ran to them whenever in despair, and they always welcomed me with open arms. The memories of our chitchats over lunch, sipping wine together, sparkle my reminiscence of these years in Halifax. I cannot thank them enough, and they can never wholly grasp how valuable they are to me.

My thanks goes to all my friends and colleagues at Dalhousie University, especially Kaveh Arjomandi, Davood Rezaei, Peyman Khosravi, Sara Baftechi, Shiva Eslami, Mohammad Yahyaei, Pejman Razi, Morteza Mehrzadi, Ramadan Esmaeel and Ahmed Shouman. I cherish all the good times and beautiful memories, the lunch breaks, coffee breaks, beer breaks and so on.

Last but not least, I would like to express my deep gratitude to Dr. Farid Taheri. He believed in me, provided me with financial support throughout my PhD research and wisely supervised me, enabling me to liberally pursue my scholarly interests. Without his guidance and constant support in every respect, this attaining degree would have been indeed impossible. I also like to thank my supervisory committee members, Dr. Tamunoiyala Koko and Dr. Jiunn-Ming Chuang. My gratitude goes to Dr. Kamran Nikbin as well, the external examiner of the thesis. Furthermore, the financial support of the Atlantic Innovation Fund through C-CORE, and also that provided by Dalhousie University are kindly appreciated.

Chapter 1

Introduction

1.1 Offshore Oil and Gas Production & Pipelines

Oil and natural gas have long been sources of energy for the continuous and ever-increasing demand of humans for energy. While the adverse effect of burning fossil fuels and its effect on global climate is causing increased concern, still, oil and natural gas are and will be the main sources of energy in the foreseeable future of the energy market.

Onwards from the 1980's, the share of offshore oil and gas production is steadily increasing. Moreover, in recent years, hydrocarbon resources in shallower waters and reasonably benign environments have been mostly exploited. Thus the oil and gas industry has been compelled to move into harsher environments in recent years, and will continue its explorations and productions into deeper waters and hostile environments.

Pipelines are a key element in offshore oil and gas production. Two main types of pipelines function in an offshore oil/gas field. The intrafield pipelines transfer the crude product from wellheads and manifolds to platforms, while export pipelines carry the product to facilities located on the shore. A typical offshore hydrocarbon field with pipelines serving different functions is shown in Figure 1.1 (taken from [1]). The large capital cost of offshore pipelines is an always present issue in offshore hydrocarbon projects, and thus, their expenditure should not become the weak link that prohibits the project developments.

Virtually all offshore pipelines are made of steel alloys with considerable ductility. In order to achieve an economically competent pipeline design, the plastic deformation capacity of the material has to be utilized. As such, it has to be shown that the inelasticaly deformed pipeline can safely sustain relevant loadings. Such design strategies has been foreseen in most of the major pipeline design codes, such as DNV [2]

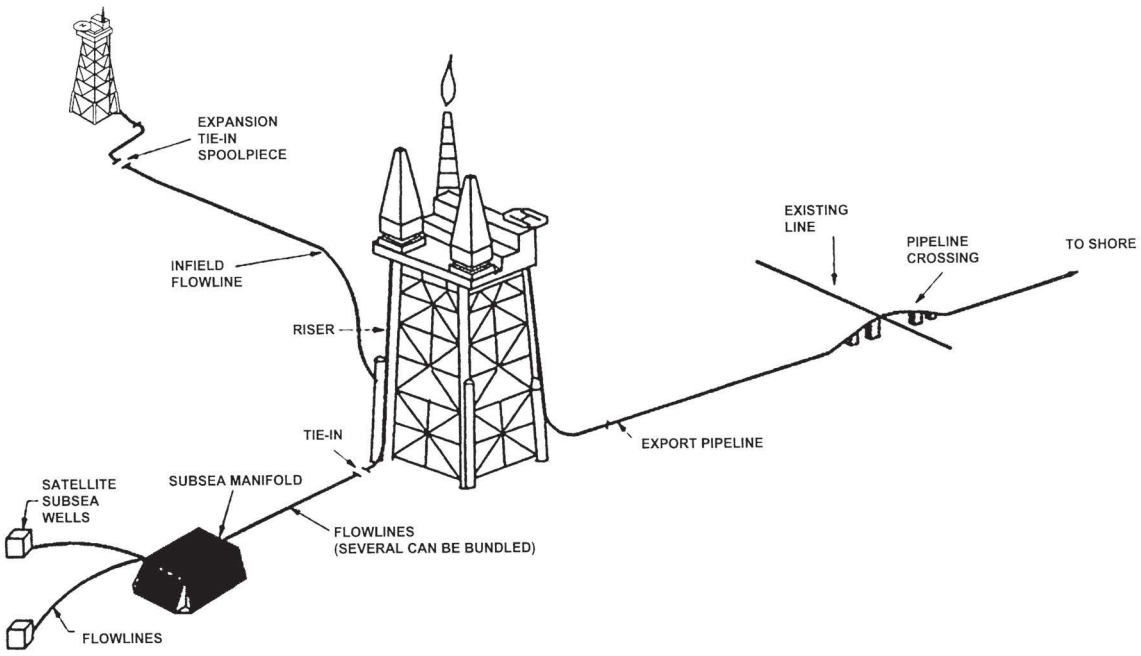

Figure 1.1. A typical offshore hydrocarbon facility showing pipelines serving different functions, taken from [1].

and API [3].

A typical offshore pipeline is subject to bending during many relevant loading scenarios. These scenarios occur both during installation and operation of pipelines. Some of the loading scenarios in which the pipeline undergoes bending are shown in Figure 1.2 (taken from Refs. [4–7]). The prominent failure mode on the tensile side of a bended pipeline is due to potential fracture of the pipe wall, which, upon occurrence would render the structure out of service with substantial economic and environmental impacts. A welding defect generally termed *crack*, could trigger such a failure mode. Traditionally, an empirical *workmanship* criteria on the critical size of such defects were common in the offshore industry. However, nowadays the application of fracture mechanics principles to assess the integrity of the flawed pipeline is more common. Throughout this thesis, where the behavior of a cracked pipeline is under investigation, an external semi-circumferential part through crack centered at the 12 o' clock position of the pipe section (i.e. undergoing the maximum bending stress and strain) is considered. This is believed to be representative of real-life weld defects

observed in offshore pipelines.

1.2 Thesis Objectives

The theoretical and experimental background to application of fracture mechanics for assessment of components undergoing very limited plastic deformation is well understood and documented. The current codes, such as BS7910 [8], are generally tailored for such applications (i.e. for linear elastic fracture mechanics (LEFM)). However, the same does not hold true for components undergoing large scale yielding (LSY), such as the case of interest in this thesis, namely pipelines subject to large plastic strains. The issue of applying fracture mechanics principles to components undergoing LSY is still a young and evolving one, with several unanswered questions and debates. Indeed, in the context of offshore pipelines, it was only in 2006 that the first guideline targeting their fracture assessment appeared, which is DNV-RP-F108 [9]. Still, the DNV guideline [9] basically recommends the usage of BS7910 [8] with some modifications for pipelines subject to large plastic strains. Some of the major issues which are not reflected in the current codes of practice, and/or require more research for their justification, our outlined below:

(i) The crack driving force (in BS7910 [8] and DNV [9]) is a load-based equation tailored for LEFM. Furthermore, its use requires limit-load definitions, which in turn introduces non-uniform and unquantified approximations to the crack driving force calculations. More suitable formulations can be developed by accounting for the displacement-based loadings occurring in such pipelines.

(ii) The applicability of a fracture parameter (such as the J-integral) or even incorporation of an additional constraint parameter (such as the J-Q fracture theory) to characterize the fracture response up to extreme plastic deformation levels is not generally justified.

(iii) In order to use constraint-matched laboratory specimens for fracture assessment of cracked pipeline subject to extreme plastic strains, the state of crack-tip constraint for such pipelines should be accurately evaluated. Of special importance

is the crack-tip constraint under LSY and biaxial stress states (i.e. which is relevant to a combined loading condition).

(iv) Treatment of an important material feature, namely, the Lüders plateau which is present in the stress–strain curve of many pipeline steels, is only foreseen in an approximate manner.

(v) A peripheral issue is that of strain concentration factors. These factors are required for the accurate prediction of strains. Comprehensive collections of concentration factors for a variety of situations are available, which are mostly based on a linear elastic solution. However very few general formulations are available for problems in which nonlinearities play a major role on the physical response. An important and practical example is the strain concentration in the field joint of a concrete coated offshore pipeline.

The work presented in this thesis mainly addresses these issues, by using advanced nonlinear 3D finite element (FE) analysis as the primary tool. All FE analysis are performed using the ABAQUS [10] software package. The general aim was to develop new methodologies and/or to gain a better understanding of application of fracture mechanics principles and justification of their use for assessment of offshore pipelines subject to large plastic strains. Specifically, new methodologies are proposed in relation to items (i) and (v) above, while extensive investigations are undertaken in consideration of issues noted in (ii), (iii) and (iv) above.

1.3 Layout of Thesis

This thesis is in the paper based format, and is structured in nine chapters including the present one, along with two appendices. Six of the chapters, namely Chapters 3 to 8, are original research articles, either accepted for publication or published in peer-reviewed journals. The copyright agreement forms with the respective publishers can be found in Appendix B.

The second chapter of the thesis presents a thorough literature review on both the principles of fracture mechanics, and also their application to assessment of pipelines undergoing large plastic strains.

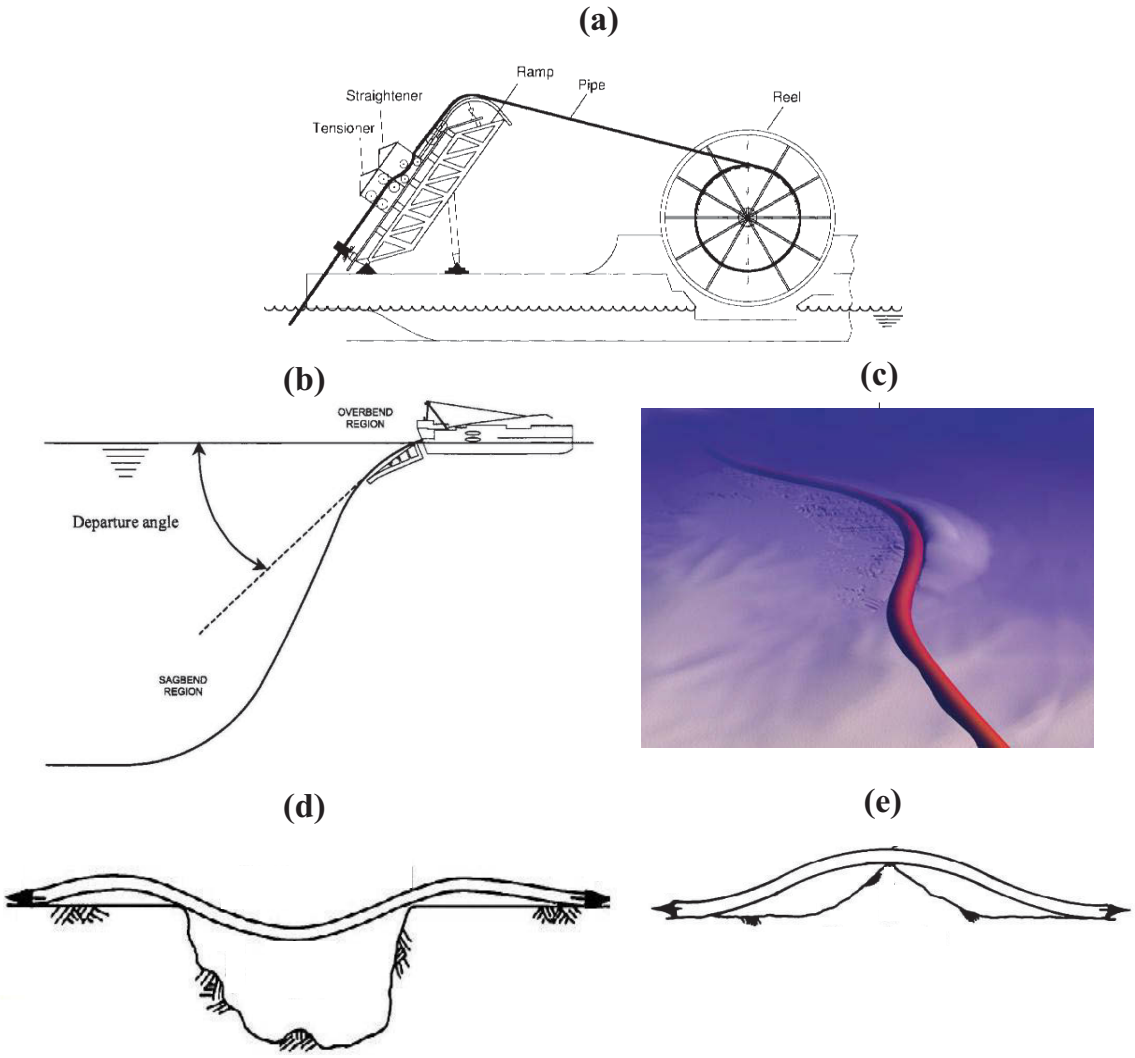

Figure 1.2. Some loading scenarios in which the pipeline undergoes bending, **(a)** The reeling installation method, the pipe undergoes severe plastic bending when bent over the reel drum (taken from Ref. [4]), **(b)** The S-lay installation method (taken from Ref. [5]), **(c)** Lateral buckling (snaking) of the pipeline due to thermal stresses (taken from Ref. [6]), **(d)** Free-spanning of the pipeline (taken from Ref. [7]), **(e)** The pipeline bent to cross a seabed obstruction (taken from Ref. [7]).

Chapters 3 and 4 investigate the peripheral issue of strain concentration in concrete coated pipelines. Chapter 3 provides the details of a FE modeling framework capable of capturing the strain concentration phenomena, and its comparison to benchmark test data (those available in the literature). It also presents a comprehensive parametric study on various pipeline features affecting strain concentration in such pipelines. Chapter 4 builds on the FE framework of the previous chapter and discusses the development of a design equation for prediction of the strain concentration factor in X65 pipelines.

In Chapter 5 of this thesis, a new crack driving force estimation scheme is proposed and calibrated to the results of 300 nonlinear FE models. The developed reference strain equation predicts the J-integral of cracked pipelines as a linear function the uncracked bending strain. A wide and practical range of geometric, material and loading parameters are considered in the derivation of the equation. Comparisons with other available estimation schemes are also presented in the chapter.

The effect of the Lüders plateau of the material stress–strain curve, on the fracture response of cracked pipelines is discussed in Chapter 6 of this thesis. The developed models are also used to investigate the near-tip stress fields and crack-tip constraint levels in the presence of the Lüders plateau. Finally, a micro-mechanical damage integral approach is used to quantify the effect of Lüders plateau on material's toughness. Based on these, an equation is proposed that can satisfactorily predict the effect of the Lüders plateau on material toughness, as a function of strain hardening capacity and Lüders termination strain values.

In Chapter 7, the J-Q fracture theory is incorporated to investigate the near tip stress and strain fields of cracked pipelines subject to extreme plastic bending. These fields are further compared with those obtained from a standard K-T modified boundary layer (MBL) model. In case of favourable similarity, the comparison could justify the admissibility of the J-Q framework for characterizing the near-tip stress and strain fields in cracked pipelines up to LSY levels. Furthermore, a formula is presented for prediction of the crack-tip constraint (characterized by Q) in such pipelines, which approximates Q as a linear function of the global bending strain. Finally, constraint

matching studies are performed for justification of the use of SENT[1] specimens for fracture assessment of cracked pipelines.

Crack-tip constraint under biaxial stress states in pipelines subject to LSY is investigated in Chapter 8 of this thesis. 3D FE models of pipelines were developed utilizing a voided plasticity material defining the zone ahead of their crack front, thus enabling ductile crack growth simulation. The constraint-matched SENT and deeply-cracked SENB[2] specimens are also considered. Comprehensive comparison of the R-curves and also plastic strain and stress triaxiality fields ahead of the propagating crack among these three systems further aided understanding of the crack-tip constraint levels in cracked pipelines.

The main conclusions drawn from the present research are summarized and outlined in Chapter 9 of this thesis, along with some recommendations for future research in this field.

In order to efficiently and automatically perform the numerous and rather complicated FE preprocessing tasks required throughout this thesis, various Python scripts have been developed for the ABAQUS/CAE [10] environment. As a typical sample of these, a detailed explanation of the scripts utilized for the FE modeling tasks of Chapter 8 are presented in Appendix A. Free copies of all these in-house developed scripts can be obtained from the author[3].

[1] single edge notch tensile
[2] single edge notch bend
[3] n.nourpanah@dal.ca

Chapter 2

Literature Review & Background to the State of the Art in Fracture Assessment

In this chapter fundamentals of fracture mechanics, as relevant to the study of integrity and fracture response of offshore pipelines are discussed. Also, the available literatures on applying these principles to the specific case of offshore pipelines subject to large plastic strains are reviewed. Also, a brief literature review on the peripheral issue of strain concentration in concrete coated pipelines (dealt with in chapters 3 and 4 of this thesis) is presented.

2.1 Strain Based Design & the Necessity of Fracture Assessment

To address the ever more stringent cost constraints of offshore pipeline designs, there has been a growing interest in utilizing the structures' and their material to their fullest capacity. Thus, the Strain Based Design (SBD) approach was developed for pipeline design during the nineties, by which the cost and conservatism of the more traditional stress-based approaches could be reduced. SBD takes advantage of the well-known ductility property of steel, that is to safely undergo large plastic deformations. The SBD framework imposes limiting strain values, rather than limiting stresses, for justification of pipeline integrity [11–13].

SBD would only be advantageous and applicable for structures that are subject to displacement-controlled loadings (at least partially). This can be understood by envision of a typical force-displacement equilibrium path of a ductile structure loaded up to the nonlinear response region as shown in Figure 2.1 (a moment-curvature curve for example). If the loading is displacement controlled, noting the ductile regime, a perturbation from the target design displacement could still be safely accommodated by the structure. On the other hand, if the structure is load-controlled, even a very small perturbation of load around the limit load could cause failure. Thus, for SBD

to be beneficial, the structure should be utilized in the plastic deformation region, in addition to the (at least partially) displacement-controlled loading [11–13].

Fortunately, a number of the most critical loading conditions imposed on a pipeline, both during their installation and operation, have a displacement-based nature and thus, justifying the applicability of SBD. These include, and are not limited to: pipelines conforming to the curvature of a stinger, reel drum and/or bathymetry of a rough seabed, and also buried pipelines subject to seabed motion such as subsidence due to freeze-thaw cycles, mudslides and seismic activity [1, 4, 5, 14, 15]. All these loading scenarios subject the pipeline to bending. Additionally, the pipeline undergoes internal pressure under operational conditions. The combined action of bending and internal pressure on the pipeline can be regarded as a partially displacement controlled condition, for which the SBD framework is still applicable [11]. Based on these, a number of the leading pipeline design codes such as DNV [2] and API [3] have endorsed SBD and provide relevant guidelines. Based on their importance, the pure bending, and also the combined bending plus internal pressure loading scenarios have been considered in this thesis.

Two of the most prominent failure modes of offshore pipelines under bending are local buckling of the pipe wall on the compression side, and fracture on the tensile side. Research on the local buckling subject have satisfactorily pushed the allowable compressive strain limits to quite large values[1], as manifested in DNV [2] and API [3] guidelines for example. Such large values can adequately accommodate even the most severe loading conditions, such as those occurred during reeling. On the other hand, the tensile limit strain is restricted because of the potential fracture of the pipeline girth welds containing a hypothetical welding defect. Integrity assessment for this case includes a fracture mechanics analysis of the component, which is termed as the Engineering Criticality Assessment (ECA) in the relevant literature. The basic philosophy of ECA is based on the relationship among defect size, mechanical properties, material toughness, and applied loading [16, 17]. Principles of fracture mechanics are incorporated to establish the relationship, and the final outcome of the ECA is to establish tolerable defect sizes for given material properties and loading, or vice

[1]For example, the crtical local buckling equation of API [3] reads $\varepsilon_{crit} = t/(2D)$. For a pipe with $D/t = 15$ under pure bending, this equation predicts a critical bending strain of $\varepsilon_{crit} = 3.33\%$.

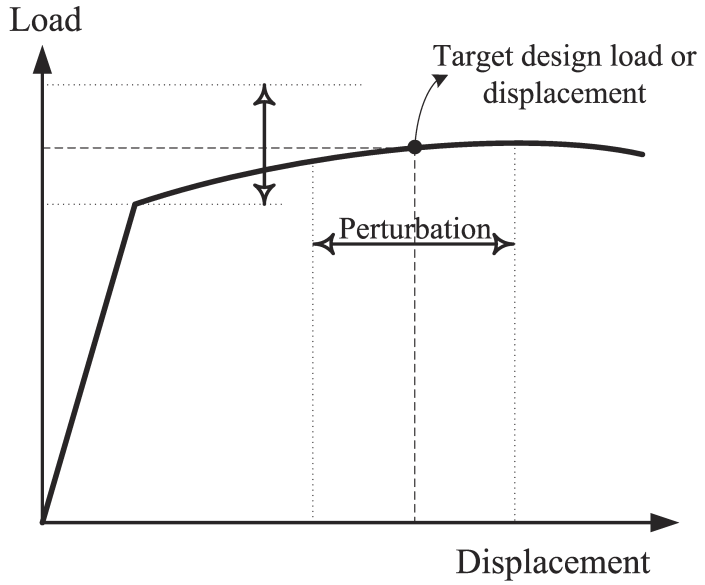

Figure 2.1. A schematic force-displacement equilibrium path of a ductile structure showing the SBD framework

versa. According to DNV [2], ECA is mandatory for pipelines subject to accumulated plastic strains greater than 0.3%. All reeled pipes fall into this category (nominal strain levels in the range of 1∼4% occur during reeling). Moreover, pipelines during installation (accounting for the strain concentration causes), free spanning pipelines, and pipelines subject to seabed motion might undergo strain levels which require an ECA for their integrity justification. The accumulated plastic strain is defined as:

$$\varepsilon_p = \sqrt{\frac{2}{3}\left(\varepsilon_{pL}^2 + \varepsilon_{pH}^2 + \varepsilon_{pR}^2\right)} \tag{2.1}$$

Fracture mechanics assessment of flawed components has been widely applied in practice and documented in design codes (e.g. BS7910 [8]). However the current ECA approaches are based on criteria developed in the Eighties, mainly under stress/load based design assumptions with very limited allowable plastic deformation, which would lead to excessive conservatism for strain-based conditions. DNV-RP-F108 [9] was the first code specifically tailored for ECA of offshore pipelines subject to large plastic strains. However, still many aspects of ECA applied to offshore pipelines subject to large plastic strains require more research and development. Some of these

aspects are further outlined, followed by a review of the available technical literature on the associated issues.

Common to all aspects of SBD, is the accurate prediction of strain. The nominal strain is readily calculable from the displacement-based loading configuration. However, several local effects would cause strain concentrations, which also have to be taken into account [2]. The most prominent of these causes are:

- Variations and imperfections in cross sectional area between adjacent pipe joints[2].
- Stiffening effects of concrete coating.
- Yield stress mismatch between weld metal and pipe material, or material variations (yield stress and strain hardening capacity) between adjacent pipe joints.

The overture of the present thesis consists of Chapters 3 and 4 which thoroughly investigate the second item above, that is strain concentration in field joint of concrete coated offshore pipelines. The rest of the material in this thesis investigates various aspects of the fracture mechanics assessment of offshore pipelines subject to large plastic strains. A comprehensive literature review on fundamental aspects of fracture mechanics and its application to offshore pipelines subject to large plastic strains is presented in section 2.2 onwards.

2.1.1 Strain Concentration in Concrete Coated Pipelines

The on-bottom stability requirement of high diameter offshore pipelines laid on the seabed usually requires the addition of a concrete weight coating over the steel pipe. A thin anti-corrosion layer (ACL) is situated between the steel pipe and the concrete coating. The concrete coating has discontinuities at locations of the field joints[3] (FJ) to facilitate girth welding of 12 m long pipe joints. Upon application of bending, the bare steel pipe in the FJ undergoes strain concentration, which can be described by a strain concentration factor, SCF:

$$\text{SCF} = \frac{\varepsilon_{\text{FJ}}}{\varepsilon_g} \tag{2.2}$$

[2]pipe joint: 12 m long line pipe.

[3]A field joint refers to the joint established by girth welding of two adjacent pipe joints in the field.

This type of strain concentration phenomenon has been investigated via full-scale test setups by Archer and Adams [18], Akten et al. [19], Verley and Ness [20] and Ness et al. [21]. Archer and Adams [18] investigated epoxy ACL's, and found out that the shear transfer capacity is strongly affected by the type and method of coating application, load conditions and load sequence. Akten et al. [19] performed full scale one-end lift bend test on 28, 30 and 36 inch diameter pipes with coating thickness of 62, 90 and 120 mm. They concluded that continuous steel cages should be used in the concrete coating to minimize the extent and width of concrete cracks. Also slotting of the concrete would only be beneficial for the thickest of the coatings. Furthermore, the applied curvature during laying was justified as safe. Verley and Ness [20] reported the results of full scale bending tests on 16 and 20 inch diameter coated pipes with polyethylene and asphalt ACLs. Constant moment, four point bending was applied to a pipe string consisting of one pipe joint welded between two half-length joints. They concluded that SCF is closely related to the shear transfer from the concrete to the steel through the ACL. Also cyclic tests did not cause higher SCF than that in the static tests. Ness et al. [21] monitored the laying of a 40 inch pipe with 70 mm coating thickness over a stinger with a radius of 283 m in a water depth of 197 m with 44 strain gauges. Their results showed very little strain concentration (SCF $\approxeq$ 1.15).

Lund et al. [22] presented a semi-analytical approach for SCF estimation, which considered arbitrary material behavior for steel and concrete while neglecting concrete sliding in the formulation. The equilibrium of forces between pipe and coating was used to determine the moment-curvature of the coated and uncoated segments, used to establish the SCF. Their results showed good agreement in comparison with test results of Akten et al. [19]. Ness and Verley [23] included the effect of possible sliding of coating in the semi-analytical model of Lund et al. [22] via an iterating method, which resulted in SCF predictions in agreement with tests of Verley and Ness [20].

Endal [24] performed shell FE analysis of an X65 pipe with 20 inch diameter, 17.9 mm wall thickness, 0.3 MPa ACL shear strength and 80 mm coating thickness. Realistic response results were obtained, however, up to the concrete crushing point. The sliding of coating towards the FJ and also the realistic shear stress distribution in ACL were captured. Sævik et al. [25] used the theory of sandwich structures and

formulated a concrete coated pipe finite element, which showed a good agreement with more complicated 3D FE models.

Currently, the state of the art in investigating the strain concentration of coated pipelines is either experimental investigation or semi-analytical formulations, quantifying the phenomenon with the SCF. As an alternative to the costly and time-consuming test setups and experiments, or the semi-analytical formulations which introduce a certain level of simplification, a 3D FE simulation of the problem including nearly all the sources of complexity and nonlinearity can be undertaken. The initial goal of the current study is to prepare a FE model which would include the most important sources of nonlinearity, and to verify the predicted response against available test results. This robust FE modeling framework would be subsequently used to investigate the effect of variation of each parameter on the SCF. These aspects are targeted in Chapter 3 of this thesis. Furthermore, based on the trends observed in the initial parametric study, an extensive parametric study encompassing most of the practical design situations would be performed. The ultimate goal would be establishing empirical design equations for predicting the SCF. It is believed that such a tool would improve the practical design of offshore pipelines, as it provides the accuracy enjoyed by sophisticated nonlinear FE simulations via a set of simplistic design equations. Such an analysis is described in Chapter 4 of the present thesis.

2.2 Single Parameter Fracture Mechanics (SPFM)

In consideration of the very complex (and still under debate) micro-mechanisms of material fracture, the fundamental task in engineering fracture mechanics is to provide semi-empirical or phenomenological parameters which can satisfactorily correlate the initiation and growth of cracks in two different bodies. The two different bodies would be the full-sized structure of interest, and (preferably) a laboratory-scale specimen. In other words, the fracture toughness of the material could be approximated (in terms of the respective semi-empirical parameter) by loading a laboratory test specimen to fracture, and in turn comparing it to the crack driving force in the actual structure (again, in terms of the respective semi-empirical parameter). Most of the common fracture specimens along with their abbreviations are shown in Figure 2.2.

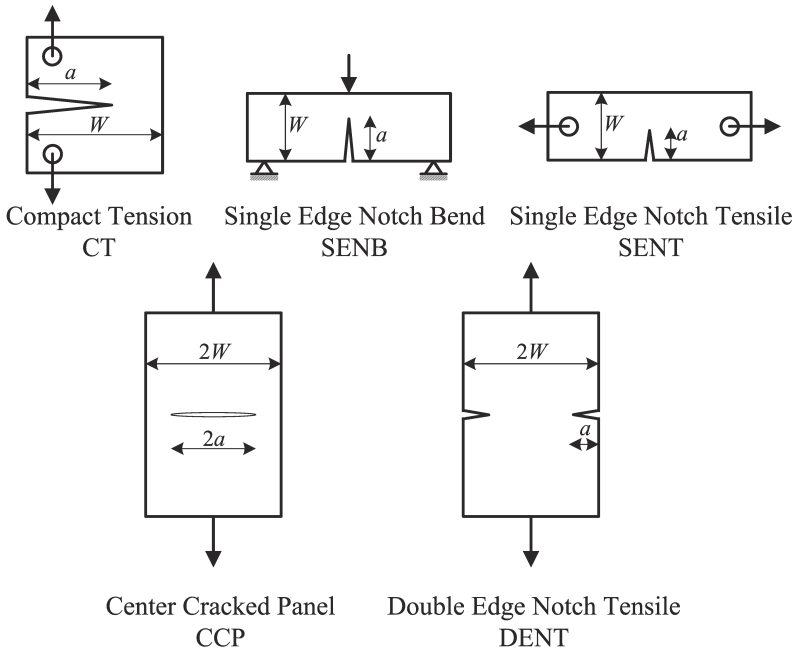

Figure 2.2. Some common fracture specimens and their abbreviations.

The actual fracture micro-process is active over very small length scales. For this order of length scales, the continuum idealization and thus the concepts of *stress* and *strain* break down. Still, it can be assumed that this process is controlled and driven by the near crack-tip stress and strain fields. Therefore, a suitable candidate for the phenomenological parameter(s) used in characterizing fracture of materials would be a parameter (or a set of parameters) that can accurately describe the state of stresses and strains in the vicinity of the crack tip (which presumably engulfs the fracture process zone.) Historically, there was an interest to use a single phenomenological parameter. The linear elasticity analysis of Williams [26] provided such a parameter, namely the stress intensity factor, K. Williams [26] showed that for a crack[4] in an elastic media loaded in Mode-I (crack opening mode), the stress field ahead of the crack tip would follow Equation (2.3). The conventions of a cracked body in mode I loading is shown in Figure 2.3 (after Hutchinson [27]).

$$\sigma_{ij} = A_{ij}(\theta) r^{-1/2} + B_{ij}(\theta) + C_{ij}(\theta) r^{1/2} + \dots \tag{2.3}$$

[4]The original analysis was for an infinite wedge with an arbitrary interior angle, and the crack is a special case of the wedge with an interior angle equal to π.

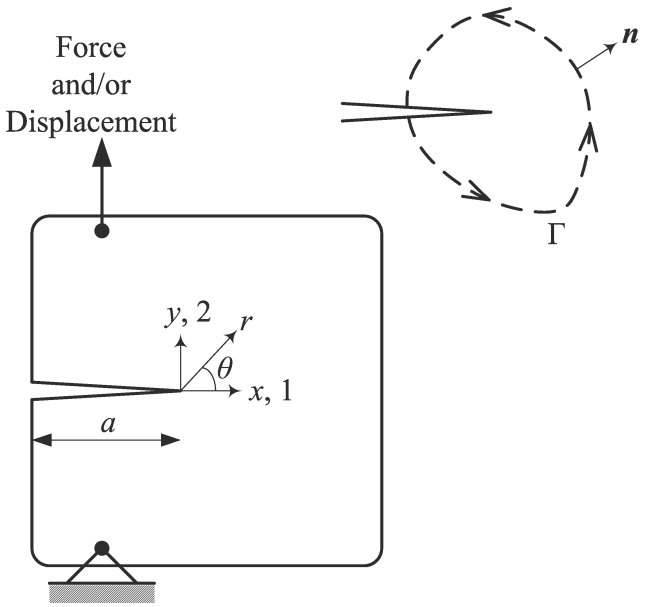

Figure 2.3. The conventions of a cracked body loaded in mode I; after Hutchinson. [27].

The first term in Equation (2.3) has a square root singularity with respect to r. That is, as $r \to 0$, the first term would dominate the solution. Hence, in the vicinity of the crack tip, K would single-handedly characterize the stress (and strain) fields, such that:

$$\sigma_{ij} = \frac{K}{\sqrt{2\pi r}} f_{ij}(\theta) \tag{2.4}$$

Thus, K can be used as a semi-empirical fracture parameter, able to transfer the information on severity of crack tip stress and strain fields. Regarding the elasticity solution that K is derived from, use of K is limited to situations with limited inelastic deformation response, hence the term linear elastic fracture mechanics (LEFM). While some amount of inelasticity is always present in the vicinity of a stressed crack tip, still, LEFM can be used for many problems in which the size of the inelastic region is small compared to the relevant dimensions of the body (e.g. the crack length, a, or the uncracked ligament length, $W - a$). This situation is generally termed small scale yielding (SSY). The main applications of LEFM are brittle fracture (in which fracture of the material precludes large scale yielding, LSY, of the structure), and also high-cycle fatigue crack growth (in which the low loading levels cause relatively small crack tip plastic zones).

The currently used steel grades for offshore pipelines have substantial ductility

and (can) undergo significant amounts of plastic deformation prior to fracture. Thus, application of LEFM and K would not be admissible if the assessment of the structure loaded up to LSY is required. The J-integral, originally proposed by Rice [28], has been shown to be a suitable parameter for situations were elastic-plastic fracture mechanics (EPFM) is required. J is defined as (see Figure 2.3 for illustration of the contour path Γ and its unit outward normal n):

$$J = \int_{\Gamma} \left(W_s n_1 - \sigma_{ij} n_j u_{i,1} \right) \mathrm{d}s \tag{2.5}$$

where W_s is the strain energy density of the material ($W_s = \int_0^{\varepsilon} \sigma \, \mathrm{d}\varepsilon$), and u_i are the displacement components. Simply put, J plays the same role for EPFM as K does for LEFM. Hutchinson [29] and Rice and Rosengren [30] both showed the near-tip stress and strain fields of an elastoplastic material can be characterized solely with J (hence the term *HRR* singularity). The *HRR* singularity assumes a Ramberg-Osgood uniaxial stress–strain relationship, represented by:

$$\frac{\varepsilon}{\varepsilon_y} = \frac{\sigma}{\sigma_y} + \alpha \left(\frac{\sigma}{\sigma_y} \right)^n \tag{2.6}$$

Approaching the crack tip, $r \to 0$, the elastic strains can be assumed negligible with respect to the plastic strains, thus:

$$\frac{\varepsilon}{\varepsilon_y} = \alpha \left(\frac{\sigma}{\sigma_y} \right)^n \tag{2.7}$$

By using the J_2 deformation plasticity theory, the uniaxial stress–strain relation of Equation 2.7 can be generalized to multiaxial stress states [27]:

$$\frac{\varepsilon_{ij}}{\varepsilon_y} = \frac{3}{2} \alpha \left(\frac{\sigma_e}{\sigma_y} \right)^{n-1} \frac{S_{ij}}{\sigma_y}, \qquad \sigma_e = \left(\frac{3}{2} S_{ij} S_{ij} \right)^{1/2} \tag{2.8}$$

For such a material, the *HRR* singularity stress and strain fields are defined by Equation (2.9) [29, 30], which shows that for EPFM, the stress field is only a function of J. As long as the *HRR* singularity continues to characterize the near-tip fields, J can be deemed as a suitable phenomenological parameter for EPFM.

$$(\sigma_{ij})_{\mathrm{HRR}} = \sigma_y \left(\frac{J}{\alpha \sigma_y \varepsilon_y I_n r} \right)^{\frac{1}{n+1}} \hat{\sigma}_{ij}(\theta, n)$$

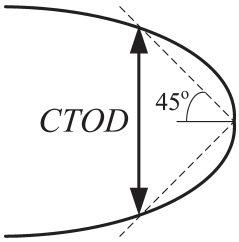

Figure 2.4. Definition of $CTOD$ as the crack opening at intersection of rays with the blunted crack flanks.

$$(\varepsilon_{ij})_{\text{HRR}} = \alpha\varepsilon_y \left(\frac{J}{\alpha\sigma_y\varepsilon_y I_n r} \right)^{\frac{n}{n+1}} \hat{\varepsilon}_{ij}(\theta, n) \tag{2.9}$$

Tabulations of the dimensionless θ-variation functions $\hat{\sigma}_{ij}$ and $\hat{\varepsilon}_{ij}$ and also the normalizing constant I_n can be found in Ref. [31]. Under SSY conditions, J and K would have a unique relationship:

$$J = \frac{K^2}{E'} \tag{2.10}$$

Based on experimental observations, Wells [32] suggested the use of the crack tip opening displacement ($CTOD$ or δ_t) as a fracture mechanics parameter. Later on, Shih [33] showed that J and $CTOD$ do indeed have a general relationship as shown in Equation (2.11). The $CTOD$ definition of Shih [33] is shown in Figure 2.4. Thus, $CTOD$ forms an acceptable fracture parameter for application in both EPFM and LEFM.

$$CTOD = d(\alpha\varepsilon_y, n)\frac{J}{\sigma_y} \tag{2.11}$$

Regardless of the choice of fracture mechanics parameter, the assessment of a cracked structure is performed by comparison of crack driving force in the structure to the critical fracture toughness of the material obtained from laboratory specimens. In terms of J for example, the condition $J < J_c$ would assure that the crack would not grow under the considered loading. A more descriptive picture of fracture toughness of a material can be grasped by the resistance or R-curve, which basically describes the fracture toughness of the material as a function of crack growth (e.g. J_R as a function of Δa). Figure 2.5 shows a schematic R-curve for a typical ductile intermediate-strength steel (such as a grade X60 pipeline steel, in terminology of API-5L [34]). For a typical steel discussed, the fracture toughness $J_R(\Delta a)$ may increase to twice the value of J_c with a crack advance of as little as $\Delta a \approxeq 1 \sim 2$ mm [27]. Thus, provided that ductile

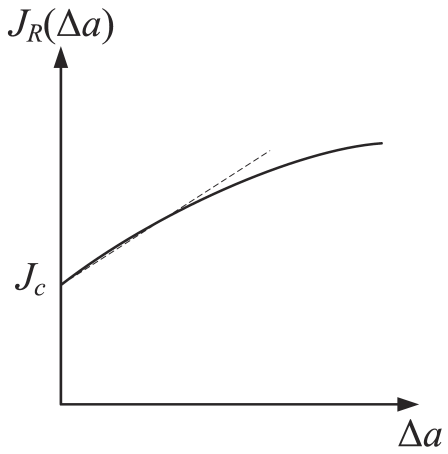

Figure 2.5. Schematic of a J-R-curve for a ductile steel

crack growth proceeds in a stable manner, this increase in fracture toughness of the material can be safely utilized (as the option has been foreseen in modern design guidelines [8, 9]). The conditions of stable crack advance can be formulated as [27]:

$$\frac{\mathrm{d}J}{\mathrm{d}a} < \frac{\mathrm{d}J_R}{\mathrm{d}\Delta a} \tag{2.12}$$

2.3 Crack Driving Force Estimation Schemes

For LEFM applications, linear elasticity can elegantly provide the crack driving force (in terms of K) of a wide variety of practical cracked body configurations [16]. On the contrary, for EPFM applications, the solution of crack driving force (in terms of J) for only a few idealized geometries are available [27]. Such analytical solutions are based on boundary value problems with a nonlinear material response (such as Equation (2.7)) and therefore are remarkably complex or even impossible to achieve. Thus, the applicability of EPFM relies heavily on developing estimation schemes for J in various cracked body configurations. The prominent developments in this field, including the Electric Power Research Institute (EPRI) scheme of Kumar et al. [35], the reference stress method of Ainsworth [36] and the reference strain method of Linkens et al. [37] are reviewed in the following sections.

2.3.1 The Electric Power Research Institute (EPRI) Scheme

The EPRI scheme developed by Kumar et al. [35] is based on the idea of splitting J into an elastic J_e and plastic part J_p. While J_e could be basically related to K via Equation (2.10), the *HRR* singularity solution is used to define J_p. In other words, J_e represents the contribution of a material following the first term on the RHS[5] of Equation (2.6), while J_p corresponds to a material following the second term on the RHS of Equation (2.6). The total J-integral is approximated as:

$$\begin{aligned} J &= J_e(a_e) + J_p(a) \\ &= \frac{K^2(a_e)}{E'} + \alpha\sigma_y\varepsilon_y l_1 h_1 \left(\frac{P}{P_y}\right)^{n+1} \end{aligned} \tag{2.13}$$

where a_e in Equation (2.13) is the *modified* crack length. The *modification* is based on Irwin's idea (i.e. adding the size of the plastic zone to the actual crack depth to account for plasticity in SSY, see Anderson [16]). However, also the effect of strain hardening is included in formulation of a_e, as discussed by Kumar and Shih [38]. Furthermore, P is the applied load while P_y is a limit load of the cracked body (i.e. the load at which the net cross section yields [16]). h_1 in Equation (2.13) is a plasticity function which is generally dependant on the geometry of the cracked body and also post-yield properties of the material (n). h_1 has to be calculated using FE analysis for the desired cracked body. Some practical configurations have been analyzed and their h_1 functions have been tabulated in the EPRI technical report [35].

2.3.2 The Reference Stress Scheme and Guideline Recommendations

The EPRI scheme [35] has two drawbacks. First, it is only suitable for idealized material response such as a Ramberg-Osgood (RO) stress–strain curve given in Equation (2.6). This is actually a minor drawback as RO-type curves can actually approximate a variety of elastoplastic uniaxial responses with a very good accuracy. Second and most importantly, the EPRI scheme requires extensive tabulation of the h_1 function which requires nonlinear FE analysis and might not be readily available for a configuration of interest. Moreover, Miller and Ainsworth [39] have shown that some of the

[5] right hand side.

FE analysis preformed for establishing the h_1 functions do not meet self-consistency requirements (especially SENT configurations with shallow cracks). The reference stress method of Ainsworth [36] overcomes these drawbacks by introducing σ_{ref} which is defined as:

$$\frac{\sigma_{ref}}{\sigma_y} = \frac{P}{P_y} \tag{2.14}$$

Substituting Equation (2.14) into Equation (2.13), while making simplifying assumptions and approximations, and also incorporating minor modifications as explained in Milne et al. [40], the final form of the reference stress method J estimation scheme as implemented in BS7910 [8] and also DNV [9] is achieved:

$$J(a) = J_e(a)\left(\frac{E\varepsilon_{ref}}{\sigma_{ref}} + \frac{\sigma_{ref}^3}{2\sigma_y^2 E\varepsilon_{ref}}\right) \tag{2.15}$$

where $J_e(a)$ is calculated from Equation (2.10).

Miller and Ainsworth [39] have verified the reference stress scheme against the EPRI method and showed that the reference stress method produces an average over-prediction of 5%. However, on a case by case basis, over-predictions as much as 20% and under-predictions as large as 40% have also been observed [39].

In order to utilize Equation (2.15) for fracture assessment of cracked pipelines subject to bending, the procedures outlined in BS7910 [8] and DNV [9] could be followed. The reference stress σ_{ref} for a pipeline with a semi-circumferential part-through external[6] crack[7] subject to bending can be calculated using Kastner's limit load solution [41] as recommended in BS7910 [8] and DNV [9]:

$$\sigma_{ref} = \frac{\sigma_{unc}\left[\pi\left(1-\frac{a}{t}\right) + 2\left(\frac{a}{t}\right)\sin\left(\frac{c}{r_m}\right)\right]}{\left(1-\frac{a}{t}\right)\left[\pi - \left(\frac{c}{r_m}\right)\left(\frac{a}{t}\right)\right]} \tag{2.16}$$

Equation (2.16) is actually derived from Kastner's plastic limit load solution [41] of a cracked pipeline subject to tension (rather than bending). Nonetheless, codes recommend its use for bending loads too [8, 9]. The reference strain (ε_{ref}) used in Equation (2.15) is the corresponding strain to σ_{ref} determined from the material's true

[6] BS7910 recommends the same σ_{ref} for internal and external semi-circumferential part-through cracks.

[7] See Figure 5.4 for a schematic of this type of crack.

uniaxial stress–strain curve. Furthermore, σ_{unc} and its corresponding strain (ε_{unc}) are the applied bending stress and strain. However, the effect of all other stress/strain concentrators (other than the crack itself) should be included in σ_{unc} and ε_{unc}. As briefly noted in Section 2.1, these include effects of misalignments or wall thickness differences between adjacent pipe joints, or the stiffening effect due to a concrete coating (as noted in Section 2.1.1 and fully investigated in Chapters 3 and 4, in which strain concentration factors based on elastoplastic FE analysis will be derived), etc. Considering the fact that for the majority of these cases, elastoplastic concentration factors are not readily available, DNV [9] recommends usage of Neuber's method [42], which is expressed as:

$$\sigma_{unc} \times \varepsilon_{unc} = \sigma_{nom} \times \varepsilon_{nom} \times k_t^2 \tag{2.17}$$

The elastic stress concentration factor (k_t) is much more available than elastoplastic stress and strain concentration factors (such as the k_t formulas provided in DNV [9]). Equation (2.17) represents a hyperbola in the σ_{unc}-ε_{unc} space, and its intersection with the materials true stress–strain curve yields the value of σ_{unc} and ε_{unc} for use in Equation (2.16).

2.3.3 The Reference Strain Scheme

The reference stress method discussed in Section 2.3.2 was developed in the 1980's for (mainly) the power generation industry applications. On these grounds, the reference stress method was tailored for load-controlled situations in which LSY of the component was not generally permitted. Furthermore, application of the reference stress method requires the use of plastic limit load solutions (such as Kastner's [41] solution used in Equation (2.16)). Miller [43] notes that a realistic plastic limit load solution should account for material's strain hardening, and also finite strain and finite deformation effects. These effects have been commonly neglected and instead, a simple limit analysis (such as the lower-bound plasticity theorem, or the strength of material approaches with very significant simplifying assumptions) has been performed [43]. Furthermore, a very wide variety of limit load solutions are usually available for a specific cracked configuration and a clear-cut consensus might not be obvious (e.g. see Miller's review [43]). Thus, the mere dependency of the reference stress method

on limit load definitions includes additional and unquantified approximation in estimation of the crack driving force.

Milne et al. [40], Ainsworth [44] and Zerbst et al. [45] provide useful insight on various terms in Equation (2.15). The first term ($E\varepsilon_{ref}/\sigma_{ref}$) describes both the limiting elastic and fully plastic behaviors. The second term, $\sigma_{ref}^3/(2\sigma_y^2 E\varepsilon_{ref})$, describes the response in between these two limits, namely, the small scale yielding regime, where the general behavior is elastic, but J exceeds its elastic value, and a minor plasticity correction is provided by the second term. The second term is designed such that it has a negligible effect in the elastic domain ($\sigma_{ref}/\sigma_y \ll 1$) and in the fully plastic domain in which $E\varepsilon_{ref}/\sigma_{ref} \gg 1$. Based on these, the second term could be safely neglected for LSY conditions. In addition to this simplification, Linkens et al. [37] also used the *uncracked* stress and strain (σ_{unc}, ε_{unc}) instead of the *reference* stress and strain (σ_{ref}, ε_{ref})[8]. The final outcome is the *reference strain* formulation. The reference strain formulation is extremely suitable for displacement controlled situations in which the cracked body also undergoes LSY. By incorporating these simplifications, including a safety factor of 2, and also substituting the general form of the LEFM stress intensity factor ($K = F\sigma\sqrt{\pi a}$) in Equation (2.15), the final form of the reference strain J-estimation scheme reads [37]:

$$J = 2F^2\pi\sigma_{unc}\varepsilon_{unc} \tag{2.18}$$

Regarding the underlying simplifying assumptions of the reference strain scheme, Equation (2.18) is particularly attractive for fracture assessment of pipelines subject to large plastic strains. It has a *strain-based* format and does not require a limit load definition. The nominal strain in a displacement-controlled situation is readily obtained from consideration of the geometric conformity of the pipeline (e.g. during reeling $\varepsilon_{nom} = D/(2R_{hub})$ [9]). Furthermore, Equation (2.18) is in accord with results of tests performed on reeled pipelines by Pisarski et al. [46], and also detailed FE results of Østby et al. [47] and Pisarski et al. [48]. All of these revealed a similar linear evolution of fracture response parameter J with total uncracked strain ε_{unc}.

[8]Basically, the uncracked stress value is magnified using a limit load solution (such as Equation (2.16)) to establish the *reference* stress. Thus, σ_{ref} accounts for the effect of the crack on increasing the stress levels.

However, Tkaczyk et al. [49] showed that although Equation (2.18) can qualitatively capture the fracture response of reeled pipelines, the quantitative accuracy is not sufficient.

Several attempts have been made to improve the accuracy of fracture response estimation schemes of pipelines subject to plastic bending (such as reeled pipelines) and/or simplifying them. Taking advantage of the (nearly) linear evolution of fracture response with the applied nominal strain, Østby [50] proposed a set of strain based equation by fitting them to the results of a series of line-spring shell FE model simulations. However, the limitations of the considered defect geometries and the considered strain levels did not render the approach attractive for application to common reeled pipelines. Tkaczyk et al. [51] applied the modified reference stress approach of Kim and Budden [52] to the limit load solution of Kastner et al. [41]. Although the approach resulted in improved accuracy, it still did not take advantage of a strain-based formulation.

In Chapter 5 of this thesis, the basis of the reference strain method is utilized to develop an accurate and practical reference strain J-estimation scheme suitable for SBD of pipelines subject to extreme plastic bending (the prominent application being reeled pipelines). Detailed 3D FE models will be used to calibrate the developed equation.

An issue relevant to thick-wall pipelines (low D/t) is the so-called Lüders plateau. For such pipelines, usually seamless manufacturing is favored. In seamless pipelines, the elastic part of the material's stress–strain curve is followed by a perfectly plastic response (i.e. the Lüders plateau), and strain hardening begins only after the termination of this plateau. The discussed J-estimation schemes cannot be used to explicitly show the effect of the Lüders plateau on the fracture response (at best, only the approximate effect of the Lüders plateau could be reflected with these schemes). As such, in Chapter 6 of this thesis, fully nonlinear 3D FE models are developed and the effect of a Lüders plateau with various values of termination strain is discussed on the fracture response of such pipelines. Furthermore, the effect of Lüders plateau on fracture toughness of such pipelines is also investigated in Chapter 6 using a ductile damage integral as reviewed in section 2.6.1.

2.4 Two Parameter Fracture Mechanics (2PFM) and Constraint Effects

As discussed, the SPFM framework is based on the idea of the similarity of the crack-tip fields in different cracked bodies, with the information on these fields being conveyed through a single parameter. While this approach is sound for SSY situations, crack tip fields under LSY conditions cannot generally be described by a single parameter. McClintock [53] was the first to demonstrate this fact through slip-line analysis (assuming a rigid-perfectly plastic material) of several plane strain specimens. His analysis revealed that the near tip stress and deformation fields under LSY are a strong function of geometry and loading mode. Some of the common laboratory specimens and their abbreviations are shown in Figure 2.2. For example, McClintock showed that under fully plastic conditions, the DENT and CCP specimens have maximum crack opening stress values of $\approxeq 3\sigma_y$ and $\approxeq 1.15\sigma_y$ respectively [53].

Another implicit assumption in the SPFM framework is that the critical fracture toughness and the R-curve are only material properties. In other words, fracture tests on test specimens with different geometric shapes and different loading modes should ideally yield in the same fracture toughness data. Similar to the case on near crack tip fields, the fracture toughness obtained from tests undergoing LSY is strongly dependent on geometry and loading mode. Begley and Landes [54] investigated J vs. Δa R-curves of CCP and CT specimens, and showed that the R-curve of the CCP specimen (under tension) has a substantially higher slope than that obtained from the CT specimen (loaded predominantly in bending). Also, Hancock and Cowling [55] investigated the crack tip opening displacement at the initiation of ductile tearing ($CTOD_c$) and observed the $CTOD_c$ of a SENT specimen to be approximately ten times that obtained from a DENT specimen of the same material. Parks [56] summarizes that in both sets of experiments, the specimens having a higher fracture toughness (both in terms of initiation toughness and R-curve slope) are the ones that have lower crack tip stress triaxiality obtained from the slip-line analysis of McClintock's [53]. The stress triaxiality is defined as:

$$\text{Stress Triaxiality} = \frac{\sigma_m}{\sigma_e} \tag{2.19}$$

The dependency of fracture toughness on geometry and loading mode is generally

and loosely termed *constraint*. Literally, crack tip constraint can be understood as a structural obstacle against plastic deformation that is induced mainly by the geometric and physical boundary conditions but can also arise due to material mismatch or residual stresses [57]. Constraint is closely related to stress triaxiality near the crack-tip. Higher triaxiality/constraint promotes fracture, because the input of external work (e.g. measured by J), would, to a lesser extent, be dissipated by the global plastic deformation, but rather be available to enhance local material degradation and damage [57, 58].

A high constraint/triaxiality cracked body will generally lead to lower toughness value with a brittle type fracture, while low constraint/triaxiality cracked bodies of the same material will have a higher toughness and a ductile type fracture [56]. Parks [56] associates high constraint/triaxiality with:

(i) all states of SSY; and

(ii) virtually all load levels (SSY and LSY) of deeply-cracked bodies in which the uncracked ligament is predominantly subjected to bending.

On the contrary, shallow-cracked bodies in which the uncracked ligament is mostly under tension have a low crack-tip stress triaxiality and low constraint. McMeeking and Parks [59] and Shih and German [60] used detailed plane strain finite element analysis on various specimen geometries to investigate their near tip stress and strain fields and compared them to the standard *HRR* fields. They identified limits of loading in these geometries for J-dominance[9]. In high constraint/triaxiality configurations, the *HRR* solution continued to describe the crack tip stress and strain fields up to LSY, and thus the SPFM framework was deemed to be applicable to them by utilizing either J or $CTOD$.

Later on, fracture mechanics research was aimed at developing constraint theories such that the near-tip stress and strain fields of various cracked bodies with different levels of constraint could be satisfactorily described. In this regards, two parameter

[9] J-dominance refers to a situation in which the *HRR* solution (which describes the intensity of the near-tip fields as a function of J) satisfactorily characterizes the near tip stress and strain fields. This provides the grounds for applicability of SPFM with J as the crack driving force and fracture toughness parameter.

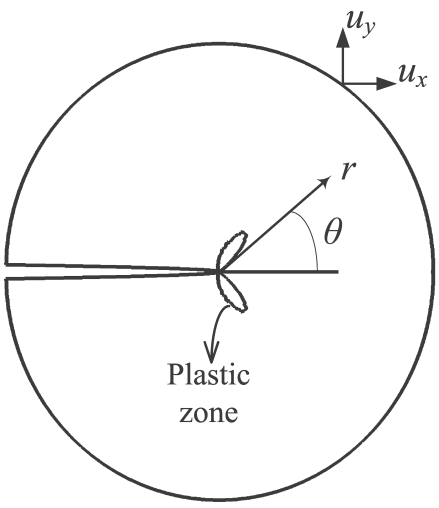

Figure 2.6. A schematic of the MBL model and its conventions

fracture mechanics (2PFM) theories have been proposed, which utilize an additional constraint parameter. The primary parameter, J or $CTOD$, characterizes the scale of crack tip deformation, while the additional constraint parameter reflects the varying levels of crack tip stress triaxiality in different bodies. The most prominent 2PFM theories, are the J-T formulation of Betegon and Hancock [61] (further developed, explained and advocated by Al-Ani and Hancock [62] and Hancock et al. [63]), the J-A_2 formulation [64–66], and finally the J-Q theory of O'Dowd and Shih [67, 68] (further developed, explained and advocated in Refs. [69–72]). These three theories will be briefly explained below.

2.4.1 The J-T Formulation

The modified boundary layer (MBL) model is used for derivation of both the J-T and the J-Q formulations. The MBL is a plane strain circular disk which represents a hypothetical crack tip, and is loaded at its circular boundary with tractions (or displacements) of the Williams asymptotic solution (such as Equations (2.3) and (2.4)). If the size of the crack tip plastic zone is small with respect to the radius of the MBL, application of the Williams linear elastic solution as boundary conditions is justified. Figure 2.6 shows a schematic of an MBL model and its conventions.

Betegon and Hancock [61] used the MBL model and included the first (singular) and also the second term (non-singular) of the Williams asymptotic solution (Equation (2.3)) in their analysis. Thus the tractions at the boundary of the MBL would read:

$$\sigma_{ij} = \frac{K}{\sqrt{2\pi r}} f_{ij}(\theta) + T\delta_{1i}\delta_{1j} \tag{2.20}$$

in which the T-stress acts parallel to the crack flanks, and has thus been neglected in the traditional SPFM approach. The MBL model was loaded at its boundary with displacements corresponding to the tractions given in Equation (2.20), represented by:

$$\begin{aligned} u_x &= \frac{K_I}{E}(1+\nu)\sqrt{\frac{r}{2\pi}}\cos(\theta/2)[\chi - \cos\theta] + (1-\nu^2)\frac{T}{E}x \\ u_y &= \frac{K_I}{E}(1+\nu)\sqrt{\frac{r}{2\pi}}\sin(\theta/2)[\chi - \cos\theta] - \nu(1+\nu)\frac{T}{E}y \end{aligned} \tag{2.21}$$

where $\chi = 3 - 4\nu$ under plane strain conditions.

Betegon and Hancock [61] showed that the resulting near tip stress fields of such an analysis forms a family of stress profiles which are all approximately parallel to the *HRR* distribution, and the particular member of the family is determined by the T-stress. Positive values of T-stress resulted in stress distributions converging to the high triaxiality *HRR* distribution, while negative values of the T-stress result in the profiles falling markedly below the *HRR* distribution (i.e. low stress triaxiality). Thus, they argued that the level of crack-tip constraint/triaxiality is correlated to the elastic T-stress. In other words, different geometries could be ranked by their constraint based on their respective T-stress. The following general formula for the near-tip crack opening stress was proposed:

$$\left(\frac{\sigma_{\theta\theta}}{\sigma_y}\right)_T = \left(\frac{\sigma_{\theta\theta}}{\sigma_y}\right)_{T=0} + \alpha_1\left(\frac{T}{\sigma_y}\right) + \alpha_2\left(\frac{T}{\sigma_y}\right)^2 \tag{2.22}$$

in which α_i are generally functions of the strain hardening index, n.

While the T-stress is defined only for elastic materials, it has been shown that the elastic T-stress can correlate constraint/triaxiality up to LSY levels [61–63]. Furthermore, Hancock et al. [63] successfully used the J-T formulation to rank fracture test data (both initiation toughness and R-curve slope) among specimens with various levels of constraint.

2.4.2 The J-A_2 Formulation

The *HRR* solution is basically the first term in an asymptotic solution of the crack-tip stress and strain fields. Later on, the J-A_2 three-term solution was proposed [64–66], in which the near tip stress field of a power-law material is represented by[10]:

$$\frac{\sigma_{ij}}{\sigma_y} = A_1 \left[\left(\frac{r}{L_1} \right)^{s_1} \hat{\sigma}_{ij}^{(1)}(\theta) + A_2 \left(\frac{r}{L_1} \right)^{s_2} \hat{\sigma}_{ij}^{(2)}(\theta) + A_2^2 \left(\frac{r}{L_1} \right)^{s_3} \hat{\sigma}_{ij}^{(3)}(\theta) \right] \tag{2.23}$$

where the stress angular functions $\hat{\sigma}_{ij}^{k}(\theta)$ ($k = 1, 2, 3$) and the stress power exponents s_k depend on n. Moreover, A_1 and s_1 are related to the *HRR* singularity field and J:

$$A_1 = \left(\frac{J}{\alpha \varepsilon_y \sigma_y I_n l_1} \right)^{-s_1}, \qquad s_1 = -\frac{1}{n+1} \tag{2.24}$$

Thus, Equation (2.23) establishes a description of the near-tip fields as a function of two parameters, namely J and A_2 (the constraint/triaxiality parameter). Zhu and Leis [73] have successfully utilized the J-A_2 formulation to correct the J-R-curves of high constraint specimens for application to fracture assessment of low constraint pipes.

2.4.3 The J-Q Formulation

Using an MBL model loaded with the first two terms of the Williams solution [26] (i.e. Equation (2.20)) in which the FE model included large geometry change (LGC) effects, O'Dowd and Shih [67, 68] used dimensional similarity arguments and showed that the near-tip fields up to LSY conditions could be satisfactorily described by two terms. These are: (i) J, which sets the size scale over which large stresses and strains develop (the fracture process zone), and (ii) Q, which controls the stress triaxility levels in this zone [67, 68]. They showed that in an annular region ahead of the crack tip, the stress field is defined by:

$$\sigma_{ij} = (\sigma_{ij})_{\text{Ref}} + Q\sigma_y \delta_{ij} \qquad \text{for} \qquad r > J/\sigma_y \qquad \& \qquad |\theta| < \pi/2 \tag{2.25}$$

The reference field (i.e. $(\sigma_{ij})_{\text{Ref}}$ in Equation (2.25)) could be considered as the *HRR* field [29, 30] or the SSY distribution obtained from MBL model with $T = Q = 0$, which

[10] The same assumptions as the *HRR* derivations have been used, that is, a power-law uniaxial relationship (Equation (2.7)) which is extended to multiaxial stress states using the J_2 deformation plasticity theory (Equation (2.8)).

yields more consistent results [67, 68]. O'Dowd and Shih [68] recommend extracting Q from the crack opening stress distribution at a distance of $r = 2 \times J/\sigma_y$, in which the LGC effects are minimized[11]. The ability of the J-Q approach to rank the fracture toughness data (both the initiation toughness and the slope of the R-curve) from specimens with different levels of constraint has been showcased in Refs. [69–72].

While the original J-Q formulation was developed based on 2D plane strain MBL analysis, several researchers have argued validation of the approach to 3D cracks [69, 71]. These heuristic arguments pointed out that at sufficiently remote locations from the intersection of the crack front and external body surface ($s/c < 1$)[12], and in the neighborhood of the crack tip ($r \to 0$), plane strain conditions would indeed prevail (i.e. the out of plane strains become negligible with respect to the singular in-plane strains). As such, the J-Q description of Equation (2.25) would hold true, and accordingly, the pair of $J(s)$ and $Q(s)$ could completely characterize the 3D near tip fields [69, 71]. Furthermore, an operational average definition of constraint, Q_{ave}, was proposed [69]. This quantity has been observed to satisfactorily rank the toughness and R-curve slopes in 3D geometries with different levels of crack tip constraint [74]. Mathematically, Q_{ave} is represented by:

$$Q_{ave} = \frac{1}{s_b - s_a} \int_{s_a}^{s_b} Q(s)\, \mathrm{d}s \qquad \text{at} \qquad \theta = 0, \qquad r = 2 \times J_{ave}/\sigma_y \tag{2.26}$$

where the upper and lower integration limits (s_a and s_b, respectively) correspond to that length of the crack in which the fracture process is active. Faleskog [74] carried the integration over the crack front length in which $Q(s)$ was approximately constant. Also, J_{ave} is calculated the same way as Q_{ave}, that is by integrating it along the crack front.

In all the reviewed 2PFM constraint theories, a description of the near tip stress and strain fields (which presumably drive the fracture process) is sought in terms of two parameters. Based on the specifics of each formulation, the near tip fields are extracted from FE analysis of the required cracked body, and the constraint parameter is calculated accordingly. Parks [56] provides a comprehensive review of

[11] A complete illustration of the J-Q near tip stress and strain fields can be found in Chapter 7 of this thesis.

[12] See for example Figure 7.8 in Chapter 7 for r, θ, s coordinates as relevant to a 3D crack.

2PFM constraint theories.

The 2PFM constraint theories expand the applicability limits of the more restrictive SPFM (which is basically applicable to LEFM, and EPFM situations with J-dominance). However, a 2PFM approach would be valid as long as these theories are capable of describing the near tip stress and strain fields. While detailed studies have shown that for example, the J-Q approach can satisfactorily describe the near tip fields of most 2D specimens up to substantial levels of LSY [69–71], the existence of an identifiable 2PFM near tip field is not necessarily guaranteed for any arbitrary cracked body up to LSY. Even for some 2D specimens (such as the deeply cracked SENB with $a/W = 0.5$ in Ref. [68]), the near-tip fields cease to resemble identifiable 2PFM fields at very high levels of LSY (which is caused by the global bending stresses interfering with near tip stress fields). In other words, while an operational definition of a constraint parameter is readily available at any load level (such as by using Equation (2.25) for Q), there is a risk that the actual near-tip field will not resemble a 2PFM field. Based on these, Parks [56] cautions that any constraint study should involve detailed and careful studies of the respective near-tip stress and strain fields.

In this thesis, the J-Q approach has been selected for studying on pipeline crack-tip constraint.

2.5 Crack Tip Constraint in Pipelines

The crack-like defects of interest for fracture assessment of offshore pipelines are generally caused by welding flaws. The height of these flaws are governed by the weld pass height, resulting in crack-like defects with a height of $2 \sim 6$ mm [9]. Furthermore, the primary bending load considered in this thesis causes the uncracked ligament in the pipe wall to be subjected mostly to tension. These situations cause such cracked pipelines to have a low crack tip constraint.

Based on a 2PFM philosophy, the laboratory specimen used for fracture toughness data should have similar crack-tip constraint to the structure of interest, in this case being cracked pipelines under LSY conditions. However, traditionally and in the interest of conservatism, deeply cracked high-constraint specimens have been recommended by codes (such as the CT and SENB with $a/W \geqslant 0.5$ [75]) which provide

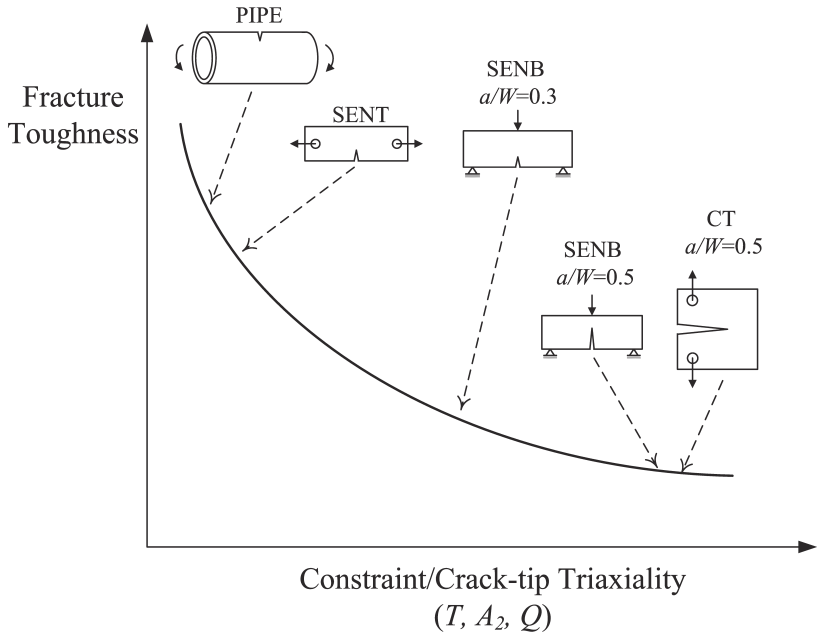

Figure 2.7. Schematic of ranking different cracked configurations based on their respective crack-tip constraint; after Chiesa et al. [76].

the lowest fracture toughness of the material. 2PFM formulations and the insight they have provided on crack-tip constraint, render the traditional approach of using high constraint fracture specimens as overly conservative. In the context of 2PFM and based on a detailed constraint match study, a more suitable (and probably more economical) specimen can be selected to determine the fracture toughness data of a material for assessment of a cracked structure of interest. The concept of constraint matching is schematically shown in Figure 2.7 (after Chiesa et al. [76]).

Pisarski and Wignal [77] and also Nyhus et al. [78] both investigated and compared the J-Q trajectories of three systems, namely (i) a typical cracked pipeline subject to plastic bending, (ii) SENT specimens with crack depth same as the pipes (e.g. constraint matched SENT) and (iii) traditional deeply cracked SENB specimens. Both of these studies showed similarity of the J-Q trajectory between the pipe and the constraint matched SENT. Based on these, DNV [9] recommends the use of constraint matched SENT specimens for fracture assessment of reeled pipelines. It is noted that both mentioned studies do not include detailed near-tip *field matching*, which is mandatory for the applicability of a 2PFM approach [56]. Based on close examination

of J-Q trajectories, Cravero and Ruggieri [79] and Silva et al. [80] demonstrated the suitability of constraint-matched SENT specimens for fracture assessment of high pressure pipelines with axial flaws. In the spirit of these works and also by including detailed field matching studies, the crack-tip constraint in cracked pipelines subject to extreme plastic bending will be investigated in Chapter 7 of this thesis.

2.6 Numerical Simulation of Ductile Crack Growth

The *phenomenological* approach to fracture (such as the J-integral approach in EPFM) which has been discussed thus far, forms the backbone of the current fracture assessment procedures such as BS7910 [8] and DNV [9]. However, it would be highly desirable to directly model the process of ductile crack growth in the cracked configuration of interest. Such an explicit analysis can, for example, directly provide information on the fracture failure mode of a structure (rather than using Equation (2.12) to assess the stability of crack growth). As another example, R-curves could be simulated in lieu of experimental setups (which might be increasingly costly or even impossible for full-scale structures). The backgrounds of numerical techniques of crack growth simulations in a FE framework would be reviewed, and its relevance to the present thesis will be discussed in what follows.

2.6.1 Mechanism of Ductile Fracture in Metals

It is commonly agreed that the mechanism of ductile fracture in metals is described by the sequence of void nucleation, growth and finally coalescence [16]. The small impurity particles which are virtually always present in a metallic material serve as nucleation sites for micro-voids. The nucleation of a micro-void occurs when the stress applied is sufficient to break the particle to matrix interface bond, or break the particle itself [16].

The plastic strain and mean stress (hydrostatic stress) cause enlargement of the microvoids. Further growth would lead to coalescence of neighboring voids, which is caused by a necking or slipping mechanism in the ligament between two enlarged neighboring voids, and is mainly controlled by plastic strain. Successive coalescence

of neighboring voids leads to crack growth and finally, rupture of the uncracked ligament [16]. The sequential steps leading to ductile fracture in a material are shown in Figure 2.8 (from Ref. [16]).

McClintock [81], and Rice and Tracey [82] studied the growth of a single void in a rigid-plastic infinite continuum subject to a triaxial stress field. Both studies showed that the growth rate of the void follows an exponential function of stress triaxiality (σ_m/σ_e). Rice and Tracey [82] developed the following semi-empirical equation for the growth of an initially spherical void:

$$\ln\left(\frac{\bar{R}}{R_0}\right) = 0.283 \int_0^{\varepsilon_p} \exp\left(\frac{1.5\sigma_m}{\sigma_y}\right) \mathrm{d}\varepsilon_p \tag{2.27}$$

In Equation (2.27), $\bar{R}$ is the mean radius of the void, since the initially spherical void can deform to an ellipsoid. Moreover, for strain hardening materials, σ_y in Equation (2.27) should be replaced by σ_e [16]. Anderson et al. [83] used Equation (2.27) to formulate a local *damage integral* (Φ_D), hypothesizing that ductile failure occurs upon the void radius reaching a critical value:

$$\Phi_D = \int_0^{\varepsilon_p} \exp\left(\frac{1.5\sigma_m}{\sigma_e}\right) \mathrm{d}\varepsilon_p \tag{2.28}$$

Building upon the approach of Anderson et al. [83], the damage integral is incorporated in Chapter 6 of this study to investigate the effect of the materials Lüders plateau on their fracture toughness, as mentioned in Section 2.3.

2.6.2 The Voided Plasticity Material Model

The key ingredient in developing a FE model capable of direct simulation of ductile crack growth is a constitutive material model that can incorporate the effect of ductile damage (i.e. void nucleation, growth and coalescence as discussed) on the response of the material. Commonly, the Mises yield potential (J_2 plasticity[13]) is used to describe the plastic flow of metals, while an associated flow rule describes the relationship between the increments of stress and plastic strain. The J_2 incremental plasticity theory only considers the Mises stress (the second invariant of the stress tensor, J_2) in

[13]The equivalent Mises stress is directly proportional to the second invariant of the stress tensor, J_2, hence the name J_2 plasticity.

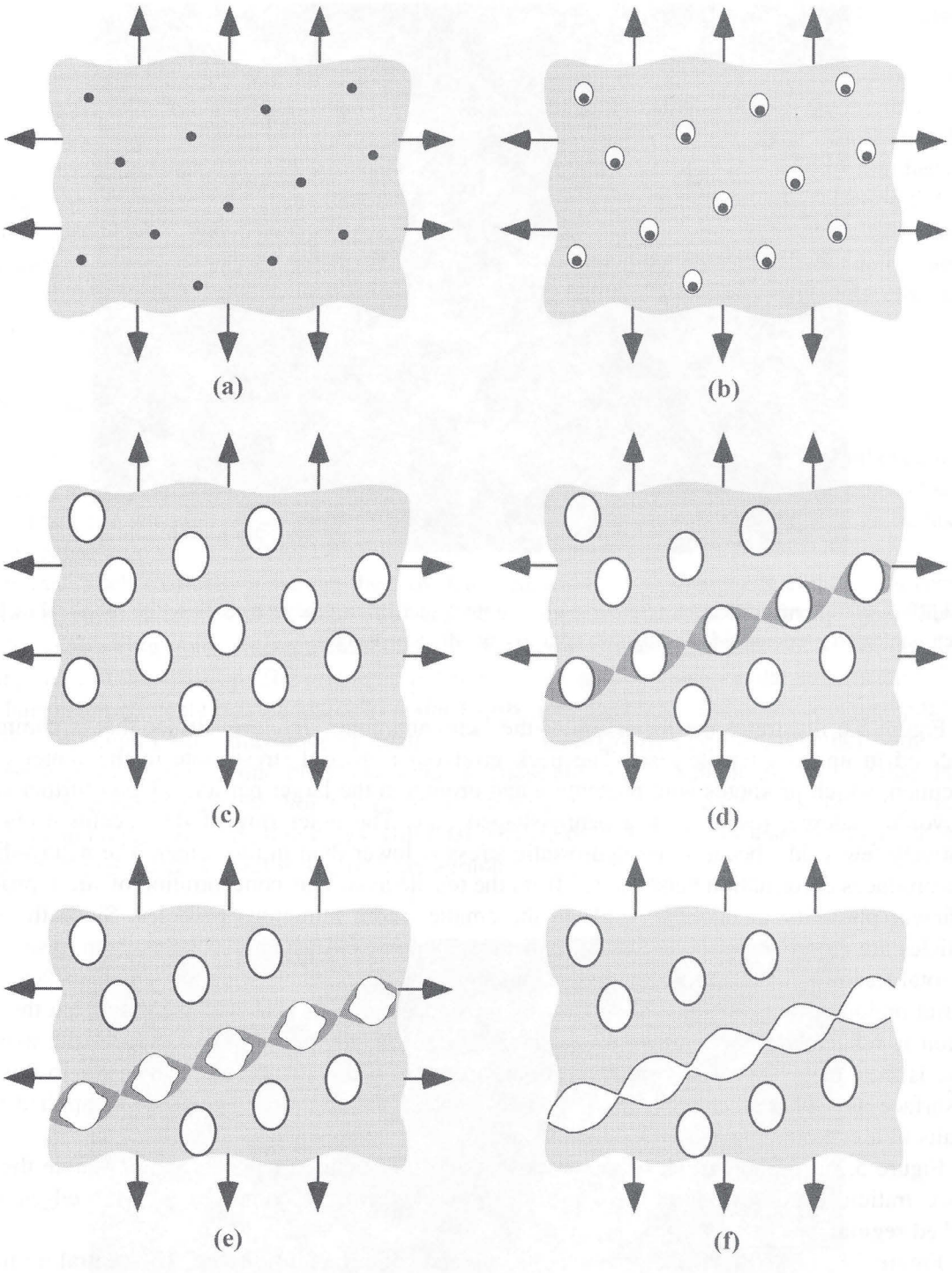

Figure 2.8. Schematic of the ductile fracture sequence: (a) inclusions in the material (b) void nucleation (c) void growth (d) strain localization between voids, (e) necking between voids, and (f) void coalescence and fracture. Taken from Ref. [16].

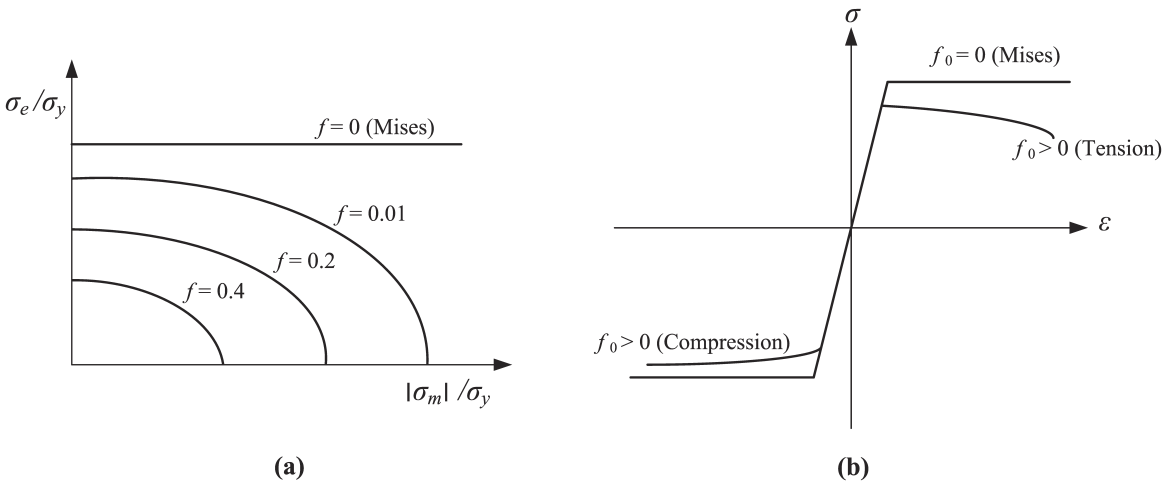

Figure 2.9. Schematic comparison of void-free and voided materials, **(a)** yield surfaces in the σ_m-σ_e space, and **(b)** uniaxial stress strain curves in tension and compression. Both figures from Ref. [10].

yielding and plastic flow of the material. However, void growth which is the prominent factor in ductile damage and fracture, is mostly governed by the mean stress (the first invariant of the stress tensor), σ_m, or, more generally, stress triaxiality (σ_m/σ_e).

Gurson [84] considered a continuum (matrix) which contained an initial void. Using the upper-bound plasticity theorem, he showed that the yield potential of such a material could be approximated by the following function:

$$\Phi(\sigma_e, \sigma_m, \sigma_f, f) = \left(\frac{\sigma_e}{\sigma_f}\right)^2 + 2q_1 f \cosh\left(\frac{3q_2\sigma_m}{2\sigma_f}\right) - \left(1 + q_3 f^2\right) = 0 \qquad (2.29)$$

The first term on the RHS of Equation (2.29) is the usual J_2-plasticity yield loci, while the second and third terms introduce the effect of voids and their growth due to the mean stress σ_m. For a non-porous material (i.e. $f = 0$), the function returns back to the J_2-plasticity yield potential. Figure 2.9a (after Ref. [10]) schematically compares the yield surfaces of a void-free material (Mises or J_2 plasticity) with voided materials having various levels of void volume fraction f, in the σ_m-σ_e space. Figure 2.9b (after Ref. [10]) schematically shows the effect of void growth (larger values of f) on softening the tensile uniaxial stress–strain curve with respect to a perfectly plastic void-free material.

Gurson [84] assumed that $q_1 = q_2 = q_3 = 1$ in Equation (2.29). Tvergaard [85] showed that by setting $q_1 = 1.5$, $q_2 = 1.0$ and $q_3 = q_1^2$, a better fit to the experimental

load-displacement curves could be achieved. These values have been widely used in the literature when using the voided plasticity yield potential of Equation (2.29). However, more recently, Faleskog et al. [86] showed that the values of q_1 and q_2 would depend on both strain hardening (n) and the elastic strain limit ($\varepsilon_y = \sigma_y/E$).

Upon the application of load, the void volume fraction, f, would increase, both due to enlargement of the existing voids, and also, to a lesser extent, due to nucleation of new voids. Thus the rate of void volume fraction increasing would be:

$$\mathrm{d}f = \mathrm{d}f_{gr} + \mathrm{d}f_{nucl} \tag{2.30}$$

The matrix material surrounding the void undergoes an incompressible plastic flow (due to the incompressibility of plastic deformation). Thus, based on the law of conservation of mass, the growth rate of the existing voids would be related to the incremental volumetric plastic strain components:

$$\mathrm{d}f_{gr} = (1 - f)\ \mathrm{d}\varepsilon^p_{ii} \tag{2.31}$$

Needleman and Rice [87] proposed an empirical equation to approximate the void growth rate caused by nucleation of new voids as a function of mean and flow stress rates and equivalent plastic strain rate:

$$\mathrm{d}f_{nucl} = A_1\,\mathrm{d}\varepsilon_p + A_2(\,\mathrm{d}\sigma_f + \,\mathrm{d}\sigma_m) \tag{2.32}$$

Chu and Needleman [88] assumed a normal distribution for the rate of void nucleation intensity. Based on this, for strain controlled nucleation (in which $A_2 = 0$), the coefficient A_1 reads [88]:

$$A_1 = \frac{f_n}{s_n\sqrt{2\pi}} \exp\left[-\frac{1}{2}\left(\frac{\varepsilon_p - \varepsilon_n}{s_n}\right)^2\right] \tag{2.33}$$

while for stress controlled nucleation (in which $A_1 = 0$), A_2 would read:

$$A_2 = \frac{f_n}{s_n\sqrt{2\pi}} \exp\left[-\frac{1}{2}\left(\frac{\sigma_f + \sigma_m - \sigma_n}{s_n}\right)^2\right] \tag{2.34}$$

where ε_n and σ_n are the mean nucleation strain and stress, respectively, and s_n is the standard deviation.

The voided plasticity material model along with the void growth rate rules as defined above can be used to model ductile crack growth. The assumption that neighboring voids do not interact is implicit in such an approach. On the contrary, the final phase of an increment of ductile crack growth includes necking of the matrix between two neighboring voids, leading to the final coalescence. This last phase is marked by a rapid loss of stress carrying capacity of the element. As per Equation (2.29), the voided material loses its stress bearing capacity upon the void volume fraction f reaching $1/q_1$. Even assuming Tvergaard's [85] suggestion of $q_1 = 1.5$ (rather than Gurson's original $q_1 = 1$), means that the void volume fraction at failure is 66.7% ($f_F = 1/1.5 = 0.667$). This value by far exceeds the realistic values of f_F observed in tests; in fact, once the void volume fraction reaches 10 to 20%, only a minimal increase in the nominal strain could cause fracture [16]. To account for these effects, Tvergaard and Needleman [89] introduced a modification to the original Gurson yield potential, which introduces a rapid loss in stress carrying capacity of the material for $f > f_c$ (hence, the model is commonly referred to as the Gurson-Tvergaard-Needleman (GTN) model). They suggested using f^* instead of f in Equation (2.29), defined as:

$$f^* = \begin{cases} f & \text{for } f \leqslant f_c, \\ f_c + \dfrac{f_F^* - f_c}{f_F - f_c}(f - f_c) & \text{for } f_c < f < f_F, \\ f_F^* & \text{for } f \geqslant f_F. \end{cases} \tag{2.35}$$

where $f_F^* = (q_1 + \sqrt{q_1^2 - q_3})/q_3$. Considering that it is common to take $q_3 = q_1^2$, it is seen that $f_F^* = 1/q_1$). The void volume fraction at initiation of void coalescence is denoted by f_c, while f_F represents the void volume fraction at final fracture where the stress carrying capacity of the element vanishes.

Zhang et al. [90] performed plane strain FE analysis of a unit cell containing an initial hole (representing a hypothetical void) which was subject to a biaxial stress state (with $\sigma_x = 0.3\sigma_y$). Upon growth of the hole, a neck forms. Final fracture of the unit cell was defined as the load level in which the dimension of the neck approaches zero. Based on this analysis they provided the following empirical formula for evaluation of f_F:

$$f_F = 0.15 + 2f_0 \tag{2.36}$$

The parameters required for calibration of the GTN model for a specific material are usually determined by fitting load-displacement curves of tests with FE model predictions [91].

Zhang et al. [90] incorporated the limit load of Thomason [92] to predict the coalescence of neighboring voids, and termed the approach as the Complete Gurson Model (CGM). Thomason's criterion is based on the limit load of a necking mechanism between neighboring voids. For a 3D state, the criterion predicts coalescence when [90, 92]:

$$\frac{\sigma_1}{\sigma_f} = \left[\varphi_1 \left(\frac{1}{r_v} - 1\right)^2 + \frac{\varphi_2}{\sqrt{r_v}}\right](1 - \pi r_v^2) \tag{2.37}$$

where σ_1 is the current maximum principal stress at the material point, r_v is the void space ratio, $r_v = \sqrt[3]{(3f/4\pi)e^{(\varepsilon_1+\varepsilon_2+\varepsilon_3)}}/(\sqrt{e^{(\varepsilon_2+\varepsilon_3)}}/2)$ and ε_1, ε_2 and ε_3 are the principal strains ($\varepsilon_1 > \varepsilon_2, \varepsilon_3$), $\varphi_1 = 0.1$ and $\varphi_2 = 1.2$ are constants fitted by Thomason [92]. In the CGM approach, direct definition or calibration of f_c is not required, regarding that Equation (2.37) predicts coalescence and f_c is an outcome of the model. However, the simple area reduction model (necking mechanism) inherent in Equation (2.37) and the CGM approach is far too simplistic to capture the complex void interactions leading to coalescence [16]. Hence, use of the CGM approach does not necessarily enhance the accuracy of the solution (as opposed to using the GTN model without the CGM extension).

2.6.3 Further Simplification: The Cell Model Approach

In a series of papers, Xia and Shih [93–95] stated that a more feasible modeling approach could be achieved by using the GTN material definition to describe only the region corresponding the initial crack plane, ahead of the crack tip (the so-called row of voided cells), while using a conventional elastoplastic material definition to model the remainder of the body. This approach was supported by experimental data of ductile crack growth in most metals that exhibit a planar propagation path (see Figure 2.10a for a schematic of planar ductile crack growth. Figure 2.10 is taken from Ruggieri et al. [96]). They further stated that the size of the GTN elements (D_0) used to model the crack front should be in the micro-level order, thus, roughly representing the average

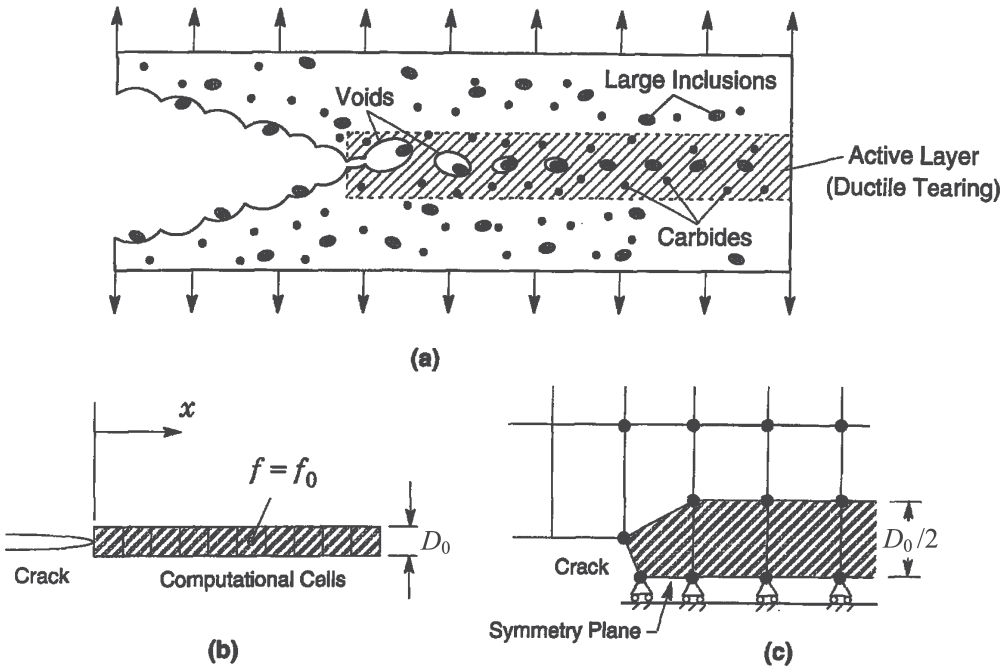

Figure 2.10. Schematic of the *cell model* approach to ductile crack growth, **(a)** void growth and coalescence ahead of the crack tip, **(b)** arrangement of the *void cells* ahead of the initial crack tip and **(c)** arrangement of the crack tip in a FE mesh. From Ruggieri et al. [96].

spacing between large inclusions (voids) in the material, ahead of a crack. In other words, each element ahead of the crack is assumed to contain a single void. With this modeling approach, the crack tip element would go extinct once its void volume fraction reaches f_F, thus the crack would grow an increment equal to D_0. This process would continue till the final failure stage. Figure 2.10b shows a typical arrangement of the *voided cells* ahead of the initial crack tip, each assumed to contain a single void with an initial void volume fraction of f_0. Figure 2.10c shows the arrangement elements in an FE mesh (the size of *void cell* elements are $D_0/2$ regarding symmetry).

Xia and Shih [94] also showed that the contribution of void nucleation (due to the second phase particles) to the void volume fraction increase could be neglected, and $\mathrm{d}f$ could be assumed to be driven by the growth of the existing voids (i.e. $\mathrm{d}f = \mathrm{d}f_{gr}$ and $\mathrm{d}f_{nucl} = 0$, see Equation (2.30)). This simplification is extremely convenient, as the void growth rate due to nucleation (Equations (2.32), (2.33) and (2.34)) are still under debate. Xia et al. [97] used the *cell model* approach to establish the R-curves

of several commonly used fracture specimens, and obtained a very good agreement with experimentally determined R-curves. Ruggieri et al. [96] extended the approach to model 3D cracks in different specimens. Their results also showed good agreement with their experimental data.

Brocks et al. [91] used the GTN material model in FE simulations of static fracture tests and also dynamic Charpy tests, and observed a good agreement between their numerical and experimental results on R-curves and load-displacement curves. Chen and Lampert [98, 99] incorporated the CGM extension (to the GTN material model framework), and studied ductile tearing of SENT specimens [98] and also 3D elliptical cracks in plates [99], and obtained satisfactory agreement between their numerical and experimental results.

FE codes with an explicit solution algorithm (such as ABAQUS/Explicit [10]) could have an element removal capability, which can eliminate the damaged element from the FE mesh when $f = f_F$ and thus simulating crack growth. In the context of pipelines subject to large plastic deformations, recent research by Sandvik et al. [100] and Dybwad et al. [101] both presented comparison of full scale test results on pipelines to predictions of nonlinear FE models (utilizing the cell model approach coupled with the element removal technique to accommodate ductile crack growth), showing satisfactory agreement.

2.6.4 Fracture Failure Mode & Constraint in Pipelines Undergoing Ductile Crack Growth

Strictly speaking, the various 2PFM constraint theories as reviewed in Section 2.4 are based on the analysis of a stationary crack. O'Dowd et al. [102] analyzed stress fields ahead of a growing crack, and observed that in configurations which have a low constraint/triaxiality before initiation of crack growth, the constraint/triaxiality would increase upon crack growth. Thus, the 2PFM theories cannot continue to characterize the near-tip fields after initiation of crack growth[14]. Moreover, to the best of the author's knowledge, up to now, no generally accepted constraint theory exists

[14]Interestingly, as noted in Section 2.4, constraint parameters have been shown to satisfactorily rank the R-curve slope of different specimens, in addition to their initiation fracture toughness values.

for characterizing the near tip stress and deformation fields ahead of a propagating crack.

A more direct approach to constraint similarity studies (to determine the suitable fracture test specimen for assessment of the engineering structure of interest) is to directly compare the R-curves of different configurations. The discussed FE methods for simulation of ductile crack growth could conveniently yield such information. A comparison on the near-tip fields ahead of a growing crack (among different configurations) would also provide additional justification for the selection of a particular test specimen for assessment of a the structure of interest.

A less attended, yet equally important issue (from practical point of view) is investigation of the crack-tip constraint under bi-axial stress fields (i.e. the pipeline subject to internal pressure and bending would have such a stress state in the pipe wall). Indeed, the question of constraint-match for such situations is an open one. Quoting DNV [9]:

> "Operation normally involves internal pressure plus axial strain i.e. a bi-axial stress state. If SENT specimens are employed for assessing the operation phase it must be substantiated, by analysis or experience, that the constraint in the pipe, under operational conditions, is not higher than in the specimen."

In consideration of crack-tip constraint as discussed above, both Cravero et al. [103] and Xu et al. [104] investigated R-curves under combined loading situations (using FE simulations of ductile crack growth). Cravero et al. [103] compared R-curves of constraint matched SENT specimens with plates subject to biaxial loading (as a simplification of a pipe subject to combined loading). Xu et al. [104] considered 2D SENT specimens and pipelines with a full circumferential crack subject to tension and internal pressure (thus enabling the use of 2D axisymmetric FE models), and again demonstrated the suitability of the constraint matched SENT specimen. With respect to a realistic cracked pipeline, both analyses are based on major simplifications in the cracked configuration geometry.

Chapter 8 of the present thesis builds up on these ideas and presents a thorough investigation on the crack-tip constraint of pipelines subject to combined bending

and internal pressure. Furthermore, the fracture failure mode of such pipes is also parametrically investigated using the same 3D FE models of pipeline which include ductile crack growth.

Some of the analyses performed in this thesis, in part target the investigation of pipelines that undergo a few load cycles of plastic straining. This is especially true for the case of reeled pipelines in which the pipeline is subjected to at least two symmetrical plastic strain cycles. DNV [9] suggests that these few pre-strain cycles do not significantly affect the fracture toughness of the steel material, and monotonic tests on specimens suffice for establishing the fracture toughness of the material. In line with the DNV recommendations, recently Tkaczyk et al. [105] experimentally investigated SENT specimens from X70 pipeline steels subject to a tension–compression–tension load cycle, and concluded that the plastic pre-strain cycle neither increases the void volume fraction ahead of the *current* crack tip, nor does it affect the fracture resistance curves (R-curves). Based on these, in chapters dealing with fracture response characteristics (such as Chapters 6, 7 and 8), a monotonic loading is considered. Nonetheless, it is believed that the issue of the effect of pre-strain on the fracture response is still under debate, with the possibility of new conclusions to be drwan in the future.

Chapter 3

A Comprehensive Parametric Finite Element Study on the Development of Strain Concentration in Concrete Coated Offshore Pipelines

Nikzad Nourpanah and Farid Taheri

Department of Civil and Resource Engineering, Dalhousie University, Halifax, Nova Scotia, Canada, B3J 1Z1.

Accepted for publication in ASME Journal of Pressure Vessel Technology.

3.1 Abstract

The strain concentration at the field joint (FJ) of the commonly-used concrete coated offshore pipelines is considered and discussed in this paper. The details of a 3D finite element (FE) modeling framework, developed using the commercial software ABAQUS, are presented. The numerical results are verified against the experimental results available in the literature. The FE model considered in this study captures several nonlinear phenomena associated with the problem, including the plastic deformation of the steel and anti-corrosion layer (ACL) material, the cracking and crushing of the concrete and also the large deformation effects. The developed FE framework is subsequently used to perform a parametric study to assess the effect of each influencing parameter on the strain concentration factor (SCF) developed within the FJ region. The influence of the geometric features of the coated pipe and the relevant mechanical properties of the materials, as well as various combined loading scenarios are investigated. As well, the influence of the post-yield properties of steel (especially, steel's strain hardening capacity) is also considered. Results indicate that pipeline diameter, thickness and coating thickness affect the SCF more than the strength of either concrete coating or ACL. The combination of the internal pressure loading or

tensile loading with the primary bending load (causing a biaxial stress state), is found to also increase the SCF significantly after steel yielding is initiated. Moreover, these combined loading scenarios cause different and more severe plastic deformation patterns in the FJ.

Keywords: Concrete Coated Pipelines, Strain Concentration, Combined Loading, Inelastic Bending

3.2 Introduction

Strain Based Design (SBD) is an established and accepted approach for design of pipelines [12], and is also well documented in several of the leading pipeline design codes (e.g. DNV [2] and API [3]). SBD can be used whenever the loading on the structure is of a displacement nature, which holds true for offshore pipelines, for which the most critical loading conditions are displacement controlled (e.g. pipelines deformed to conform to curvature of a stinger or reel drum, or conformation to the bathymetry of a rough seabed, and/or those due to seismic events). Under such conditions, the plastic capacity of steel can be safely utilized, resulting in major cost savings in comparison to the traditional stress-based design methods. However, utmost care should be exercised in calculating the strains. This is due to the fact that at high levels of strain, there is a risk for fracture of the material, initiated - for example- by defects in the girth welds. In this regards, all pipeline design codes require more stringent criteria for material selection and testing/quality assurance procedures for pipelines that undergo large strains. For example, DNV [2] requires the so-called *Engineering Criticality Assessment* for establishing defect and tolerance criteria for pipelines undergoing plastic strain exceeding 0.3% (common for pipelines installed with stinger in deep waters); it also requires additional material specifications when the accumulated plastic strain exceeds 2% (common to pipelines installed by the reeling method).

In the context of SBD, all causes of strain concentration should be considered during a design. Within this category, the strain concentration at field joints of concrete coated pipelines subject to bending is a well-known phenomenon. Upon a survey of the literature, the research on this topic conducted thus-far, can be classified as: (i) experimental investigations [18–21, 106], (ii) semi-analytical formulations [22, 23, 106, 107],

(iii) finite element (FE) simulationsc̃itependal94 (iv) FE formulations [25], and finally (v) design equation development based on FE analysis results [108]. One of the notable works is the iterative semi-analytical model of Ness and Verley [23, 106], which was validated against experimental results and FE simulations of Endal [24]. The semi-analytical model of Ness and Verley [23, 106] is an extension of Lund et al.'s model [22]. The difference in the two models is only the inclusion of the slippage of coating on the steel pipe in the former model. The aforementioned model includes the most major nonlinearities of the problem, except the post-crushing behavior of the concrete coating.

In this paper, the FE simulation of the problem is considered as an alternative to the experimental and semi-analytical approaches. Using the developed FE modeling framework, a benchmark FE model is constructed based on the experimental data of Ness and Verley [106], and the response characteristics are compared to establish the robustness of the FE framework. Furthermore, this FE modeling framework would be utilized to conduct a parametric study with the aim of investigating the effect of different geometric, material and loading parameters on the resulting strain concentration and its variation as a function of the applied bending load.

3.3 Mechanics of Strain Concentration

Offshore pipelines normally consist of a series of 12-m long linepipes, girth welded together either onshore or offshore on an installation vessel. The resulting *pipe string* is lowered on the seabed over a stinger. The pipe string can be considered as an infinitely long beam subject to (mainly) bending load. Each pipe joint is covered with an anticorrosion layer (ACL). Hot asphalt was widely used as ACL in the past; while currently, fusion bonded epoxy is preferred due to environmental restrictions [109]. Except for the pipelines with very low diameters, most pipelines are required to have a concrete coating. The primary objective of this coating is to provide negative buoyancy to the pipeline and enhance its stability when laid on the seabed. A subsidiary function of the concrete coating is to cover the ACL and provide a mechanical protection for it [2, 15]. As seen in Figure 3.1a (adopted from Ref. [110]), approximately a 350 mm long portion (at each end of a 12-m linepipe), is left uncoated for welding

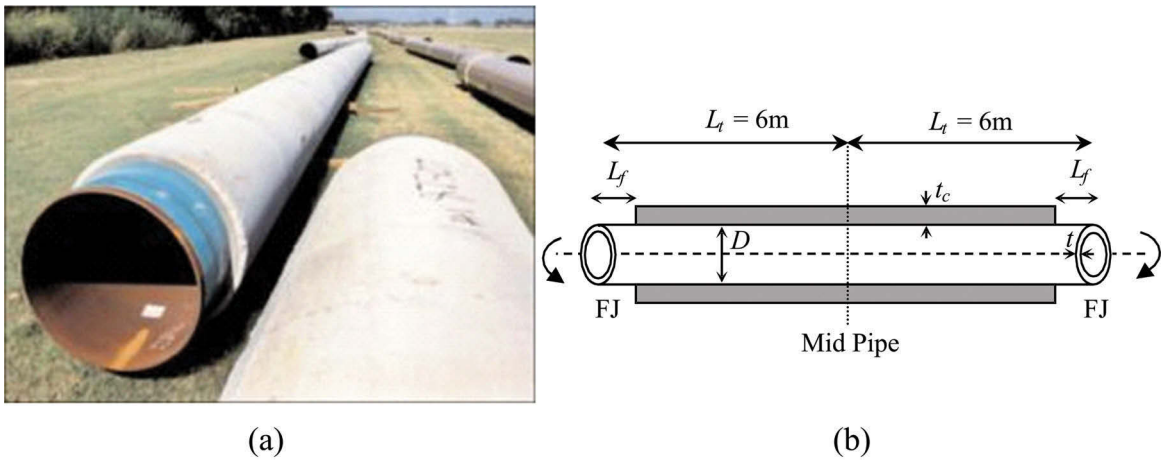

Figure 3.1. (a) Typical concrete coated pipes with their field joint (FJ) regions (from Ref. [110]) and **(b)** Schematic of a coated linepipe with the relevant dimensions and identifiers.

purposes at the so-called *Field Joints* (FJ). The concrete coating stiffens the pipe section, except at the FJ region. A schematic of the described pipe is also shown in Figure 3.1b.

Upon the application of bending, the regions away from the FJ react as a composite section (i.e. the concrete coating stiffens the pipe section). However, as the FJ is approached, the compressive force developed in the concrete coating is transferred to the steel pipe through the shear stress developed within the ACL. The limited shear capacity of the ACL (generally $\tau_y = 0.1 \sim 0.5$ MPa [22]) can only accommodate a limited magnitude of the compressive force developed within the coating. Thus, upon increase of bending, the ACL's shear capacity would become exhausted, allowing the concrete coating to slide over the steel pipe in a small region near the FJ. The length of this *slide region* (L_{slide}) is such to provide the shear resistance in the ACL (V_{ACL}) required to transfer the axial compressive force developed in the concrete (N_c) to the steel pipe. It is outside this *transfer length* region where the classical bending assumption of *plane sections remaining plane* would hold valid.

There are essentially three distinct zones in the system, namely: (i) the FJ, where only the bare steel pipe bears the applied bending moment, (ii) a region sufficiently far from the FJ, where the stiffness of the concrete coating is fully utilized (also where the *plane section* assumption would hold), and (iii) the transfer zone in between

these two regions, whose bending stiffness varies between the two mentioned limits. Being subject to a (nearly) constant moment along the pipeline length, the steel material in zone (i) would be subjected to a larger magnitude of strain in comparison to the stiffer zones (ii) and (iii), thus giving rise to a strain concentration in the FJ and the nearby region where sliding occurs. This concept is illustrated via the schematic moment-strain curves of the FJ and coated pipe as depicted in Figure 3.2. For practical purposes, the provision of the Strain Concentration Factor (SCF) would be beneficial. The SCF would indicate the severity of the strain concentration in the FJ. In this paper, SCF's definition suggested by Igland and Moan [111], as presented by the following equation, is adopted:

$$\mathrm{SCF} = \frac{\varepsilon_{\mathrm{FJ}}}{\varepsilon_g} \tag{3.1}$$

In equation (3.1), $\varepsilon_{\mathrm{FJ}}$ is the tensile bending strain in the FJ. An average definition of the bending strain along the tensile chord in the FJ zone is used in order to achieve a more robust definition of the SCF. Thus, $\varepsilon_{\mathrm{FJ}}$ is calculated by integrating the tensile bending strain along L_{FJ}:

$$\varepsilon_{\mathrm{FJ}} = \frac{1}{L_{\mathrm{F}}} \int_0^{L_{\mathrm{F}}} \varepsilon_{11}\, \mathrm{d}x \tag{3.2}$$

Furthermore, the global bending strain, ε_g, in Equation (3.1) could be calculated by the Euler beam theory. For a pipe under pure bending the strain can be calculated by:

$$\varepsilon_g = \frac{\kappa D}{2} = \frac{R_z D}{2L_t} \tag{3.3}$$

It is acknowledged that Equation (3.3) and its underlying assumptions are not strictly correct, since materials undergo plasticity. In addition, in the vicinity of the FJ, where the cross section of the pipe rapidly changes, again the underlying assumption of Equation (3.3) would not be strictly correct. However, for the relatively small levels of inelastic bending that will be considered in this study ($\varepsilon_g \cong 0.3\%$), and also in view of the small length of the FJ as compared to linepipe's length, the errors associated with the use of Equation (3.3) would be negligible. For a more robust

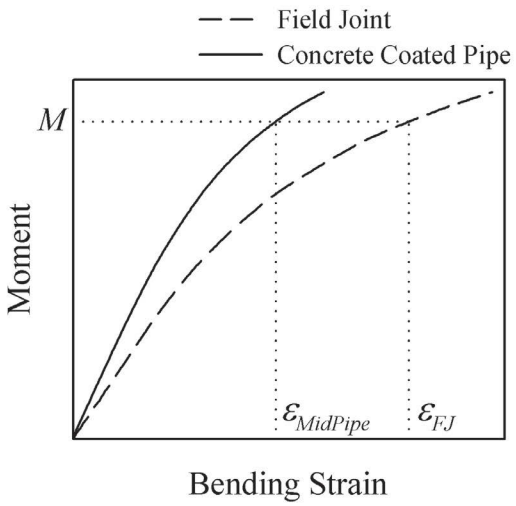

Figure 3.2. Schematic illustration of the moment-strain variation within a typical coated pipe and its FJ region, resulting into strain concentration.

definition of SCF, one can use the average value of the tensile bending strain, ε_{ave}, instead of ε_g in Equation (3.1). ε_{ave}, along the linepipe length, is defined as:

$$\varepsilon_{ave} = \frac{1}{L_t} \int_0^{L_t} \varepsilon_{11} \, \mathrm{d}x \tag{3.4}$$

Under the application of pure bending, the value of ε_{ave} (extracted from FE results) and ε_g would be very similar (e.g. $\varepsilon_{ave}/\varepsilon_g < 1.03$ for all cases considered in the parametric study in which pure bending was considered). Thus, for the pure bending case-studies, the magnitude of ε_g that was used to establish the SCF (i.e. Equation (3.1)), was calculated per Equation (3.3). On the other hand, in the case-studies that considered the combined loading states (i.e. a bending load combined with an internal pressure or a tensile load), the ε_g calculated per Equation (3.3) would not correctly represent the resulting axial strain; in those situations the use of ε_{ave} as per Equation (3.4) would better represent the resulting bending strain. Therefore, for those loading cases, the relationship presented by Equation (3.4) was used to establish the value of the resulting strain.

As for the recommended target value SCF, Bai [1] recommends a SCF of 1.2 in the absence of more detailed analysis. However, Nourpanah and Taheri [108] have

however shown that for coated pipelines with grade X65 steel, this value would only be accurate for pipes that are not heavily coated, or when the bending strain is relatively low. More specifically, a SCF of 1.2 occurs only for configurations in which the dimensionless *coating parameter*, λ, is greater than 30, where the coating parameter[1] was defined as [108]:

$$\lambda = \frac{Dt}{\varepsilon_g t_c^2} \tag{3.5}$$

where ε_g should be in percentage for use in Equation (3.5).

From a practical point of view, the strain concentration phenomena would be of concern under two different scenarios with differing load levels. First and foremost, strain concentration would be of concern during pipe-laying, while the pipe string is bent over the stinger as being laid on the seabed. In the context of SBD and the displacement controlled nature of the loading, in such a case, the plastic bending capacity of the pipe section can be utilized. Thus, the relevant governing failure mode during a conventional pipe-lay would be in the form of crushing of the concrete coating [2]. In other words, bending strains should be such to avoid crushing of the concrete, which has been observed to occur at a strain of $0.2 \sim 0.3\%$ [20, 22, 107]. Such a bending strain would also induce slight inelastic bending of the steel pipe, in addition to more significant localized plasticity in the FJ due to the strain concentration effect.

The second scenario of interest would be the resulting strain concentration while the pipeline is in-service (i.e. pipeline laid on the seabed). Within this scenario, the pipeline would undergo bending due to a variety of reasons, such as: pipelines snaking (due to thermal expansions), trawl loads, and free spanning of the pipelines. For this second category, inelastic bending of the steel pipeline is usually not permitted, and thus lower bending strains, $\varepsilon_g < 0.2\%$ would be of interest.

The mentioned two loading scenarios would also develop different strain concentration responses. Upon the initiation of loading, the SCF would attain a high value, but decreasing steadily and nearly linearly as a function of the increasing global bending strains (ε_g). This decreasing trend would be due to the fact that as bending of the linepipe proceeds, the coating would start slipping over the steel pipe, and thus

[1] A complete discussion on the coating parameter can be found in Chapter 4 of this thesis

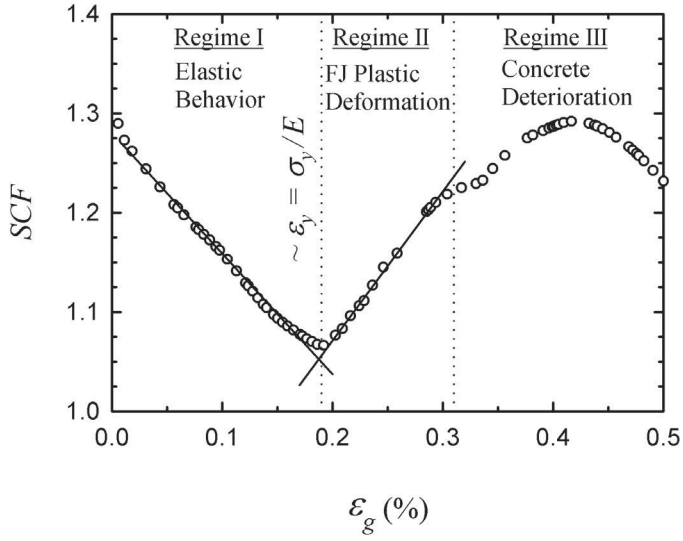

Figure 3.3. Schematic illustration of the variation of SCF as a function of the global bending strain ε_g.

reducing the SCF. This would hold true until the yielding of the steel pipe initiates. At this stage, localized plasticity in the FJ would cause the SCF to increase rapidly. Upon further increase in bending, the concrete would start crushing and its stiffness would deteriorate, thus, tending to decrease the SCF. In other words, after the concrete crushing has been initiated, two opposing factors would drive the SCF; these are the localized plasticity of the FJ, which would elevates the SCF, and the deterioration of the coating, which would relieve the SCF.

In summary, the variation of the SCF as a function of the global bending strain would go through three different regimes, as schematically depicted in Figure 3.3. Within Regime I the steel pipe would remain elastic and the strain in the coating would be less than that causing crushing. Initiation of inelastic bending in the pipe marks the beginning of Regime II, while the coating remains intact. During Regime III the coating is deteriorating, and the inelastic bending of the pipeline would be progressing. The SCF response during pipe-laying is therefore characterized by Regime II, while that within Regime I corresponds to the in-service loading conditions. Moreover, the SCF can be described rather accurately as a linear function of ε_g within both of these behavioral regimes.

There would also be several highly nonlinear phenomena associated with the bending of a concrete coated pipeline, depending on the level of loading. Two of these nonlinear aspects which would significantly influence the SCF from the early steps of loading are: (i) the inability of concrete to bear tension (concrete-cracking), and (ii) the low shear capacity of the ACL material (which results in premature yielding of the ACL within Regime I). Furthermore, the ACL behaves as a nearly perfectly plastic material after the initial leading. Upon progression of the bending strains into Regimes II and III, the elastic limit of the steel material would be surpassed, subsequently followed by the initiation of crushing of the concrete coating. In addition, the large geometry change (LGC) effect would prevail throughout the loading history.

It should be noted that the tests of Ness and Verley [106] included cyclic loading representing different stages of a pipe lay scenario (i.e. over-bend, pipeline passing over rollers, sagbend and unloading). Their results showed that the SCF attains its maximum value during the first loading peak and successive loading cycles do not result in higher levels of SCF. Based on this, in the current study montonic static loads on the pipeline are investigated[†].

3.4 Finite Element Modeling Framework

The general purpose commercial FE software, ABAQUS 6.8 [10] was used to effectively model the behavior of the system, accounting for all the mentioned nonlinearities. The constitutive relations for the ACL and steel materials could be incorporated in the 3D FE analysis based on the rate-independent associated J_2 incremental plasticity theory, in conjunction with the Mises plastic potential and isotropic strain hardening as implemented in ABAQUS [10]. Note that in general, the ACL has a visco-plastic behavior; however, this time-dependant response could be neglected during the relevant pipeline loading scenarios (short period loading).

The concrete coating is modeled with a *damaged plasticity model* of the ABAQUS. This model uses a modified Drucker-Prager yield surface, and can be categorized as a non-associated incremental plasticity model. It has the capability to model

[†]This paragraph does not appear in the published paper, and is added here to the manuscript of the thesis based on the suggestion of the examining committee.

post-cracking and post-crushing behavior of concrete in tension and compression, respectively [10], which is of interest in the present study. LGC effects were also accounted for in all the analyses. For that, ABAQUS sets up the incremental equations of equilibrium in an updated Lagrangian framework. For treatment of elasto-plasticity with consideration of LGC effects, the deformation rate is used by ABAQUS as a suitable strain measure, while its work conjugate, the Jaumann rate of the Kirchoff stress, is deployed as an appropriate stress measure [10]. However, the Cauchy (true) stress and logarithmic strains are reported as output for the sake of convenience.

As stated earlier, the noted long pipe strings are formed by a series of 12 m long pipes connected with FJs.

Therefore, it would only be necessary to model a 12 m long section in order to investigate the strain concentration variation. Furthermore, the symmetry in geometry and boundary conditions permits quarter symmetric modeling (see Figure 3.4a). The mid-pipe cross section follows the rotation of a master node, while it is constrained to remain plane but free to ovalize. The following Multi-Point Constraint formulation was used to model the conditions:

$$\tan R_z = \frac{x_j - x_{\text{mn}}}{y_j - y_{\text{mn}}} \tag{3.6}$$

where x_j and y_j are the coordinates of the j^{th} node located on the mid-pipe cross section and x_{mn} and y_{mn} are the coordinates of the master node, all corresponding to the deformed pipe. The appropriate rotation, R_z, is then imposed on the master node, causing the pipe to bend up to a level that induces the required global bending strain, ε_g, as calculated by Equation (3.3). In the cases where an axial tensile load is also considered, the load is applied on the same master node; in such a loading scenario, both the bending and tensile load would be applied simultaneously. In other cases where the internal pressure is also considered in addition to bending, a distributed pressure is defined on the inner pipe surface, while the bending load is applied only after the pipe has been pressurized. These loading scenarios are believed to be representative of most practical loading scenarios.

A total of 12,160 isoparametric, eight-node continuum elements with reduced integration and hour-glass control (C3D8R) of ABAQUS [10] were used in each pipeline model. The choice of the reduced integration technique is mandatory in this case in

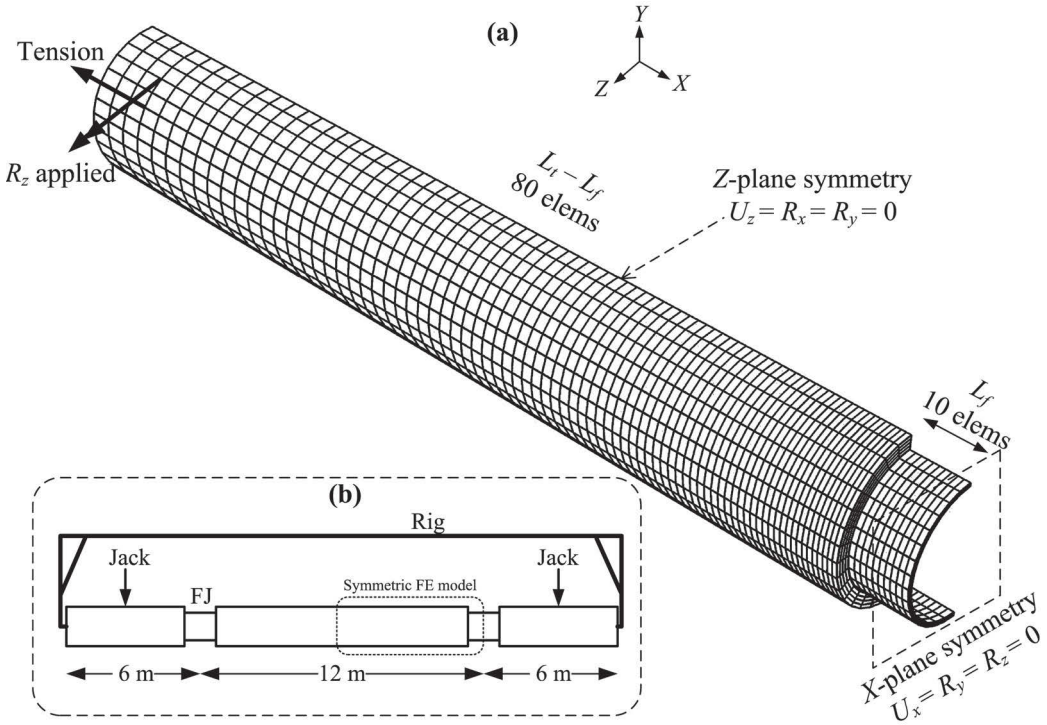

Figure 3.4. **(a)** A typical FE mesh along with the BCs ($L_t = 6000$ mm and $L_f = 350$ mm) and **(b)** Schematic of the four-point bending test setup of Ness and Verley (taken from Ref. [106]).

order to avoid the shear locking often associated with the fully integrated elements, when they are subject to bending. In order to achieve a finer mesh near the FJ where coating slippage occurs, the mesh is exponentially biased in the longitudinal direction with a ratio of 5. The concrete coating and steel pipe are each modeled with 4 elements through the thickness, while the ACL is modeled with a single layer of elements. The half-circumference was discretized by 16 rows of elements. Careful mesh convergence studies showcased the robustness of the described mesh. Figure 3.4a illustrates a general pipeline model showing the mesh characteristics and the applied loads and boundary conditions (BC).

The maximum global bending strains, ε_g, considered in this study is approximately 0.3% (covering the practical global bending strain values as depicted in Regimes I and II, shown in Figure 3.3). This level of bending would not normally cause any local buckling of the pipe wall on the compression side. This fact could be verified by comparison of ε_g with the critical buckling strain, ε_{crit}, which for example could be

roughly estimated by the following empirical formula [3, 112]:

$$\varepsilon_{crit} = \frac{t}{2D} \tag{3.7}$$

For the parametric study, it has been assumed that the uniaxial stress–strain response of the steel material could be described by an elastic response followed by a power law plasticity response, which is represented by:

$$\varepsilon = \begin{cases} \sigma/E & \text{for } \sigma \leqslant \sigma_y, \\ \varepsilon_y \left(\sigma/\sigma_y\right)^n & \text{for } \sigma > \sigma_y. \end{cases} \tag{3.8}$$

The concrete behavior is assumed to be linear elastic up to a stress of $0.45f_c^{'}$, with its modulus of elasticity calculated by [113]:

$$E_c = 4750\sqrt{f_c'} \tag{3.9}$$

Subsequent to the linear elastic part, a parabolic stress–strain relationship is adapted for establishing the compressive stress of the concrete, according to [114]:

$$f_{con} = \frac{2f_c^{'}(\varepsilon/\varepsilon_0)}{1 + (\varepsilon/\varepsilon_0)^2} \tag{3.10}$$

where ε_0 is the strain corresponding to the max stress ($\approxeq 0.2\%$ [106]). The parabolic relationship is assumed to be valid up to the ultimate strain, which is taken as 0.3% [113]. A linear descending relationship has been assumed to control the softening behavior after the ultimate strain. The complete schematic curve is presented in Figure 3.5. The tensile strength of concrete is neglected.

Usually, push-off tests are performed on a 1.5∼2 m portion of a coated pipeline, which consists of pushing off the concrete coating over the steel pipe. This is to ensure that the coating-ACL bond is stronger than the ACL material itself (i.e. ensuring shear failure would occur in the ACL) [15], in addition to documenting the shear strength of the ACL material, τ_y. Noting that such a test resembles an axisymetric stress state and by assuming a Mises failure criterion, the yield stress of the ACL material can be evaluated to be equal to $\sqrt{3}\tau_y$, which is used hereby to establish the uniaxial stress–strain response of the ACL material. To overcome FE convergence issues, a very low strain hardening capacity is assumed for the post-yield response. The elastic modulus of ACL is assumed to be $^1/_{100}$ of steel.

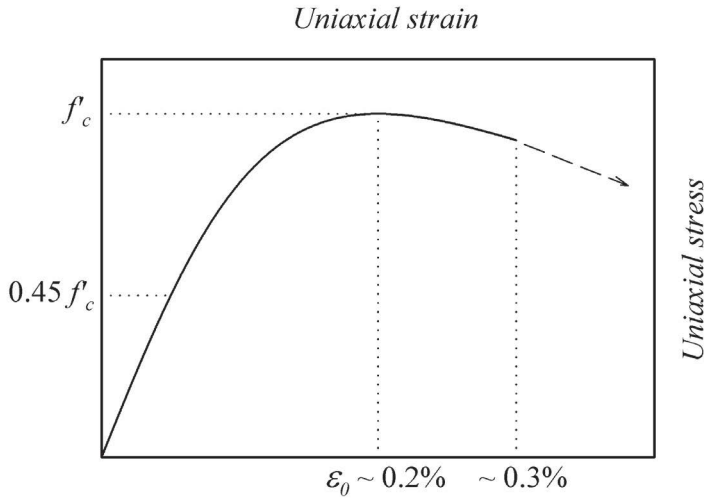

Figure 3.5. Schematic uniaxial stress–strain response of concrete.

Table 3.1. Specifics of the concrete coated pipeline benchmark model.

D (mm)	t (mm)	t_c (mm)	t_{ACL} (mm)	$f_c^{'}$ (MPa)	τ_y (MPa)
517	18.5	80	6	36.4	0.5

3.5 Benchmark Model and Verification

Ness and Verley [106] conducted a series of 4-point bending tests on concrete coated pipelines. In order to verify the above described FE modeling framework, a FE model of Test #3 of Ness and Verley [106] is developed here, and the representative response characteristics are compared. The coated pipeline features are presented in Table 3.1. A schematic diagram of Ness and Verley's [106] test setup is shown in Figure 3.4b as a means for comparison to the FE model shown in Figure 3.4a. The pipeline was loaded up to a global bending strain of $\varepsilon_g = 0.33\%$, as per the benchmark test.

Uniaxial stress–strain curve of the steel material was back-calculated from the global moment-strain response found in Ref. [106]. Comparison of the bending moment-strain response is presented in Figure 3.6, with the moment being normalized with respect to the fully plastic moment of the pipe, $M_p = \sigma_y D^2 t$, with $\sigma_y = 450MPa$. The *equivalent* curve in the figure is obtained by averaging the Moment-strain response

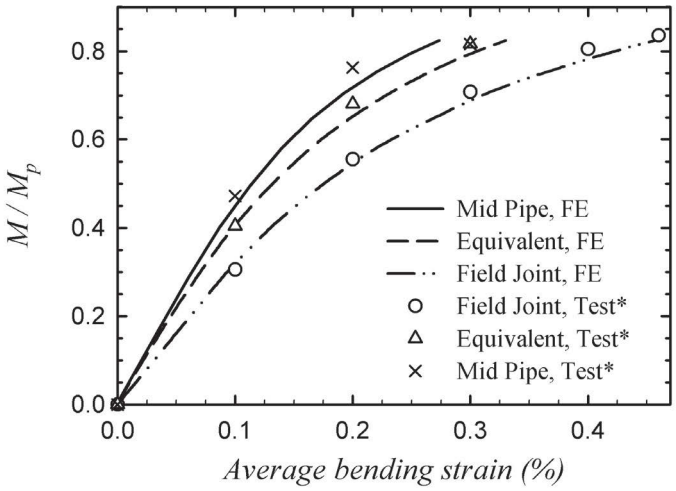

Figure 3.6. Moment-strain response of the benchmark pipeline model. *Symbols represent the experimental data of Ness and Verley [106].

at several sections along the pipeline. As seen, a very good agreement between the FE results and the test data is observed within the field joint region, while the agreement is slightly less favorable for the mid-pipe region, especially at the higher bending strains (as identified by the mid-pipe curve). This could be due to the fact that at this stage in the experiment, the concrete coating had started crushing [106]. Moreover, the maximum moment evaluated by the FE model is in the same order of that observed experimentally (i.e. $\approxeq$ 1800 kN-m). Based on these observations, the FE model is deemed capable of capturing the global bending response with acceptable accuracy.

As a local response characteristic, the distribution of the average bending strain along the pipe length, starting from pipe's mid-span ($x/L_t = 0$, see the schematic in Figure 3.7) up to the FJ ($x/L_t = 1$) is illustrated in Figure 3.7 for six successive values of ε_g, ranging from 0.05% to 0.33%. At regions near the mid-span of the pipe ($x/L_t < 0.5$), the average bending strain is nearly constant and is very near the value of ε_g. At approximately $x/L_t \approxeq 0.5$, the average bending strain starts increasing, reaching a maximum as the FJ is approached (i.e. as $x/L_t \rightarrow 1$), indicating the development of strain concentration at the FJ. The length corresponding to the region

where transition from the constant strain to the FJ strain occurs can be considered as the length in which the coating is slipping on the steel pipe (i.e. the shear capacity of the ACL is insufficient to utilize the complete bending stiffness of the coating). Thus, based on Figure 3.7, sliding occurs from $x/L_t < 0.5$ up to the FJ; so $L_{slide} \approxeq 0.5L_t - L_f$ (this results is approximately valid for all cases considered in this study). As seen, the FE results are in good general agreement with the test results, both in trend and magnitude. The test data show larger strain values than those produced by the FE model in the FJ region. Two reasons are postulated for this behavior:

1. The very high strain values observed in the test data were caused by the local plastification of steel due to the local variations in mechanical properties of steel, as explained by Ness and Verley [106]. This is supported by the fact that other local high strain regions were also observed in the experiments [106].

2. The presence of the girth weld in the FJ would also cause additional strain concentration, for example due to the Heat Affected Zone (HAZ) of the weld.

In any case, the inclusion of such effects in the numerical model was not in the scope of the present work, and therefore, the FE model cannot predict this type of large highly localized strains. The largest discrepancies in Figure 3.7 are seen in the curves corresponding to $\varepsilon_g = 0.25\%$ and 0.33%. Again, this difference is most probably due to the concrete coating crushing, which is believed to initiate at $\varepsilon_g \approxeq 0.25\%$. Also, it should be noted that the fluctuations seen in the axial strain distribution near the mid-span of pipe ($x/L_t \approxeq 0$) in Figure 3.7 are believed to be as a result of the imposed boundary condition and are not of practical importance. The fluctuations fade away after $x/L_t > 0.1$.

Based on the observed satisfactory agreement between the experimental and benchmark model results, the FE modeling framework is deemed accurate and suitable for further use in the subsequent parametric FE study.

3.6 Parametric FE Study on Strain Concentration

The parameters affecting the variation of strain concentration can be grouped into three categories. The most important of these are the geometric features of the coated

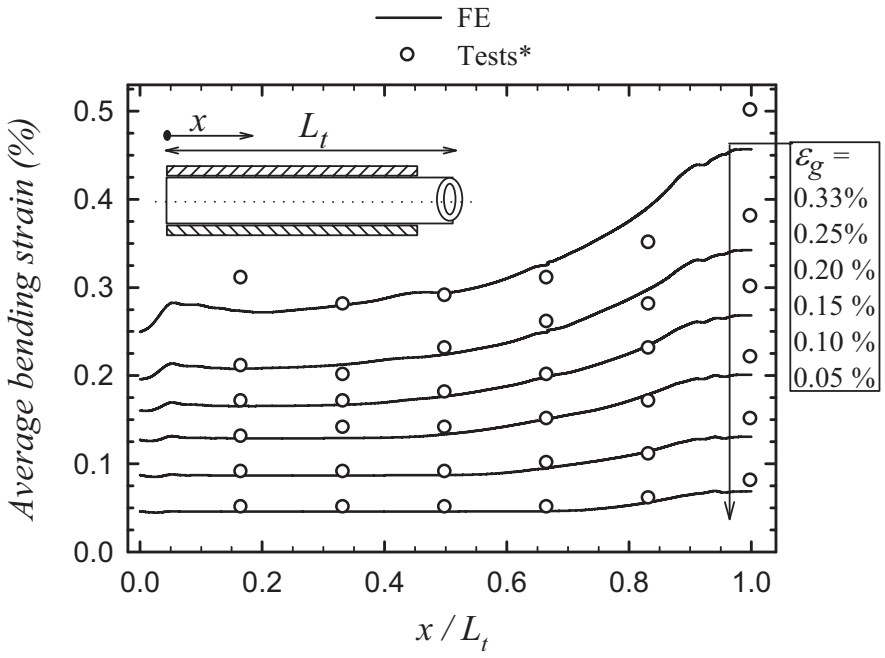

Figure 3.7. Distribution of the average bending strains along the length of pipeline. *Circles represent the experimental data of Ness and Verley [106].

Table 3.2. Specifics of the master case coated pipeline ($t = 20$ mm)

D/t	t_c (mm)	$f_c^{'}$ (MPa)	τ_y (MPa)	σ_y (MPa)	n	L_f (mm)	σ_h/σ_y	N/N_y
40	80	40	0.3	400	10	350	0	0

pipeline, which include: geometry of the steel pipeline described via D/t ratio, the thickness of the concrete coating (t_c), and the FJ length (L_f). The second category of the investigated parameters consists of the mechanical properties of the materials. These include the compressive strength of the concrete coating ($f_c^{'}$), the shear strength of the ACL (τ_y), the yield stress (σ_y) and the strain hardening index (n) of the steel material. Finally, the third category investigates the influence of the applied loading state; the effect of different levels of internal pressure and tensile load combined with the applied bending will also be considered. To initiate the parametric study, a master case is considered first, and the effect of each parameter for this case is investigated by varying that specific parameter while keeping the other parameters stationary. The characteristics of the master case coated pipeline are presented in Table 3.2.

The elastic modulus of steel is taken as $E = 200$ GPa and $\nu = 0.3$ for all models. All pipeline models are loaded up to a global bending strain of $\varepsilon_g = 0.3\%$. A brief description of the parameters considered in the parametric study is given below, with the summary of the specific values reported in Table 3.3:

- Coated pipelines with a D/t ranging from 20 to 60, in increments of 10, were considered in the parametric study.

- The investigated range for t_c was from 40 mm to 150 mm in increments of 20 mm. It should be noted that DNV [2] suggests a minimum of 40 mm coating thickness, while 150 mm is usually the maximum practical coating thickness [15].

- The range of 20 MPa to 60 MPa in increments of 10 MPa was considered for $f_c^{'}$. Note that the minimum value of $f_c^{'}$ permitted by DNV is 40 MPa [2].

- The range considered for shear capacity of the ACL was $0.1 \sim 0.7$ MPa range in increments of 0.1 MPa. This range covers the practical values in coated pipelines [22].

- The investigated pipe's yield strengths (σ_y)were from 350 MPa to 550 MPa in increments of 50 MPa. This range covers the steel grades commonly used in offshore pipelines (i.e. X52 to X80 in API-5L [34] terminology).

- To investigate the influence of the post yield response of steel, five strain hardening indices of $n = 5 \sim 25$ in increments of 5 were considered. Additionally, a perfectly plastic material was also considered (i.e. $n \to \infty$). This last material model can be regarded as a representation of the steel exhibiting a Lüders plateau, which is a feature observed in some seamless low D/t linepipes [4]. The uniaxial true stress–strain curves corresponding to this range of hardening indices is shown in Figure 3.8.

- To study the influence of FJ length, L_f was varied from 200 mm to 500 mm. However, this parameter has been seen to have negligible effect on the SCF.

- The influence of the applied loading was considered in twofold:

Table 3.3. Summary of the parameters and their variation range considered in the study ($t = 20$ mm).

Parameter	Range	Increment
D/t	$20 \sim 60$	10
t_c (mm)	$40 \sim 150$	20
$f_c^{'}$ (MPa)	$20 \sim 60$	10
τ_y (MPa)	$0.1 \sim 0.7$	0.1
σ_y (MPa)	$350 \sim 550$	50
n	$5 \sim 25, \infty$	5
σ_h/σ_y	$0 \sim 0.8$	0.1
N/N_y	$0 \sim 0.9$	0.1

(i) The effect of internal pressure combined with the applied bending was investigated by varying the pressure ratio σ_h/σ_y from 0 to 0.8 in increments of 0.1 (identified as B+P load case). It was assumed that the internal pressure is related to the hoop stress (σ_h) via the thin-wall formula (i.e. $p(D/t - 1) = 2\sigma_h$).

(ii) The effect of axial tensile load combined with the applied external bending was investigated through varying the magnitude of the applied load ratio N/N_y from 0 to 0.9 in increments of 0.1 (identified as B+T load case).

The mentioned parameters are believed to be the most significant ones, while other parameters such as the rebar or steel cage in the concrete coating (with the usual cross section area amounting to $1 \sim 3\%$ of concrete's cross-section area) are known to have marginal effect on SCF [15, 22].

In order to increase the efficiency of the analyses, in-house Python scripts were developed in the ABAQUS environment to automate and expedite the large amount of pre and post-processing efforts involved with such parametric FE studies.

3.7 Parametric FE Study Results and Discussion

The influence of D/t is illustrated in Figure 3.9. Coated pipes with lower D/t exhibit larger SCF in both Regimes I and II. This is due to the fact that since the coating

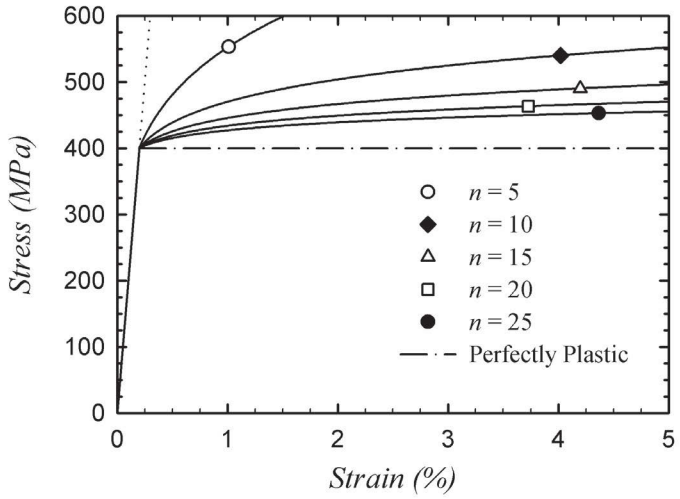

Figure 3.8. Uniaxial true stress–strain response of the steel for the considered range of strain hardening indices.

thickness is fixed at the master case value ($t_c = 80$ mm), a reduction in D/t results in a lower bending stiffness of the steel pipe compared to the coating. The increase of SCF with decreasing values of D/t becomes more pronounced for higher values of ε_g.

Figure 3.10 shows the effect of coating thickness, t_c (normalized by the minimum allowable thickness, $t_{c,\,\min} = 40$ mm) on the variation of SCF. For $t_c/t_{c,\,\min} > 1.5$, the coating thickness affects the SCF in a rather linear manner for all the values of ε_g considered. The slope of the family of curves presented depends on the magnitude of the applied global bending strain. Interestingly, the lowest slopes occur for values of $\varepsilon_g = 0.15\%$ and 0.2%, which approximately corresponds to the global strain at the transition point of Regime I to II. The effect is most severe for the lowest and also highest values of ε_g in the two loading regimes considered, respectively.

The effect of concrete coating's compressive strength, $f_c^{'}$, on SCF is illustrated in Figure 3.11. It is evident that concrete coatings with a relatively higher compressive strength tend to increase SCF; this effect is however modest for values of $f_c^{'}$ grater than 40 MPa. The effect of $f_c^{'}$ on SCF is twofold. Firstly, $f_c^{'}$ increases concrete's elastic modulus, E_c, and hence the coating's bending stiffness and the SCF. This effect is more pronounced at the beginning of Regime I loading in which the elastic

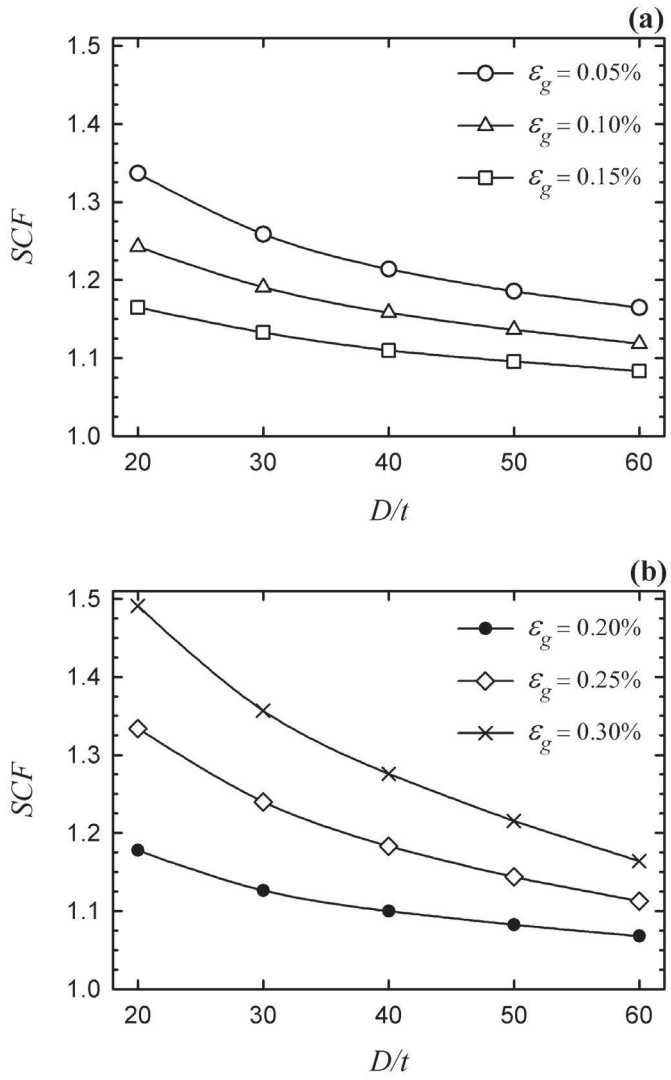

Figure 3.9. Effect of D/t on SCF for **(a)** Regime I loading and **(b)** Regime II loading.

bending stiffnesses govern the strain concentration behavior. Secondly, $f_c^{'}$ increases the maximum axial compressive capacity of the coating (N_c) which in turn increases the SCF at the end of Regime II loading. In accord with this explanation, it is observed that the curves corresponding to the beginning of Regime I ($\varepsilon_g = 0.05\%$ curve) and the end of Regime II ($\varepsilon_g = 0.3\%$ curve) in Figure 3.11 are most affected by changes in $f_c^{'}$.

Figure 3.12 illustrates how the increasing values of ACL's shear strength, τ_y, cause the SCF to increase within all loading regimes. This effect, however, is very minor for

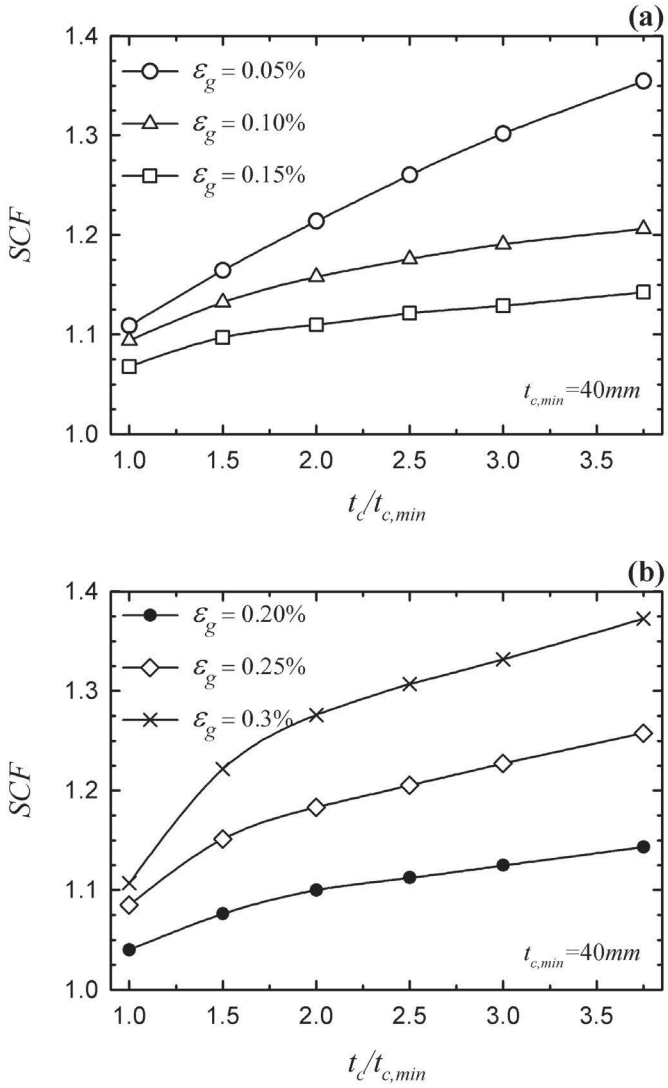

Figure 3.10. Effect of the coating thickness on SCF in **(a)** Regime I loading and **(b)** Regime II loading.

$\tau_y > 0.5$ MPa, for which the curves show an asymptotic behavior. This suggests that for $\tau_y \cong 0.5$ MPa, the shear force developed in the ACL can fully accommodate the maximum axial compression developed in the concrete coating and further increase in τ_y does not affect the SCF. Indeed, if the maximum shear force developed in the ACL (V_{ACL}) is equated to the axial concrete coating capacity (N_c), the threshold for τ_y would be calculated as approximately 0.5 MPa. Note that $V_{ACL} = \tau_y \pi D L_{slide}$ (the shear strength of the ACL is developed along the whole circumference [22, 106], and also $L_{slide} \cong 0.5L_t - L_f$ as explained for Figure 3.7). Also, N_c is calculated by

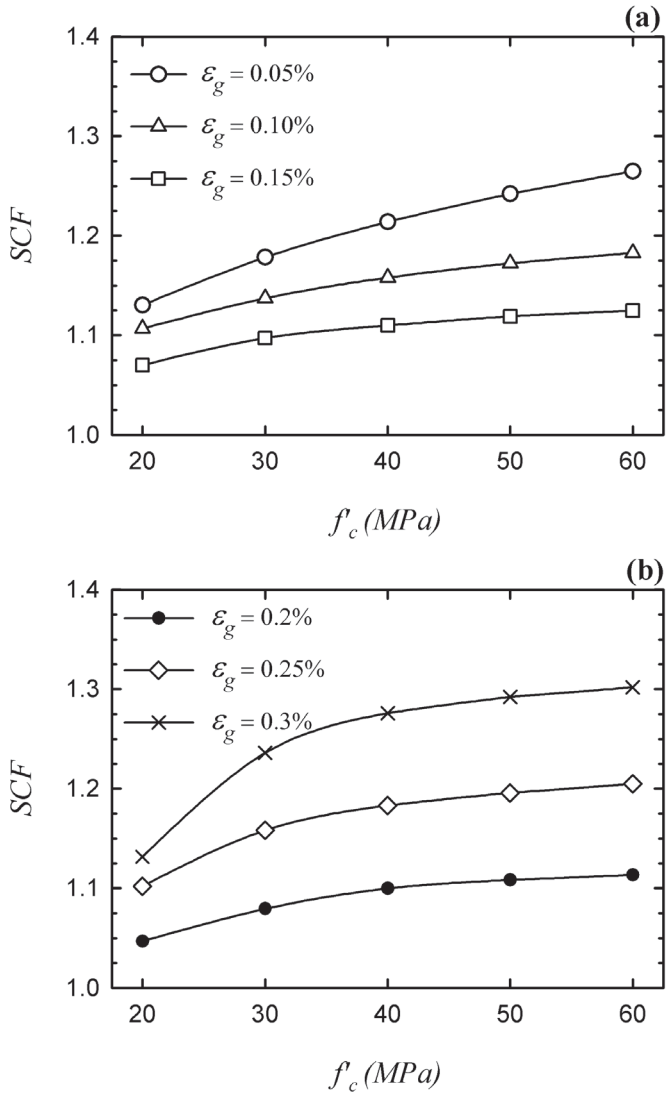

Figure 3.11. Effect of concrete coatings compressive strength (f'_c) on SCF for **(a)** Regime I loading and **(b)** Regime II loading.

integrating the concrete stress (which follows the curve in Figure 3.5) over the cross section area being under compression.

Since the mechanical response of steel remains linearly elastic within Regime I, the effect of steel's yield strength, σ_y, would only be of concern only within Regime II loading history, as illustrated in Figure 3.13. The trend shows that the increase in steel's yield stress would cause a reduction in SCF. This is due to the fact that higher values of σ_y would delay the yielding of steel which in turn reduces the localized

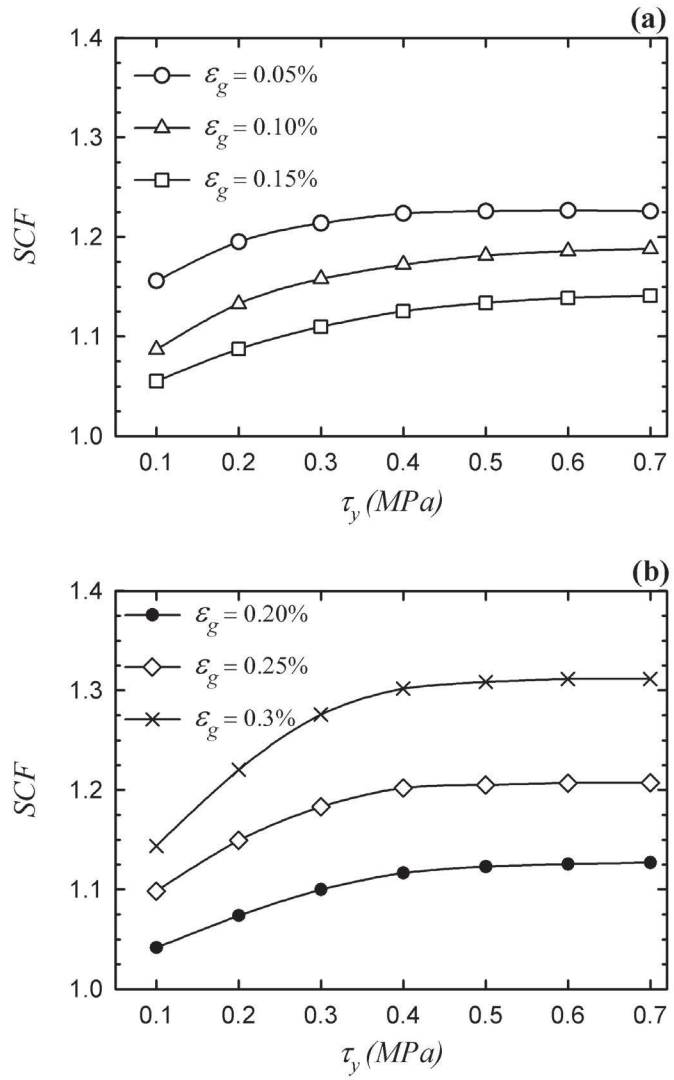

Figure 3.12. Variation of SCF as a function ACLs shear strength (τ_y) for **(a)** Regime I loading, and **(b)** Regime II loading.

plastic deformation of the FJ, thus resulting in lower values of SCF.

Similar to the effect of steel's yield strength, variation of the strain hardening index, n, only affects the SCF at higher values of ε_g (Regime II loading). This effect is illustrated in Figure 3.14, and it is observed that an increase in the values of n (i.e. lowering the strain hardening capacity) could significantly increase the SCF. The perfectly plastic limiting case ($n \to \infty$) also shown, causes the most severe increase in SCF.

The evolution of SCF as a function of the average axial strain ε_{ave}, for varying

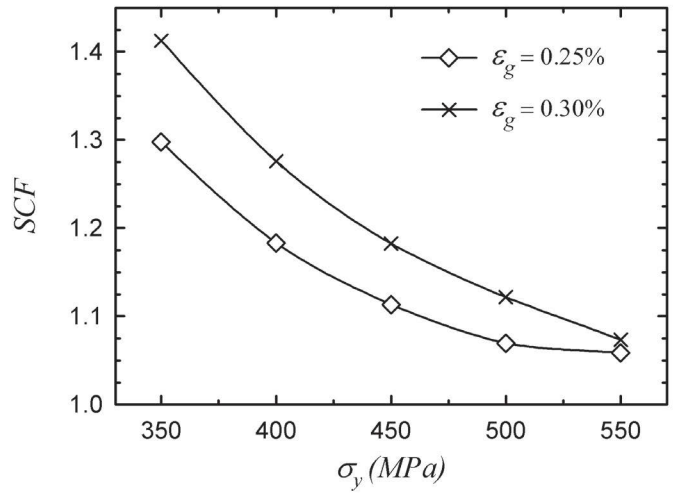

Figure 3.13. Effect of steels yield strength, σ_y, on the SCF.

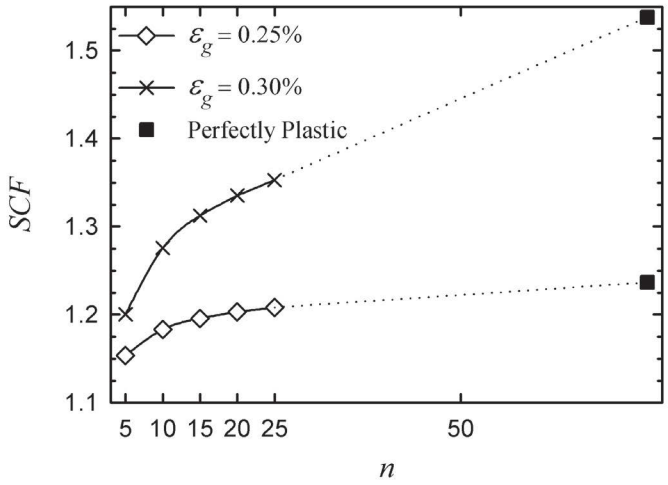

Figure 3.14. Effect of the strain hardening index, n, on SCF, along with the perfectly-plastic case $n \to \infty$.

levels of hoop stress (σ_h/σ_y) is shown in Figure 3.15. It is observed that higher values of hoop stress would significantly elevate the SCF curves. Moreover, higher values of the hoop stress would raise the rate of increase of SCF as a function of ε_{ave} within Regime II loading. For the highest value considered (i.e. $\sigma_h/\sigma_y = 0.8$) in Regime II, the SCF increases very quickly for small increments of ε_{ave}.

A sharp transition exists between Regime I and II for the case of pure bending loading as observed in Figure 3.3, identified by the intersecting lines. In the presence

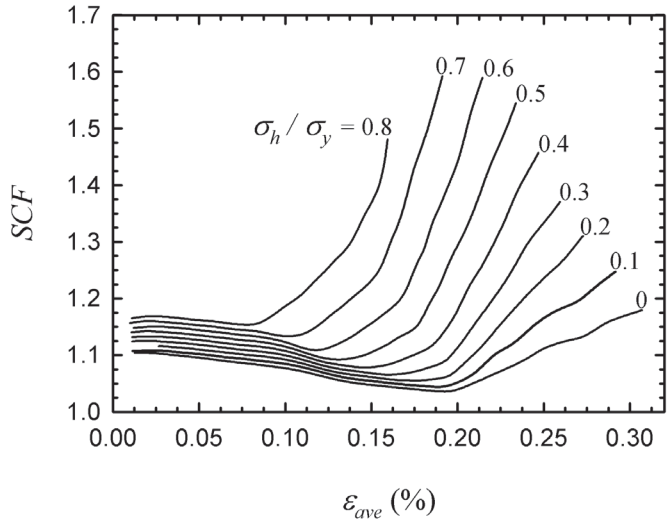

Figure 3.15. Evolution of SCF versus ε_{ave} for the family of combined hoop and bending loads (B+P).

of internal pressure, the transition would become more gradual. This effect is more pronounced for higher values of σ_h/σ_y as can be observed in the family of curves illustrated in Figure 3.15. It should also be noted that while all the pipes presented in Figure 3.15 were subjected to bending strain of $\varepsilon_g = 0.3\%$, it is observed that ε_{ave} would not reach the same value of $\approxeq 0.3\%$. This is probably due to the biaxial stress state effect. It is postulated that the effect of hoop stress on SCF is very significant within Regime II, while its effect on SCF in Regime I is quite marginal.

Figure 3.16 shows the influence of the applied tensile load (N/N_y) on the SCF. It can be seen that the tensile load can significantly increase the SCF after the steel undergoes the initial yielding. However, before that stage, the effect of N/N_y is less pronounced. As can be seen, even for the lowest magnitude of the tensile load considered (i.e. $N/N_y = 0.1$), the increase of SCF compared to the master case pipe (in which $N/N_y = 0$) is evident.

At this juncture, it should be noted that the strain concentration behavior of combined loading cases is fundamentally different from that observed for pipes undergoing pure bending. Under pure bending, the neutral axis is shifted toward the compressive chord by a small amount due to the added stiffness of the concrete coating on the compression chord. Nevertheless, the localized regions in the tensile and compressive

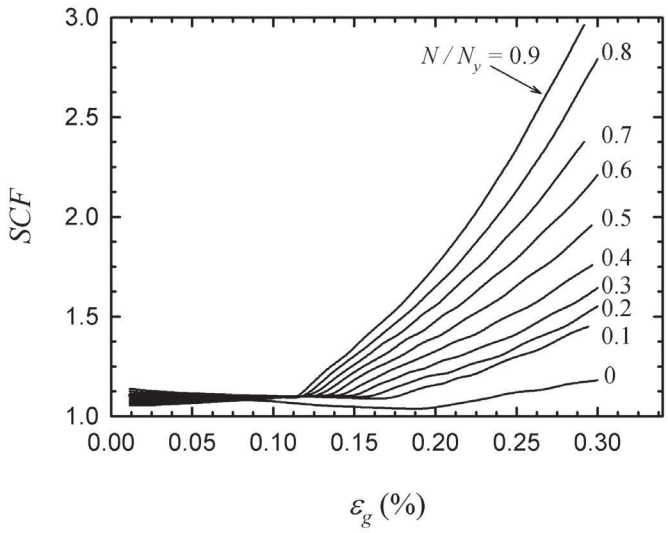

Figure 3.16. Effect of tensile load (N/N_y) combined with bending load (B+T) on SCF.

chords within the FJ that undergo plasticity are still comparable. For the combined B+P loading case, the hoop stress causes the compressive chord to yield earlier and thus undergo more severe plastic deformation than the tensile chord. This behavior can be visualized by considering the Mises yield surface and the different loading paths corresponding to the tensile and compressive chords, as shown in Figure 3.17 (see also explanations of Bruschi et al. [107] for treatment of the hoop stress effects). On the other hand, under the B+T loading case, the compressive chord might not even yield, and thus the localized plasticity of the FJ is confined mainly on the tensile chord. Moreover, the plastic deformations under the combined loading cases would be much more severe than that under the pure bending case. These described differences can be further visualized via Figure 3.18, which illustrates the equivalent plastic strain (ε_p) contours for the three loading cases.

3.8 Concluding Remarks

Strain concentration at the Field Joint (FJ) of concrete coated pipelines subject to pure bending and also combined loading states were investigated in this study. Firstly, a finite element (FE) modeling framework was presented for consideration of the most prominent sources of nonlinearity in such coated pipes. The integrity of the FE results

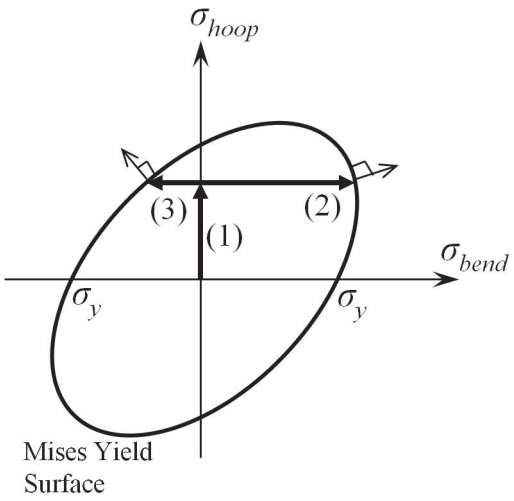

Figure 3.17. Schematic illustrating the Mises yield surface and the different load paths: (1) initial pressurization, (2) bending of the tensile chord, and (3) bending of the compressive chord.

was verified by comparing them with the experimental results of Ness and Verley [106]. The FE model was further utilized to perform a parametric FE study, investigating the influence of various parameters on the strain concentration factor (SCF) in coated pipelines. It was observed that the concrete compressive strength, $f_c^{'}$, and also shear strength of ACL material had a marginal influence on the SCF. On the other hand, the geometric characteristics of the coated pipeline (specifically, D/t and coating thickness t_c) were observed to affect the SCF throughout the loading history. Pipes with lower (D/t) and also higher coating thickness (t_c) experienced larger SCF. The post-yield characteristics of steel, including its yield strength (σ_y), and strain hardening index (n) also generated a significant influence on SCF at higher bending loads, within which the localized FJ plasticity governs the strain concentration behavior. As a finale, the effect of two combined loading scenarios, namely (i) bending plus internal pressure and (ii) bending plus axial tension, on the SCF was also considered. The results indicated that during the application of low to moderate bending loads, in which the response of the steel pipe remained elastic, the addition of either an internal pressure or tensile load did not seriously alter the SCF. Nevertheless, at higher bending loads, under which yielding of the steel pipe became eminent, the addition of both the internal

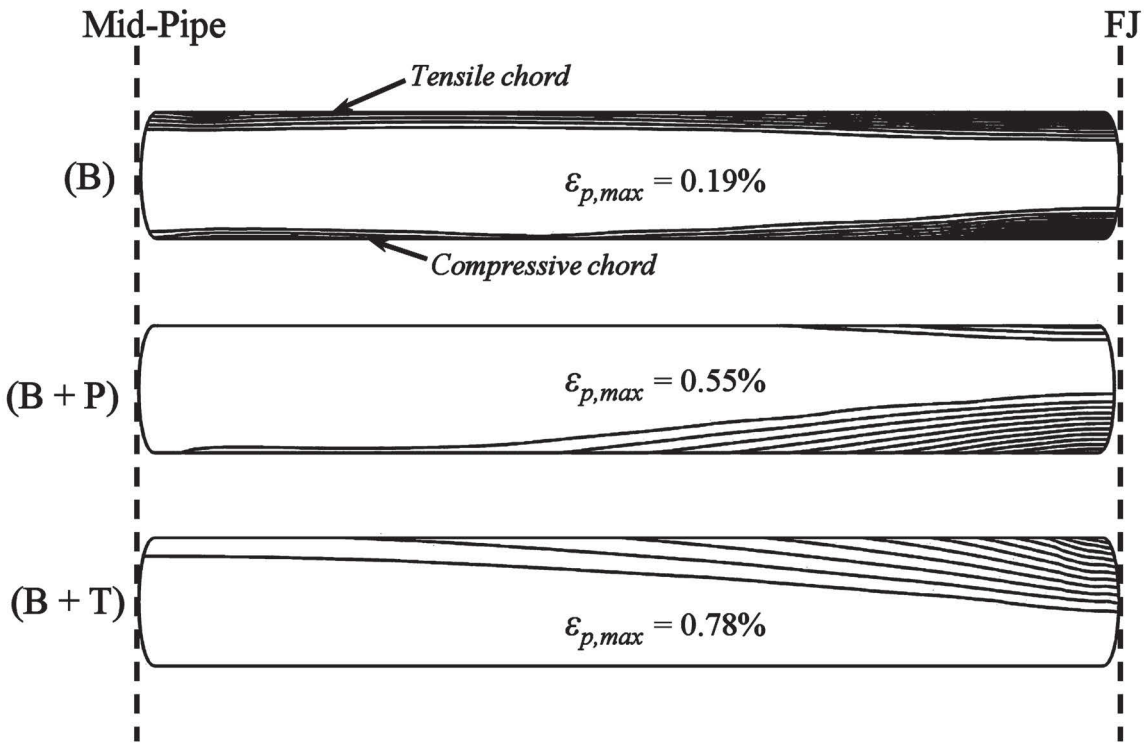

Figure 3.18. Contours of the equivalent plastic strain in the steel pipe subject to: **(Top)** pure Bending; **(Middle)** Bending + Pressure ($\sigma_h/\sigma_y = 0.5$) and **(Bottom)** Bending + Tension ($N/N_y = 0.5$). Concrete coating and ACL are hidden for clarity.

pressure and tensile load increased the value of SCF by a significant margin.

It is believed that the results presented here could be of practical interest to offshore pipeline design engineers, especially under the framework of strain based design (SBD) philosophy.

Acknowledgments

The financial support of the Atlantic Innovation Fund is gratefully appreciated.

Chapter 4

A Design Equation for Evaluation of Strain Concentration Factor in Concrete Coated X65 Pipelines

Nikzad Nourpanah and Farid Taheri

Department of Civil and Resource Engineering, Dalhousie University, Halifax, Nova Scotia, Canada, B3J 1Z1.

Published in Journal of Marine Structures, 2009, vol. 22, pp. 758–769.

4.1 Abstract

An extensive parametric study using detailed nonlinear finite element (FE) models, was conducted in order to develop a design equation for predicting Strain Concentration Factor (SCF) in field joints of X65 concrete coated pipelines under bending. Dimensions of the pipeline and coating, material properties of the coating and anti corrosion layer, as well as the loading level, were included in the design equation. Buckingham's theorem was incorporated to simplify the equation by introducing non-dimensionalized parameters. The design equation was fitted to FE data using the nonlinear least square regression, resulting in, margin of safety definitions using the confidence interval concept for practical applications. The interactive effect of parameters on SCF was studied, leading to the introduction of a single non-dimensional *coating parameter* that can accurately describe the upper limit of the SCF. This study concluded with a definition of a critical *coating parameter* which can be used to assess safe combinations of coating thickness and installation loads, thus preventing excessive strain concentration.

Keywords: strain concentration factor, concrete coated offshore pipes, strain-based design, finite element analysis, parametric study, design equation, X65 steel

4.2 Introduction

Strain Based Design (SBD) is a modern design philosophy tailored for offshore pipelines [11], also implemented in major pipeline design codes (e.g. DNV [2] and API [3]. The goal is to safely utilize the plastic capacity of steel and thus reduce the overall costs. The method is applicable to pipelines subject to *displacement-controlled* loading conditions. Noting that most critical loadings on an offshore pipeline are displacement-controlled (e.g. as a result of bending over stinger, uneven seabeds, reeling, etc.), SBD can be used to define alternative safe limits for the structure, rather than the more conservative traditional stress-based design methods. However, it should be kept in mind that higher plastic strains require more stringent criteria for material selection and testing/quality assurance procedures. For example, DNV [2] requires the utilization of the so-called *Engineering Criticality Assessment* (ECA), for establishing defect and tolerance criteria for pipelines undergoing plastic strain exceeding 0.3% (common in pipelines installed with stingers in deep waters). It also requires additional material specifications when the accumulated plastic strain exceeds 2% (common to pipelines installed using reeling). The accumulated plastic strain is defined as:

$$\varepsilon_p = \sqrt{\frac{2}{3}\left(\varepsilon_{pL}^2 + \varepsilon_{pH}^2 + \varepsilon_{pR}^2\right)} \tag{4.1}$$

where ε_p is the accumulated plastic strain, ε_{pL} is the plastic portion of the principal longitudinal strain, ε_{pH} is the plastic portion of the principal hoop strain and ε_{pR} is the plastic portion of the principal radial strain.

All the mentioned codes emphasize the importance of accurate prediction of strain, including all the associated strain concentration effects. A primary cause of strain concentration in Field Joint (FJ) of an offshore pipeline is due to the discontinuity of concrete coating, which, according to DNV [2], must be accounted for. The mechanics of this seemingly simple phenomenon are rather complicated, especially for modern designs in which the materials undergo plastic deformations. The problem is further complicated by the coating slippage over the pipeline prompted by the limited shear strength of the anti corrosion layer (ACL). For a complete discussion on the mechanics of this problem, reference can be made to [22, 23, 106, 115]. Previous research on this problem include tests and measurements during installations [18–21, 106], simplified

semi-analytical formulations [22, 23, 106], finite element (FE) modeling [24, 25, 115] and parametric studies [22, 23, 106, 116]. It can be stated that the experimental, theoretical and FE simulations of the problem up to now provide sufficient insight to the problem, which was used here to derive a design equation for practical use. Based on the FE modeling procedure described and validated by the authors elsewhere [115], and by extending the parametric study given in [116], a large number of FE analysis were performed in order to formulate a simple design equation for predicting the Strain Concentration Factor (SCF) for API-5L [34] grade X65 steel, which seems to be the most commonly used steel grade for deepwater pipelines [5]. To the best of the author's knowledge, no similar design equation exists in the literature, with the exception of that in ref. [111], which is based on a simplified FE model, and does not include the post-crushing behavior of concrete that makes it unsuitable for high strain levels. The motivation for proposing the new design equation is to provide the practicing engineer with a preliminary tool, when tests or detailed FE simulations are not feasible. In this paper, a quick review of the FE modeling framework which was outlined in detail in [115] is presented. Subsequently, the details of the parametric study, derivation of the design equation and finally a simplification of the design equation for prediction of upper bounds of SCF are presented.

4.3 Main Features of Finite Element Modeling

An anticorrosion layer (ACL), which is usually made of a polymeric or bituminous material, is commonly used to cover each pipe joint. Subsequently, the pipe joint is covered with a concrete coating, which provides the sufficient weight required for stability of the pipe on seabed. In order to facilitate welding of pipe joints, approximately 35 cm at each end of the pipe is left uncoated. This uncoated region is referred to as the field joint (FJ). Figure refms01 shows a typical uncoated segment of such pipes.

All three parts, namely (i) the steel pipe, (ii) the ACL and (iii) the concrete coating are included in the FE model. In this study a typical 12 m long pipe joint was considered. Due to symmetry in geometry and boundary conditions (BC's), only one

Figure 4.1. Concrete coated pipes, and the uncoated portion. From Ref. [110].

quarter of the system was modeled, as shown in Figure 4.2[1]. The general purpose FE package, ABAQUS 6.8 [10], was used. All the mentioned parts were modeled using the 8-node isoparametric reduced integration continuum (brick) elements (C3D8R). The behavior of the constituent steel and ACL were modeled using the plasticity model, whereas the *damaged plasticity model* was used for the concrete coating. The plasticity model incorporated an associated J_2-flow theory plasticity, using the Mises yield surface and the isotropic hardening option. The *damaged plasticity model* used a modified Drucker-Prager yield surface, and can be categorized as a non-associated flow-theory plasticity model. This framework also has the capability to model softening behavior of concrete caused by cracking and crushing of concrete in tension and compression respectively [10], which was of interest in this study. Based on Equation (4.3) (see section 4.4), rotations required to cause global strain levels of 0.15, 0.20, 0.25 and 0.33% were calculated and imposed on one end of the pipeline, as shown in Figure 4.2.

The stress–strain curve used for X65 steel is shown in Figure 4.3a, with yield stress, defined as stress corresponding to 0.5% total strain [34], and ultimate strengths of 448 MPa and 600 MPa, respectively. Based on a survey of literature, the proportional stress (defining the elastic limit) and the elastic modulus are assumed as 350 MPa and

[1]The presented Figure 4.2 is slightly more detailed than that in the published article.

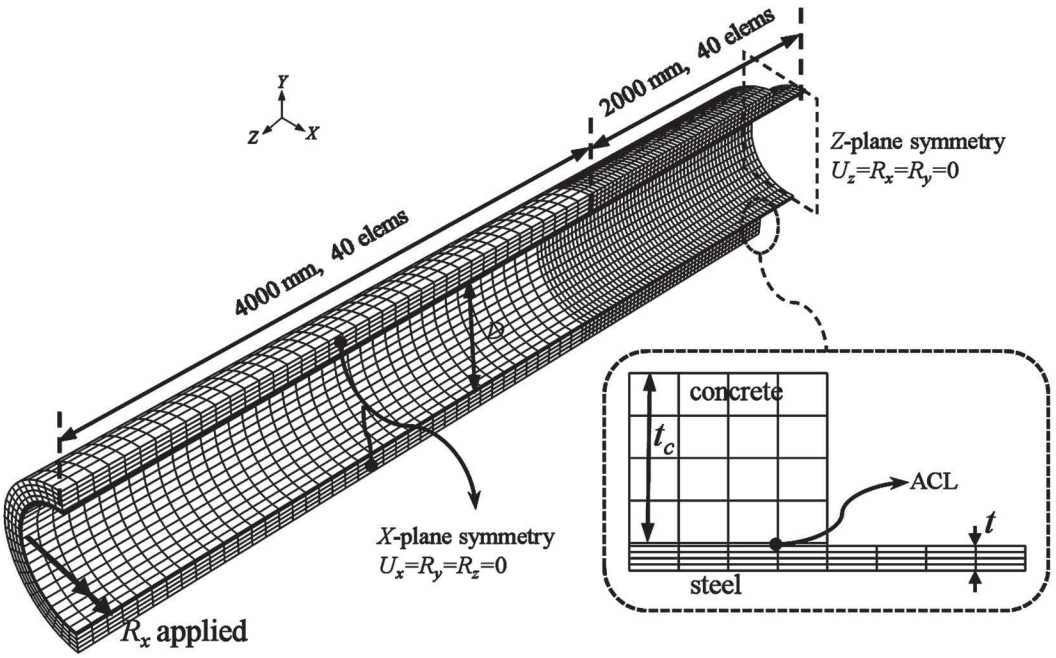

Figure 4.2. A quarter symmetric FE model (6 m long) showing the boundary conditions and longitudinal mesh characteristics (also, 16 elements in half circumference and 4 elements through thickness of steel and concrete each, and 1 element through thickness of ACL).

210 GPa, respectively. Furthermore, a continuous post-yielding curve was assumed rather than having a flat plateue (Lüder's effect). Although the curve was not constructed from actual tensile tests, it can be deemed as a representative stress–strain curve for large diameter seam-welded X65 pipelines [117].

The stress–strain curve used for concrete is shown in Figure 4.3b. The curve covers the full range of concrete behavior including the post crushing softening behavior. The curve has a parabolic form, defined by [114]:

$$f_{con} = \frac{2f_c^{'}(\varepsilon/\varepsilon_0)}{1+(\varepsilon/\varepsilon_0)^2} \tag{4.2}$$

where $f_c^{'}$ is the compressive strength of concrete and the rest of the parameters are defined in Figure 4.3b. The particular value of equal to 0.2% is the concrete crushing strain observed during offshore pipeline installations [106]. The tensile strength of concrete was neglected (i.e. 1 MPa).

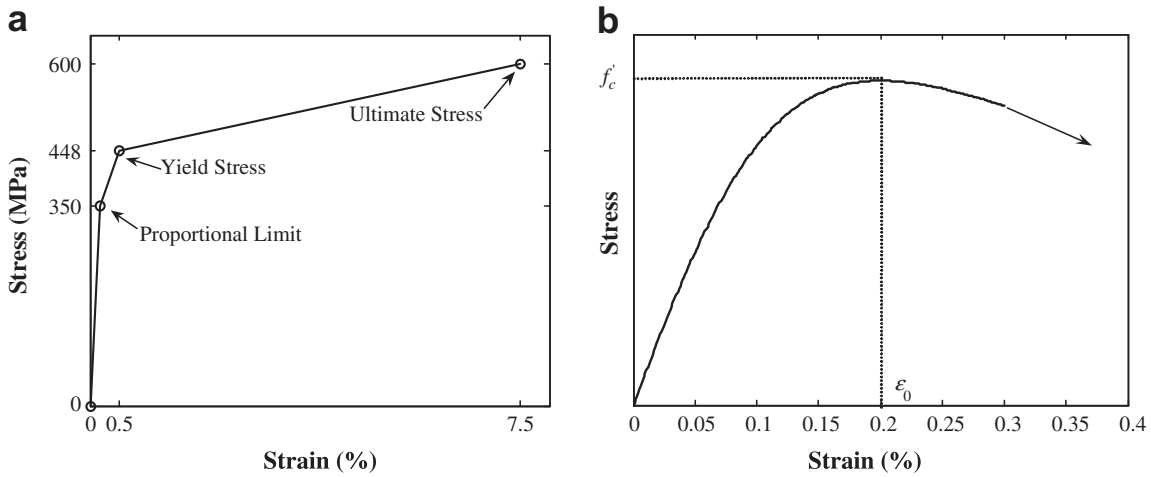

Figure 4.3. **(a)** Assumed stress–strain curve of X65 steel and **(b)** typical parabolic curve for concrete.

4.4 Parameters Affecting the SCF

Generally speaking, the SCF of offshore pipelines at FJ is a function of dimensions of the structure, material properties of steel, concrete and ACL, and also the strain level (or alternatively, the curvature of the pipeline). However it was not practical to examine all these parameters together and investigate their combined effect on SCF. Therefore, the most important ones were included in the parametric study. The selected parameters are the outside diameter D, wall thickness t, coating thickness t_c, compressive strength of concrete $f_c^{'}$, shear strength of the ACL τ_y and global bending strain ε_g (which is a measure of loading level). These parameters are believed to be the most important ones, while the other parameters such as the axial force and the rebars in the concrete coating (whose cross-section area in such systems amounts to $1 \sim 3\%$ of concrete's cross-section area) would have a less significant influence on SCF [22].

As can be seen in Table 4.1, to achieve all possible combinations of D, t, t_c, $f_c^{'}$ and τ_y, a total number of $2 \times 2 \times 3 \times 3 \times 3 = 108$ FE analyses were required with results of each analysis considered at four strain levels (ε_g). The results of all analysis were post processed, and the maximum value of SCF, as defined by the following equation [111],

Table 4.1. Variation of parameters included in the FE parametric study

Parameter	**Range** (# of samples)
D (mm)	457–813 (2)
t (mm)	17.5–25.4 (2)
t_c (mm)	40–80–120 (3)
$f_c^{'}$ (MPa)	30–40–50 (3)
τ_y (MPa)	0.1–0.3–0.5 (3)
ε_g (%)	0.15–0.20–0.25–0.33 (4)

was recorded:

$$\text{SCF} = \frac{\varepsilon_{\text{FJ}}}{\varepsilon_g} \tag{4.3}$$

where ε_{FJ} is the maximum bending tensile strain in the FJ region obtained from the FE analysis results and ε_g is the maximum global longitudinal strain as predicted by the Euler beam theory. For a pipe under pure bending, the global strain can be calculated by:

$$\varepsilon_g = \frac{\kappa D}{2} = \frac{R_x D}{l} \tag{4.4}$$

whereκ is the curvature of pipeline, R_x is the rotation angle at pipeline ends (in Radians), and l is the length of pipeline.

Equation (4.4) was based on the classical beam theory assumption that plane sections remain plane, which does not hold true as plasticity develops. However, for the global levels of strain limited to 0.33% the above equation provides acceptable results. It should be noted that although tensile strain was used for calculation of SCF (because it is the critical parameter for promoting crack growth and potential fracture in girth welds), the compressive strain might attain a slightly larger magnitude. This phenomenon was observed in tests conducted by Ness et al. [106] and numerical simulations [115], and can be due to the fact that the plane section assumption is less admissible in the vicinity of discontinuity (at FJ), and the rather large amount of plasticity developed in that region.

In addition to the data from the 108 FE models, data from the previous parametric study conducted by the authors [116], which included 23 FE models, were also included for the derivation of the proposed design equation. Our earlier study (the 23 FE

models), also considered pipelines with the dimensions in between the ranges given in Table 4.1 (e.g. 711 mm outside diameter). Thus, in total, the results of 131 FE models were used for derivation of the design equation.

4.5 Derivation of the SCF Design Equation

A functional relationship can be written to relate to the other parameters:

$$\varepsilon_{\max,\mathrm{FJ}} = F\left(D, t, t_c, f_c{}', \tau_y, \varepsilon_g\right) \tag{4.5}$$

It should be noted that Equation (4.5) is not fully encompassing, in the sense that only the effect of parameters outlined in Table 4.1 have been considered in its development. In other words, the steel's materials properties (i.e. the yield strength and hardening) have not been included in the parameterization, mainly due to the fact that only one grade of steel (X65) has been considered in this investigation. In order to simplify defining the functional relationship , the Buckingham dimensional analysis theorem was used. The theorem states that a given functional relationship can be expressed with a fewer number of dimensionless parameters, with the reduction being always equal or less than the number of fundamental dimensional units of the problem, which in the present case equals two (force [F] and length [L]). However, the only dimensionless parameter for $f_c{}'$ and τ_y can be their ratio. That ratio would not represent any trend in variation of SCF. On the other hand, if a range of steel properties had been included in the study, then the ratios of $f_c{}'$ and τ_y, over the strength properties of steel, would have made useful dimensionless parameters. Therefore, only the geometric parameters are non-dimensionalized, resulting in:

$$\mathrm{SCF} = \frac{\varepsilon_{\mathrm{FJ}}}{\varepsilon_g} = F\left(\frac{t_c}{t}, \frac{t_c}{D}, f_c', \tau_y, \varepsilon_g\right) \tag{4.6}$$

In order to interpret the physical meaning of the ratios t_c/t and t_c/D introduced in Equation (4.6), the following expression can be used:

$$\frac{I_c}{I_s} \propto \frac{(D+2t_c)^4 - D^4}{D^4 - (D-2t)^4} = \frac{\dfrac{t_c}{D} + 1.5\left(\dfrac{t_c}{D}\right)^2 + \left(\dfrac{t_c}{D}\right)^3 + 2\left(\dfrac{t_c}{D}\right)^4}{\dfrac{t}{D} - 1.5\left(\dfrac{t}{D}\right)^2 + \left(\dfrac{t}{D}\right)^3 - 2\left(\dfrac{t}{D}\right)^4} \tag{4.7}$$

where I_c and I_s are the second moment of area of coating and steel pipe, respectively[2]. If t/D and t_c/D are sufficiently small, then their higher power terms can be neglected (i.e. the thin ring assumption. Therefore the expression in Equation (4.7) will only be a function of t_c/t . Thus, t_c/t would also represent I_c/I_s (which obviously affects the SCF), if both cross sections can be assumed as *thin*. While this assumption is indeed valid for the steel pipe, it may not be valid for the coating. In other words t_c/D would be a measure of divergence from the so-called *thin* assumption discussed above. Generally speaking, Equation (4.7) is equivalent to t_c/t, with inclusion of a correction factor as a function of t_c/D. After a series of trial and errors, and also observation of the general trend of SCF variation as a function of each parameter, as observed in [116], the following design equation is proposed:

$$\hat{\text{SCF}} = \beta_1 + \beta_2 \left(\frac{t_c}{t}\right)^C \tag{4.8}$$

where

$$C = \beta_3 + \beta_4 \frac{t_c}{D} + \beta_5 f_c^{'} + \frac{\beta_6}{\tau_y} + \beta_7 \frac{\varepsilon_g}{0.0015}$$

in which $f_c^{'}$ and τ_y are in MPa and ε_g is dimensionless (e.g. mm/mm). The β_i coefficients in Equation (4.8) would be determined from regression of the FE data (Note that β_5 and β_6 have units of MPa^{-1} and MPa respectively, while the rest of the βs are unitless). It should be noted that various combinations of parameters were considered prior to finalizing the form shown in Equation (4.8). In spite of Equation (4.8) having a rather simple form, it best describes the trend of the massive number of results obtained through the large number of FE analyses. Equation (4.8) predicts the SCF mainly as a function of t_c/t and allowing modification of other parameters. Moreover, the slipping length of the concrete coating over the steel pipe is a function of β_6/τ_y [22]; and the slipping length itself affects the SCF by smoothing the longitudinal strain distribution [116]. Equation (4.8) is nonlinear in terms of β_i, thus iterative nonlinear regression techniques are required for establishing the coefficients [118]. The procedure is initiated by defining the mean square error, E:

$$E = \frac{1}{n} \sum_{i=1}^{n} \left(\text{SCF}_{\text{FE}} - \hat{\text{SCF}}\right)^2 \tag{4.9}$$

[2]As a first approximation, the cracking of concrete coating is negelected in establishing I_c/I_s in Equation (4.7)

Table 4.2. Coefficients of the proposed SCF design equation.

β_1	β_2	β_3	β_4	β_5 (MPa^{-1})	β_6 (MPa)	β_7
1.0	0.15	−1.0	4.05	0.0087	−0.0515	0.5135

where n is the total number of the series of data obtained through FE analyses, which in this case would be (e.g. 131 × 4 FE models with SCF values extracted at four levels of ε_g). Incorporating the least square concept, the coefficients β_i were found by minimizing the error, that is:

$$\frac{\partial}{\partial \beta_i} E = 0 \qquad \text{for} \qquad i = 1 \text{ to } 7 \tag{4.10}$$

Equation (4.10) leads to seven nonlinear algebraic equations in terms of β_i which had to be solved iteratively. The partial derivatives in Equation (4.10) can be evaluated analytically; however, it is more efficient to use the forward difference numerical scheme for their evaluation. The above mentioned procedure is available in the Statistical Toolbox of the MATLAB (7.1) program (MathWorks, Boston, MA). The final results for the coefficients of Equation (4.8) obtained through MATLAB are presented in Table 4.2.

Figure 4.4 shows the ratio of the proposed SCF design equation, Equation 4.8, to SCF from the FE data. For the majority of cases, the ratio was bounded between 0.9 and 1.1 (or error of ±10%). Even for the few cases where the errors fell out of these bounds, the ratio was still limited to 0.85 and 1.2 (or error of ±20%). Thus, it can be stated that Equation (4.8) can satisfactorily and practically predict the SCF with reasonable accuracy for grade X65 steel.

In order to make Equation 4.8 more robust for practical use, a margin for conservatism needs to be defined. This can be best done by using the concept of confidence interval. This concept prescribes the probability range that would include the predicted statistical results. This concept can be represented mathematically by:

$$P(\hat{\text{SCF}} - \Delta < \text{SCF}_{\text{FE}} < \hat{\text{SCF}} + \Delta) = (1 - \xi) \times 100\% \tag{4.11}$$

where $(1 - \xi) \times 100\%$ is the desired confidence level, Δ is half-width of the confidence interval and P is the probability. The half-width of confidence interval, Δ, was calculated using the Matlab Statistical Toolbox for four confidence levels. The maximum

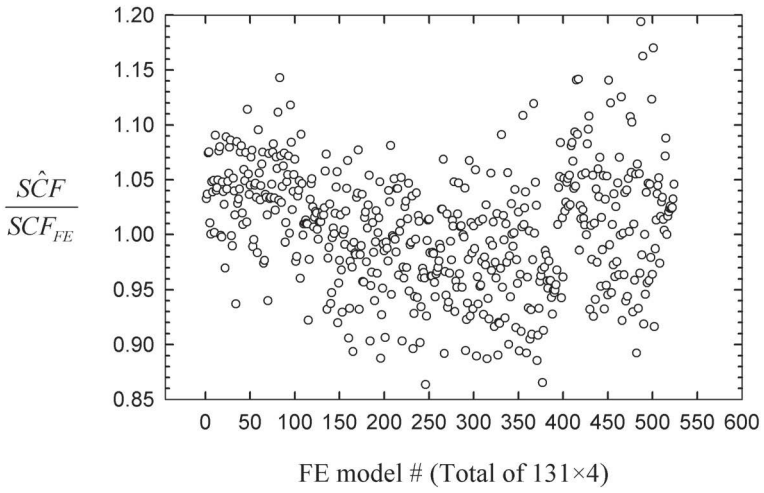

Figure 4.4. Ratio of the SCF predicted by Equation (4.8) to SCF from FE data.

Table 4.3. Design confidence factors applicable to Equation (4.8) as a function of confidence level.

Confidence level (%)	ξ	$(\Delta/\hat{\text{SCF}})_{\max}$	Design confidence factor
99.9999	1×10^{-6}	0.0737	1.0737
99.99	1×10^{-4}	0.0583	1.0583
99	1×10^{-2}	0.0385	1.0385
95	1×5^{-2}	0.0292	1.0292

ratio of Δ over the predicted SCF obtained using Equation (4.8) can be interpreted as a design confidence factor for design purposes. The results are presented in Table 4.3.

As an example, applying a safety factor of 1.0583 from Table 4.3 to predictions of Equation (4.8), one would have a 99.99% probability that the predicted SCF is equal or greater than the exact SCF calculated by FE. Thus, the final format of the design equation is as follows:

$$\text{SCF}_{\text{des}} = \eta \times \hat{\text{SCF}} \tag{4.12}$$

where SCF_{des} is the recommended value for design, $\hat{\text{SCF}}$ is the prediction of Equation (4.8) and η is the safety factor corresponding to the desired confidence level from Table 4.3.

The influence of different parameters on the SCF predicted using Equation (4.8) was also investigated. Variations of SCF as a function of t_c/t (the primary parameter) and t_c/D, $f_c^{'}$, τ_y, ε_g (the secondary parameters) are shown in Figures 4.5a to 4.5d, respectively. It should be noted that the high values of SCF in the upper left corner of Figure 4.5a correspond to the geometric combinations that are impractical and rarely used in practice (for example the extreme point of Figure 4.5a can correspond to a pipeline with $D = 457$ mm, $t = 20$ mm and $t_c = 137$ mm, which is indeed a disproportionate configuration[3]. The influence of the secondary parameters became more pronounced at larger values of the t_c/t ratio. In all cases, an interaction effect of the parameters was observed on the SCF, however their degrees of influence are somewhat different. For instance, the gradient of the SCF surface increases sharply as t_c/D increases, while it increases nearly linearly as a function of $f_c^{'}$. The trend takes an asymptotic behavior as a function of τ_y , and finally increased strongly with respect to variation in ε_g. Thus, among the secondary parameters, t_c/D affected SCF most severely, followed by ε_g having a rather modest effect on SCF. In contrast, increasing τ_y had an insignificant influence on the SCF after a certain limit, while $f_c^{'}$ affected the SCF nearly linearly.

The above mentioned influences and trends of each parameter on the SCF, prompted the formulation of a new non-dimensional parameter which accounts for only the more influencing parameters, that is t_c/t, t_c/D and ε_g. Indeed, by upgrading the *geometry parameter* developed in our earlier study [116], and including ε_g, a new *coating parameter* can be introduced, which predicts the SCF trend quite satisfactorily. The *coating parameter*, λ, is defined as:

$$\lambda = \frac{Dt}{\varepsilon_g t_c^2} \tag{4.13}$$

where ε_g is the global strain (in percent).

The values of SCF obtained from FE analyses are plotted in Figure 4.6 as a function of λ; an identifiable trend is visible in the diagram. Furthermore, a curve was fitted to the upper limit of the data, which yields the following relationship:

$$\mathrm{SCF_{UL}} = 1.35 + \frac{7}{\lambda^{1.7}} \tag{4.14}$$

[3]Such a thick-walled pipeline ($D/t \approxeq 23$) would usually not require such a heavy coating with $t_c = 137$ mm.

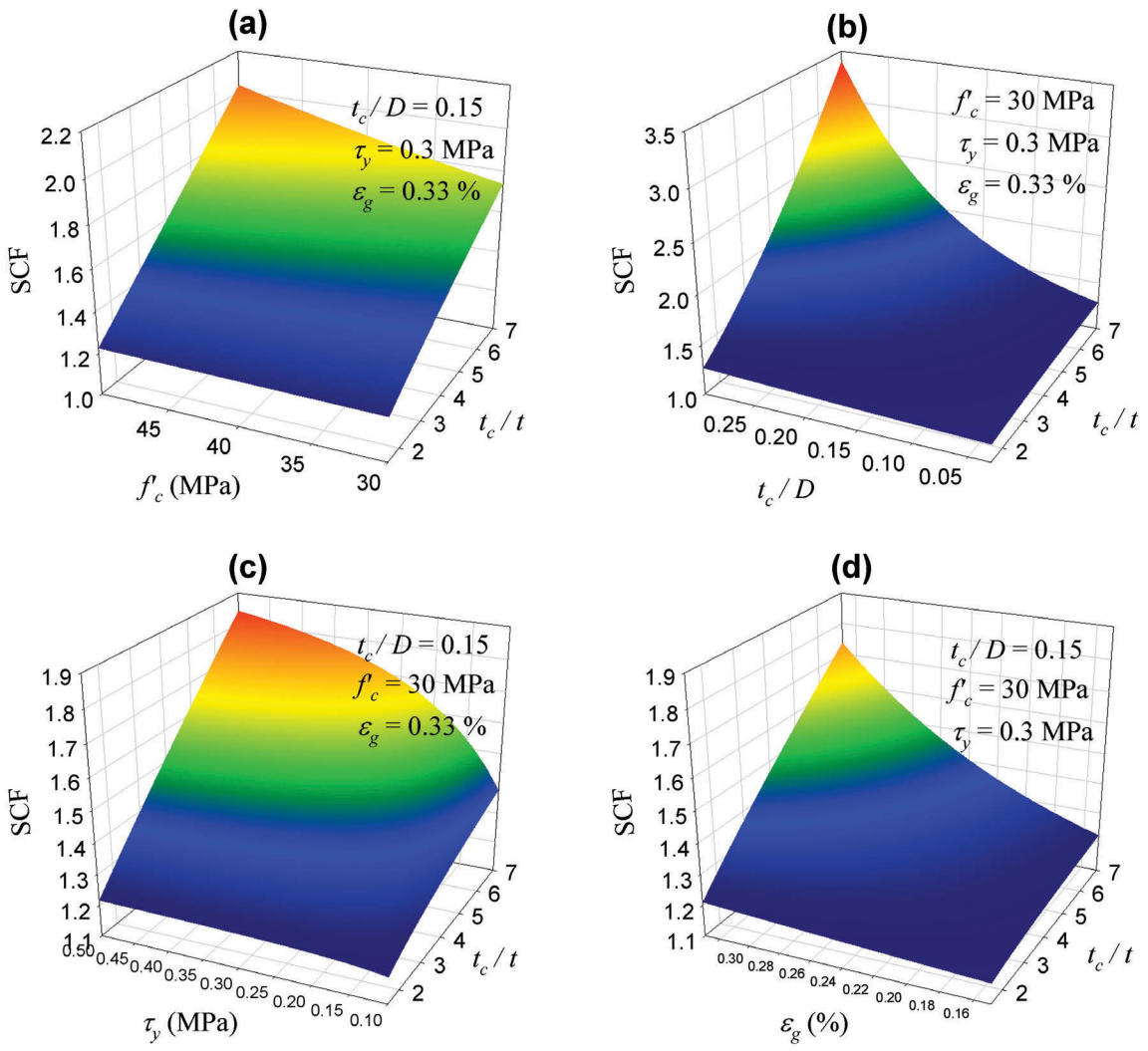

Figure 4.5. SCF as a function of **(a)** t_c/t and t_c/D, **(b)** t_c/t and $f_c^{'}$, **(c)** t_c/t and τ_y and **(d)** t_c/t and ε_g.

Equation (4.14) predicts an asymptotic SCF value of 1.35 for large values of λ. The *rule of thumb* value for SCF has been suggested as 1.2 [1]. Interestingly, the data for $\lambda \geqslant 30$ fits this value; however a single regression curve cannot capture this trend. Moreover, Equation (4.14) and Figure 4.6 provide one valuable piece of information: if the value of λ is less than a critical value, the SCF would sharply increase and become very sensitive to small variations in geometric and material properties and the global strain level. From a general perspective, the critical value of λ would be approximately 8 (see Figure 4.6). In addition to the critical value of λ, Equation

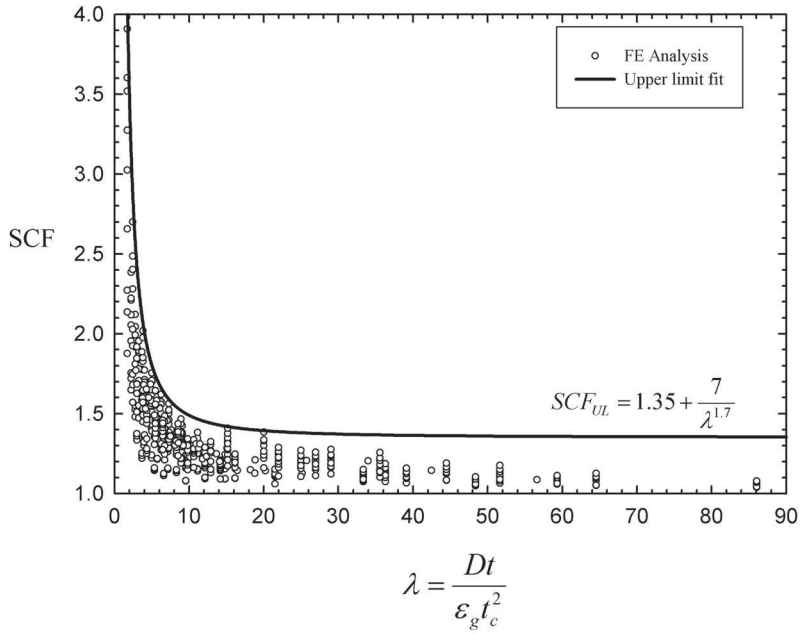

Figure 4.6. SCF from FE results versus the *coating parameter* (λ), and the upper limit of Equation (4.14).

(4.14) and Figure 4.6 can be readily used in the preliminary design stage in order to grasp appropriate combinations of dimensions and loading. For example, in order to install a pipeline with $D = 711$ mm, $t = 19.1$ mm and $t_c = 80$ mm, ε_g should be limited to 0.265%, or conversely, the curvature curvature radius of the stinger should be limited to $R_s = D/(2\varepsilon_g) = 134$ m (assuming $\lambda_{crit} = 8$) in order to avoid excessive strain concentration. Alternatively, one would need to conduct a detailed FE analysis.

It is worth noting that if the values of the relative errors shown in Figure 4.4 are plotted against λ, it would be seen that larger errors are associated with smaller values of λ. This indicates that Equation (4.8) would be more reliable for practical values of λ (i.e. $\lambda > 8$.)

Finally the case study considered by other investigators (see Refs. [106, 115]), were used here to assess our predictions. The pipeline used in the case study had the following data: $D = 517$ mm, $t = 18.5$ mm, $t_c = 80$ mm, $f_c^{'} = 36.4$ MPa and $\tau_y = 0.5$ MPa. The results are compared in Table 4.4. For all values of ε_g, Equation (4.14) satisfactorily predicts an upper margin. The general agreement between predictions of Equation (4.8) and the test and numerical data is also generally good, especially for the

Table 4.4. Comparison of SCF predicted by Equations (4.8) and (4.14), tests [106] and FE analysis [115].

Source	SCF			
	$\varepsilon_g = 0.15\%$	$\varepsilon_g = 0.20\%$	$\varepsilon_g = 0.25\%$	$\varepsilon_g = 0.33\%$
Test [106]	1.4	1.4	1.4	1.4
FE [115]	1.34	1.33	1.35	1.37
Equation (4.8)	1.25	1.32	1.42	1.62
Equation (4.14)	1.49	1.57	1.68	1.88

$\epsilon_g = 0.2$ and 0.25% cases. The observed minor discrepancy at other values of ϵ_g (0.15 and 0.33%) might be due to the fact that the stress–strain curve of the tests conducted in Ref. [106][4] and those incorporated in our earlier numerical investigation [115] (which was a special case) was a lot *weaker* than the *general* curve (Figure 4.3a) that was used to conduct our study. It is therefore suggested that Equations (4.8) and (4.14) should be used with caution if the steel grades response differs significantly from that shown in Figure 4.3a.

4.6 Concluding Remarks

An extensive FE parametric study was conducted in order to derive a design equation for evaluation of SCF in field joints of concrete coated pipelines. This study was based on evaluating the strain concentration factor (SCF) via 108 FE models, representing different geometric (D, t, t_c) and material ($f_c^{'}$, τ_y) properties. The SCF values were extracted at four different stages of loading or global bending strain (ε_g). The investigation also included 23 other FE models from the previous work of the authors [116]. The Buckingham dimensional analysis theorem was incorporated to introduce dimensionless parameters and simplify the regression procedure. Nonlinear regression techniques were used to establish the proposed design equation. The variations in margin of error associated with the proposed equation were also investigated

[4]Ness and Verley [106] have reported a lot of scatter in the stress–strain curves obtained from different coupons. Thus, they used the moment-curvature of the pipe to *back-calculate* the uniaxial stress–strain curve.

and were observed to be within acceptable limits. Furthermore, the confidence interval concept was used to define a design confidence factor in order to further propose a means for establishing the safety margin for practical applications. The effect of each parameter and their interaction on the SCF was shown using 3D plots, and the most influential parameters were identified. It was seen that all parameters affect the SCF only for higher values of D/t_c. It was also observed that the SCF is more sensitive to D, t, t_c and ε_g rather than material properties ($f_c^{'}$, τ_y). Based on this, a non-dimensional *coating parameter*, λ, was introduced which could describe the variation of SCF reasonably well. A simplified equation based on λ was also proposed. A critical value of $\lambda_{crit} \approxeq 8$ was observed to exist, below which the SCF would increase very rapidly, being sensitive to the variation in geometric and material properties. Conversely, the SCF would attain an asymptotic behavior above λ_{crit}. The proposed simplified design equation can be used to estimate SCF (or limiting values of coating thickness and loading level) in the preliminary design phases. It should be noted that the proposed design equations were established based on detailed computational models that include most of the nonlinear geometric and material related phenomena. It is believed that the presented work would be of interest in practical design of offshore pipelines.

Acknowledgments

The financial support of the Atlantic Innovation Fund is gratefully appreciated.

Chapter 5

Development of a Reference Strain Approach for Assessment of Fracture Response of Reeled Pipelines

Nikzad Nourpanah and Farid Taheri

Department of Civil and Resource Engineering, Dalhousie University, Halifax, Nova Scotia, Canada, B3J 1Z1.

Published in Journal of Engineering Fracture Mechanics, 2010, vol. 77, pp. 2337-2353.

5.1 Abstract

As a result of recent increase in exploitation of hydrocarbon resources in harsher environments and also installation techniques which utilize the materials plastic deformation capacity, accurate assessment of fracture response of pipelines subject to large plastic strains (e.g. typical of reeled pipes) has attracted particular interest nowadays. In this paper, an approach, based on the evaluation of the J-integral, is developed for assessing the integrity of such pipelines, manifested in a model of a pipeline with a circumferential part-through crack subjected to plastic bending. The proposed approach is an extension of the reference strain method developed earlier by other researchers, and takes advantage of the displacement controlled loading nature in such pipes (thus being suitable for Strain Based Design methodologies), and the resulting high strain levels, which often cause fracture response of the material in the plastic regime. The developed formulation relates the fracture response of the pipe (in terms of the non-dimensionalized J-integral) as a linear function of the bending strain in the pipe at its uncracked state. A series of 300 3D nonlinear finite element models using the ABAQUS software were analyzed in preparation of the equation that could assess the fracture response of such pipes with great accuracy. The resulting equation, calibrated by the finite element results, can predict the fracture response of pipes with a maximum error of 2% for a practical uncracked material strain range of

$1.5\% \leqslant \varepsilon_{unc} \leqslant 4\%$.

Keywords: Fracture, Reeled pipes, J-integral, Plasticity, Strain based design

5.2 Introduction

Reeling is one of the most efficient installation/construction methods for offshore pipelines, with its first application dating back to 1944, during World War II. The technique has advanced and improved and today a fleet of reel vessels is available worldwide. A brief description of a typical pipeline reeling system is as follows: 12 m long line-pipes are girth welded into 1 km *stalks* in an onshore spool base facility (contrary to traditional S-lay and J-lay, for which offshore welding is required), enjoying the privileges of onshore welding operations and avoiding the tight time constraints and large cost of offshore welding. The stalks are then welded together forming a several kilometer long pipe string, which is subsequently bent over a hub and loaded on a reel vessel which travels to the installation site. The pipeline is installed by gradually unreeling it from the hub [4, 14]. Figure 5.1 shows a schematic of a typical reel vessel and hub (taken from Ref. [4]). The main structural feature of this method is that the pipeline material undergoes significant plastic strains. During reeling on, the nominal uncracked strain in the pipeline can be calculated by [9]:

$$\varepsilon_{unc} = \frac{D/2}{R_{hub} + D/2} \approxeq \frac{D}{2R_{hub}} \tag{5.1}$$

Noting that reelable pipes generally have a diameter of 4 to 18 inches and hubs of today's active fleets have a radius of 6.1 m to 9 m [4], the nominal strain is normally in the $1 \sim 4\%$ range, thus significantly exceeding the elastic limit of the material. Limit states relevant to reeled pipes are concerned with the local buckling of the compression side and fracture on the tensile side in such pipes. Considering the displacement controlled nature of the reeling operation and its equivalent counterpart in pipeline design, the Strain Based Design (SBD), that is, the notion of consideration of the allowable strains would be a justified approach for assessing the integrity of the pipeline, rather than use of the traditional stress-based approaches. It has been noted that the selection of a suitable wall thickness and an appropriate tension during installation could safely accommodate the mentioned strain levels on the pipe's

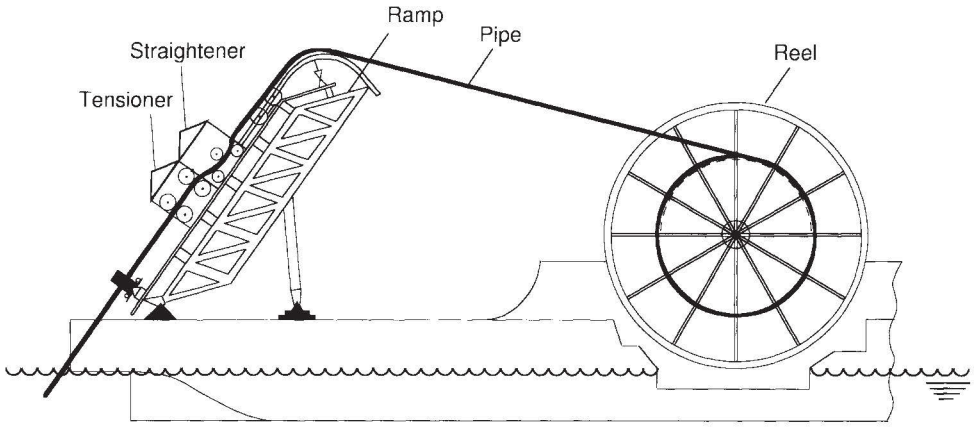

Figure 5.1. Schematic of the reeling installation method. From Ref. [4].

compression side [4, 47], thus harnessing the strain to an allowable strain limits as per code requirements [2]. However, a fracture mechanics analysis, referred to as the *Engineering Criticality Assessment* (ECA), ought to be performed to justify the integrity of the pipeline, its girth welds and the status of a hypothetical defect undergoing such levels of strain. For instance, DNV-OS-F101 [2] requires an ECA in situations involving accumulated plastic strains greater than 0.3%, which includes all reeled pipelines. Additionally, it requires more stringent material specification where the accumulated plastic strain would be greater than 2%. The accumulated plastic strain is defined as:

$$\varepsilon_p = \sqrt{\frac{2}{3}\left(\varepsilon_{pL}^2 + \varepsilon_{pH}^2 + \varepsilon_{pR}^2\right)} \tag{5.2}$$

The first design code completely devoted to ECA of reeled pipelines is DNV-RP-F108 [9]. The flaw assessment procedure of the document is based on that of BS7910 [8], with adjustments to make it suitable for pipelines experiencing large plastic strains. However, the guidelines of BS7910 [8] are developed for load controlled situations, where development of large plastic strains are normally not justified. Tkaczyk et al. [49] reviewed the fracture response of reeled pipelines based on most of the available assessment schemes relevant to offshore reeled pipelines, and concluded that the available assessment approaches do not provide an accurate prediction of the fracture response of a reeled pipeline. Furthermore, Pisarski and Cheaitani [119] investigated

the fracture response of reeled pipelines by comparing FE results to predictions of BS7910 [8]. The predictions were noticeably lower than the FE results. They noted that this shortcoming could be overcome by the necessity to incorporating the effects of welding residual stresses and weld overmatch, thereby yielding in conservative estimates. Several attempts have been made to improve the accuracy of fracture response estimation schemes and/or simplifying them. In the context of reeled pipelines, these include the strain-based equations of tsby (2005b) and the modified reference stress solution of Tkaczyk et al. (2009). Taking advantage of the (nearly) linear evolution of fracture response with the applied nominal strain, Østby [50] proposed a set of strain based equation by fitting them to the results of a series of line-spring shell FE models. However, the limitations of the considered defect geometries and strain levels did not render the approach attractive for application to common reeled pipelines. Tkaczyk et al. [51] applied the modified reference stress approach of Kim and Budden [52] to the limit load solution of Kastner et al. [41], which is more commonly used in the offshore industry; they also considered more relevant defect geometries that usually occurrs in offshore reeled pipelines. Although the approach resulted in improved accuracy, it still does not take advantage of a strain-based formulation.

Jayadevan et al. [120] (2004) and Østby et al.[47] investigated the fracture response of pipelines subject to large plastic deformations under tension and bending, respectively. Their results clearly indicated the superiority of using the total strain in formulating the fracture response under large plastic strains over the traditional load-based approaches. The simplicity of a strain-based formulation is manifested in Figure 5.2, which shows the fracture response of a typical circumferentially cracked pipeline, quantified as $J/(\sigma_y t)$, under bending, both as a function of load (dashed line) and as a function of strain (solid line). Region 1 indicates that the bulk behavior is elastic with confined plasticity at the crack tip (small scale yielding); Region 2 indicates that plasticity develops in the whole pipe thickness (noting that the strain levels relevant to reeling fall in this region), while Region 3 is due to instability and collapse of the uncracked ligament.

In the work presented in this paper, a strain-based formulation is developed for assessing the fracture response of reeled pipelines, which upgrades the *reference strain*

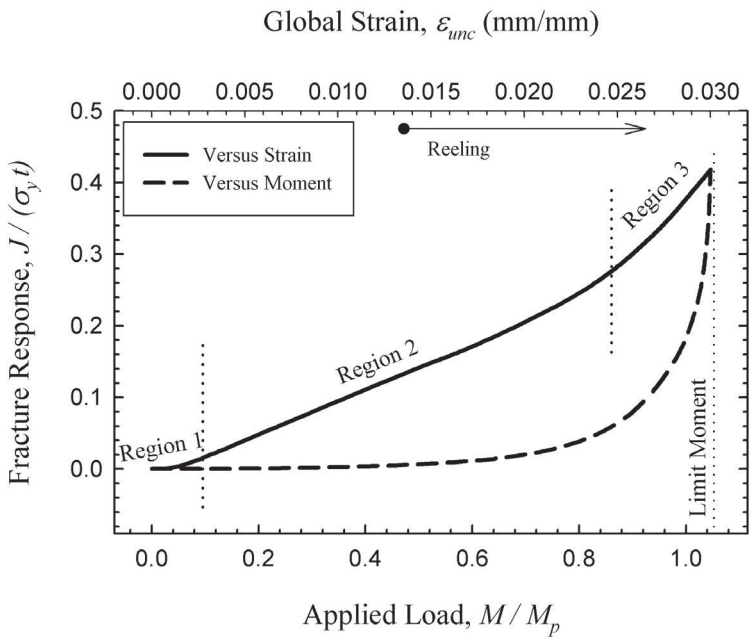

Figure 5.2. Fracture response of a typical circumferentially cracked pipeline as a function of the global strain (solid line) and load (dashed line), $D/t = 15$, $a/t = 0.5$, $2c/(\pi D) = 0.1$, $\sigma_y/\sigma_u = 0.659$.

approach of Linkens et al. [37]. The developed formulation takes advantage of the mentioned features relevant to reeled pipelines, namely the displacement controlled loading, high plastic strains, incorporation of SBD in pipeline design codes, and also the simplistic strain-based fracture formulation, which can additionally be made, needless of the limit loads definitions.

5.3 The Reference Strain Method

The path independent J-integral of Rice [28] and the crack tip opening displacement ($CTOD$) of Wells [32] are the two most prominent parameters that can satisfactorily characterize initiation and/or growth of a crack/flaw in ductile materials, where the limits of small scale yielding and the linear elastic fracture mechanics (LEFM) are surpassed [16, 27]. While the J-integral has a theoretical background in characterizing the near-tip stress fields with the so-called HRR singularity (after Hutchinson [29] and Rice and Rosengren [30]), and the concept of $CTOD$, as a fracture parameter was

initially based on experimental observations. Nevertheless, in general, the two parameters can be corelated [33]. Furthermore, in consideration of the issue of J-dominance situation and the necessity of using a two parameter fracture characterization [67], it was shown by Pisarski and Wignal [77] that the constraint of a circumferentially cracked pipe geometry (under loading levels relevant to reeled pipelines), is similar to that of the SENT (Single Edge Notch Tensile) specimen[1]. Based on this observation, DNV-RP-F108 [9] suggests using SENT to evaluate fracture toughness rather than the traditional SENB (Single Edge Notch Bend) specimen, as suggested by BS7910 [8], and thus justifies the single parameter fracture mechanics approach.

A brief background on the current J-estimation schemes, as suggested by DNV-RP-F108 [2] follows. For a material having a uniaxial stress–strain curve of the Ramberg-Osgood form, represented by Equation (5.3), the J integral can be approximated by the EPRI (Electric Power Research Institute) scheme of Kumar et al. [35] via Equation (5.4).

$$\frac{\varepsilon}{\varepsilon_y} = \frac{\sigma}{\sigma_y} + \alpha \left(\frac{\sigma}{\sigma_y}\right)^n \tag{5.3}$$

$$J = J_e(a_e) + J_p(a) = \frac{K^2(a_e)}{E'} + \alpha\sigma_y\varepsilon_y l_1 h_1 \left(\frac{P}{P_y}\right)^{n+1} \tag{5.4}$$

where $\varepsilon_y = \sigma_y/E$ and $J_e(a_e)$ is the elastic contribution to J, with a_e being the modified crack length. This modification (a_e) essentially accounts for the plastic zone correction in small scale yielding, whose effect would be reduced at higher loads, where plasticity effects are manifested in the *fully plastic* J_p term. The fully plastic term, J_p, represents a situation in which elastic strains are negligible, i.e. Equation (5.3) is modified as:

$$\frac{\varepsilon}{\varepsilon_y} = \alpha \left(\frac{\sigma}{\sigma_y}\right)^n \tag{5.5}$$

Kumar et al. [35] tabulated values of the h_1 function appearing in Equation (5.4) for some test specimen configurations and some simple cracked bodies. In his pioneering work, Ainsworth [36] developed the reference stress J estimation scheme, which is not limited to materials following a Ramberg-Osgood curve, and does not require tabulations of FE results (e.g. the h_1 functions in Equation (5.4)). This approach was

[1]Chapters 7 and 8 of the present thesis investigate this issue in much more detail and indeed confirm the crack tip constraint similarity of pipelines and SENT specimens.

further verified against the EPRI method by Miller and Ainsworth [39] and was observed to have an average over-prediction of 5%. The reference stress in their method is defined as:

$$\frac{\sigma_{ref}}{\sigma_y} = \frac{P}{P_y} \tag{5.6}$$

Substituting Equation (5.6) into Equation (5.4), while making simplifying assumptions and approximations, and also incorporating minor modifications as explained in Milne et al. [40], the final form of the J estimation scheme of BS7910 (and also DNV-RP-F108) is achieved:

$$J(a) = J_e(a)\left(\frac{E\varepsilon_{ref}}{\sigma_{ref}} + \frac{\sigma_{ref}^3}{2\sigma_y^2 E\varepsilon_{ref}}\right) \tag{5.7}$$

$$J_e(a) = \frac{K^2(a)}{E'}$$

Miller and Ainsworth [39] have verified the reference stress scheme against the EPRI method and showed that the reference stress method has an average over-prediction of 5%. However, on a case by case base, over-predictions as much as 20% and underpredictions as large as 40% were also observed [39].

DNV-RP-F108 [9] recommends using the limit load solution of Kastner et al. [41] to calculate the reference stress (Equation (5.6)). Introduction of the reference stress and strain in Equation (5.7) includes the effect of material's strain hardening capacity in determination of J. Furthermore, the geometric features of the cracked body are also included implicitly via the LEFM stress intensity factor (K) term. The first term ($E\varepsilon_{ref}/\sigma ref$) in Equation (5.7) describes both the limiting elastic and fully plastic behaviors. The second term ($\sigma_{ref}^3/(2\sigma_y^2 E\varepsilon_{ref})$) describes the behavior in between these two limits, namely the small scale yielding regime, where the general behavior is elastic but J exceeds its elastic value, and a minor plasticity correction is provided by the second term. The second term is designed such that it has a negligible effect in the elastic domain ($\sigma_{ref}/\sigma_y \ll 1$) and in the fully plastic domain in which $E\varepsilon_{ref}/\sigma_{ref} \gg 1$ [40, 44, 45]. Figure 5.3 shows the contribution of each term to J/J_e (by assuming equality of reference strain and applied strain), and it is observed that the minor plasticity correction term has insignificant effect for strains larger than 1%.

By neglecting the second term in (5.7), replacing reference stress and strain with their *uncracked body* values, some simplifying assumptions and introducing a safety

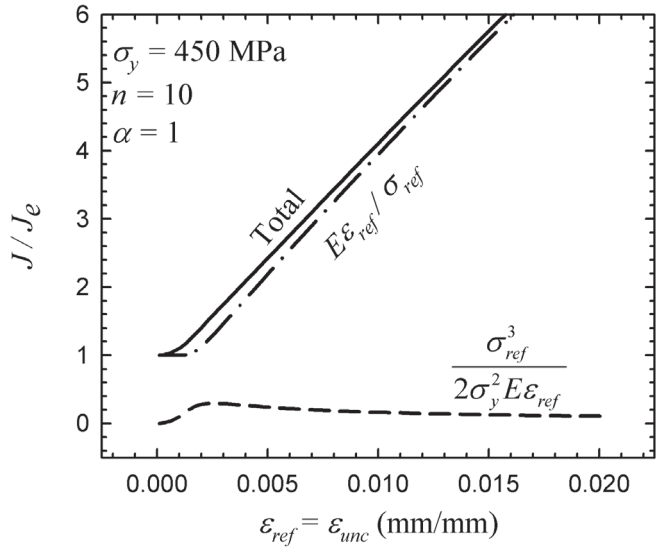

Figure 5.3. Influence of the minor plasticity correction term on the J-integral in the reference stress method.

factor of 2, Linkens et al. [37] proposed a *reference strain* formulation which is very straightforward for displacement controlled situations (note the general form of the LEFM stress intensity factor $K = F\sigma\sqrt{\pi a}$), embedded in the equation:

$$J = 2F^2\pi a\sigma_{unc}\varepsilon_{unc} \tag{5.8}$$

Equation (5.8) is in accord with test results on reeled pipelines of Pisarski et al. [46], detailed FE results of Refs. [47, 48, 50] which showed a similar evolution of fracture response parameter with total uncracked strain. However results of Tkaczyk et al. [49] indicate that although Equation (5.8) can qualitatively capture the fracture response of reeled pipelines, the quantitative accuracy is not sufficient. This is probably because for severe cracks, the difference between the reference strain and the uncracked strain becomes large and thus the underlying assumption of Equation (5.8) would be violated. Nevertheless, the reference strain approach is a very attractive alternative to the present load-based estimation schemes for application to reeled pipelines. Indeed the displacement controlled loading and the strain level pertinent to reeled pipelines justify the simplifying assumptions of the reference strain method. Based on these facts, the reference strain approach is selected as a basis for development a more accurate J assessment approach for reeled pipelines. The general form

of the proposed equation would be:

$$\frac{J}{\sigma_y t} = f_1 \varepsilon_{unc} + f_2 \tag{5.9}$$

where ε_{unc} is in %.

Generally, f_1 and f_2 are functions related to pipe and crack geometries and mechanical properties of the material. Equation (5.9) is developed based on Equation (5.8), where σ_{unc} is replaced by σ_y, and the LEFM geometric magnification factor F is omitted (since as will be seen, all the pertinent geometric effects are included in f_1 and f_2). Moreover t is used instead of a as a characteristic dimension of the pipe (a parameter analogous to l_1 as used in Equation (5.4)). Incorporation of f_2 (the intercept) was necessary to ensure accurate results. Furthermore, Equation (5.9) does not require a limit load definition (i.e. P_y in Equation (5.6)), in order to evaluate the fracture response. The values of f_1 and f_2 were established by conducting a series of parametric FE analyses, by which the response of a whole range of pipe geometries, crack geometries, and material properties relevant to offshore reeled pipelines were examined.

5.4 Parametric Finite Element Modeling

As stated, in order to establish an accurate reference strain J approximation approach, results from a series of FE models were analyzed using the ABAQUS software, version 6.8 [10]. A pipe with an external, part-through circumferential, surface breaking crack/flaw, subject to bending was investigated. The geometric features of the cracked cross section are shown in Figure 5.4. The crack has a *canoe* shape with its fillet radius equal to the crack depth ($r_1 = a$), which is believed to be representative of real weld defects observed in offshore pipelines. It should be noted, however, that the crack shape does not influence the fracture behavior at the crack center, where the maximum J occurs [121]. Only a segment of the pipe with the length of $L = 2D$ was modeled. Results produced by Jayadevan et al. [120] and Østby et al. [47] indicated that this length would be sufficiently long to capture the strain and stress discontinuity caused by the crack. Moreover, due to symmetry in geometry and boundary conditions, only a quarter of the pipe geometry was modeled (see Figure 5.5). Eight-node fully

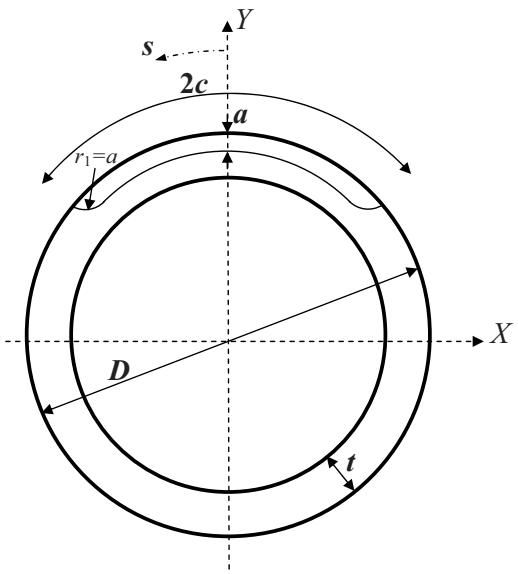

Figure 5.4. Geometric features of the pipeline cross section and the part-through external circumferential crack.

integrated continuum elements (C3D8) were used. The C3D8 elements are susceptible to shear locking in bending, however the longitudinal density of the mesh was carefully investigated and seen to be sufficient to avoid locking (note that use of the reduced integration version of this element resulted in rather mesh dependent values of J-integral). Bending was applied to the pipe by applying rotation to a master node connected to the pipe end via a set of multi-point-constrains (MPCs). The applied rotation was such that it would cause a longitudinal (uncracked) strain of 4% in the outermost fiber. This rotation was calculated as per the Euler beam theory, assuming that a plane section would remain plane after deformation. It is acknowledged that as plasticity develops, the actual behavior deviates from this assumption; however, the errors would be insignificant [119]. The rotation-strain relationship is governed by:

$$R_x = \frac{2\varepsilon_{unc}L}{D} \tag{5.10}$$

The J_2 deformation plasticity and Small Geometry Change, SGC, (small strain) assumptions were incorporated (see discussion below for justification). An initially sharp crack front was modeled with a so-called *focused spider web mesh*. Figure 5.5 shows a sample FE model and close-ups of the near-tip spider web mesh, along with

the applied boundary conditions[2]. Within the spider web mesh, the crack tip region (a half-tube with a radius of 1 mm surrounding the crack tip) was modeled with 10 rows of elements covering the circumference of the lower $\pi/2$ sector, and 6 rows of elements for the upper $\pi/2$ sector, and 10 rows of elements in the radial direction), leading to singular elements at the crack tip (the radial dimension of crack tip singularity elements was set at 50 μm), with the 8 node solid elements degenerated to 6 node wedge elements. In these elements, the overlapping nodes were not merged together, thereby allowing the initially sharp crack tip to blunt as load was increased, providing enhanced accuracy [16]. Mesh convergence studies were performed, investigating both the global behavior and the J-integral values, providing confidence in the established mesh. Each FE model consists of 12000$\sim$15000 solid elements, depending on the specific cracked pipe geometry. J-integrals were extracted for 10 consecutive rings of elements around the crack tip (excluding the first ring corresponding to the singular elements) using the *contour integral* feature of the ABAQUS, which utilizes the Virtual Crack Extension (VCE) technique of Parks [122]. The extracted 10 J-integral values were practically path-independent (with a maximum difference less than 5%), providing additional confidence in the results. However, an average of these 10 values was used.

In reference to extracting the J-integral values, two approaches can be incorporated: **(i)** the incorporation of the J_2-deformation theory of plasticity alongside SGC (small strain) assumption, as incorporated, for example by Pisarski and Cheitani [119] and Tkaczyk et al. [51]; or, **(ii)** the more elaborate, but much more computationally expensive approach, which is the combined use of the J_2 incremental plasticity theory alongside LGC (finite strain) assumption, as used for example, by Jayadevan et al. [120] and Østby et al. [47]. Noting the importance of computation effort in any large-scale parametric study, it is highly desirable to use the first approach, so long as it could be justified. The monotonic bending of the pipe suffices the proportionality requirement (i.e. principal components of stress increasing in proportion) to justify the use of the deformation plasticity theory [27]. To confirm the assumption, however, three models (with crack geometry of $a/t = 0.1$, 0.3 and 0.5) were analyzed using

[2]The presented Figure 5.5 is slightly more detailed than that in the published article.

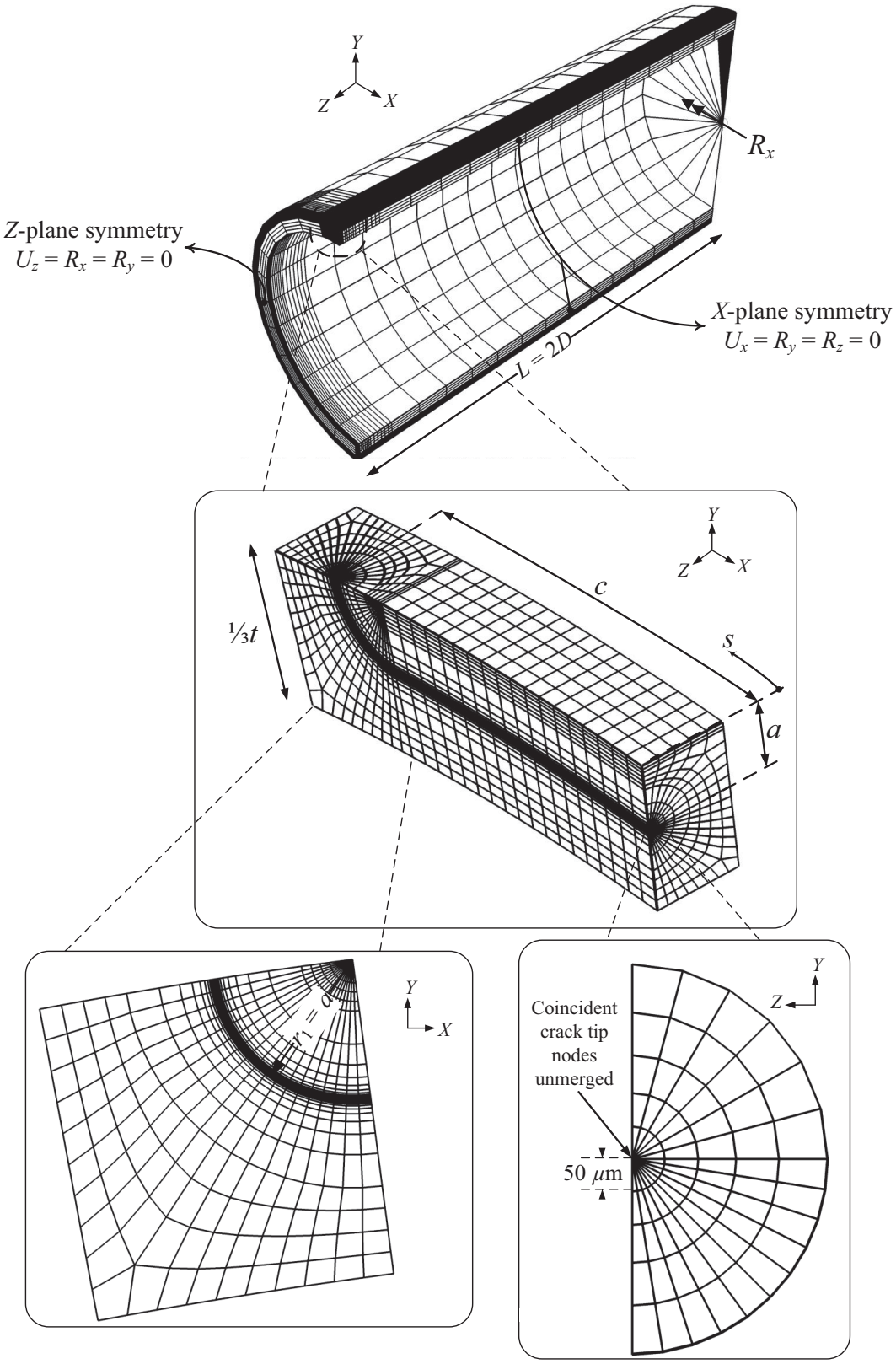

Figure 5.5. FE model of the typical configuration, showing boundary conditions close-ups of the focused spider web mesh of the crack tip.

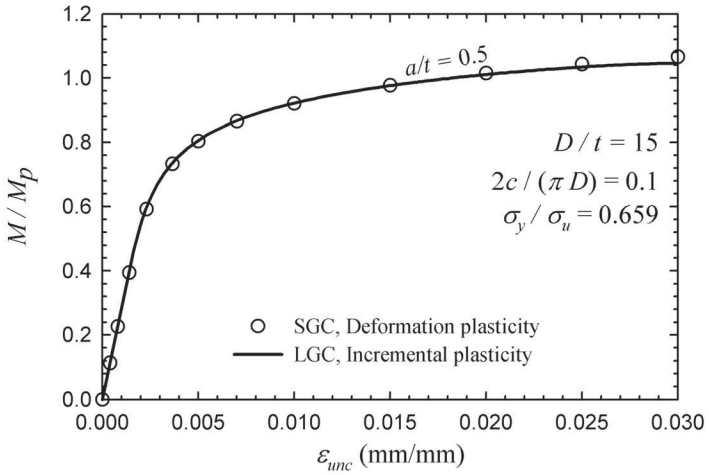

Figure 5.6. The moment versus uncracked strain curves based on two different FE modeling assumptions.

both the approaches to further establish the suitability of the modeling assumptions incorporated in the parametric study. It should be noted that the three FE models for the second assumption set had minor differences in their mesh in comparison to that shown in Figure 5.5; including an initially blunt crack tip with 25 μm radius, and also use of 20-node fully integrated hybrid continuum elements, C3D20H (note that use of hybrid elements, or alternatively reduced integration elements, is necessary in LGC analysis in order to avoid volumetric locking encountered at the near crack-tip elements which undergo very severe plastic straining), and also use of adaptive meshing feature of ABAQUS for the near-tip elements in order to smooth the highly distorted element shapes near the blunting crack tip.

Figure 5.6 shows the moment-strain curve based on the two sets of assumptions discussed above. As can be seen a very good agreement is observed, indicating that both assumption sets could capture the same global behavior (note that the results for $a/t = 0.1$ and 0.3 were indistinguishable and are not presented in the figure). Moreover, Figure 5.6 indicates that the SGC mesh using C3D8 elements is sufficiently refined such that over-stiffness from shear locking is avoided.

Figures 5.7a-c show the normalized crack opening stress along the uncracked ligament at the crack center for the three cases. As expected, the stresses from the two approaches converge together after a distance of $r\sigma_y/J > 1 \sim 2$ ahead of the crack

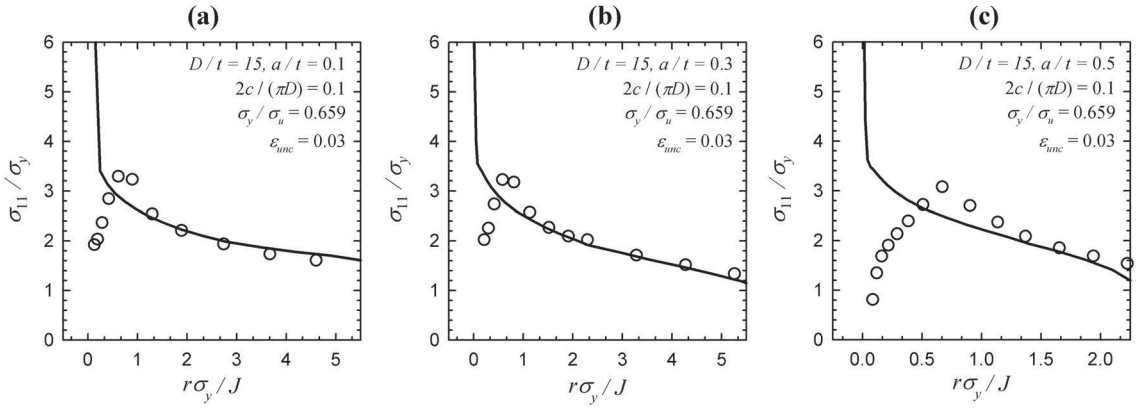

Figure 5.7. Distribution of the crack opening stress along the uncracked ligament based on two modeling approaches for three models **(a)** $a/t = 0.1$, **(b)** $a/t = 0.3$, and **(c)** $a/t = 0.5$. Solid line indicates deformation plasticity and SGC while open circles indicate incremental plasticity and LGC formulation.

tip, which is in concert with the results found in a significant number of available literature on the 2D crack tip fields (e.g. O'Dowd and Shih [67]). In other words, results of the LGC-based and SGC-based formulations would only differ in the near vicinity of the crack tip, which is affected by crack tip blunting, presumably the *fracture process zone*, in which the finite strain effects become important ($r\sigma_y/J > 1 \sim 2$). Such an agreement in the results, as observed in Figure 7, was also present between other stress and strain components. Moreover, the J-integral values obtained from the SGC analysis were slightly higher than the corresponding LGC solution, which is reasonable, having in mind the equivalency of J-integral and energy release rate, since including LGC effects generally increases the stiffness. Based on these observations, the use of J_2-deformation plasticity alongside SGC (small strain) assumption is deemed suitable for the purpose of evaluating the J-integral, with the overprediction regarded as an implicit safety margin.

The pipe and crack geometry can be described by non-dimensional parameters D/t, a/t and $2c/(\pi D)$, while the material's mechanical properties considered here are the yield strength σ_y and the strain hardening coefficient n(see Equation (5.3)), which can be converted to the more practical parameter σ_y/σ_u. However, FE simulations have shown that in the global plastic behavior regime (as relevant to strains occurred during reeling), the fracture response parameter would not be affected by the yield

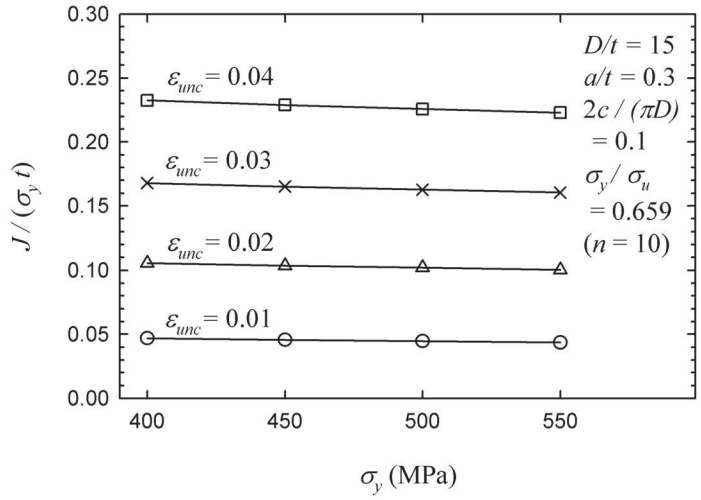

Figure 5.8. Effect of variation of yield strength on the fracture response.

strength value [50]. Furthermore, a model was analyzed for a range of yield strengths (400, 450, 500, 550 MPa), a range covering most of the commonly used grades of steel (i.e. X60 to X80; see API-5L [34]). Figure 5.8 shows the fracture response for the noted range, and the independence of the fracture response from the yield strength is observed.

Following the above discussion, f_1 and f_2 in Equation (5.9) are therefore functions of four parameters, namely: D/t, a/t, $2c/(\pi D)$ and σ_y/σ_u. Based on different permutations of these parameters as per Table 5.1, 300 FE models ($5 \times 5 \times 4 \times 3$) were constructed (100 different geometries for each of the three strain hardening levels), which are believed to cover all the practical situations relevant to reeled pipelines. The material stress–strain curve was assumed to follow the Ramberg-Osgood model, as per Equation (5.3). The following material properties were consistent in all models: $E = 200$ GPa, $\sigma_y = 450$ MPa, $\alpha = 1$ and $\nu = 0.3$. In order to convert the hardening index, n, to the more useful σ_y/σ_u ratio, the ultimate strength, σ_u, was defined as the stress corresponding to 15% uniaxial strain (note: this value has been quoted to be the lower limit of ultimate strain for offshore pipeline steels [4]). The corresponding stress–strain curves are shown in Figure 5.9.

It is worth noting that pre-processing, processing and post-processing of these 300 FE models were automatically performed using an in-house developed Python-based

Table 5.1. Range and sampling values of different geometric and material parameters.

Parameter	Value
D/t	10, 15, 20, 25, 30
a/t	0.1, 0.2, 0.3, 0.4, 0.5
$2c/(\pi D)$	0.05, 0.1, 0.15, 0.2
σ_y/σ_u (n)	0.659 (10), 0.757 (15), 0.846 (25)

script developed for ABAQUS, which significantly expedited the study (noting the complexity of the FE mesh, as shown in Figure 5.5).

At his juncture, it should be noted that most of the pipelines with relatively low D/t used for reeling are seamless; as a result, their materials' stress–strain curve may exhibit a Lüders plateau. Intuitively one may conclude that the Ramberg-Osgood model represented by Equation 5.3 cannot capture response of the material at high strain ranges. However, our experience indicates that a Ramberg-Osgood fit of the actual material stress–strain curve could still produce satisfactory predictions of the fracture response (see also O'Dowd [71] for some results on 2D test specimens). A case study was considered in ordere to establish the admissibility of the aforementioned statement. In the case study, we considered a realistic stress–strain curve exhibiting the Lüders plateau, which was approximated by three Ramberg-Osgood fits (see Figure 5.10a). In this case, the Lüders plateau was assumed to follow the elastic portion of the curve and extends up to a strain of 1.5% (Kyriakides et al. [123] noted that the termination of Lüders plateau usually occurs in the 1∼3% strain range). The strain hardening portion of the curve (after the Lüders plateau) was assumed to follow a power-law model, as per Equation 5.5. The three Ramberg-Osgood fits considered here, as seen in Figure 5.10a, corresponded to: **(i)** the best fit to the post-yield strain hardening portion of the stress–strain curve, **(ii)** a best fit, mainly conforming to the elastic portion of the curve, and **(iii)** an average (median) fit.

The fracture response obtained from the FE analyses using the above mentioned material modeling schemes are shown in Figure 5.10b for a typical case. As expected, the post-yield fit agrees very well with the realistic curve at higher strain levels, while the best fit to the elastic region shows a better agreement for lower strain levels.

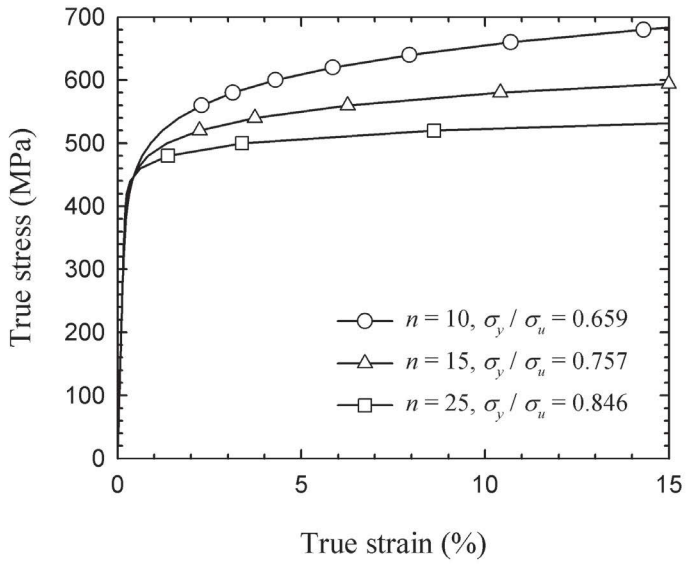

Figure 5.9. Uniaxial stress-strain curves for the material with three different strain hardening capacities considered in the parametric FE study.

Also, the average fit predicts an intermediate response throughout the whole strain range. In summary, although all the Ramberg-Osgood-based fits could more or less reasonably capture the fracture response, the use of the elastic fit is recommended here, since it results in a conservative estimation throughout the entire strain range. Therefore, the use of Ramberg-Osgood material model (Equation (5.3)) for describing the material response for the subsequent FE parametric study was deemed suitable.

5.5 Results and Discussion

The values of functions f_1 and f_2 were established based on the results of 300 FE models analyzed in this study. The values are presented in Tables 5.2 and 5.3. For each FE model, the value of the normalized fracture response ($J/(\sigma_y t)$) was extracted at five strain levels (i.e. ε_{unc} = 1.5, 2, 2.5, 3 and 4%, respectively). The variation of the J along the crack front was observed to be generally a function of geometric configuration and material properties; however, the maximum value of the J always occurred in the crack center, as depicted in Figure 5.11a and b. Figure 5.11a depicts the distribution for four different crack geometries and it is seen that increase of crack

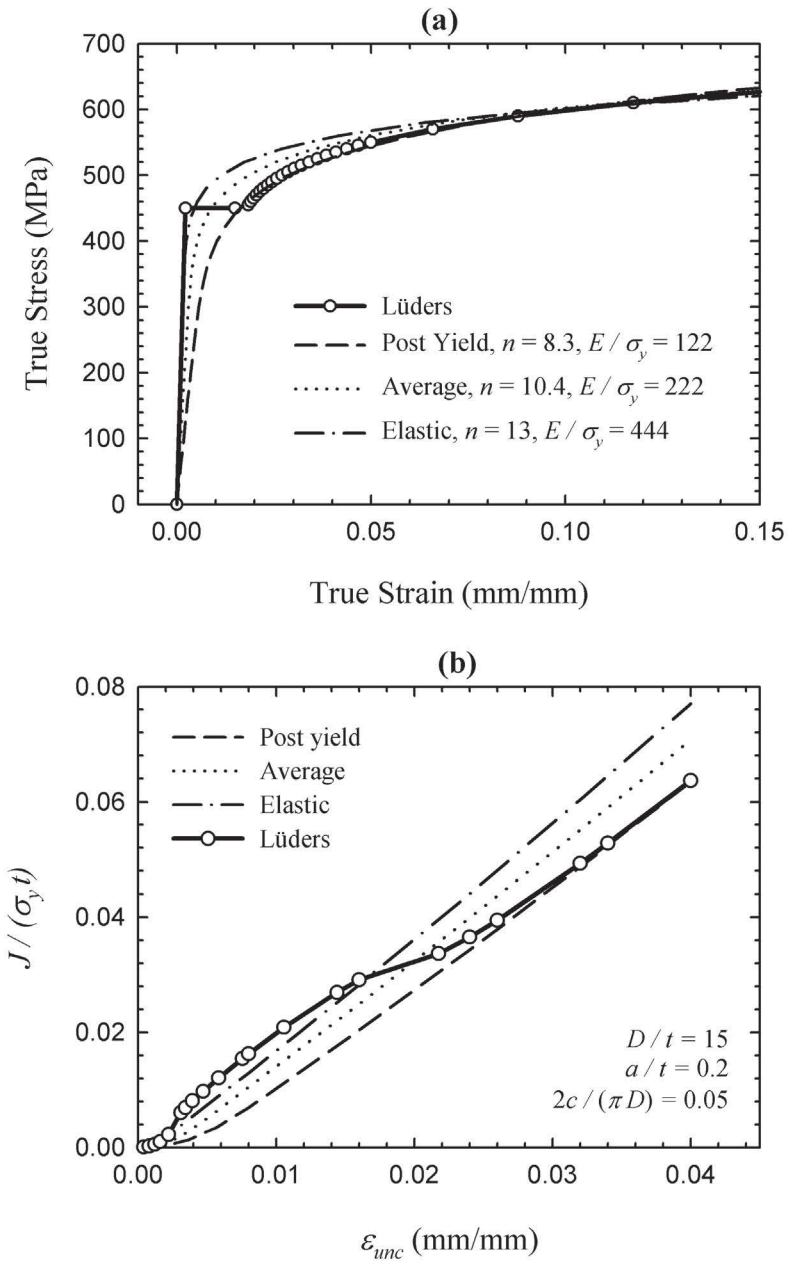

Figure 5.10. **(a)** A realistic stress-strain curve exhibiting the Lüders plateau alongside three Ramberg-Osgood fits and **(b)** Fracture response of a pipeline based on the four different stress–strain curves.

depth and crack length both result in steeper curves, i.e. the J integral decreases more rapidly along the crack length. Figure 5.11b shows the distribution for four different pipe geometries and material properties. Furthermore, the distribution shape did not change as a function of uncracked strain. As observed, common to all the distributions is the fact that the J is maximum at the crack center, which is in agreement results of Parks and Wang [124] for a cracked plate under bending, and thus justifying extracting J at the crack center location.

A linear regression through these values provides the values of f_1 and f_2 coefficients for each case. In conclusion, with the use of Equation (5.9), and the established values of f_1 and f_2, listed in Tables 5.2 and 5.3, one could predict the fracture response, in the practical strain range of $1.5\% \leqslant \varepsilon_{unc} \leqslant 4\%$, with an accuracy of $\pm 2\%$ (error is defined as $|J_{eq.9} - J_{FE}| / J_{FE}$). The proposed method's accuracy is therefore more than the other currently available schemes thus rendering the methodology suitable and effective for fracture analysis (ECA) of reeled pipelines.

Although the effect of each of the considered parameters, and also their interactive effect on fracture response, $\bar{J} = J/(\sigma_y t)$, can be assessed with Equation (5.9), a series of representative plots from the FE results are presented next. The evolution of fracture response versus ε_{unc} is shown in Figure 5.12a-d, for a family of a/t, D/t, $2c/(\pi D)$ and σ_y/σ_u values respectively. A linear trend is observed in all the figures. The slope of the ($\bar{J}$-ε_{unc}) line (i.e. the f_1 function) is dependent on the specific parameter considered. Increasing any of the four parameters would increase the fracture response; however, each parameter affects the slope in a different manner. Figure 5.12a indicates that the rate of change of the J is strongly dependent on a/t. Also, moving from shallow cracks (a/t of 0.1 and 0.2) to deep cracks (a/t of 0.3, 0.4 and 0.5), would significantly increase the rate of change of the J. However, unlike the effect of a/t, the influence of D/t on the rate of change of the J is rather uniform (see Figure 5.12b). Moreover, Figure 5.12c reveals that increasing $2c/(\pi D)$ from 0.05 to 0.1 would strongly affect the fracture response slope, while an increase from 0.15 to 0.2 would increase the slope in a more modest manner. Finally, Figure 5.12d exhibits the pronounced influence of strain hardening, σ_y/σ_u, on the rate of change of the J; while increase of σ_y/σ_u from 0.659 to 0.757 does not seriously alter the slope of the

Table 5.2. Variation of $Arctan(f_1)$ in degrees as a function of a/t, $2c/(\pi D)$, D/t and σ_y/σ_u for use in Equation (5.9); linear interpolation permitted.

	$2c/(\pi D) = 0.05$			$2c/(\pi D) = 0.10$			$2c/(\pi D) = 0.15$			$2c/(\pi D) = 0.20$		
	σ_y/σ_u:			σ_y/σ_u:			σ_y/σ_u:			σ_y/σ_u:		
	0.659	0.757	0.846	0.659	0.757	0.846	0.659	0.757	0.846	0.659	0.757	0.846
$a/t = 0.1$												
D/t:												
10	0.418	0.390	0.375	0.450	0.424	0.411	0.460	0.435	0.423	0.461	0.436	0.425
15	0.435	0.407	0.389	0.463	0.436	0.421	0.468	0.441	0.426	0.467	0.440	0.425
20	0.445	0.415	0.397	0.468	0.439	0.422	0.470	0.441	0.424	0.469	0.439	0.422
25	0.450	0.420	0.401	0.470	0.440	0.422	0.472	0.441	0.422	0.470	0.439	0.420
30	0.454	0.422	0.402	0.472	0.441	0.422	0.473	0.441	0.421	0.472	0.440	0.419
$a/t = 0.2$												
D/t:												
10	0.998	0.962	0.958	1.284	1.283	1.339	1.431	1.467	1.590	1.487	1.553	1.735
15	1.152	1.123	1.131	1.463	1.496	1.606	1.573	1.656	1.864	1.591	1.701	1.977
20	1.249	1.230	1.253	1.539	1.600	1.760	1.611	1.721	1.994	1.605	1.735	2.072
25	1.306	1.296	1.333	1.566	1.648	1.851	1.610	1.738	2.057	1.592	1.732	2.106
30	1.340	1.340	1.390	1.573	1.670	1.907	1.598	1.734	2.086	1.574	1.717	2.113
$a/t = 0.3$												
D/t:												
10	1.647	1.641	1.708	2.681	2.845	3.229	3.420	3.836	4.704	3.902	4.602	6.066
15	2.200	2.241	2.384	3.545	3.920	4.634	4.410	5.214	6.743	4.936	6.214	8.801
20	2.605	2.696	2.915	4.109	4.681	5.701	5.020	6.195	8.397	5.519	7.307	10.985
25	2.906	3.049	3.340	4.490	5.245	6.566	5.400	6.906	9.768	5.848	8.071	12.801
30	3.127	3.318	3.676	4.760	5.690	7.314	5.643	7.447	10.955	6.034	8.628	14.374
$a/t = 0.4$												
D/t:												
10	2.130	2.181	2.357	4.286	4.599	5.367	6.168	7.002	8.885	7.813	9.473	12.917
15	3.233	3.335	3.627	6.172	6.790	8.214	8.687	10.350	13.834	10.774	13.892	20.047
20	4.107	4.259	4.657	7.608	8.640	10.832	10.549	13.151	18.340	12.888	17.528	26.251
25	4.783	4.994	5.514	8.709	10.195	13.197	11.960	15.498	22.337	14.438	20.550	31.544
30	5.311	5.604	6.265	9.596	11.536	15.335	13.072	17.524	25.905	15.629	23.121	36.060
$a/t = 0.5$												
D/t:												
10	2.422	2.539	2.832	5.477	6.037	7.422	8.673	10.177	13.430	12.059	14.917	19.992
15	3.927	4.124	4.640	8.464	9.638	12.308	13.332	16.278	21.981	18.188	23.322	31.051
20	5.193	5.483	6.242	11.126	13.055	17.123	17.351	21.877	29.814	23.240	30.545	40.085
25	6.262	6.682	7.717	13.456	16.189	21.624	20.742	26.791	36.498	27.346	36.505	47.136
30	7.195	7.772	9.101	15.490	19.031	25.733	23.626	31.046	42.060	30.743	41.403	52.620

Table 5.3. Variation of f_2 as a function of a/t, $2c/(\pi D)$, D/t and σ_y/σ_u for use in Equation (5.9); linear interpolation permitted.

	$2c/(\pi D) = 0.05$			$2c/(\pi D) = 0.10$			$2c/(\pi D) = 0.15$			$2c/(\pi D) = 0.20$		
	σ_y/σ_u:			σ_y/σ_u:			σ_y/σ_u:			σ_y/σ_u:		
	0.659	0.757	0.846	0.659	0.757	0.846	0.659	0.757	0.846	0.659	0.757	0.846
$a/t = 0.1$												
D/t:												
10	-0.002	-0.001	0.000	-0.002	-0.001	-0.001	-0.002	-0.001	-0.001	-0.002	-0.001	-0.001
15	-0.002	-0.001	0.000	-0.002	-0.001	-0.001	-0.002	-0.001	-0.001	-0.002	-0.001	-0.001
20	-0.002	-0.001	0.000	-0.002	-0.001	-0.001	-0.002	-0.001	-0.001	-0.002	-0.001	-0.001
25	-0.002	-0.001	0.000	-0.002	-0.001	-0.001	-0.002	-0.001	-0.001	-0.002	-0.001	-0.001
30	-0.002	-0.001	0.000	-0.002	-0.001	-0.001	-0.002	-0.001	-0.001	-0.002	-0.001	-0.001
$a/t = 0.2$												
D/t:												
10	-0.005	-0.003	-0.002	-0.006	-0.004	-0.003	-0.007	-0.005	-0.004	-0.007	-0.006	-0.005
15	-0.005	-0.004	-0.002	-0.007	-0.005	-0.004	-0.008	-0.006	-0.005	-0.008	-0.006	-0.006
20	-0.006	-0.004	-0.003	-0.007	-0.006	-0.005	-0.008	-0.006	-0.006	-0.008	-0.006	-0.006
25	-0.006	-0.004	-0.003	-0.008	-0.006	-0.005	-0.008	-0.006	-0.006	-0.008	-0.006	-0.006
30	-0.006	-0.004	-0.003	-0.008	-0.006	-0.005	-0.008	-0.006	-0.006	-0.008	-0.006	-0.006
$a/t = 0.3$												
D/t:												
10	-0.009	-0.007	-0.006	-0.015	-0.012	-0.013	-0.020	-0.018	-0.022	-0.023	-0.024	-0.032
15	-0.012	-0.009	-0.007	-0.020	-0.018	-0.018	-0.026	-0.025	-0.030	-0.030	-0.032	-0.045
20	-0.014	-0.011	-0.009	-0.023	-0.021	-0.022	-0.030	-0.030	-0.036	-0.034	-0.038	-0.055
25	-0.015	-0.012	-0.010	-0.026	-0.024	-0.025	-0.032	-0.033	-0.042	-0.036	-0.042	-0.063
30	-0.016	-0.013	-0.011	-0.028	-0.026	-0.028	-0.034	-0.036	-0.046	-0.038	-0.045	-0.071
$a/t = 0.4$												
D/t:												
10	-0.012	-0.010	-0.009	-0.026	-0.024	-0.027	-0.040	-0.040	-0.052	-0.053	-0.058	-0.085
15	-0.019	-0.015	-0.014	-0.038	-0.034	-0.040	-0.055	-0.057	-0.078	-0.072	-0.085	-0.131
20	-0.023	-0.019	-0.017	-0.046	-0.043	-0.052	-0.066	-0.072	-0.102	-0.086	-0.107	-0.173
25	-0.027	-0.022	-0.019	-0.052	-0.051	-0.063	-0.075	-0.084	-0.124	-0.097	-0.126	-0.211
30	-0.030	-0.024	-0.021	-0.057	-0.057	-0.073	-0.083	-0.096	-0.144	-0.105	-0.144	-0.247
$a/t = 0.5$												
D/t:												
10	-0.014	-0.012	-0.012	-0.035	-0.034	-0.043	-0.058	-0.063	-0.088	-0.086	-0.102	-0.145
15	-0.023	-0.019	-0.019	-0.053	-0.053	-0.071	-0.089	-0.100	-0.143	-0.132	-0.161	-0.228
20	-0.030	-0.025	-0.024	-0.070	-0.073	-0.098	-0.117	-0.136	-0.197	-0.173	-0.218	-0.309
25	-0.036	-0.030	-0.030	-0.085	-0.090	-0.124	-0.142	-0.169	-0.249	-0.208	-0.271	-0.387
30	-0.041	-0.035	-0.035	-0.099	-0.107	-0.149	-0.165	-0.200	-0.299	-0.239	-0.320	-0.463

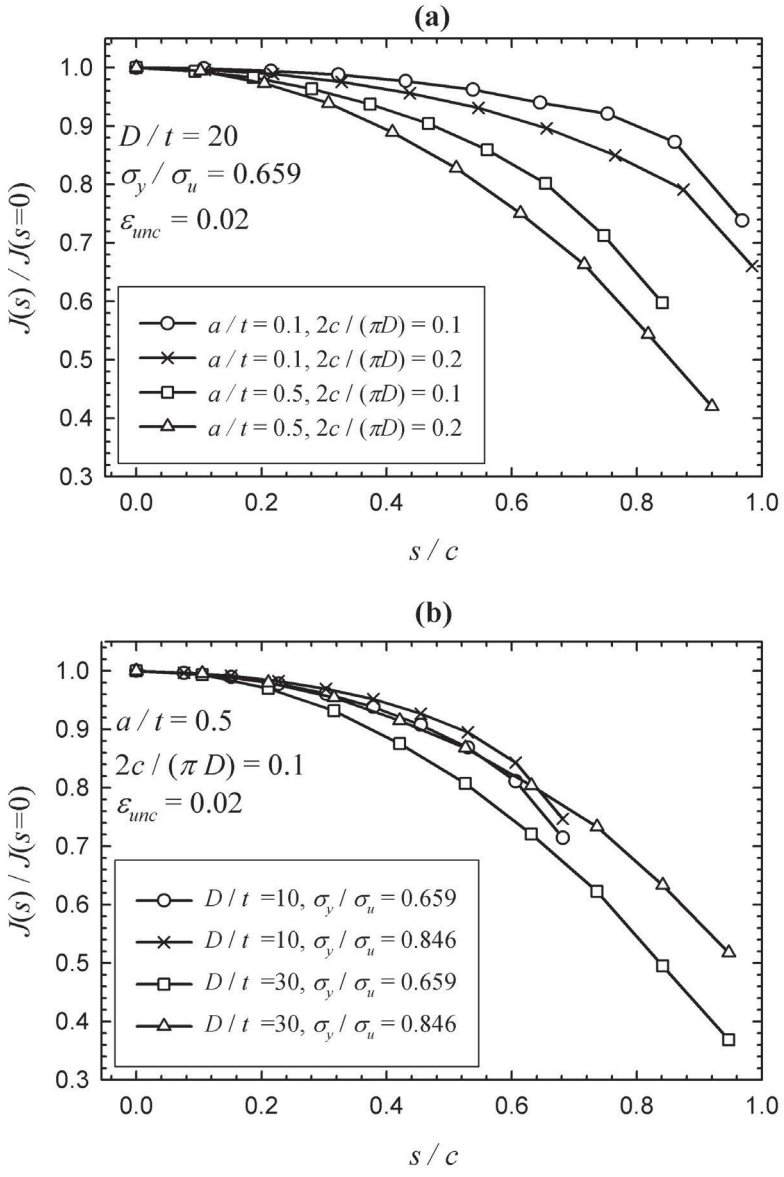

Figure 5.11. Distribution of J along the crack length: **(a)** for various crack geometries and **(b)** for various pipe geometries and material properties.

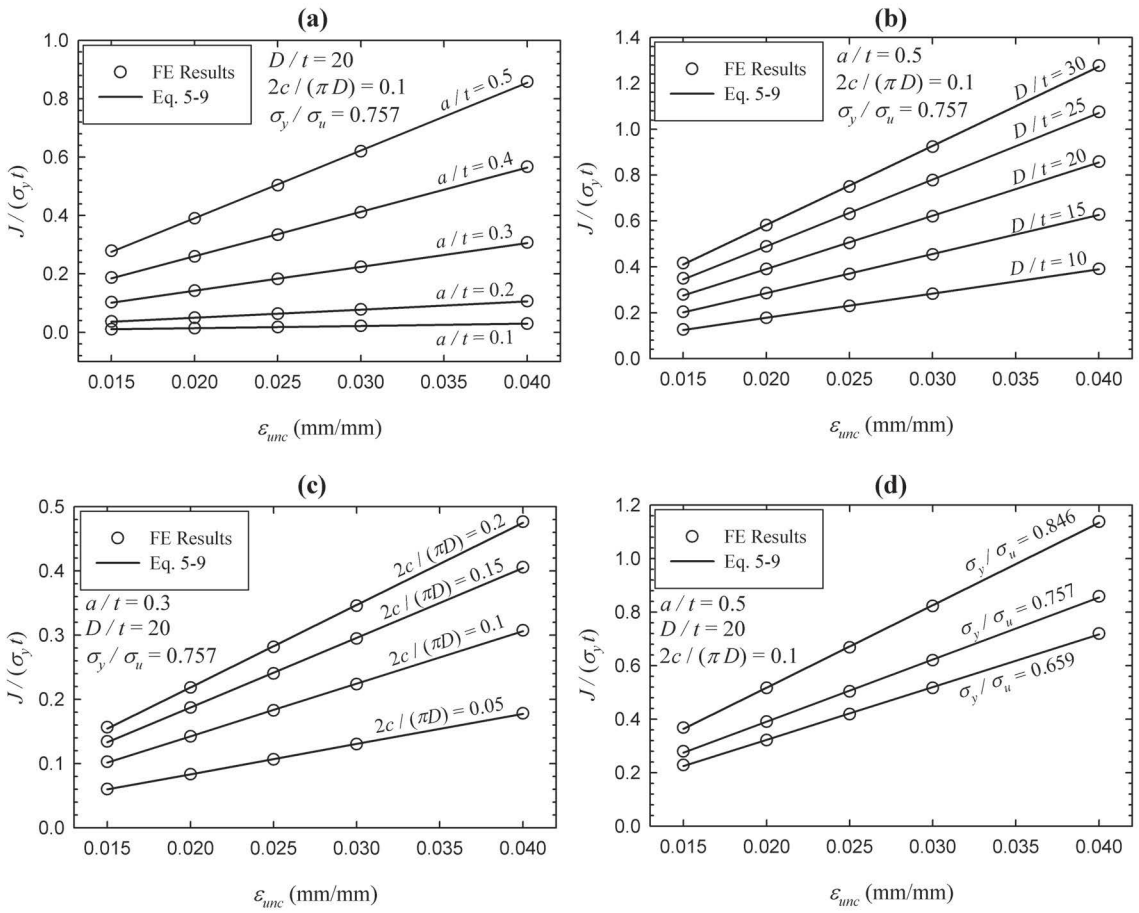

Figure 5.12. Evolution of the fracture response versus uncracked strain for **(a)** various a/t values, **(b)** various D/t values, **(c)** various $2c/(\pi D)$ values, and **(d)** various $\sigma_y\sigma_u$ values.

line, the increase from 0.757 to 0.846 would seriously affect the slope. This is justified considering the fact that σ_y/σ_u of 1 ($n \to \infty$) signifies a perfectly plastic material in which the fracture response would be theoretically unbounded (upon reaching the limit moment). This negative effect of the decreased strain hardening capacity (which is a drawback of high grade steels (e.g. X80, X100, X120) on fracture response is manifested in design codes (see for example DNV-OS-F101 [2], which limits σ_y/σ_u to 0.85 for reeled pipelines.)

The *interactive* effect of the parameters considered earlier on the fracture response were investigated and the results are presented in Figure 5.13. Figure 5.13a shows the interaction of a/t and D/t on fracture response at ε_{unc}, while keeping the other

parameters at a specified value. The same data is presented twice, once as a function of a/t for a family of D/t values (the solid line), and vice versa (see the dotted symbolized line). Considering the solid lines, again, shallow cracks with a/t of 0.1 and 0.2 produce nearly the same fracture response values, while for deep cracks with a/t of 0.3, 0.4 and 0.5, the fracture response strongly depends on a/t. As seen, the $\bar{J}$ versus a/t curve is strongly nonlinear, with D/t influencing its variation. It is evident that interaction of a/t and D/t strongly influences the fracture response, with their combinations at large values of $a/t > 0.3$ and $D/t > 20$, leading to very high levels of fracture response. Moving to the dotted lines, the $\bar{J}$ versus D/t curve is more or less linear for all values of a/t. Furthermore, the effect of D/t on fracture response is most significant only for a/t of 0.4 and 0.5, and for shallow cracks with a/t of 0.1 and 0.2, $\bar{J}$ is nearly constant for all values of D/t. This indicates that reeling of pipes with relatively larger D/t would only be safely achievable so long as deep cracks are detected and prevented.

Figure 5.13b shows the interaction of a/t and σ_y/σ_u on the fracture response. The solid line exhibits the nonlinear shape of the $\bar{J}$ versus a/t curve, with $2c/(\pi D)$ significantly altering the variation of the curve for deeper cracks with a/t of 0.3, 0.4 and 0.5. The dotted line illustrates that crack length parameter, $2c/(\pi D)$, does not drastically affect the shallow cracks with a/t of 0.1 and 0.2. Furthermore, a kink is observed in the curve at $2c/(\pi D)$ of 0.1 for deep cracks with a/t of 0.4 and 0.5, which showcases the strong interaction of deep and long cracks on magnifying $\bar{J}$.

The interaction of a/t and σ_y/σ_u is presented in Figure 5.13c, which is observed to have less influence on the fracture response, in comparison to the interactions shown in Figures 5.13a and b. It can be seen that the variation of σ_y/σ_u does not affect the fracture response of shallow cracks with a/t of 0.1 and 0.2, and only affects the deeper cracks. For the deeper cracks (i.e. with a/t of 0.4 and 0.5), a kink is observed in the dotted lines at a σ_y/σ_u of 0.757, again demonstrating the detrimental influence of a steel with low strain hardening, as a perfect plasticity limit of $\sigma_y/\sigma_u = 1$ is approached.

The interactive effect of D/t and $2c/(\pi D)$ is shown in Figure 5.13d. The dotted lines show a nearly linear variation of $\bar{J}$ with respect to $2c/(\pi D)$ for the case of

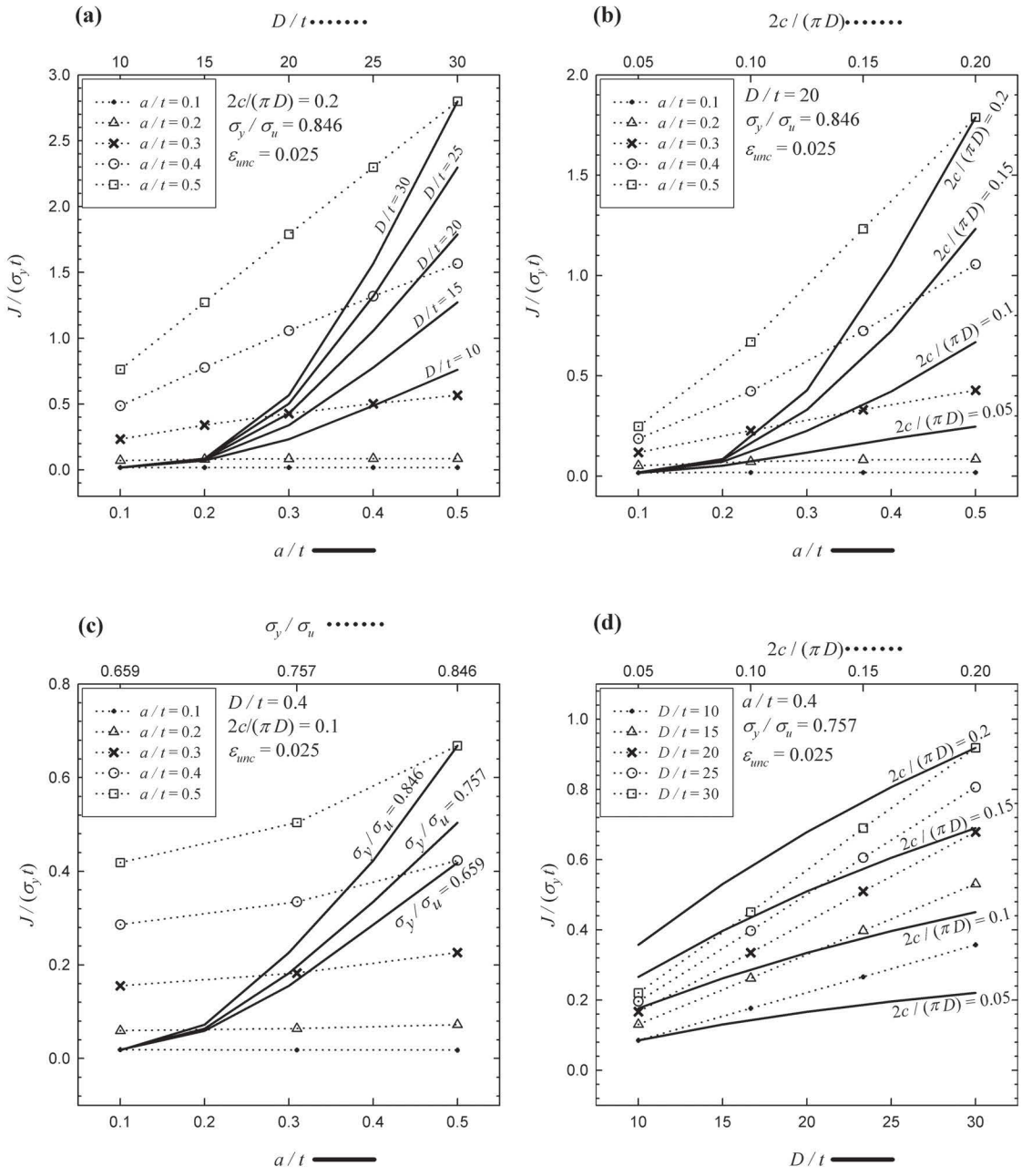

Figure 5.13. The interactive effect of pairs of parameters on the fracture response, while keeping the other parameters constant: **(a)** fracture response as a function of a/t and D/t, **(b)** fracture response as a function of a/t and $2c/(\pi D)$, **(c)** fracture response as a function of a/t and σ_y/σ_u, and **(d)** fracture response as a function of D/t and $2c/(\pi D)$.

$a/t = 0.4$. On the contrary, the variation of $\bar{J}$ as a function of D/t follows an asymptotic trend. Furthermore, even for the lowest crack length with $2c/(\pi D)$ of 0.05, increasing the D/t will lead to higher values of fracture response.

It should be noted that visualization of the complete interaction of all the parameters is not possible, as it requires a 5-dimensional space; thus Figure 5.13 can only give a sense of the general trends and interaction patterns. However, the use of Equation (5.9) along with the values of the f_1 and f_2 functions presented in Tables 5.2 and 5.3, provide a quantitative means for assessing the influence of all the parameters combined.

The presence of a crack affects the strain and stress in a region around it. A potential means of assessing the impact of a crack is through investigating the longitudinal strain (ε_{11}) distribution along the length of the pipe, which would have a constant value for an ideally defect-free case subject to bending, as per Equations (5.1) and (5.10). Figure 5.14a-d show this strain distribution along the pipe length as a function of each of the four investigated parameters, respectively, while keeping the other parameters at a specified value. Inspection of the results presented in the four figures reveals that a/t has the most pronounced effect on the strain distribution (Figure 5.14a), followed by $2c/(\pi D)$ (Figure 5.14b), while the variation of D/t and σ_y/σ_u does not seriously alter the strain distribution (see Figures 5.14c and d respectively). Figure 5.14a shows that for shallow cracks with a/t of 0.1 and 0.2, the longitudinal strain reaches 80% of the uncracked strain value (ε_{unc}) at a very short distance ($x/D \approxeq 0.05$, see schematic in Figure 5.14), while for deeper cracks (i.e. a/t of 0.3, 0.4 and 0.5), the same percentile of strain occurs at approximately $x/D \approxeq 0.5$. Additionally, the distribution trend for these deep cracks is somewhat different than that for shallow cracks. Furthermore, the results also justify the validity of the assumption that one could perform adequate and somewhat accurate finite element modeling of the system by considering a half-length of pipe equal to twice its diameter ($L = 2D$).

In all the four Figures (i.e. Figures 5.14a-d), negative values of the strain are observed in the vicinity of the crack location, as most evident in Figure 5.14a (i.e. for a/t of 0.3, 0.4 and 0.5). This phenomenon can be explained by noting that the crack causes a discontinuity in the stress flow through the pipe wall, which results

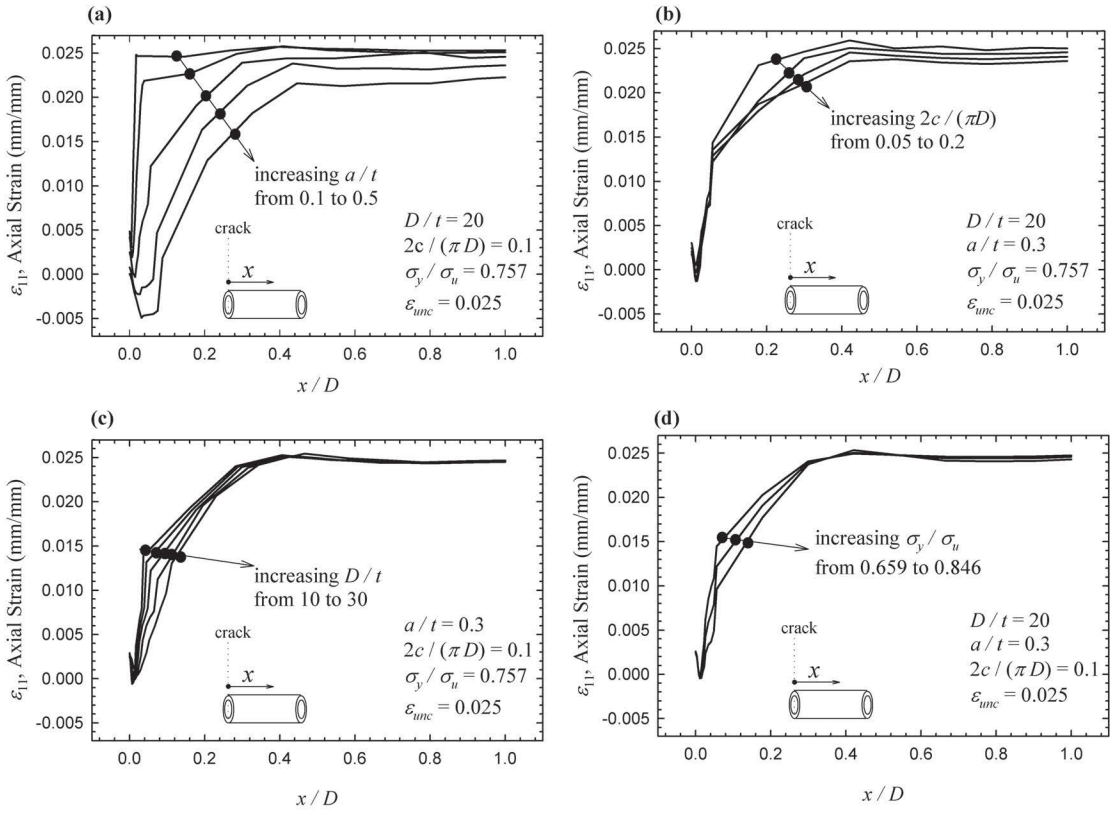

Figure 5.14. Distribution of the axial strain along the pipeline length ahead of the crack: **(a)** for a family of a/t values, **(b)** for a family of $2c/(\pi D)$ values, **(c)** for a family of D/t values, and **(d)** for a family of σ_y/σ_u values.

in unbalanced stresses at the vicinity of the crack, which in turn causes a secondary bending of the pipe wall. Figure 5.15 shows the deformed shape of the pipe wall in the vicinity of a fully displaced (opened) crack, in which the deformations and negative strain caused by the secondary moment are illustrated. A free body diagram of the pipe wall in the vicinity of a crack would show that the secondary moment would be a linear function of crack depth, a. This is in accord with Figure 5.14a-d; as noted, specifically, the negative strains in Figure 5.14a increase with increasing a/t, while in Figure 5.14b-d which correspond to a constant value of $a/t = 0.3$, the negative strain remains constant within each family of curves.

Tkaczyk et al. [51] compared their developed modified reference stress solution (i.e. that based on the DNV approach with a modification function applied to Kastner's [41] limit load solution) to a number of other J-estimation approaches (namely

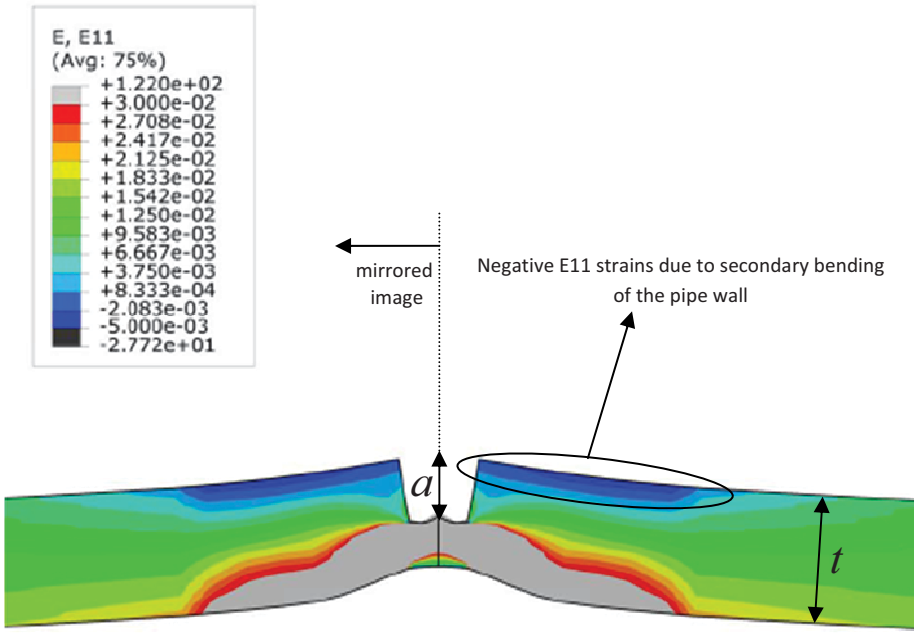

Figure 5.15. Deformation of the pipe wall in vicinity of the crack showing the secondary bending and resultant negative strains.

the DNV-RP-F108 [9] procedure (with Kastner's limit load), and the strain-based equations of Østby [50]). The comparison of their results, along with the results of the proposed reference strain formulation (i.e. Equation (5.9), which also correspond to 3D FE results with a maximum of 2% error), are presented in Figures 5.16a-b. The results in Figure 5.16a correspond to a X65 grade steel idealized with a Ramberg-Osgood fit (Equation (5.3)), while Figure 5.16b is for a X70 steel, whose stress–strain curve includes a Lüders plateau, but its material response was only approximated with a Ramberg-Osgood fit. As noted by Tkaczyk et al. [51], the DNV-RP-F108 [9] over-predicts the J for some cracked geometries (see Figure 5.16a), and under-predicts the J in some other cases (see Figure 5.16b). Noting that the midrange fracture toughness for both steel grades is $J_c = 400$ N/mm [51] it is evident that the final outcome of the ECA is highly sensitive to the value of J, rendering an accurate prediction of the J as highly crucial, hence, desirable. The agreement between the proposed reference strain formulation (Equation (5.9)), which also correspond to 3D FE results with a maximum of 2% error) and results of Tkaczyk et al. [51] is reasonably good for the

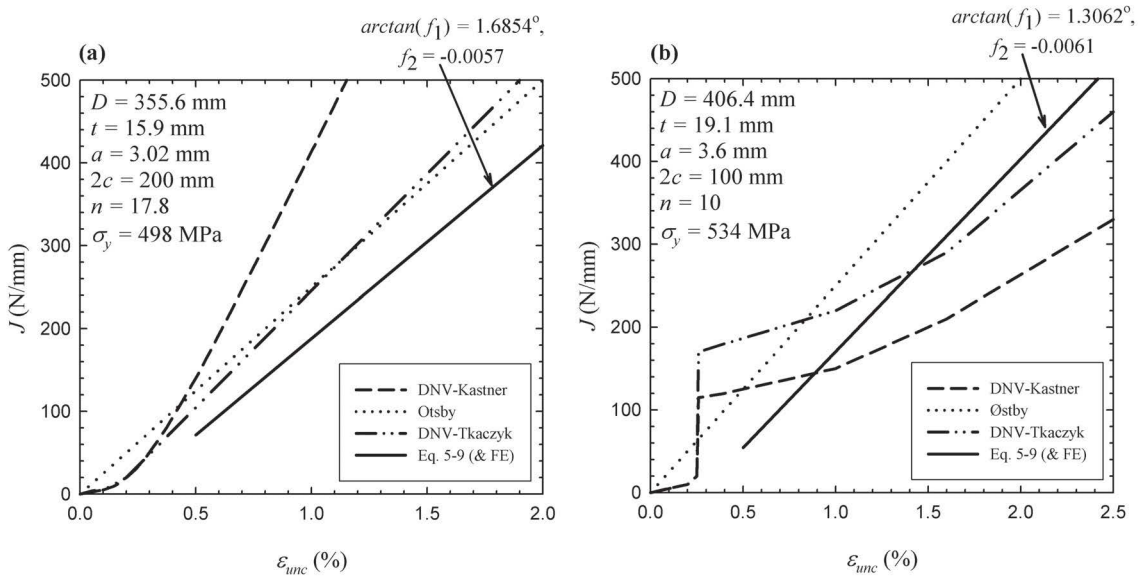

Figure 5.16. Comparison of various J-estimation schemes (from Tkaczyk et al. [51]) with the results obtained from Equation (5.9) for **(a)** X65 steel idealized with Ramberg-Osgoods model and **(b)** X70 steel with a Lüders plateau, approximated with a Ramberg-Osgood fit.

depicted strain range; however, larger discrepancies could be anticipated as higher values of strain are approached. The formulation of Tkaczyk et al. [51] are based on FE models in which the pipes are subjected to tensile loading, based on the postulation that the fracture response of a pipe under tension would be similar, or slightly higher than that of a pipe under bending, following the findings of Østby et al. [47]. This assumption might be the source of the mentioned accumulated discrepancy between the two approaches at higher strain values.

5.6 Summary and Conclusions

In the current study, a J-estimation scheme was developed for assessing the integrity of reeled pipelines. The proposed approach is an extension and modification of the reference strain method proposed by Linkens et al. [37], which itself was based on the earlier reference stress method of Ainsworth [36] and the EPRI scheme of Kumar et al. [35]. The developed reference strain formulation (Equation (5.9) in this paper) takes advantage of the displacement controlled loading nature which occurs during reeling, and also the resulting high strain levels, often leading to a fracture response

of the pipe in the plastic regime of its material. The developed formulation predicts the fracture response of the pipe (per non-dimensionalization of the J-integral) as a linear function of the axial strain in the pipe at its uncracked state (ε_{unc}). The slope and intercept of the linear function relate to the geometry and material properties of the pipe. A series of 300 3D-FE models were used to calibrate the equation for range of pipelines, crack geometries and also material properties, which are believed to cover most of the practical combinations relevant to reeled pipelines. The assumptions of small geometry changes, SGC, and deformation plasticity were adopted in developing the proposed equation in favor of attaining lower computational costs. The admissibility of these assumptions was validated by the use of more complex FE models. The developed formulation predicts the fracture response with a maximum error of 2% for a strain range of $1.5\% \leqslant \varepsilon_{unc} \leqslant 4\%$ with respect to the FE results, which is believed to be more accurate than the currently used assessment approaches. The most important summary and conclusions of this study are as follows:

- The underlying assumptions of the reference strain method of Linkens et al. [37] were reviewed and proved to be justified for strain levels relevant to reeled pipelines.

- In order to justify the use of deformation plasticity alongside the Small Geometry Change (SGC) assumption for the parametric FE models, three typical cases were also modeled using the incremental plasticity theory and Large Geometry Change (LGC) formulations. Comparison of the moment-strain results revealed that the analysis based on the former set of assumptions could accurately capture the global behavior of cracked reeled pipelines. As for the *local* behavior, the crack tip stress and strain fields obtained based on the two approaches were in agreement with each other, except for the very near vicinity of the crack tip influenced by crack tip blunting. Moreover, the former approach resulted in slightly higher J values. Based on the observed consistency, use of the deformation plasticity with SGC assumption was justified for further use in the parametric study.

- In concert with the observations of Østby [50], it was observed that the variations

in the yield strength would only marginally affect the fracture response in the plastic regime, thus justifying the representation of the material behaviour with a single parameter, namely the strain hardening capacity.

- Although the pipe and crack geometries and also material properties do influence the distribution shape of the J integral along the crack length, it was observed that the maxima would always occur at the crack center. Based on this, J values extracted from this location were used to calibrate the reference strain formulation of Equation (5.9).

- The maximum error of less than 2% obtained through the use of the proposed relation (i.e. Equation (5.9)), clearly indicates that indeed the fracture response of reeled pipelines in the plastic regime is a linear function of uncracked strain for the practical wide range of pipe/crack geometry and the material properties considered herein. This also justifies the use of the total uncracked strain as the most suitable parameter for describing fracture response of reeled pipelines.

- The parametric studies presented here (Figures 5.12 and 5.13) illustrated the influence of variation of various parameters on the fracture response. It was shown, however that the crack depth affected the fracture response most notably. In addition, the behavior of shallow cracks with a/t of 0.1 and 0.2 was markedly different than that of deeper cracks with a/t of 0.3, 0.4 and 0.5. Also variations of D/t, crack length ($2c/(\pi D)$) and strain hardening (σ_y/σ_u) did not significantly affect the fracture response of shallow cracks. On the other hand, they did strongly interact with a/t in deeply cracked pipes. Furthermore, it was also observed that when the martial's response approached perfect plasticity (i.e. a marked reduction in the strain hardening capacity), it significantly influenced the fracture response.

- It was observed that crack depth (a/t), strongly influenced the uniform distribution of the longitudinal strain along the pipe. For the cases considered, the uniform strain distribution could be observed at a short distance away from shallow cracks ($\approxeq 0.05D$ for a typical case), while for the case of deeper cracks, this distance was observed to be significantly longer ($\approxeq 0.5D$). Moreover, the

finite element results illustrated that the pipe wall in the vicinity of the crack would undergo a secondary bending, in proportion to the crack depth.

- A note on the practical limitations of the developed reference strain J-estimation equation is in order. At the heart of the reference strain method is the assumption of negigibility of the second term of the RHS of Equation (5.7). For loading ranges before general yielding of the pipe, this assumption would be erroneous, and thus, Equation (5.9) would not be applicable. For robust use of the developed Equation (5.7), its validity range should be strictly kept in mind ($1.5\% \leqslant \varepsilon_{unc} \leqslant 4\%$). For other situations, use of the reference stress approach (such as that of the BS7910 [8]) is recommended[†].

- Finally, it is noted that welding residual stresses/strains were not explicitly included in the derivation and calibration of Equation (5.9). Still it is believed that these effects could be foreseen in the predicted J-integral value by adding known empirical values of welding residual strains (such as those recommended by BS7910 [8]) to the value of uncracked bending strain (ε_{unc}) for use in Equation (5.9)[‡].

Acknowledgments

The financial support of the Atlantic Innovation Fund is gratefully appreciated.

[†]This item does not appear in the published paper, and is added here to the manuscript of the thesis based on the suggestion of the examining committee.

[‡]Same as the preceding footnote.

Chapter 6

Effect of Lüders Plateau on Fracture Response and Toughness of Pipelines Subject to Extreme Plastic Bending

Nikzad Nourpanah and Farid Taheri

Department of Civil and Resource Engineering, Dalhousie University, Halifax, Nova Scotia, Canada, B3J 1Z1.

Accepted for publication in ASME Journal of Pressure Vessel Technology.

6.1 Abstract

The reeling technique presents an economical pipeline installation method for offshore oil and gas applications, especially for *thick-wall* (low D/t) pipelines. During reeling, the pipe is subjected to large plastic bending strains, up to 3%. In thick-wall pipes, the tensile fracture response of the pipeline/girth weld would normally be the governing limit state. Seamless linepipes are preferred for the reeling applications, in which the Lüders plateau is often exhibited in materials stress–strain response.

In this paper, the fracture response of such pipelines is investigated from a continuum perspective, using a nonlinear 3D Finite Element analysis. A typical pipeline with a hypothetical defect is considered, with the material having a range of Lüders strains and strain hardening indices. Results show that the Lüders plateau modifies the shape of the Moment-Strain response curves of the pipe, as well as the J-integral fracture response. It is observed that the response is always bounded between two limiting material models which are: (i) the elastic-perfectly plastic stress–strain response, and (ii) the conventional elastic-"strain hardening" plasticity response, without a Lüders plateau. Also, the Lüders plateau was observed to decrease the crack opening stress ahead of the crack tip, and thus, the crack tip constraint. On the other hand, presence of a Lüders plateau elevates the near-tip plastic strain and stress triaxiality fields, thus promoting ductile fracture. A micro mechanical damage integral

model coupled with a Modified Boundary Layer analysis was incorporated to study this aspect. Based on the findings of this study, it is believed that the presence of Lüders plateau could significantly alter the fracture response and toughness of pipes subject to relatively high strains.

Keywords: Lüders plateau, Fracture, Pipelines, Plastic Bending, Reeling

6.2 Introduction

The reeling installation method for offshore pipelines consists of girth welding of 12 m long line pipes to form a several kilometer long pipe string in an onshore facility and thus significantly lowering the offshore construction costs. These pipe strings are reeled over drums and loaded onto a sea going vessel, which lays the pipe on the sea bed by gradually unreeling it from the drum. The process involves severe plastic straining of the material, up to 3%; thus, only thick wall pipelines are regarded as reelable. Seamless line pipe are favored for reeling, however, in these steel grades the elastic part of the stress–strain curve is followed by a perfectly plastic response, dubbed as the Lüders plateau, and only upon the termination of this plateau does the strain hardening portion begin (see Figure 6.1 as a sample). Moreover, the governing failure mode in reeled pipelines would be mainly due to fracture of the girth weld, which needs to be assessed to ensure their integrity.

A fracture mechanics assessment of pipelines utilized for offshore oil and gas applications is a common approach nowadays. Such an assessment bypasses the traditional *workmanship* approach in which an empirical size criterion is used to assess the severity of defects and flaws caused by weld imperfections. Guidelines for fracture mechanics assessment of pipelines are well documented in several design codes, e.g. [2, 9]. Such assessments are based on comparing the crack driving force in the structure with the fracture toughness of the material obtained from standard laboratory tests. In the elastic-plastic domain which is of interest in this study, the appropriate measure for the crack driving force and toughness are either of the J-integral (J) or the Crack Tip Opening Displacement (δ_t) [27]. A noteworthy approach to estimate the crack driving force is that of the Electric Power Research Institute (EPRI) method [35], which is suitable for idealized stress–strain responses, but does not consider the Lüders

plateau. Based on some simplifying assumptions, the Reference Stress Method was also developed that could accommodate arbitrary material responses [36], which forms the backbone of current code assessment schemes such as that of Det Norske Veritas (DNV) [9]. However a detailed investigation, accounting explicitly for the effects of Lüders plateau could not be achieved by the two mentioned estimation schemes. Based on this fact, nonlinear 3D FE models are used in this study to investigate the fracture response and toughness of reeled pipelines in which the material exhibits a Lüders plateau. In this regard, moment-strain curves and evolution paths of the J-integral, the crack tip constraint levels, along with the J-δ_t relationship are discussed. Additionally, a two-parameter (plastic strain - stress triaxiality) description of the ductile damage phenomena is incorporated to illustrate the effect of the Lüders plateau on fracture toughness. The ABAQUS 6.8 software [10], equipped with Python scripts (developed in-house) to alleviate the pre and post processing stages, were used throughout this study.

6.3 Material Model

In order to investigate the effect of Lüders plateau, the following uniaxial true stress-strain response is considered:

$$\varepsilon = \begin{cases} \sigma/E & \text{for } \varepsilon \leqslant \varepsilon_y, \\ \sigma_y & \text{for } \varepsilon_y < \varepsilon \leqslant \varepsilon_L, \\ \sigma_y \left[(\varepsilon - \Delta\varepsilon_L)/\varepsilon_y\right]^{1/n} & \text{for } \varepsilon_L < \varepsilon. \end{cases} \tag{6.1}$$

The Lüders termination strain, ε_L and the strain hardening index, n, govern the post-yield shape of the stress-strain curve. E and σ_y are selected as 200 GPa and 400 MPa respectively. Moreover, variations in σ_y affect the fracture response at high plastic strains only slightly as shown in Ref. [125], and thus a single $E/\sigma_y = 500$ is used throughout this study. ε_L is between 1% and 3% for usual offshore pipeline steel grades [123]. Three values of $\varepsilon_L = 1$, 1.75 and 2.5% have been considered. Two strain-hardening indices of $n = 10$ and 25 have been considered, which are roughly equivalent to yield ratios of $\sigma_y/\sigma_u = 0.65$ and 0.85 (assuming an ultimate strain of 15%, which is the quoted minimum [4]). It is believed that the assumed material

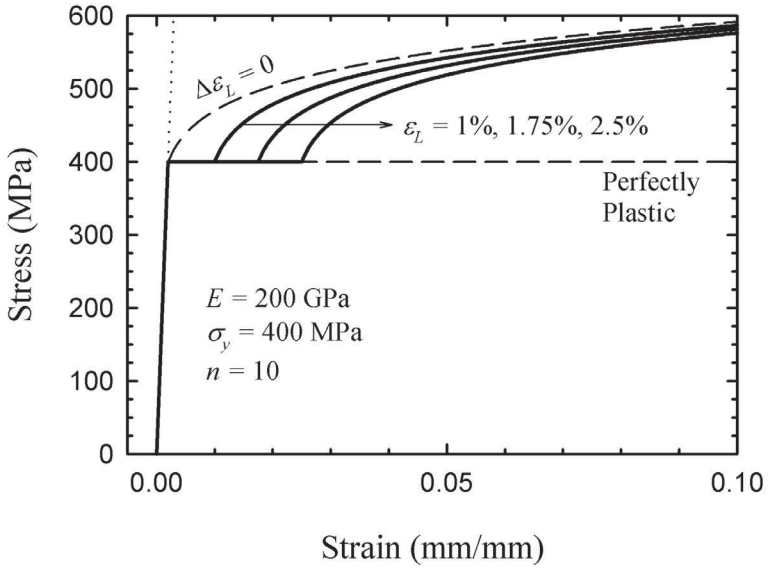

Figure 6.1. The family of uniaxial true stress-strain curves considered for the high strain hardening ($n = 10$) case.

model and parameters are representative of realistic pipeline steels. Furthermore, two limiting situations are considered: (i) the elastic- strain hardening plasticity material ($\Delta\varepsilon_L = 0$) and (ii) the perfectly plastic material ($n \to \infty$). Figure 6.1 shows the family of stress-strain curves for the high hardening material with $n = 10$. The 3D constitutive equation for FE analysis are based on the rate-independent associated J_2 incremental plasticity theory with the Mises plastic potential and isotropic strain hardening as implemented in ABAQUS [10]. Large Geometry Change (LGC) effects were accounted for in all analyses, such that a close investigation of the crack tip blunting zone is possible. ABAQUS utilizes an updated Lagrangian framework in order to formulate the incremental equations of equilibrium. For treatment of elasto-plasticity with consideration of LGC effects, ABAQUS uses the rate of deformation as the strain measure, alongside with its work conjugate, the Jaumann rate of the Kirchoff stress as the appropriate stress measure [10]. However, the stress and strains presented here are the Cauchy (true) stress and logarithmic strains.

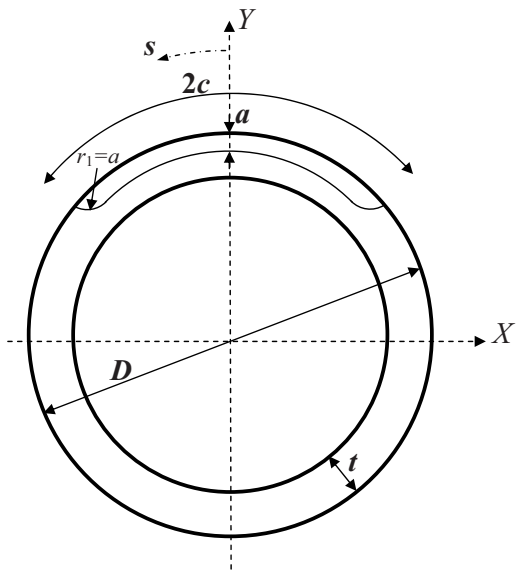

Figure 6.2. Schematic of the cracked pipeline cross section.

6.4 Finite Element Modeling

A typical thick-wall pipeline is considered with an external surface breaking part-through circumferential crack at the 12 O'clock position, which represents a hypothetical defect or flaw present in the girth weld. The crack is in the shape of a canoe, with its fillet radius equal to the crack depth. A schematic of the cracked cross section is shown in Figure 6.2. Geometric characteristics are as follows:

$D = 323.9$ mm

$t = 23.8$ mm $\quad (D/t = 13.6)$

$a = 3.57$ mm $\quad (a/t = 0.15)$

$2c = 50$ mm $\quad (2c/(\pi D) = 0.05)$

It should be noted that the flaw sizes of interest in girth welded pipelines are typically $2 \sim 6$ mm in height, as they are governed by the weld pass height [9].

Due to symmetry, a quarter FE model is considered with a length of $L = 2D$, which is known to be sufficiently long to capture the discontinuity effects caused by the crack [47, 125]. The pipeline end is constrained to a master node through a set of Multi Point Constraints. Appropriate rotation is imposed on the master node, causing the pipe to bend up to a level inducing a bending strain of $\varepsilon_g = 3\%$ on the outermost pipe fiber. This loading level covers even the extreme plastic bending that occurs during

reeling. Based on Euler's bending theory, the rotation-strain relationship reads:

$$R_x = \frac{2\varepsilon_g L}{D} \tag{6.2}$$

The underlying assumption of Equation (6.2) is that plane sections remain plane after deformation, which would not be precisely correct as the plastic deformation increases. However, in accord with the literature [119], it has been also observed here that an average of the tensile and compressive bending strains along the pipe length is in agreement with ε_g calculated from Equation (6.2), even up to extreme plastic bending.

ABAQUS's C3D8R [10], an isoparametric 8-node continuum element with reduced integration and hour-glass control is used to model the pipe. Choice of the reduced integration technique would be mandatory to avoid the volumetric locking associated with the incompressible plastic flow, especially near the blunting crack tip which undergo severe plastic deformations. The mesh density becomes finer toward the crack, forming a focused spider web mesh surrounding the crack tip. The FE mesh along with boundary conditions and a close-up of the focused mesh of the crack tip is shown in Figure 6.3[1]. A total of 31'000 elements were used to construct each FE model. Moreover, the LGC effects were accounted for, so that minute details of the near-tip fields could be captured. An initial notch radius of $0.01 \times a$ was assigned to the crack tip, in order to overcome the convergence difficulties due to finite strains of the blunting near-tip region. The domain integral method as implemented in ABAQUS was used to extract the values of J-integral [10].

6.5 Results and Discussion

A practical means for characterizing the response of pipes subject to large plastic deformations is the investigation of their moment-strain curves, as depicted in Figure 6.4. ABAQUS reports the moment by summing up the nodal contributions on the pipeline end plane (i.e. in reference to coordinates system shown in Figure 6.3, $M = 2\sum_i F_i y_i$, where F_i is the axial force of the i^{th} node on the plane, and y_i is its

[1]The presented Figure 6.3 is slightly more detailed than that in the published article.

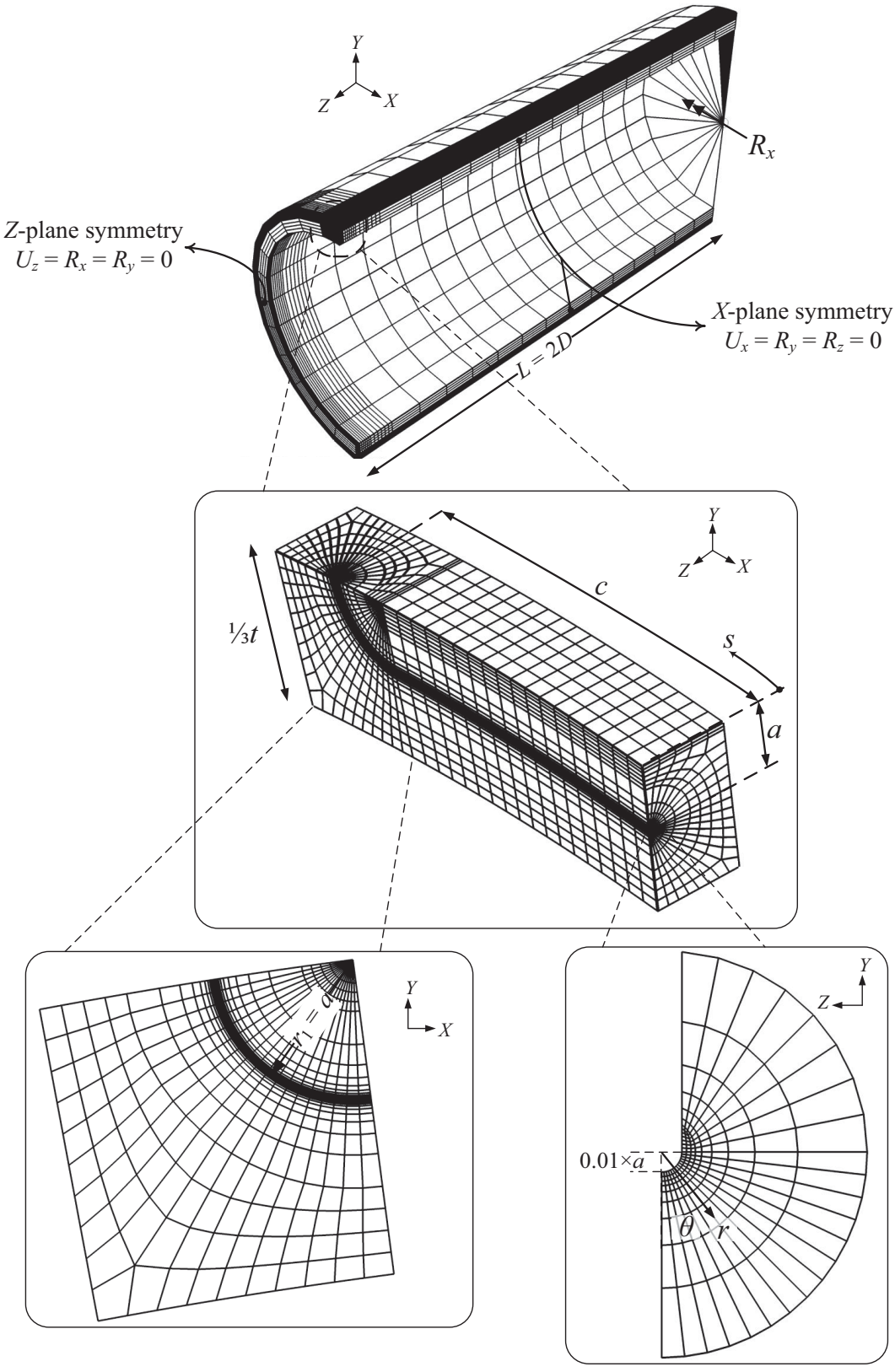

Figure 6.3. The pipeline FE mesh with the applied boundary conditions, along with close-ups of the focused mesh. The initial blunt crack tip and the local r-θ-s coordinates are shown.

y-coordinate). The figure is constructed for the family of ε_L along with the two limiting case material models. As can be seen, in all cases, the $\Delta\varepsilon_L = 0$ and the $n \to \infty$ material models, bound the response of the Lüders family. Moreover, for the family of ε_L, each curve follows the path of the perfectly-plastic material initially; however, it deviates from this path at higher strains. This deviation indicates the termination of the Lüders plateau and initiation of the strain hardening regime. Even though the axial strain in each fiber is a function of the distance measured from the neutral axis, it is worth noting that the branching takes place when ε_g becomes approximately equal to ε_L. Figure 6.4 shows that even for the smallest ε_L of 1%, the response is completely different from the $\Delta_L = 0$ limit case. Moreover, the path for the $\varepsilon_L = 2.5\%$ curve is pretty much coincident with that of the perfectly plastic material. The effect of Lüders plateau is less pronounced for the low hardening case of $n = 25$ material (Figure 6.4b).

Keeping in mind that J can conveniently characterize the fracture response in the elastic-plastic regime, the evolution of J is illustrated in Figure 6.5. Looking at the moment-based representation in Figure 6.5a, it is seen that the Lüders family are bounded between the curves corresponding to the $\Delta\varepsilon_L = 0$ and the $n \to \infty$ limits. The similarity in the trends observed in Figure 6.5a with 6.4a can be described by noting that the plastic part of J is a function of $M^{(n+1)}$, which is based on a deformation plasticity theory approximation [35]. The fracture response for the perfectly plastic material rises swiftly after the limit moment is reached at $M/Mp \cong 0.8$. Indeed this sudden increase should be avoided and thus design codes have placed a limit on the yield ratio; DNV [2] limits σ_y/σ_u to 0.85 for reeling applications. However, Figure 6.5a shows that for materials with a Lüders plateau, the fracture response follows that of the perfectly plastic material up to a certain limit and then branches off. This is certainly a disadvantage and should be carefully considered in *Load Controlled* situations. Figure 6.5b shows the strain-based evolution of J. While a linear evolution of J is observed for the $\Delta\varepsilon_L = 0$ case, this is not the case for the curves corresponding to the family of ε_L. However, for strain-based situations, a sudden rise of J is not evident. Although not shown, the low hardening material with $n = 25$ shows the same behavioral pattern.

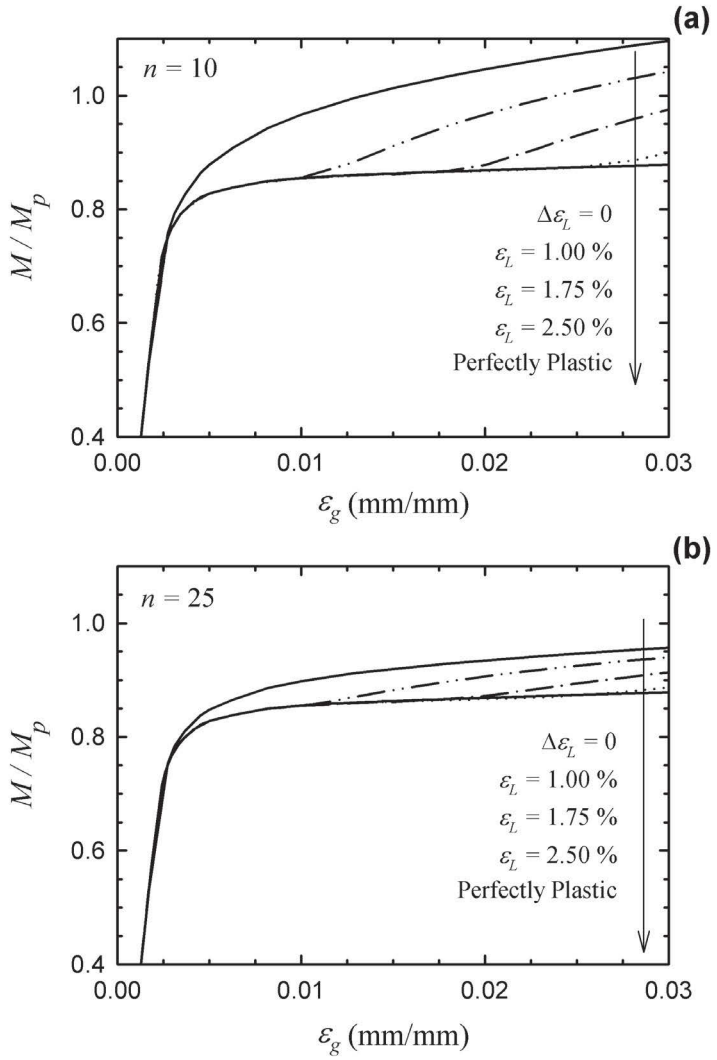

Figure 6.4. Moment-strain curves for the family of Lüders termination strains along with the two limiting cases; **(a)** for a material with $n = 10$ and **(b)** for $n = 25$.

It is well known that an additional *constraint* parameter, such as Q, is required to characterize the crack tip stress and strain fields, and subsequently, the fracture behavior [56, 68]. Thus, the crack driving force (J or δ_t) along with a constraint parameter (Q), are utilized for a two parameter fracture assessment. This would indicate that the laboratory specimen used for fracture toughness testing should have a similar crack tip constraint in comparison with the structure which is being assessed. In general, geometries with a low constraint have higher toughness and their fracture mode is usually ductile tearing, while the high constraint geometries have lower

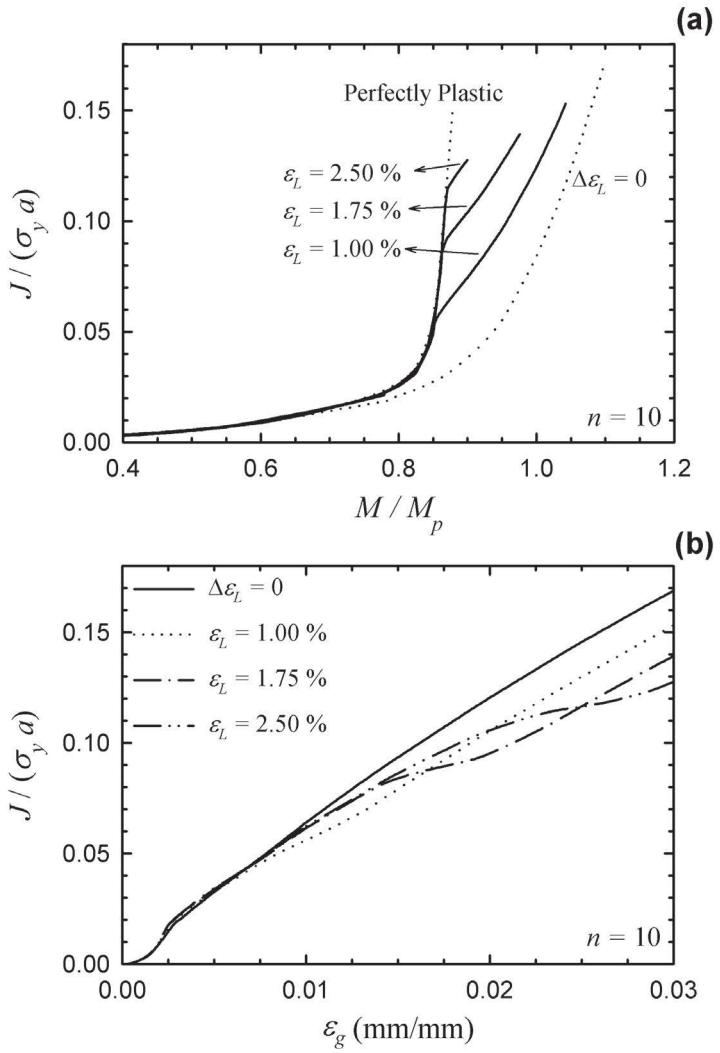

Figure 6.5. Evolution of the normalized J-integral extracted at crack center ($s/c = 0$), for the material with $n = 10$ and the family of ε_L; **(a)** as a function of applied moment and **(b)** as a function of applied global strain ε_g.

toughness and undergo brittle cleavage fracture [56, 68]. The Q parameter is defined as the normalized difference between the near tip stress field with that of a *reference* distribution corresponding to a high constraint situation such as the plane strain *HRR* field (due to Hutchinson [29], Rice and Rosengren [30]). An operational definition of Q reads [68]:

$$Q = \frac{\sigma_{11} - (\sigma_{11})_{\text{HRR}}}{\sigma_y} \tag{6.3}$$

where σ_{11} is the crack opening stress component extracted at $r = 2.0 \times J/\sigma_y$ from the crack tip. The *HRR* stress field, which assumes a power law uniaxial stress-strain response and negligible elastic strains (i.e. $\varepsilon/\varepsilon_y = \alpha(\sigma/\sigma_y)^n$) is represented by [27, 29]:

$$(\sigma_{ij})_{\text{HRR}} = \sigma_y \left(\frac{J}{\alpha \sigma_y \varepsilon_y I_n r} \right)^{\frac{1}{n+1}} \hat{\sigma}_{ij}(\theta, n) \tag{6.4}$$

where the dimensionless constant I_n and $\hat{\sigma}_{ij}(\theta$-variation functions) are tabulated in Ref. [31]. While the J-Q approach was originally for 2D geometries, heuristic arguments of O'Dowd [71] and experimental evidence of Faleskog [74] justify its application to 3D cracks. For such applications, an average definition of Q integrated along the crack length (s-coordinate in Figure 6.2 and 6.3) is convenient:

$$Q_{ave} = \frac{1}{s_b - s_a} \int_{s_a}^{s_b} Q(s)\, \mathrm{d}s \qquad \text{at} \qquad \theta = 0, \qquad r = 2 \times J_{ave}/\sigma_y \tag{6.5}$$

where J_{ave} is an average of J evaluated along the crack length (defined similar to Q_{ave}), and the integration is carried over the full crack length minus the fillet region ($s_a = 0$ and $s_b = c - a$). Moreover, $Q(s)$ is extracted from the near tip stress field using Equation (6.3) along the crack length.

Figure 6.6 shows the evolution of an average crack tip constraint, Q_{ave}, as a function of the applied global strain for the pipe with the family of ε_L and for the material with $n = 10$. The general trend shows that Q_{ave} attains a maxima, and it decreases steadily after the initial elastic regime is bypassed. Furthermore, a linear correlation is observed between Q_{ave} and ε_g in the plastic regime, which holds true for all values of the Lüders strains. The Q_{ave}-ε_g trajectories for higher values of ε_L fall successively below the $\Delta\varepsilon_L = 0$ case. The case with the lowest Lüders strain, $\varepsilon_L = 1\%$, has very close average constraint compared to the material with no-Lüders plateau. However, the trajectories for larger values of Lüders strain, $\varepsilon_L = 1.75\%$ and 2.5%, fall markedly below the $\Delta\varepsilon_L = 0$ case. The drop in Q_{ave} is more pronounced at lower loadings (at $\varepsilon_g \approxeq 0.01$), and upon further deformation (at $\varepsilon_g \approxeq 0.03$) the trajectories congregate.

Figure 6.7 shows the distribution of the normalized crack opening stress along the uncracked ligament at the crack center ($s/c = 0$). The distances are normalized by the appropriate length scale of J/σ_y, such that the admissible comparison is made possible. The maximum stress levels are capped due to finite strains in the blunting

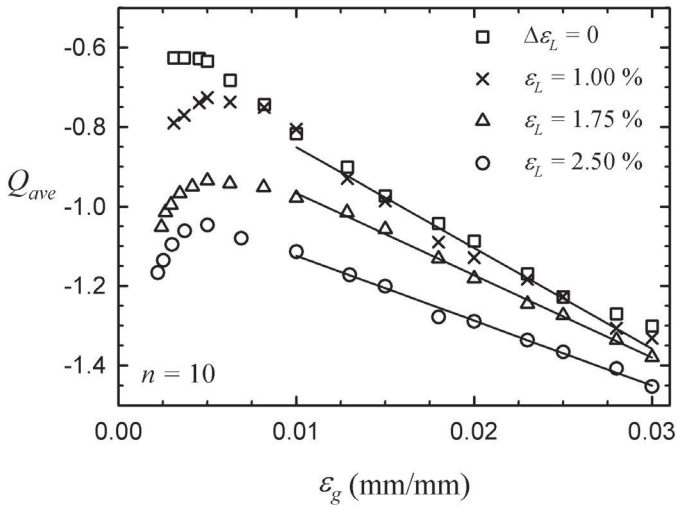

Figure 6.6. Variation of Q_{ave} as a function of ε_g for the family of ε_L (material with $n = 10$).

zone, that is, the stresses do not increase to infinity at the crack tip. This blunting zone is approximately bounded by $r/(J/\sigma_y) = 1$, which is presumably the fracture process zone. In this zone, the stress distribution for all values of ε_L closely coincide with that of $\Delta\varepsilon_L = 0$ case. This can be explained by noting that this region undergoes very high plastic strains due to the blunting deformations (e.g. $\varepsilon_p > 0.1$), and for such high strain values, the ε_L family of stress-strain curves converge to the $\Delta\varepsilon_L = 0$ case, as observed in Figure 6.1. Further beyond this finite strain zone, the stress profiles for the ε_L family uniformly decrease with respect to the $\Delta\varepsilon_L = 0$ case. For the material with the largest Lüders plateau of $\varepsilon_L = 2.5\%$, the stress profile approaches midway between the perfectly plastic and no-Lüders case. As manifested in Figure 6.7b, for the material with lower strain hardening, $n = 25$, the divergence from the $\Delta\varepsilon_L = 0$ profile becomes less noticeable.

The distribution of the crack opening stress along the crack front is depicted in Figure 6.8 (the s-coordinate is defined in Figure 6.2 and 6.3), which indicates that the drop in the stress profiles caused by the Lüders plateau continues along nearly the whole crack length, and the minor shape changes at $s/c \approxeq 0.8$ are due to the crack profile reaching the exterior pipe surface. The results illustrated in Figure 6.7a and

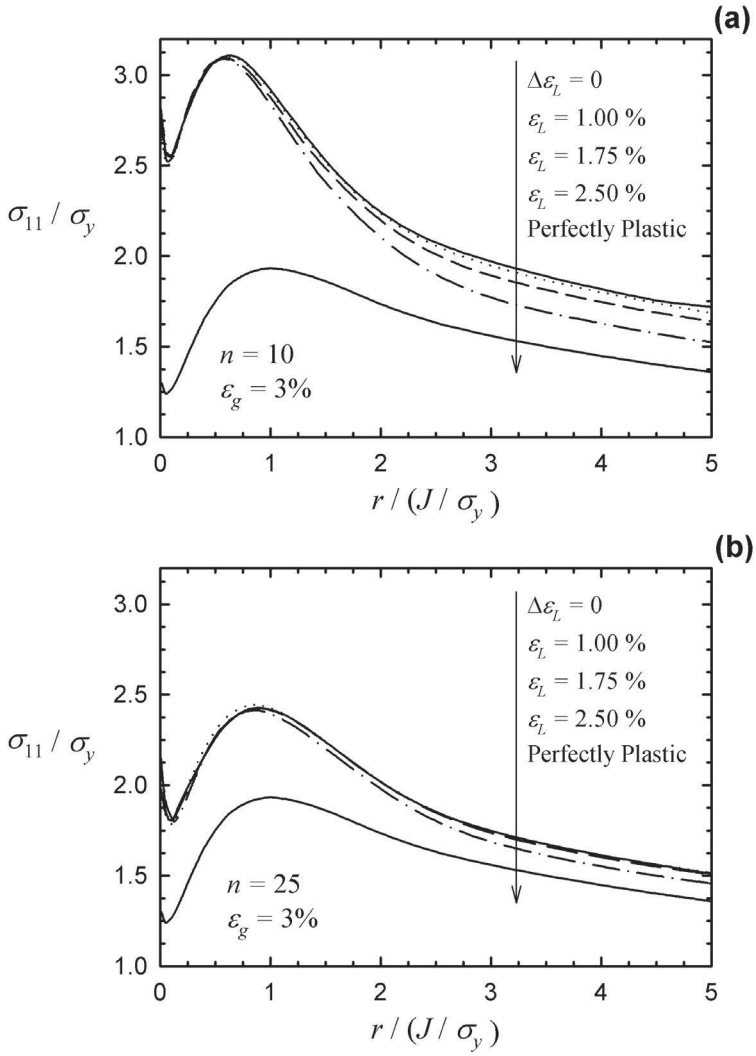

Figure 6.7. Distribution of the crack opening stress along the uncracked ligament extracted at the crack center, $s/c = 0$, for **(a)** materials with $n = 10$ and **(b)** $n = 25$.

6.8, provides the 3D distribution of the crack opening stress for the $n = 10$ case.

In the absence of a Lüders plateau, the crack tip opening displacement, δ_t, would have a unique relationship with J, represented by $\delta_t = d \times J/\sigma_y$, thus facilitating another equally applicable fracture response parameter. In the elastic-plastic regime, d is independent of the applied load and depends weakly on the material properties and rather strongly on the near tip stress triaxiality, generally referred to as the *constraint* [56, 68]. Figure 6.9 shows a plot of the crack opening parameter, d, versus ε_g for the $n = 10$ material. As seen, d increases steadily as a function of ε_L; that is, at

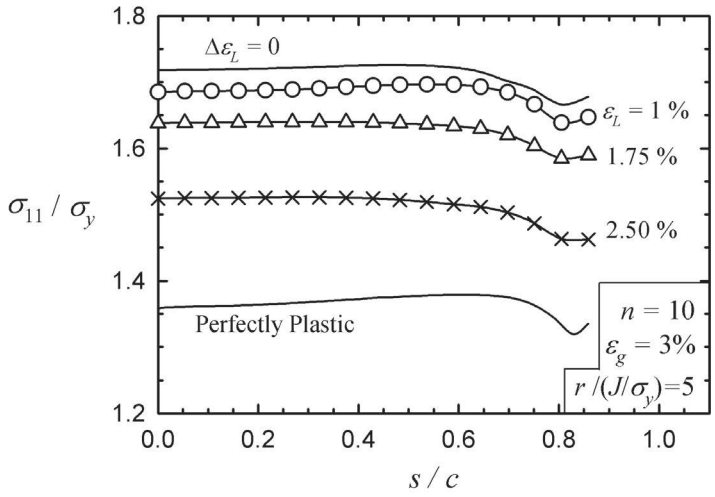

Figure 6.8. Distribution of the crack opening stress along the crack front extracted at $r/(J/\sigma_y) = 5$ for the family of ε_L and material with $n = 10$.

a specific value of loading (in terms of ε_g or J), the Lüders plateau would cause larger values of δ_t. Furthermore, considering the $\Delta\varepsilon_L = 0$ curve, it is seen that d reaches a constant value after the initial elastic response is exceeded and becomes independent of the load. However, for the family of ε_L, a slight load dependence is observed. The trends are the same for the material with $n = 25$; however the effect of Lüders plateau for the low hardening material is less pronounced.

The large plastic deformations due to blunting of the crack tip cause the appearance of the so-called *Stretch Zone*, with its size on the order of *CTOD*. Thus, the stretch zone width (SZW) could be approximated by [74]:

$$SZW \propto \delta_t = d\frac{J}{\sigma_y} \tag{6.6}$$

Regarding the crack tip deformation characteristics, it is interesting to assess the effect of Lüders strain on the *Stretch Zone*. It has been seen that for sufficiently high load levels, an increase in ε_L results in a decrease in J (see Figure 6.5), and this would consequently lead to a decrease in SZW as per Equation (6.6). On the contrary, as illustrated in Figure 6.9, an increase in ε_L raises the opening coefficient d. Thus, the Lüders strain affects the SZW in two opposing manners. The equivalent plastic

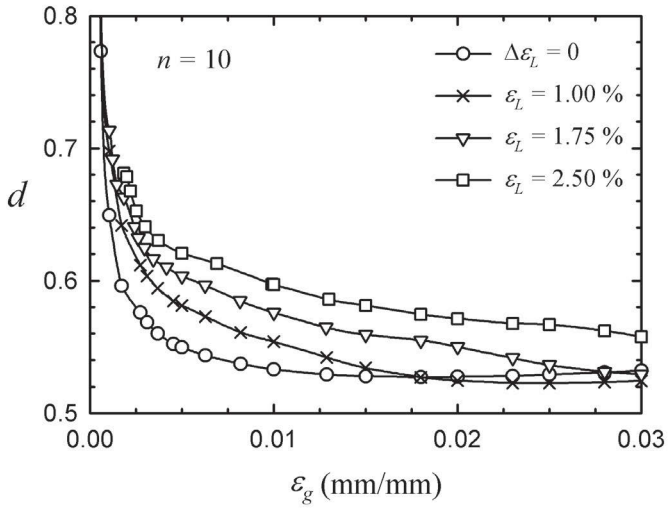

Figure 6.9. Effect of the Luders plateau on the crack opening parameter, $d = \delta_t/(J/\sigma_y)$, for the $n = 10$ material.

strain ε_p extracted along the deformed crack surface path (see schematic in Figure 6.10) would be indicative of the stretch zone characteristics [74]. Figure 6.10 shows such a plot for the material with $n = 10$ and the family of ε_L. The effect of ε_L on SZW is not straight forward (as supported by the above discussion). At increasing values of Lüders strain, ε_p is lower than the $\Delta\varepsilon_L = 0$ case up to $y^* \cong 0.25 \times \delta_t$, however, after this point and moving away from the crack tip, ε_p is greater than the $\Delta\varepsilon_L = 0$ case. For the material with $n = 25$, the same trends are observed, however, the distributions for the family of ε_L are more closely packed. Based on these, it is expected that the Lüders plateau would not significantly alter the appearance of the stretched zone.

As noted previously, the defects caused by welding imperfections have a rather small height. As a result, even while the pipe string is under global bending, the uncracked ligament is mainly under tension, thus providing low crack tip constraint (as manifested by the negative values of Q_{ave} in Figure 6.6) thereby causing ductile fracture to become the prone failure mode. Moreover, code restrictions [2] imposed on specifying sufficient ductility and strain hardening capacity of both the line pipe steel and weld consumables further ensures a ductile fracture mode, as has been verified

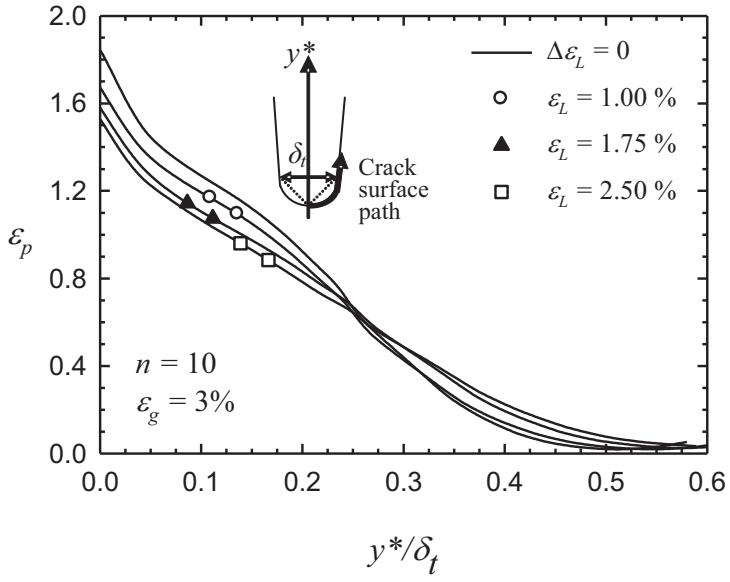

Figure 6.10. Distribution of ε_p along the *crack surface path* for the $n = 10$ material and the family of ε_L, extracted at the crack center ($s/c = 0$) at $\varepsilon_g = 3\%$.

in several full scale tests [46]. It is well known that the ductile damage phenomena is initiated by void nucleation, void growth, strain localization between the voids, thereby leading to necking, and finally void coalescence, which causes the final ductile fracture. The two main parameters controlling the described phenomena are the stress triaxiality and equivalent plastic strain in the near crack tip region [16]. In order to assess the effect of ε_L on ductile damage, the triaxility versus ε_p diagram for the $n = 10$ material is shown in Figure 6.11. The ratio of the mean stress, $\sigma_m = {}^1\!/_3\sigma_{kk}$, to the equivalent Mises stress, $\sigma_e = (1.5 \times \underline{S} : \underline{S})^{0.5}$, is incorporated in the figure, which is a representative measure of stress triaxiality [58]. The general trend is that triaxiality would be high at the beginning of loading; however, with the increase of loading it decreases, while ε_p increases steadily. It is evident that the presence of the Lüders plateau and the increase of ε_L substantially elevate and amplify the plastic strain-triaxiality curve. Though not presented, the same effect, but only less pronounced, occurs for the material with $n = 25$. As a result, it is believed that the presence of a Lüders plateau will promote ductile damage. Figure 6.12 shows the distribution of ε_p in the deformed near tip region at the crack center for two cases, namely, the $\Delta\varepsilon_L = 0$

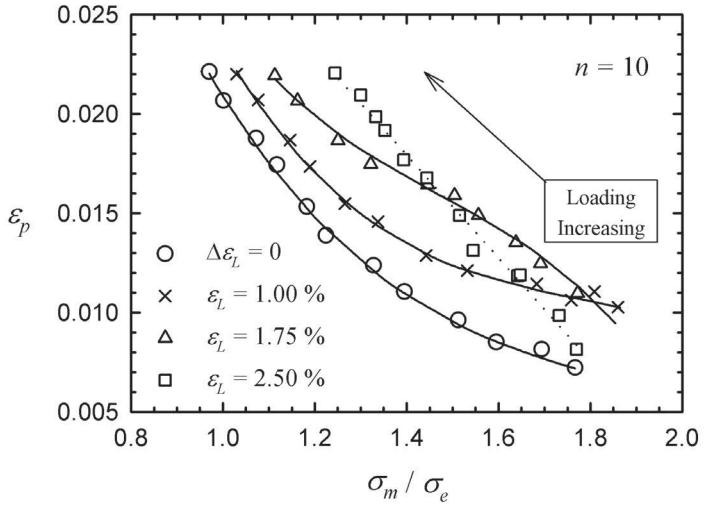

Figure 6.11. Two parameter diagram of ε_p versus σ_m/σ_e for the family of ε_L and for the material with $n = 10$. Results extracted at crack center $s/c = 0$ and from the uncracked ligament at $r = 2.5 \times J/\sigma_y$.

case and the $\varepsilon_L = 2.5\%$ cases. The plastic strains in the latter case are noticeably higher, which support the observations made in the previous statement.

The effect of the Lüders plateau on promoting ductile damage, which was explained qualitatively via Figures 6.11 and 6.12, can be further quantified by incorporating a simplistic micro mechanical damage model developed by Anderson et al. [83]. The growth rate of a single spherical void in an infinite continuum with rigid-perfectly plastic material was shown by Rice and Tracey [82] to obey a semi-empirical equation, which is represented by:

$$\ln\left(\frac{\bar{R}}{R_0}\right) = 0.283 \int_0^{\varepsilon_p} \exp\left(\frac{1.5\sigma_m}{\sigma_y}\right) \mathrm{d}\varepsilon_p \tag{6.7}$$

where $\bar{R}$ is the average radius of the void (since the spherical void deforms to an ellipsoid shape, hence the average radius) and R_0 is the initial void radius. Anderson et al. [83] hypothesized that ductile failure occurs upon the void radius reaching a critical value, and subsequently used Equation (6.7) to form a local damage integral (noting that for strain hardening material, the equivalent Mises stress σ_e should be

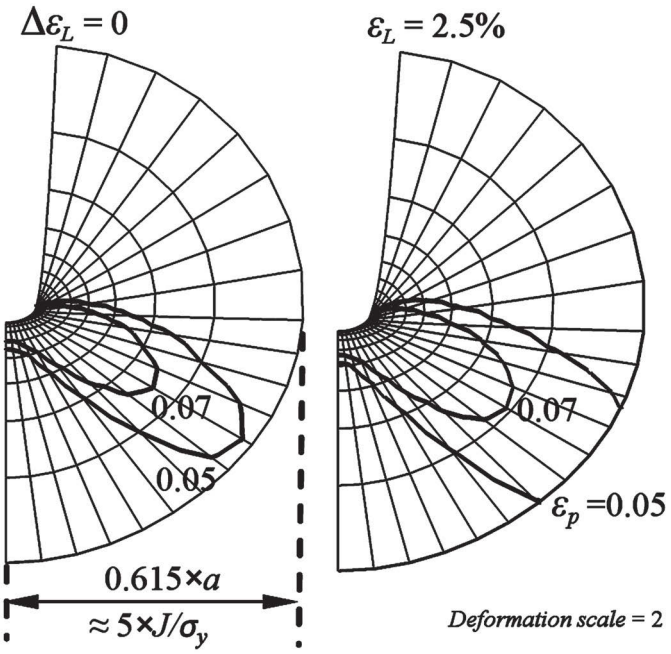

Figure 6.12. Deformed near tip region at the crack center, $s/c = 0$, for two cases ($\Delta\varepsilon_L = 0$ and $\varepsilon_L = 2.5\%$, material with $n = 10$), showing contours of ε_p.

used in Equation (6.7) instead of σ_y):

$$\Phi_D = \int_0^{\varepsilon_p} \exp\left(\frac{1.5\sigma_m}{\sigma_e}\right) \mathrm{d}\varepsilon_p \tag{6.8}$$

Following the work of Anderson et al. [83], and assuming that ductile crack growth is initiated when $\Phi_D = \Phi_{D,c}$, one can consider the distribution of Φ_D ahead of the crack tip for two different cases at the same load level, namely, one with $\Delta\varepsilon_L = 0$ and one with a Lüders plateau. The quotient of the damage integral, Φ_D, for these two cases would represent the ductile initiation toughness ratio. The concept is schematically illustrated in Figure 6.13: if one denotes the toughness of the no-Lüders material with J_0, and that of a material with a Lüders plateau by J_{crit}, referring to Figure 6.13, the respective toughness ratio could be quantified by $J_{crit}/J_0 = x_1/x_2$.

The 3D FE pipe models discussed earlier covered strain hardening indices of $n = 10$ and 25, and three Lüders strains ($\varepsilon_L = 1$, 1.75 and 2.5%). Noting that the above mentioned micro mechanical approach is based on the near tip stress and strain fields, in lieu of the computationally expensive 3D pipe models, plane strain Modified Boundary Layer (MBL) analysis could be considered as a more viable and cost-effective

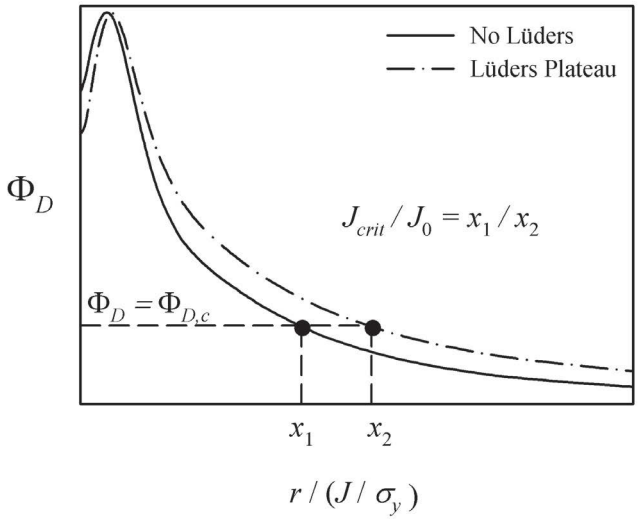

Figure 6.13. Schematic illustration of the damage integral approach (after Anderson et al. [83]), utilized to assess the Lüders plateau effect on material toughness.

alternative. The MBL analysis produces very similar near-tip information, and could be conveniently carried out for a wide range of hardening indices and Lüders strains. In this case, the MBL model would consist of a circular disk with a radius of R, loaded at its boundary with the first two terms of the Williams linear elastic singularity solution [26]. The displacements corresponding to these tractions are applied at the boundary of the MBL model, which read:

$$u_x = \frac{K_I}{E}(1+\nu)\sqrt{\frac{r}{2\pi}}\cos(\theta/2)[\chi - \cos\theta] + (1-\nu^2)\frac{T}{E}x$$
$$u_y = \frac{K_I}{E}(1+\nu)\sqrt{\frac{r}{2\pi}}\sin(\theta/2)[\chi - \cos\theta] - \nu(1+\nu)\frac{T}{E}y \qquad (6.9)$$

where $\chi = 3 - 4\nu$ under plain strain conditions.

The so-called T-stress in Equation (6.9) corresponds to the near tip constraint, and controls the size and orientation of the plastic zone in addition to the near tip triaxiality levels. Here, a value of $T/\sigma_y = -1.0$ is selected, which results in similar constraint levels to that of the considered pipelines [126]. Small Scale Yielding (SSY) conditions are enforced by limiting the plastic zone size (defined as the zone engulfed by the contour corresponding to $\sigma_e/\sigma_y = 1$) to $0.15 \times R$. As a result, application of Equation (6.9) would be justified.

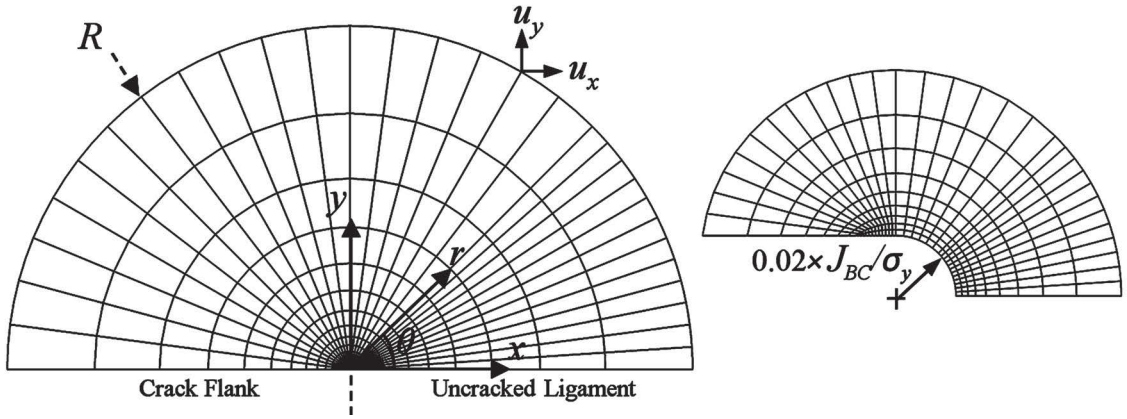

Figure 6.14. FE mesh of the MBL model along with the relevant coordinate systems and BCs **(Left)**; Crack tip mesh details showing the initial notch radius **(Right)**.

The CPE4H element of ABAQUS [10], a plane strain 4-node fully integrated hybrid element, was used for the model. A total of 1200 elements were used, forming an exponentially biased mesh towards the crack tip, with an initial notch radius of $0.02 \times J_{BC}/\sigma_y$, thus enabling the finite straining of the near tip due to blunting deformations. The radial bias ratio was approximately 5×10^5. A schematic of the symmetric MBL model is shown in Figure 6.14. Noting that SSY conditions prevail, J is uniquely related to K_I, (i.e. $J_{BC} = (1 - \nu^2) \times K_I^2/E$). Although the numerically calculated values of J do converge to the theoretical J_{BC}, the theoretical value was utilized in the analysis for the sake of consistency.

The MBL analysis was carried out for a wide range of hardening indices: $n = 10 \sim 25$, in increments of 5. For each hardening index, the no-Lüders case, $\Delta\varepsilon_L = 0$, along with 9 different Lüders strain values ($\varepsilon_L = 1\% \sim 3\%$, in increments of 0.25%) were considered. The local damage integral, Φ_D, was evaluated as per equation (6.8), along the $\theta = \pi/6$ ray. However, the lower integration limit was considered as when the crack tip had blunted about 3 times its initial notch radius (i.e. Φ_D is evaluated after $\delta_t > 3 \times 0.02 \times J/\sigma_y$). This ensured that the near tip fields would be independent of the initial notch radius [67]. The value of x_1 (with reference to Figure 6.13) was selected as $1.0 \times J/\sigma_y$ and x_2 for each case was extracted to establish the corresponding toughness ratio. Extraction of the results at such close vicinity of crack tip is justified by noting that LGC effects were accounted for in the MBL analysis and thus, minute

details of the finite strain blunting zone were available. More details on the MBL modeling technique can be found elsewhere [56, 67, 126].

Figure 6.15 shows the variation in the toughness ratio, J_{crit}/J_0, as a function of ε_L for different strain hardening indices. For all values of n, the toughness ratio decreases steadily as a function of Lüders strain. The effect of the Lüders plateau gets more pronounced for lower values of n (higher strain hardening capacity), while on the other hand, the toughness ratio vs ε_L profiles converge together for increasing values of n. Indeed, the scattered data points for the three low hardening materials (i.e. $n = 15$, 20 and 25) were very close together; and therefore, only the results for the $n = 15$ case is shown in the figure. This effect could be described by noting that the stress-strain curves for $n = 15$, 20 and 25 are actually quite similar, which could be understood by considering their very close σ_y/σ_u ratios, which are 0.76, 0.80 and 0.83 respectively for the $\varepsilon_L = 2.5\%$ case, while for example the $n = 5$ material has $\sigma_y/\sigma_u = 0.44$. The initiation toughness ratio (with respect to the no-Lüders case of $\Delta\varepsilon_L = 0$), is approximately 80% for the lowest Lüders strain of $\varepsilon_L = 1\%$, for all strain hardening indices. For the largest Lüders strain of $\varepsilon_L = 3\%$, the toughness ratio is nearly 60% for the lowest n, while the reduction ratio saturates to a value of approximately 70% for the low hardening material (i.e. with high n). Thus, the results of the micro mechanical damage approach are in accord with the results illustrated in Figures 6.11 and 6.12, confirming that the presence of a Lüders plateau would deteriorate the ductile initiation toughness with respect to the no-Lüders material. Furthermore, this effect would be more marked in high hardening material with a low n. As observed in Figure 6.15, power-law trend-lines could successfully approximate the data. Consequently, the toughness ratio could be written as:

$$\frac{J_{crit}}{J_0} = \beta \left(\varepsilon_L\right)^{\gamma} \tag{6.10}$$

where ε_L is dimensionless (mm/mm), and β and γ are fitting coefficients, which are calculated for all strain hardening indices using a least square approach (with $R^2 > 0.98$ for all fits), as presented in Table 6.1. Furthermore, second order polynomial fits could be used to interpolate β and γ values for strain hardening indices other than those enlisted in Table 6.1. The equations are:

$$\beta = -0.0017n^2 + 0.0517n - 0.016$$

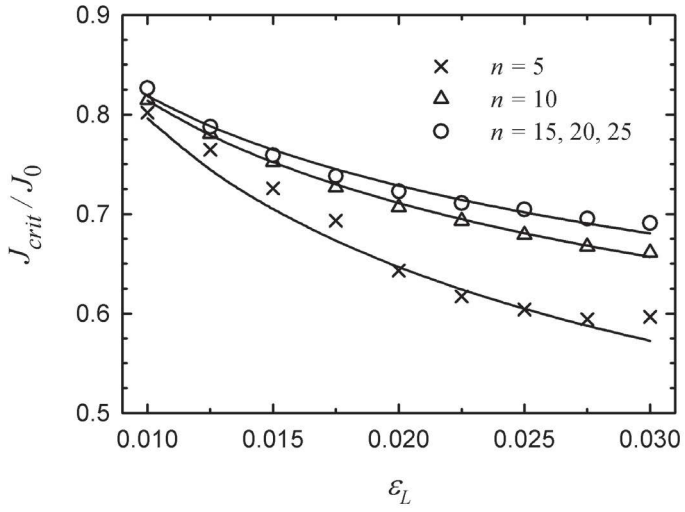

Figure 6.15. Variation of ductile initiation toughness ratio as a function of ε_L for various values of n. The symbols represent the results obtained by the MBL models and solid lines represent the power-law fits of Equation (6.10).

Table 6.1. Fit coefficients for the toughness ratio formula of Equation (6.10).

	$n = 5$	$n = 10$	$n = 15,\ 20\ ,\ 25$
β	0.2000	0.3310	0.3776
γ	–0.3000	–0.190	–0.168

$$\gamma = -0.0016n^2 + 0.046n - 0.49 \tag{6.11}$$

In light of the above discussion, a value of $n = 15$ should be used in Equations (6.11) for materials with $n > 15$.

Finally, a note on the presented results is in order. The family of stress–strain curves shown in Figure 6.1 represent idealizations of the real material behavior. In some steel materials, a sudden drop is observed in the peak yield stress followed by the Lüders plateau (i.e. the elastic to Lüders transition is marked by a sharp peak). It is believed that this phenomenon might actually result in somewhat weakening the effect of the Lüders plateau on the charcteristic response features discussed earlier. However, accurate quantification of this effect will require additional analysis.[†].

[†]This paragraph does not appear in the published paper, and is added here to the manuscript of the thesis based on the suggestion of the examining committee.

6.6 Conclusions

Effect of the Lüders plateau on the fracture response and toughness of pipelines subject to extreme plastic bending has been investigated using a comprehensive 3D nonlinear FE and MBL analysis. The salient conclusions drawn are summarized below:

- The mere presence of a Lüders plateau would significantly alter the global response of the pipeline, as exemplified by the moment-strain curves, as well as the crack driving force curves.

- The moment based representation of the J-integral revealed that the fracture response for a material with a Lüders plateau would be very similar to that of a perfectly plastic material; nevertheless, the response branches off at the final stages of loading, raising concern for the use of such materials in load controlled applications.

- The spatial-average near tip constraint parameter, Q_{ave}, was observed to decrease as a linear function of the applied global strain ε_g, while higher values of the Lüders strain, ε_L, resulted in lower constraint.

- In the finite strain near crack tip zone, Lüders plateau would not have a significant influence on the crack opening stress profiles. Nevertheless, in the micro structurally significant zone of $J/\sigma_y < r < 5 \times J/\sigma_y$, increasing the values of Lüders strain, ε_L, would cause the stress profiles to sequentially shift down uniformly from the no Lüders reference profile. This drop was also observed along the whole crack length.

- The Lüders strain increased the crack opening parameter, d, in addition to the fact that d became slightly load dependant for the materials with a Lüders plateau. It was also shown that the Lüders plateau would not significantly alter the stretch zone's appearance.

- It was observed that ε_L had a profound effect on amplifying both near tip equivalent plastic strain and stress triaxiality, thus promoting ductile damage.

- Via incorporation of a micro mechanic damage integral and based on the near tip fields extracted from MBL models (with similar constraint as pipelines), it was shown that the ductile initiation toughness decreased steadily as a function of Lüders termination strain, with a more notable effect for high strain hardening materials (low n).

The results presented here lead to the conclusion that material exhibiting a Lüders plateau could have detrimental effects both on the fracture response and toughness of pipelines subject to large plastic bending strains.

Acknowledgments

The financial support of the Atlantic Innovation Fund is gratefully appreciated.

Chapter 7

A Numerical Study on the Crack Tip Constraint of Pipelines Subject to Extreme Plastic Bending

Nikzad Nourpanah and Farid Taheri

Department of Civil and Resource Engineering, Dalhousie University, Halifax, Nova Scotia, Canada, B3J 1Z1.

Accepted for publication in Journal of Engineering Fracture Mechanics.

7.1 Abstract

This study investigates the fracture response and crack tip constraint of thick wall pipelines subject to large plastic bending. Such a circumstance frequently occurs during the installation of offshore pipelines (such as the reeling method), and accidental overloading, both inducing inelastic bending. The near tip stress and strain fields are obtained through the fully nonlinear 3D finite element models constructed to examine the response of a practical range of cracked pipeline geometries and material properties. It is observed that throughout the loading history (up to the large scale yielding of the pipeline), by incorporation of the J-Q two parameter fracture theory, the near crack tip fields do indeed resemble those obtained from a K-T modified boundary layer formulation. This analogy provides sufficient proof for the applicability of the similitude concept inherent and fundamental to any fracture assessment procedure. All the pipelines considered in this study, which had realistic crack sizes, exhibited low constraint behavior (i.e. $-1.4 < Q < -0.4$). Additionally, Q was observed to decrease as a linear function of the global bending strain. Based on this correlation, simplified design equations are presented by which the constraint of such pipelines could be effectively estimated. The equations would be suitable for incorporation in the constraint-matched integrity assessment procedures that would in turn overcome the overt conservatism produced by the use of single parameter fracture mechanics

approaches. Suitability of the low constraint laboratory specimens for fracture toughness measurements is also confirmed.

Keywords: Pipelines, Plastic Bending, Fracture, Constraint, Integrity Assessment

7.2 Introduction

With the ever-rising cost of energy and also depletion of most resources in reasonably benign environments, the oil and gas industry is compelled to move into more demanding environments (i.e. into deeper waters and into more hostile environments such as the Arctic). Reliable pipelines capable of operating in these environments and withstanding the associated extreme loadings are a key factor in such developments. The Limit State Design (LSD), together with the Strain Based Design (SBD), provides cost-effective pipeline design strategies, as manifested in most major design codes (e.g. API [3] and DNV [2]).

Pipelines, either onshore or offshore, are subjected to bending due to a variety sources, including pipelines conforming to the curvature of a stinger, reel drums and/or bathymetry of a rough seabed. Buried pipelines can also be subjected to seabed/ground motion caused by subsidence, mudslides, seismic activity and uneven settlements. Among these, reeled pipelines are subjected to the most severe inelastic bending, which induces strains up to 3%, well into the materials plastic range. For such pipelines, the potential for fracture of the girth weld on the tensile side is one of the governing limit states. Assessment of this limit state consists of conducting a fracture mechanics analysis of a hypothetical defect, which is assumed to have been caused due to welding imperfections, and is termed Engineering Criticality Assessment (ECA) in the literature. An ECA proceeds by comparing the crack-driving force of a flawed pipeline to that of a suitable test specimen. The concept of *similitude* in fracture mechanics is implicit in such an approach; that is, it is assumed that the near-tip stress and strain fields that govern the micro-structural fracture processes, are similar in any two cracked bodies (e.g. in this case, the flawed pipeline and the respective test specimen). Traditionally, these fields were assumed to be uniquely described by a single parameter (i.e. the crack driving force), which, depending on the level of loading, could be either of K, J or $CTOD$. Later on, it was shown that such a single

parameter description is only valid for certain configurations that exhibit high levels of crack-tip stress triaxiality [27, 56].

Two-parameter formulations have been therefore developed, which utilize an additional *constraint* parameter, in addition to the crack-driving force, to describe the near-tip fields. Most notable of such formulations are the J-T [61, 63], J-A_2 [66] and J-Q [67, 68] formulations. The additional constraint term is closely related to the stress triaxiality, and can satisfactorily describe the scatter in the toughness data obtained from different test configurations. In general, higher constraint/triaxiality configurations exhibit lower fracture toughness and vice versa. Moreover, high constraint configurations usually undergo brittle cleavage fracture, while ductile tearing fracture is observed in low constraint configurations. Despite the constraint dependency of the toughness data, historically, guidelines have recommended the use of high constraint test specimens, such as the deeply cracked Single Edge Notch Bend (SENB) specimen, which produces the lowest toughness data, thus adding to the conservatism of the ECA. However, recently, the provision to utilize constraint-matched test specimen is recommended by some codes. For instance, DNV [9] accepts the use of low-constraint Single Edge Notch Tensile (SENT) specimen for the assessment of reeled pipelines, based on its constraint similarity to that of circumferentially flawed reeled pipes [77, 78]. Similar studies [79, 80], have shown the suitability of SENT specimens for ECA of high pressure pipelines with axial flaws based on close examination of J-Q trajectories in the two bodies.

Generally, the near-tip fields and the constraint evolve with the increase of loading and the extent of plasticity in the structure. The existence of identifiable stress and strain fields up to fully yielded conditions is not necessarily guaranteed (examples of such situations can be found in Refs. [56, 68]), in which case, the application of ECA itself is questionable due to the similitude concept being annulled. This aspect of ECA should be carefully considered, as the core of the ECA methods date back to the Eighties. It should be noted that the ECA approach was originally developed for power industry applications in which Large Scale Yielding (LSY) was generally not permitted, and the bulk behavior of the structures of interest would remain elastic.

Based on the above, and in the spirit of the work by O'Dowd and Shih [68], in

the present work, a typical pipeline with a range of relevant crack sizes and material properties are considered and loaded to extreme plastic bending (up to 3% global strain, as occurs during reeling). Fully nonlinear 3D FE models are constructed in order to extract the near-tip stress and strain fields and are further compared to the *standard* fields generated based on the Modified Boundary Layer (MBL) models. The similarity of these two fields, up to LSY, provides sufficient proof for the similitude concept and the ECA itself (since identifiable stress fields in nearly all test specimen geometries can be found in the literature, such as Refs. [68, 70, 71]). This comparison would also yield the constraint of such pipelines, which would be further compared to those of SENT specimens in order confirm the safe utilization of such specimens for ECA purposes.

The ABAQUS version 6.8 software [10] is used for all FE analysis. Nonlinear Geometry (NLG) effect (including both finite strains and large rotations/displacements) is considered in all models in order to extract accurate information on the blunting of the crack-tip and $CTOD$. Elastic-plastic material response is considered in all FE models; the plasticity constitutive model used is based on a rate-independent associated J_2 incremental theory with the Mises plastic potential and isotropic strain hardening. ABAQUS adopts an updated Lagrangian-type framework to formulate the incremental equilibrium equations. For elastoplasticity along with NLG, ABAQUS employs the rate of deformation as the strain measure, along with its work conjugate, the Jaumann rate of the Kirchoff stress, as the suitable stress measure [10]. However, all stress and strain output reported are in the format of Cauchy (true) stress and Logarithmic strains. A piece-wise power-law hardening material with the following uniaxial stress–strain response was considered:

$$\varepsilon = \begin{cases} \sigma/E & \text{for } \sigma \leqslant \sigma_y, \\ \varepsilon_y \left(\sigma/\sigma_y\right)^n & \text{for } \sigma > \sigma_y. \end{cases} \tag{7.1}$$

where σ_y/E was selected as 0.002 and $\sigma_y = 400$ MPa. Two values of the hardening exponent (i.e. $n = 10$ and 25) were considered for all FE models. These hardening indices were considered to account for the influence of materials having *high* and *low* strain hardening capacities, respectively, which bound the commonly used offshore pipeline steel grades. These two values of strain hardening index correspond

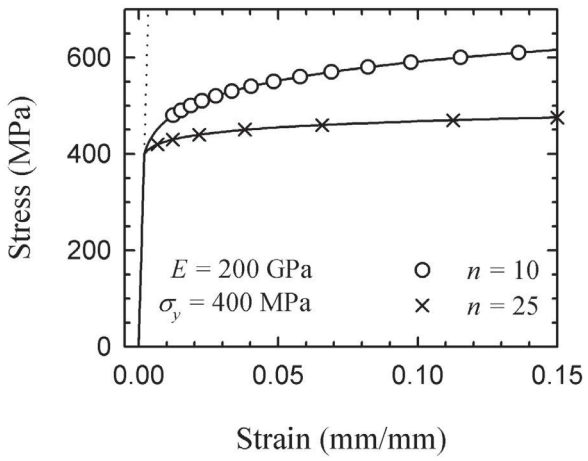

Figure 7.1. Uniaxial true stress–strain curves with the two hardening indices considered in all FE models.

to $\sigma_y/\sigma_u = 0.65$ and 0.84, respectively, by defining σ_u as the stress corresponding to 15% uniaxial strain, which is considered as the lower limit of the ultimate strain for offshore pipeline steels [4]. The two uniaxial stress–strain curves are shown in Figure 7.1. Finally, due to the large plastic deformation at the crack-tip, reduced integration or, alternatively, elements with a hybrid formulation were used to avoid the potential volumetric locking associated with the incompressible plastic flow, in all the FE models.

7.3 Review of the J-Q Near Tip Fields and the MBL model

The MBL model considers a hypothetical crack tip loaded at its circular boundary with tractions given by the first two terms of the small-displacement linear elastic asymptotic solution of an arbitrary crack-tip loaded in Mode-I, as suggested by Williams [26]. In the polar coordinates, the tractions are represented mathematically by:

$$\sigma_{ij} = \frac{K_I}{\sqrt{2\pi r}} f_{ij}(\theta) + T\delta_{1i}\delta_{1j} \tag{7.2}$$

Due to loading and geometric symmetry, a half disk plane strain FE model with an outer radius of R was constructed, with the displacements corresponding to the

tractions of Equation (7.2), applied at the outer boundary as follows:

$$u_x = \frac{K_I}{E}(1+\nu)\sqrt{\frac{r}{2\pi}}\cos(\theta/2)[\chi - \cos\theta] + (1-\nu^2)\frac{T}{E}x$$
$$u_y = \frac{K_I}{E}(1+\nu)\sqrt{\frac{r}{2\pi}}\sin(\theta/2)[\chi - \cos\theta] - \nu(1+\nu)\frac{T}{E}y \tag{7.3}$$

where $\chi = 3 - 4\nu$ under plain strain conditions.

The loading (in terms of K_I and T) was selected such that the characteristic plastic zone size (boundary of plastic zone defined as $\sigma_e/\sigma_y = 1$) was less than $0.15 \times R$, thus ensuring well-contained plasticity condition, such that Equations (7.2) and (7.3) would hold true. Moreover, the far-field J-Integral (termed J_{BC}, in order to distinguish it from the numerically calculated J) and K_I are related through:

$$J_{BC} = \frac{1-\nu^2}{E}K_I^2 \tag{7.4}$$

Nine values of the T-stress ($T/\sigma_y = 0.0$, ± 0.25, ± 0.5, ± 0.75, ± 1.00) were considered, and the results pertaining to different levels of constraint were generated. The J-Q approach of O'Dowd and Shih [67, 68] was used to quantify the constraint. The approach is based on dimensional similarity; it is argued that the near-tip fields up to LSY conditions could be satisfactorily described by the Q constraint parameter, if the distances are scaled with correct length scales (i.e. J/σ_y in this case). They showed that in the forward sector of a crack tip, within the distances of interest (i.e. $r < 5 \times J/\sigma_y$), Q would be a hydrostatic stress parameter, which would also correlate very well with the stress triaxiality (σ_m/σ_e), uniformly shifting the stress/strain profiles from a reference field:

$$\sigma_{ij} = (\sigma_{ij})_{\text{Ref}} + Q\sigma_y\delta_{ij} \qquad \text{for} \qquad r > J/\sigma_y \qquad \& \qquad |\theta| < \pi/2 \tag{7.5}$$

The reference field ($(\sigma_{ij})_{\text{Ref}}$ in Equation (7.5)) could be considered as the *HRR* field [29, 30] or the Small Scale Yielding (SSY) distribution obtained from MBL model with $T = Q = 0$, which leads to more consistent results, and is therefore used here. Ideally, Q could be extracted from FE results at any location and from any component of the stress tensor based on Equation (7.5); nevertheless, the literature recommends the use of the crack opening stress at $r = 2 \times J/\sigma_y$, where the finite strain effects have diminished [68, 70, 71].

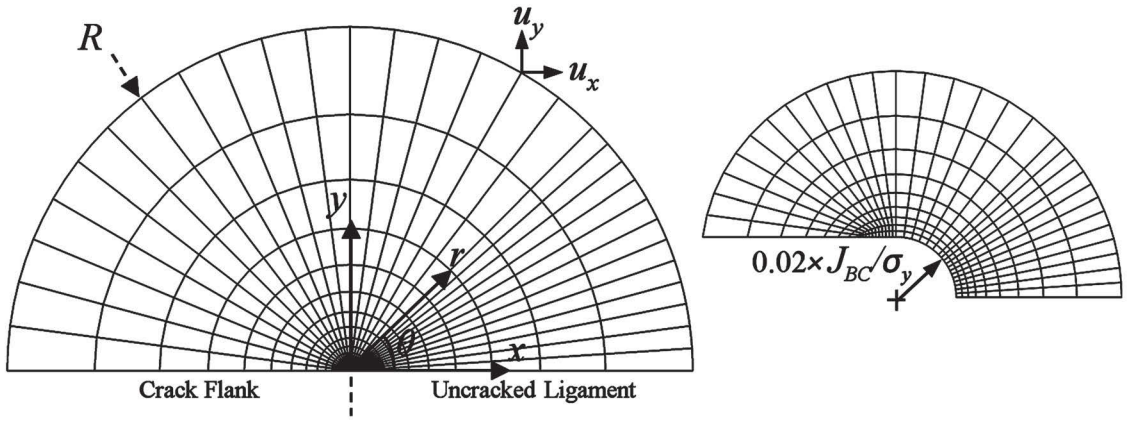

Figure 7.2. (Left) FE mesh of the MBL model along with the relevant coordinate systems and BCs. **(Right)** Crack tip details showing the initial notch radius.

ABAQUS's 4-noded plane strain continuum elements with hybrid formulation (CPE4H) were used [10]. The mesh consists of 1500 elements and was exponentially biased in the radial direction with 50 rows of elements. 30 elements were used in each row, circumferentially; 12 for the finer mesh of the first $\pi/4$ sector (required to capture the severe blunting deformations) and 18 for the rest of the $3\pi/4$ sector. An initially blunted crack tip was modeled with a radius of $0.02 \times J_{BC}/\sigma_y$. Figure 7.2 shows a typical MBL model and the initial blunted crack tip. The J-Integral values were extracted from several contours surrounding the crack-tip (each ring of element around the crack tip in Figure 7.2 is regarded as a contour) using the *Domain Integral* method implemented in the ABAQUS [10].

Figure 7.3 shows J/J_{BC} extracted from several consecutive contours surrounding the crack tip ($r/(J_{BC}/\sigma_y)$ is the radius of a contour). As seen, a slight path dependence is observed, which is known to be due to both the incremental plasticity and NLG effects. However, the J-Integrals which were extracted from the contours farther away from the crack-tip gradually converged to the exact analytical value of J_{BC} obtained by Equation (7.4). For example, in the $T/\sigma_y = 0$ and $n = 10$ case (Figure 7.3a), J extracted from a near-tip contour ($r \times \sigma_y/J_{BC} = 0.2$, contour #16) is only 50% of its analytical value (J_BC), while for a farther away contour ($r \times \sigma_y/J_{BC} = 7.45$, contour#30), the calculated J is more than 90% of J_{BC}. The convergence was slower for the negative values of T/σ_y and also for the lower strain hardening capacities

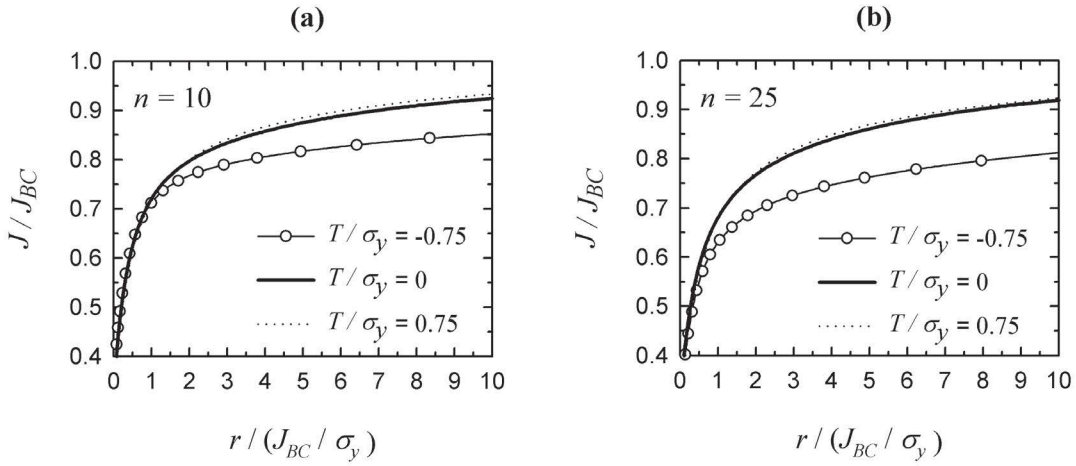

Figure 7.3. Convergence of J values as a function of radius of contour for **(a)** $n = 10$ and **(b)** $n = 25$.

(higher n), as observed in Figure 7.3.

The Q-T relationship is shown in Figure 7.4a, indicating that negative T-stress values result in very low Q values (low constraint), hence, also indicating low values of hydrostatic stress around in the near-tip region. On the other hand, Q reaches a constant value for positive values of the T-stress, resulting in near-tip stress fields being similar to the $T = Q = 0$ case. It is also noted that the strain hardening affects the relationship minimally, only showing its influence for larger absolute values of T/σ_y. Figure 7.4b shows the effect of the constraint parameter Q on the normalized $CTOD$ parameter through:

$$CTOD = d(\sigma_y/E, n; Q)\frac{J}{\sigma_y} \tag{7.6}$$

Figure 7.4b shows that at the same J, the low-constraint configurations with $Q < 0$ have considerably larger $CTOD$ than those with high constraint configurations ($Q > 0$). Moreover, the material with $n = 25$ undergoes larger crack tip deformations. These facts are also revealed by examination of the near tip deformed FE mesh for the two limiting cases of $T/\sigma_y = \pm 1.0$, as shown in Figure 7.5.

Representative components of the family of J-Q near-tip fields generated with the MBL model are shown in Figure 7.6. These include: (i) Figures 7.6a and 7.6d, showing the normalized crack opening stress ($\sigma_{\theta\theta}/\sigma_y$ along the $\theta = 0$ ray) over a

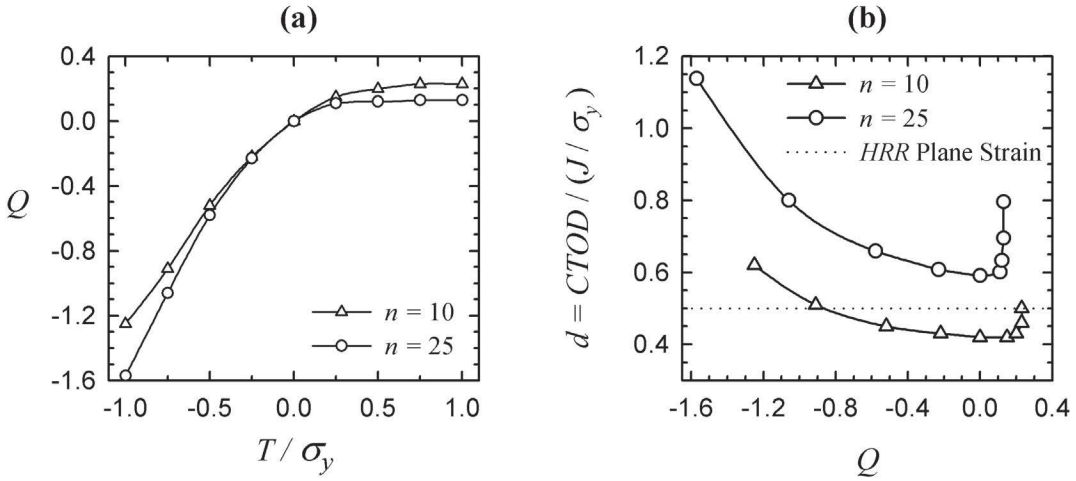

Figure 7.4. **(a)** the T-Q relationship and **(b)** the Q-d relationship.

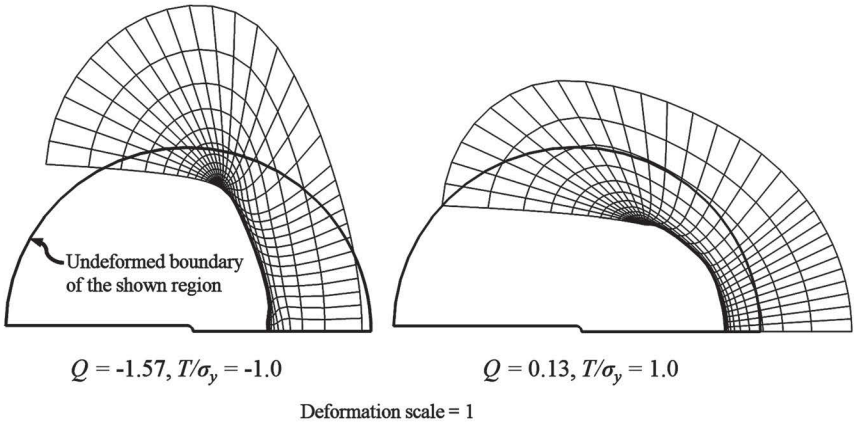

Figure 7.5. Deformed crack tip region in the MBL model with $n = 25$ material for **(Left)** low and **(Right)** high constraint (radius of the shown annular zone is $1 \times J/\sigma_y$ in the undeformed configuration).

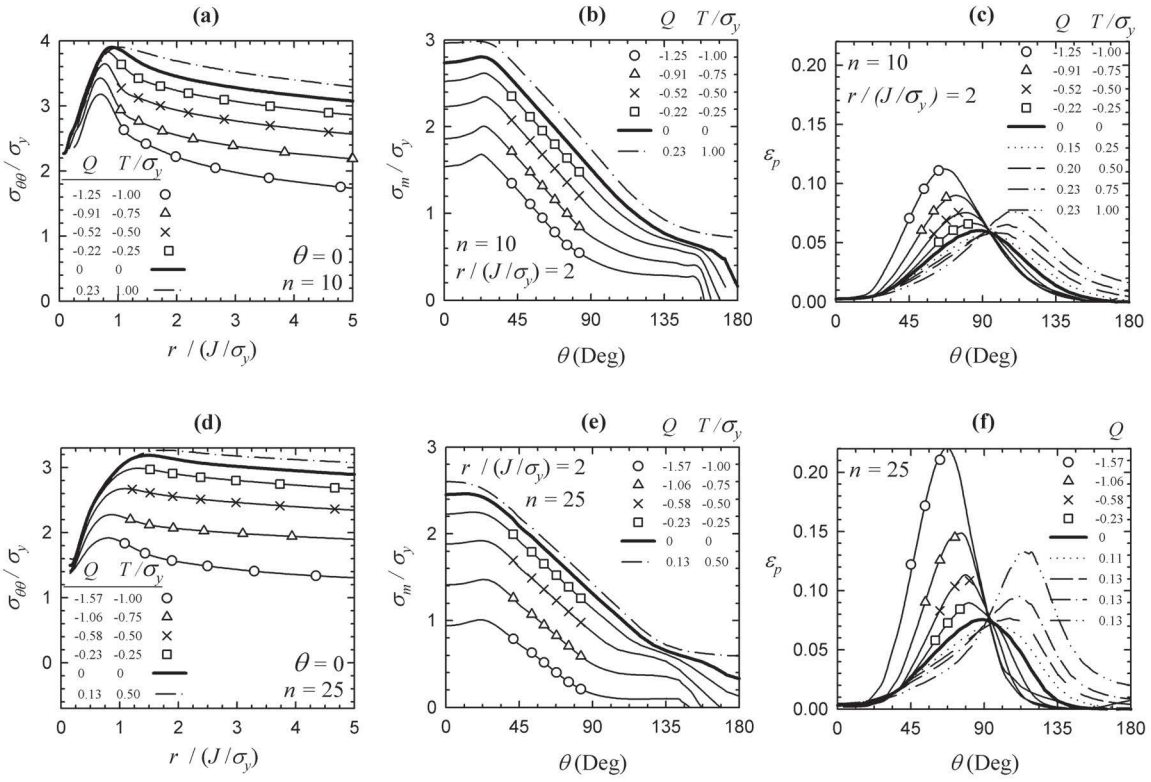

Figure 7.6. The J-Q near tip fields generated with the MBL model; radial distribution of crack opening stress for **(a)** $n = 10$ and **(d)** $n = 25$; angular distribution of hydrostatic stress for **(b)** $n = 10$ and **(e)** $n = 25$; and angular distribution of equivalent plastic strain for **(c)** $n = 10$ and **(f)** $n = 25$.

micro-structurally significant distance of $0 < r < 5 \times J/\sigma_y$, (ii) Figures 7.66b and 6e, illustrating the normalized hydrostatic stress (σ_h/σ_y) and (iii) Figures 7.6c and 7.6f, showing the equivalent plastic strain (ε_p); both of these latter two quantities are extracted along a circular path with radii of $2 \times J/\sigma_y$. The crack opening stress profiles of Figure 7.6a and 7.6d show that negative Qs decrease the stress distribution strongly and uniformly, while the positive values raise the distributions minimally. The finite strain effects (captured due to the consideration of NLG effects) caps the stress distributions, preventing them from becoming unbounded near the crack-tip at $r < 2 \times J/\sigma_y$. Moreover, high strain hardening capacities ($n = 10$) permits the development of higher stress values near the crack tip, as can be seen through comparison of the stress peaks in Figure 7.6a and 7.6d.

Further inspection reveals the uniform shift of stress distributions caused by the

negative Qs as seen in Figure 7.6b and 7.6e, especially in the first $\pi/2$ sector to which the J-Q theory is applicable. The equivalent plastic strain distributions of Figure 7.6c and 7.6f shows how the absolute value of T/σ_y increases the near-tip plastic deformations, which are more severe for negative T-stresses and also low strain hardening capacities (high n). The maxima of ε_p occurs at $\pi/2$ for the reference case of $T = Q = 0$. Shifting of the ε_p profiles observed in Figure 7.6c and 7.6f indicates that negative T-stresses (Q) cause the plastic zone to rotate towards the uncracked ligament, while positive T-stresses (Q) cause the plastic zone to rotate backwards towards the crack flanks. Unlike the case for the stress distributions, a positive T-stress (Q) significantly increases ε_p in the $\pi/2 \sim \pi$ sector. The distributions of Figure 7.6 and the discussed trends are in agreement with the similar published MBL studies; see e.g. [56, 57, 61, 63, 67, 68].

Strictly speaking, the J-Q approach is based on the 2D plane strain assumption. However, several researchers have argued validation of the approach to 3D cracks [69, 71]. These heuristic arguments pointed out that at sufficiently remote locations from the intersection of the crack front and external body surface ($s/c < 1$), and in the neighborhood of the crack tip ($r \to 0$), plane strain conditions would indeed prevail (i.e. the out of plane strains become negligible with respect to the singular in plane strains). As such, the J-Q description of Equation (7.5) would hold true (see Figure 7.8 for r, θ, s coordinates), and accordingly, the pair of $J(s)$ and $Q(s)$ completely characterizes the 3D near tip fields [69, 71]. Furthermore, an operational average definition of constraint, Q_{ave}, has been proposed [69]. This quantity has been observed to correlate the toughness and crack growth curves in 3D geometries with geometric specimen configuration reasonably well [74]. Mathematically, Q_{ave} is represented by:

$$Q_{ave} = \frac{1}{s_b - s_a} \int_{s_a}^{s_b} Q(s)\, \mathrm{d}s \qquad \text{at} \qquad \theta = 0, \qquad r = 2 \times J_{ave}/\sigma_y \tag{7.7}$$

However, our findings (see Figure 7.14 and 7.15 and their explanations) show that J_{ave}-Q_{ave} trajectories are very similar to the J-Q trajectory when extracted at the crack center ($s/c = 0.0$), thus justifying extraction of the results at this location.

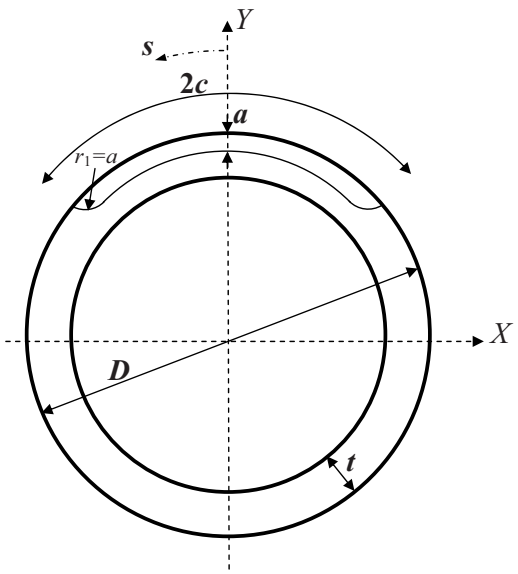

Figure 7.7. Schematic of the pipeline cross section and the canoe shaped crack.

7.4 The Cracked Pipeline Model

A pipeline with $D/t = 13.61$ ($D = 323.9$ mm and $t = 23.8$ mm), which typifies a reeled pipeline, with an external part-through surface breaking circumferential crack (representing a hypothetical defect or flaw due to welding imperfections) at its 12 o'clock position, subjected to bending is investigated. A schematic of the cracked pipeline cross section is shown in Figure 7.7, which shows the *canoe* shape of the crack, with its fillet radius equal to the crack depth. This considered crack shape is representative of real weld defects observed in offshore pipelines [47]. Due to symmetry, a quarter FE model is constructed, with a length of $L = 2D$, which is sufficiently long to capture the strain and stress discontinuity caused by the crack [47, 125] . Rotation was imposed on a reference point tied to the pipe end via a set of multi-point constraints (MPC's). The rotation was such that the outermost fiber would experience an axial (uncracked) strain of 3%, which encompasses even the extreme plastic bending that occurs during reeling. According to the Euler beam assumption (i.e. plane sections remaining plane after application of bending), pipe's end rotation can be calculated by:

$$R_x = \frac{2\varepsilon_g L}{D} \tag{7.8}$$

It is understood that as plastic deformation increases, the Euler assumption would

Table 7.1. Summary of the 12 different FE models considered (all pipelines have a $D/t = 13.61$, $D = 323.9$ mm and $t = 23.8$ mm).

Model#	a (mm)	a/t	$2c$ (mm)	$2c/\pi D$	n
1, 2	2	0.084	50	0.05	10, 25
3, 4	2	0.084	200	0.2	10, 25
5, 6	4	0.168	50	0.05	10, 25
7, 8	4	0.168	200	0.2	10, 25
9, 10	6	0.252	50	0.05	10, 25
11, 12	6	0.252	200	0.2	10, 25

not be strictly correct; however, the resulting error would be insignificant [119]. This has also been verified in this study; the average values of the compressive and tensile strains along the pipeline length obtained by the finite element analysis are indeed very close to the value of ε_g evaluated by Equation (7.8).

The flaw sizes of interest in girth welded pipelines is usually governed by the weld pass height and is typically $2 \sim 6$ mm in height [9]. Based on this, three crack depths of $a = 2$, 4 and 6 mm were considered in the FE models. Furthermore, the crack lengths considered were $2c = 50$ and 200 mm. Noting the two strain hardening indices of $n = 10$ and 25 considered for the material, the different combinations of the parameters leads to 12 FE models, which are summarized in Table 7.1. These models correspond to realistic situations and cover most of the typical flaw size and material properties relevant to pipeline practice.

The C3D8R element of ABAQUS [10] (an 8 node 3D continuum element with reduced integration and hour-glass control) was used for the FE models. A focused spider web mesh was used for the crack front. Within this focused mesh zone, the element sizes decrease exponentially nearing the crack tip, with the corresponding bias ratios between 50 to 100, depending on the crack depth. An initial notch radius equal to $0.01 \times a$ was assigned to the crack tip in order to overcome the convergence problems due to NLG effects in this zone. A total of 13 rows of elements were used in the radial direction at this zone. The size of the smallest element was on the order of $0.001 \times a$. Furthermore, 20 rows of elements were used for the circumference of the $\pi/2$ sector corresponding to the uncracked ligament, while 8 rows of elements were

used for the $\pi/2$ sector ahead of the crack flanks. A typical mesh with a close-up view of the crack tip zone is shown in Figure 7.8[1]. All models consisted of 60$\sim$70 thousand elements, depending on the crack size.

Careful mesh convergence studies were performed in consideration of all behavioral aspects of the model, including the global (moment-curvature) and local response behavior, in terms of both variations in the J and the near-tip fields, and also in consideration of uncontrolled hour-glass mesh distortions. Accordingly, the quality and density of the incorporated meshes were deemed satisfactory. The in-house developed Python scripts developed in our previous work [125] were efficiently utilized to construct the complicated FE mesh and also the trial and errors involved in establishing the mesh characteristics. Results are systematically extracted from the near-tip region at deformation levels corresponding to $\varepsilon_g = 1\%$, 2% and 3%. The constraint parameter, Q, is calculated from the crack opening stress component with the MBL distributions of $Q = T = 0$, serving as the *reference* distribution for use in Equation (7.5).

7.4.1 Near Tip Fields in Cracked Pipelines and MBL Similitude

The near tip fields of the cracked pipeline model, including the crack opening stress distribution along the uncracked ligament, and angular distributions of hydrostatic stress and plastic strain are presented for Model#1 (Figures 7.9a to 7.9c) and Model#10 (Figures 7.9d to 7.9f). Strictly speaking, the fields shown in Figure 7.9 should be identical to those in Figure 7.6 at the same magnitude of Q. Although the exact same Q values might not be available for the presented MBL and cracked pipeline model (Figures 7.6 and 7.9, respectively), the similarity in the near tip fields in the two models is evident and obvious. For example, the three crack opening stress profiles in Figure 7.9a, corresponding to the successive values of $Q = -1.15$, -0.93, -0.63 (extracted at $\varepsilon_g = 3$, 2, 1%, respectively), are bounded by the three lower profiles seen in Figure 7.6a, corresponding to the MBL model with successive values of $Q = -1.25$, -0.91, -0.5. In all cases, the crack opening stress and hydrostatic stress decrease

[1]The presented Figure 7.8 is slightly more detailed than that in the published article.

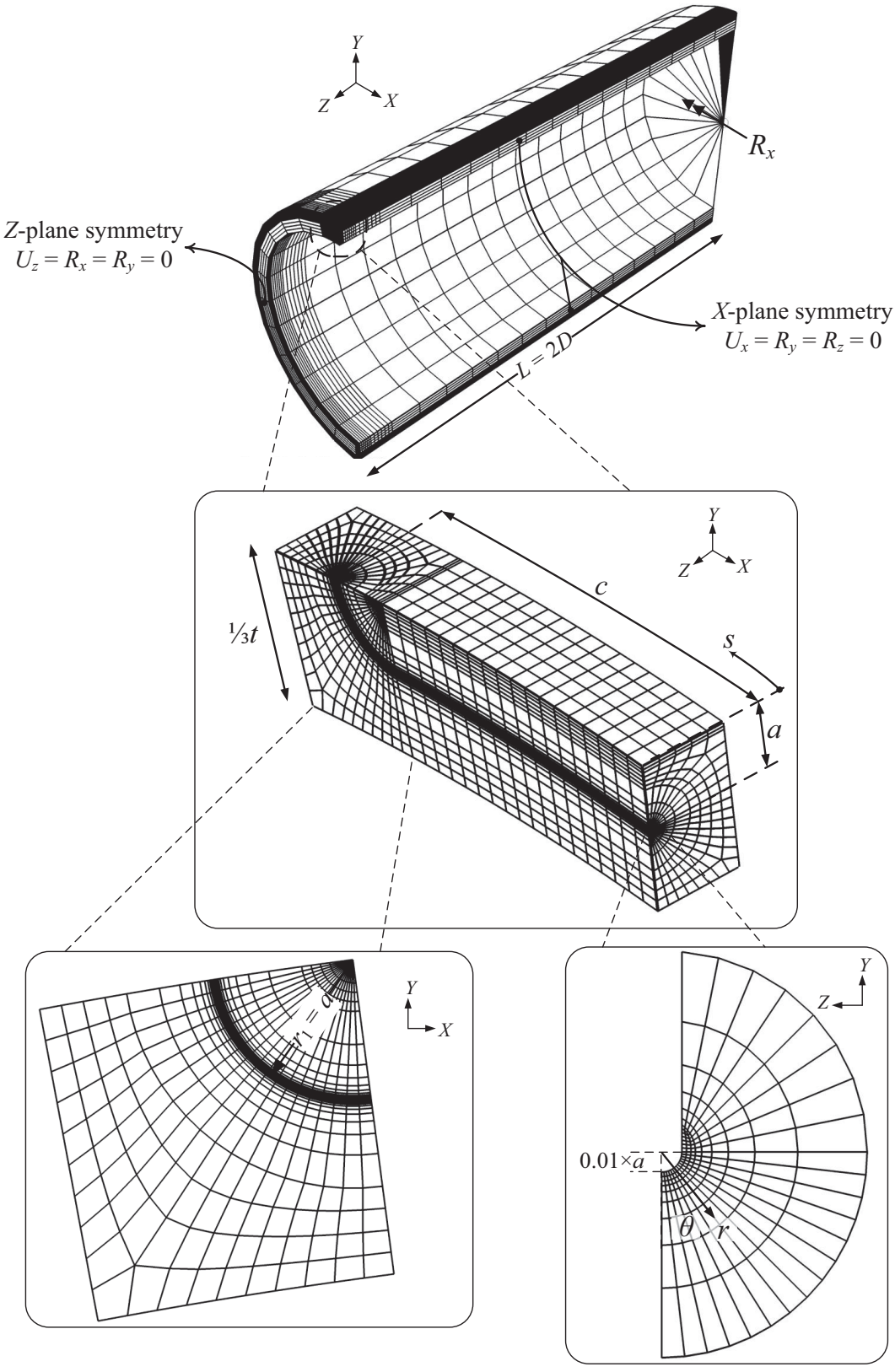

Figure 7.8. Typical cracked pipeline FE mesh including the boundary conditions and close-ups of the focused mesh in the crack tip zone. The crack tip mesh arrangement with initial notch and also the r-θ-s coordinates are shown.

with increased loading, with the effect being more prominent for high hardening material with $n = 10$. The angular distributions of the hydrostatic stress, seen in Figures 7.9b and 7.9e, are not completely identical to those of the MBL (Figures 7.6b and 7.6e) in the $\pi/2 \sim \pi$ sector in front of the crack flanks; however, this zone is outside the admissibility limit of the J-Q approach (see Equation (7.5)). Nonetheless, fair agreement is observed in the $0 \sim \pi/2$ sector, between the pipeline and MBL hydrostatic stresses. As seen, the plastic strain increases as a function of Q and ε_g, in the $0 \sim \pi/2$ sector, similar to that in the MBL model. These consistencies are not solely qualitative. For example, the maximum plastic strain for the material with $n = 10$ is $\varepsilon_p = 0.092$ at $Q = -0.91$ in the MBL model (Figure 7.6c), while Figure 7.9c (for the cracked pipeline) shows a maximum of $\varepsilon_p = 0.09$ at $Q = -0.93$ ($\varepsilon_g = 2\%$). In addition, the maxima in both models occur at $\theta \approxeq 70^\circ$. The agreement in the near tip behavioral patterns with the MBL model and all the 12 cracked pipeline FE models listed in Table 7.1 is seen in the results obtained for all the applied global strain values, even when strain is as high as ($\varepsilon_g = 3\%$, in which LSY conditions prevail. However, in favor of brevity, detailed exemplification is limited to Figure 7.9 only.

Figure 7.10 shows the crack opening stress in the near tip zone as a function of Q for all 12 FE models. Presenting the data in this manner allows a direct comparison with MBL results, which are also shown in Figure 7.10. It is emphasized that while Q is operationally defined at $r = 2 \times J/\sigma_y$, the data of Figure 7.10 are extracted at a farther distance of $r = 4 \times J/\sigma_y$. Still, reasonable agreement is observed between the near tip fields of the MBL and the cracked pipeline, up to the highest plastic bending levels causing $\varepsilon_g = 3\%$. Strictly speaking, the crack opening stress of the pipeline is within 10% of the values predicted by the MBL model for the $n = 10$ material, as seen in Figure 7.10a, while the agreement is within 15% of the MBL results for the $n = 25$ material (Figure 7.10b). As seen, the MBL distribution is cut off at $Q \approxeq -1.2$ in Figure 7.10a. This is due to the fact that generation of lower Qs would have required $T/\sigma_y < -1.0$ (see Equation (7.3)). However, for such loadings, SSY requirements would be nullified due to the development of excessively large plastic zone in the MBL model. As a result, Equations (7.2) and (7.3) would be rescinded. In any case, it is understandable from the trend seen in Figure 7.10a that agreement

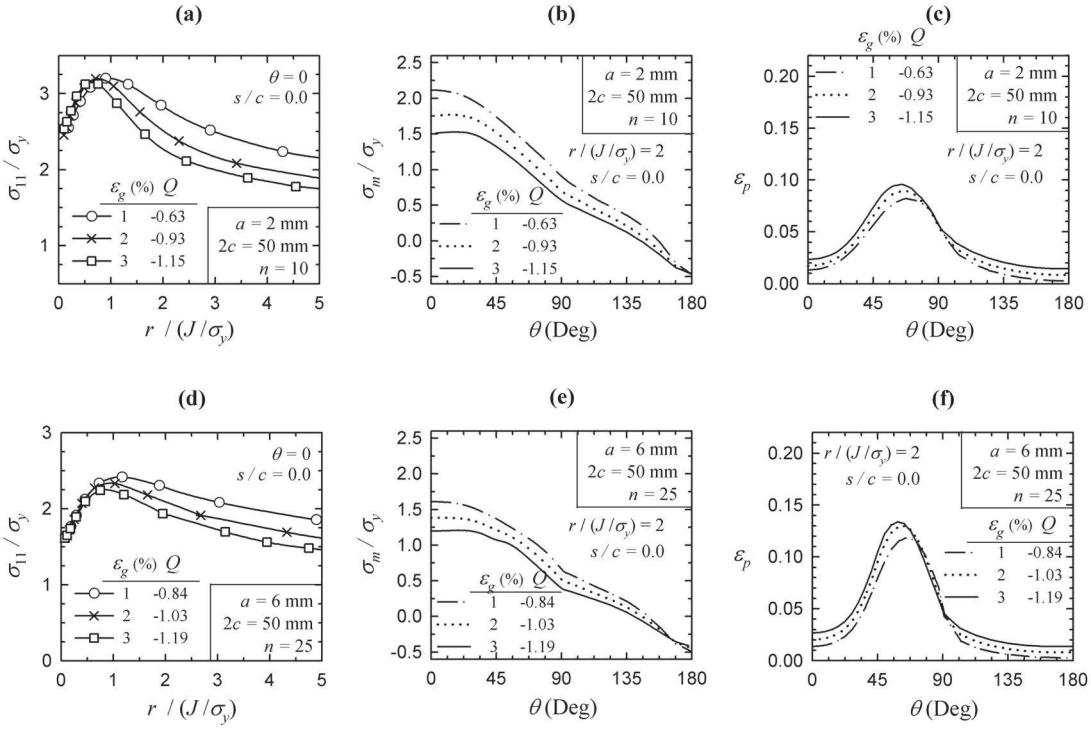

Figure 7.9. The J-Q near tip fields of cracked pipelines; radial distribution of crack opening stress for **(a)** Model#1 and **(d)** Model#10; angular distribution of hydrostatic stress for **(b)** Model#1 and **(e)** Model#10; and angular distribution of equivalent plastic strain for **(c)** Model#1 and **(d)** Model#10.

would be expected to continue to exist.

Figure 7.11 shows the near tip plastic strain contours for the MBL model and cracked pipeline Model#1, again demonstrating the identical response patterns. In regards to the foregoing discussion and the comparison of MBL and cracked pipeline near tip stress and strain fields, the following three points are noted:

1. The FE results are strictly correct at element integration locations, thus, results extraction at any other required specific location, such as at $r = 4 \times J/\sigma_y$, as reported in Figure 7.10 would be an approximation and in a sense, an average result, thus bearing some discrepancies.

2. Although both FE meshes for the MBL and pipeline models passed mesh convergence requirements, the MBL model has a much finer mesh.

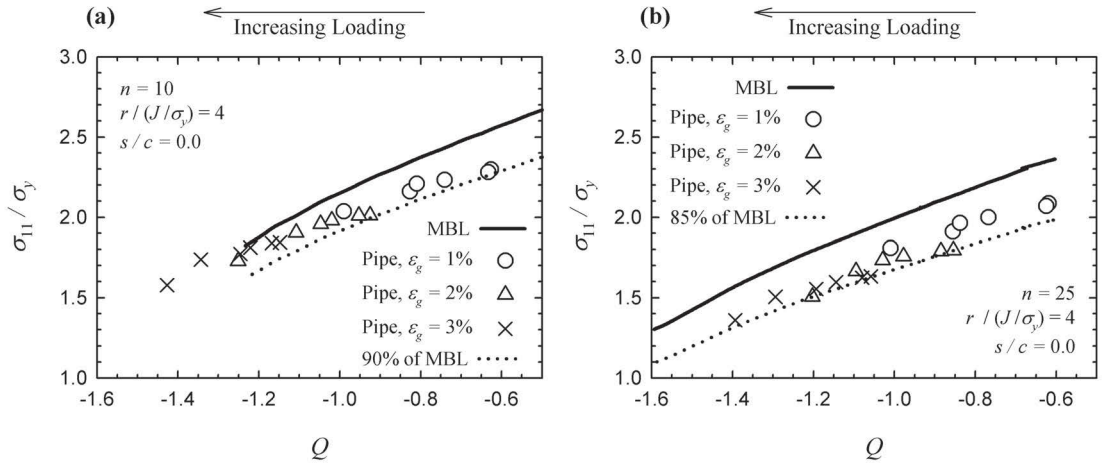

Figure 7.10. Crack opening stress as a function of Q for the cracked pipeline models and the MBL model for **(a)** $n = 10$ material and **(b)** $n = 25$ material.

3. The agreement exhibited in Figures 7.9, 7.10 and 7.11 continues to exist for all the cracked pipeline models considered and also amongst all other components of the stress and strain tensors.

Based on these and the observed similarity of the stress and strain fields, it is believed that the J-Q approach could effectively characterize the near tip stress and strain fields of flawed pipelines, up to extreme plastic bending levels, with sufficient accuracy. This in turn provides sufficient proof for the similitude concept explicit in all ECA approaches.

7.4.2 Evolution of the Constraint, Q, in Flawed Pipelines

Equation (7.5) indicates that Q is defined at a specific location near the crack tip. Nevertheless, it has been shown that the two parameter J-Q approach describes the stress and strain fields within an annular region ahead of the crack tip, described by $r < 5 \times J/\sigma_y$ and $\theta < \pi/2$, in flawed pipelines up to extreme plastic bending load levels. This region, in turn, supposedly engulfs the fracture process zone; thus, the two parameters, namely J and Q, could effectively describe the fracture initiation and crack growth.

The evolution of J as a function of ε_g is presented in Figure 7.12 for the cracked

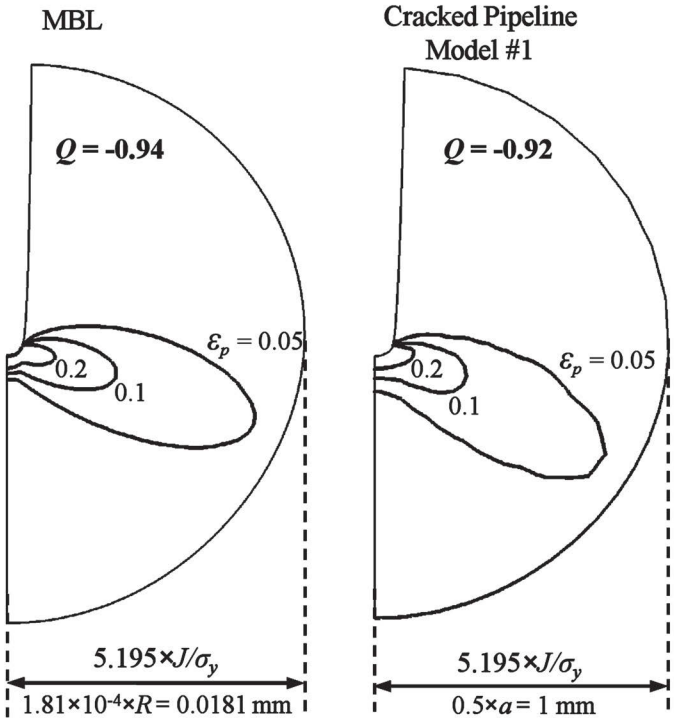

Figure 7.11. Comparison of the equivalent plastic strain at the near tip region of the MBL model and cracked pipeline Model#1 at crack center $s/c = 0.0$ at approximately equal values of Q and comparable length scales. Contour plots for successive values of $\varepsilon_p = 0.05,\ 0.1,\ 0.2$.

pipeline models with $n = 10$. For the cracks of practical interest with a maximum depth of 6 mm ($a/t < 0.252$), the strain hardening index has been observed to have minimal effect on the J-ε_g paths [125], and thus only the results for $n = 10$ are illustrated in Figure 7.12, since they closely resemble the results for $n = 25$. Common in all the sub-figures, the J-ε_g paths have an initial nonlinear shape corresponding to SSY behavior, which terminates at early loading stages (approximately at $\varepsilon_g \cong \varepsilon_y = 0.002$) when plasticity starts to spread throughout the pipe wall thickness. Consequently, the J-ε_g path follows a linear trend as pointed out by other researchers as well [47, 125]. However, this linear evolutionary trend becomes less accurate for the long cracks with $2c = 200$ mm (Figure 7.12b), and also especially for deeper cracks. As seen from the results, both crack depth, a, and crack length, $2c$, have a profound effect on amplifying the J.

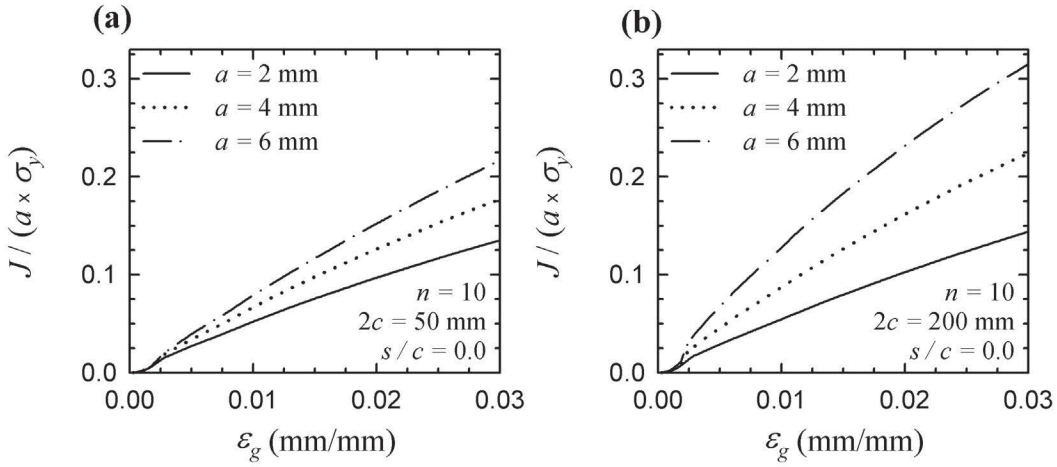

Figure 7.12. Evolution of J in the cracked the pipeline at crack center, $s/c = 0.0$, as a function of ε_g, for a family of crack depths $a = 2$, 4, 6 mm, and material hardening of $n = 10$; **(a)** $2c = 50$ mm, **(b)** $2c = 200$ mm.

Figure 7.13 shows the progression of Q as a function of ε_g for the cracked pipeline models outlined in Table 7.1. The striking feature common to all cases is that Q decreases steadily with increasing global strains in a more or less linear fashion, without a steady state portion as observed for some deeply cracked laboratory specimens [71]. Actually, this behavior is a feature of *shallow* cracks [71], which, generally speaking, pertains to all the cracks of interest in this study ($a/t < 0.252$). The practical strain range of $\varepsilon_g = 1 \sim 3\%$, results in values of Q ranging from -0.4 to -1.4. In all cases, the Q-ε_g paths for the family of crack depths, a, are more or less parallel, with the intercept decreasing steadily as a function of a. This decreasing intercept effect is more pronounced for longer cracks with $2c = 200$ mm (Figure 7.13b and 7.13d) as opposed to shorter cracks with $2c = 50$ mm (Figures 7.13a and 7.13c).

While Figure 7.13 gives a complete picture of the constraint levels in cracked pipelines, the distribution of Q along the crack length, s, should also be considered. It has been observed that Q maintains a rather constant value, nearly along the entire crack length, and only starts to change at the fillet location of the canoe shaped crack (see Figure 7.7), where the crack starts reaching the outer pipe surface. This behavior is common to all cases considered, and, as an example, the distribution of Q and J along the crack length are presented in Figures 7.14a and 7.14b, respectively,

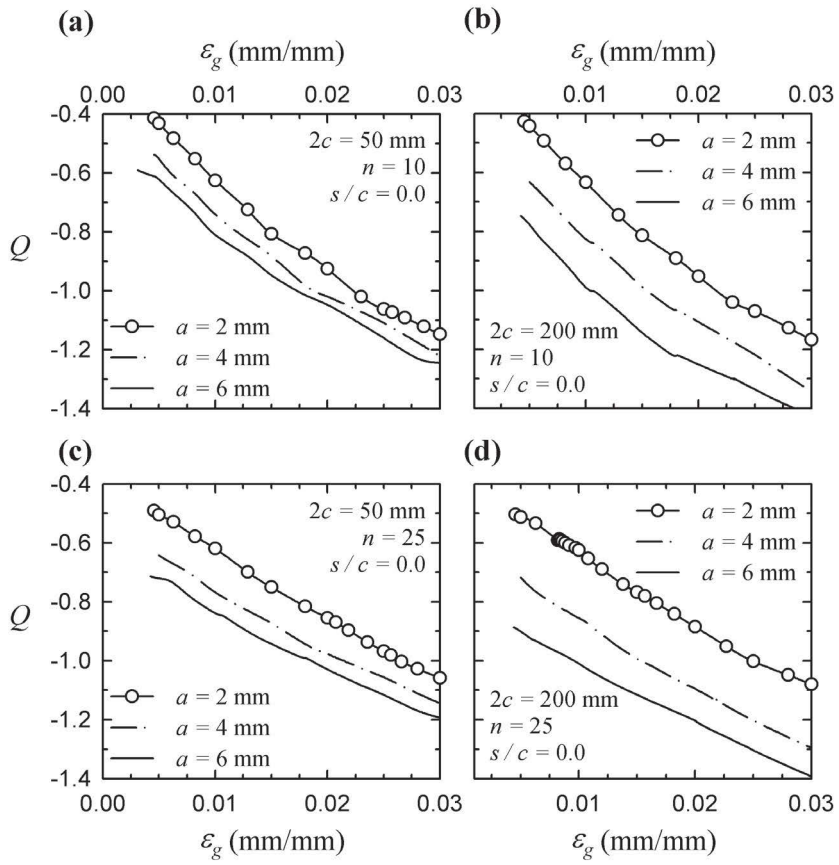

Figure 7.13. Evolution of Q in the cracked pipeline at crack center, $s/c = 0.0$, as a function of ε_g for a family of crack depths $a = 2$, 4, 6 mm; **(a)** $n = 10$, $2c = 50$ mm, **(b)** $n = 10$, $2c = 200$ mm, **(c)** $n = 25$, $2c = 50$ mm, **(d)** $n = 25$, $2c = 200$ mm.

for pipeline Model#7. Figure 7.14a shows that Q could be considered constant up to $s/c \cong 0.5$; however, a swift increase occurs near the fillet location of the canoe crack. This increase can be described by noting that the *local loading* in terms of $J(s)$, decreases as one approaches the crack end as illustrated in Figure 7.14b. In this figure, the value of J as $s/c \to 1$ is approximately half that at the crack center, $s/c = 0$, which in turn causes higher values of Q with respect to the crack center. However, a competing factor is that as the crack end is neared (i.e. as $s/c \to 1$), the constraint conditions tend to become similar to that observed in the plane stress situation (i.e. a low constraint situation). On the other hand, the crack center is more similar to the high constraint plane strain situation. Consequently, a rapid decline in

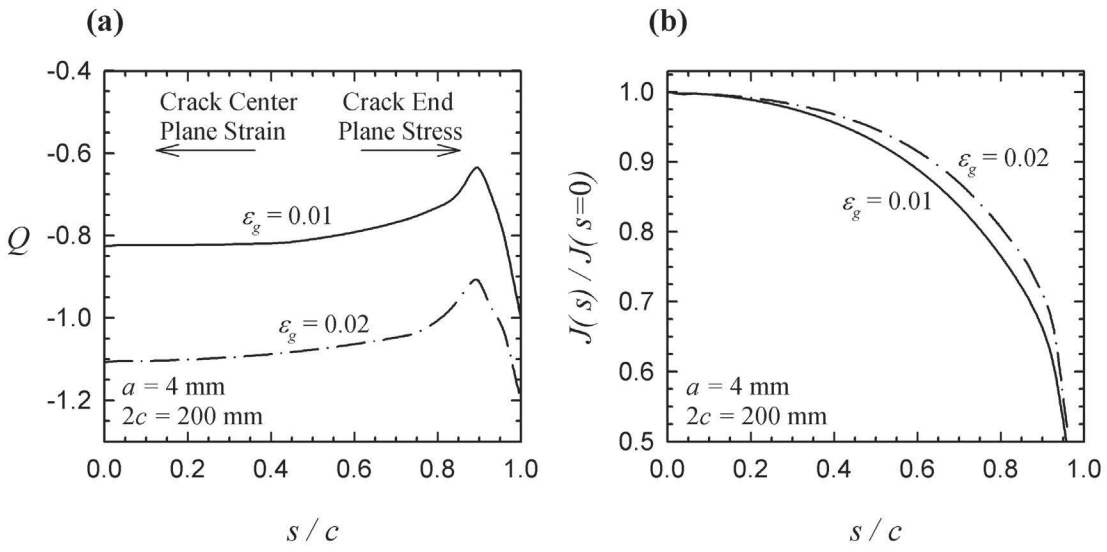

Figure 7.14. Distribution of **(a)** Q and **(b)** J, along the crack length, for pipeline Model#7 ($a = 4$ mm, $2c = 200$ mm, $n = 10$).

Q is observed very near the crack end.

The correct values of integration limits for use in Equation (7.7) are still under debate. Ideally, these limits describe a portion of the crack front length, which is deemed micro structurally significant, and encloses the fracture process zone. Faleskog [74] evaluated the integral over the portion where $Q(s)$ is essentially constant, while Silva et al. [80] used the whole crack front length as the integration domain. Here, a definition similar to that used by Faleskog [74] is incorporated; that is, Q_{ave} is evaluated along the crack length up to where the canoe fillet starts (i.e. at $s_a = 0$ and $s_b = c-a$). In order to justify the use of the Q (and J) evaluated at the crack center ($s/c = 0$), the J_{ave}-$Q(s)$ trajectories along the crack length, for a typical pipeline (Model#9), is presented in Figure 7.15a (J_{ave} is defined similar to Q_{ave}, see Equation (7.7)). In concert to the trend observed in Figure 7.14a, the family of J_{ave}-$Q(s)$ trajectories for small values of s/c are closely packed in Figure 7.15a. The local $Q(s)$ decreases nearly linearly for increasing values of J_{ave} (in the LSY regime). The intercept of these lines decreases steadily as a function of s/c. Moreover, the J_{ave}-Q_{ave} (dash-dot line) and J-Q at $s/c = 0$ (solid line) trajectories are also shown. Both these trajectories provide an upper envelope to the family of lines, and are quite similar. Although not shown,

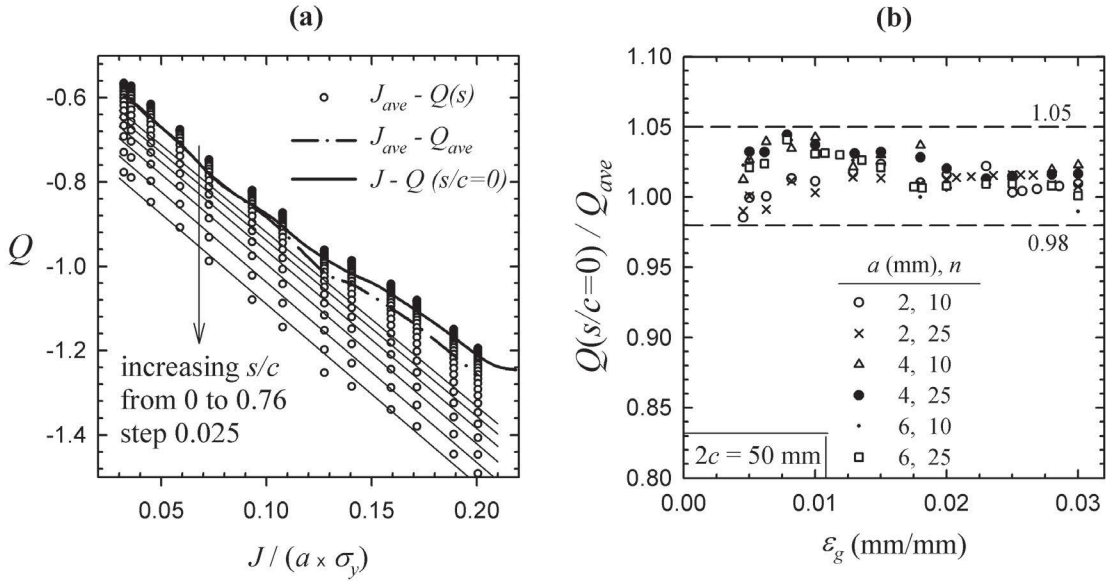

Figure 7.15. (a) J_{ave}-$Q(s)$ trajectories along the crack front for Model#9 ($a = 6$ mm, $2c = 50$ mm, $n = 10$) along with J_{ave}-Q_{ave} and J-$Q(s/c = 0)$ trajectories **(b)** Ratio of $Q(s/c = 0)/Q_{ave}$ as a function of global strain for all six models with $2c = 50$ mm.

these trends were observed in all other pipeline models as well. Indeed, Figure 7.15b shows the $Q(s = 0)/Q_{ave}$ ratio as a function of ε_g for all six models with $2c = 50$ mm, and the close scatter around unity (i.e. $0.98 < Q(s = 0)/Q_{ave} < 1.05$) demonstrates that both constraint definitions are more or less equivalent. Based on the above discussion and also considering the subjective definition of Q_{ave} as discussed, the more simple and straight forward measure of constraint, $Q(s/c = 0)$, has been adopted throughout this study.

In order to gain a better understanding on the effect of each parameter on Q, a consistent loading measure, namely $J/(\sigma_y \times a)$, has been incorporated. It is believed that the comparison of the Q parameter extracted at specific values of $J/(\sigma_y \times a)$ in different models (not necessarily at the corresponding equal values of ε_g), would effectively reveal the influence of each parameter on Q. Such results are presented in Figures 7.16a and 7.16b for the materials with $n = 10$ and $n = 25$, respectively. The trend common to all crack sizes and strain hardening indices is that Q increases as the cracks get deeper (increasing a) and longer (increasing $2c$). However, the effect of crack depth is more pronounced than crack length. Moreover, as seen, these trends

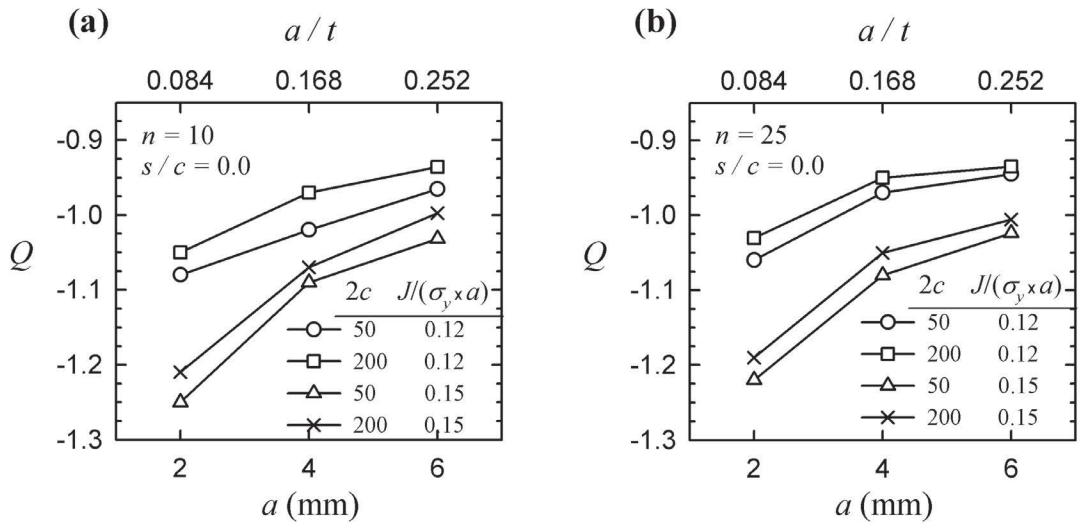

Figure 7.16. Parametric study on the effect of crack size on Q for materials with **(a)** $n = 10$ and **(b)** $n = 25$.

are true for both load levels of $J/(\sigma_y \times a) = 0.12, 0.15$. For the shallowest crack with $a/t = 0.084$, Q experiences a large decrease. Furthermore, the value of n does not seem to alter the general trend. The trend is in agreement with the previous results observed for the 2D test specimens; that is, *constraint loss* is severest in the shallow crack geometries, while the deeply cracked geometries are generally *high constraint*, in which the near crack tip fields converge to the HRR solution [59, 60, 62].

A variety of J-approximation schemes are available that can provide prediction of J, needless of a detailed FE analysis (see for example [35, 36, 51, 125]). Unfortunately, the same does not hold true for Q, for which, only Q-estimations for test specimens [68, 71], and for structures under SSY conditions are available [127]. Based on the observed nearly linear dependence of Q on ε_g in cracked pipelines (as manifested in Figure 7.13), a simple and practical equation is proposed by which the upper-bound values of Q, as a function of ε_g and a, can be readily established:

$$Q = -0.25\varepsilon_g - b_1 \qquad \varepsilon_g \text{ is in } (\%) \tag{7.9}$$

where

$$b_1 = \begin{cases} -0.3 & \text{for } a/t = 0.084, \\ -0.4 & \text{for } a/t = 0.168, \\ -0.45 & \text{for } a/t = 0.252. \end{cases}$$

Furthermore, the intercept, b_1, in Equation (7.9) could be described more generally as a function of crack depth, by the following relation:

$$b_1 = \beta_1 \left(\frac{a}{t}\right)^2 + \beta_2 \left(\frac{a}{t}\right) + \beta_3 \tag{7.10}$$

where $\beta_1 = 3.543$, $\beta_2 = -2.0833$, $\beta_3 = -0.15$. Figure 7.17a (for $a = 2$ mm) and 7.17b (for $a = 4$ mm) show the comparison of the predicted upper bound Q by Equation (7.9), and Q evaluated by FE for the cracked pipelines. As seen, the data are relatively more scattered for deeper cracks; however, in all cases, Equation (7.9) can accurately capture the general trend. Generally speaking, it is believed that the linear Q-ε_g relation holds true for moderately shallow cracks (the deepest crack considered here that the relationship applies to is $a/t = 0.252$), and for deeper cracks the linear relationship would not necessarily hold true[†]. It should also be noted that incorporation of the upper limit of Q provides a margin of conservatism. It is worth noting that as per Equation (7.9), the slope of the Q-ε_g path assumes a constant value (-0.25) for all cases, while the value of the intercept, b_1, is governed mainly by the crack depth (manifested in Equation (7.10)), and is also slightly dependant on crack length ($2c$) and material hardening index (n), which have been eluded from the equation for the sake of simplicity.

7.4.3 Constraint Similarity in Cracked Pipeline and SENT Specimens

When utilizing the J-Q two parameter fracture approach, the fracture toughness data required for the ECA integrity assessment procedure should be extracted from laboratory specimens exhibiting matching constraints with that from the cracked pipeline. DNV [9] recognizes the fact that the constraint level in cracked pipelines is similar to the low constraint SENT specimen, rather than the traditionally used deeply

[†]This sentence does not appear in the published paper, and is added here to the manuscript of the thesis based on the suggestion of the examining committee.

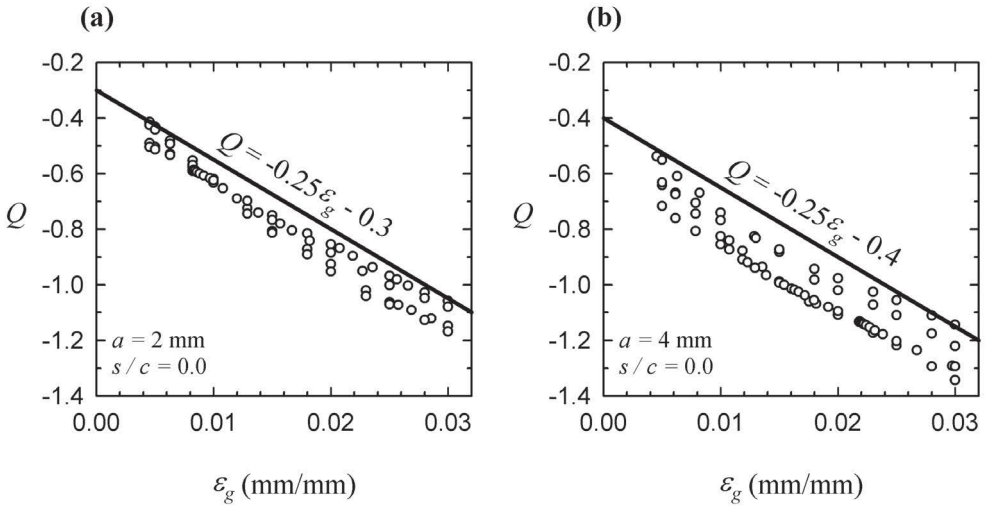

Figure 7.17. Scatter of the Q values for cracked pipelines compared to the Q values estimated by Equation (7.9) for **(a)** $a = 2$ mm (Model#1∼4) and **(b)** $a = 4$ mm (Model#5∼8).

cracked, high constraint SENB specimen. The backbone of this recommendation is based on the case studies of Refs. [77, 78], which compared the Q parameter in pipeline and SENT specimens. Parks [56] cautioned on how such mere point matching Q-extraction approaches might be inadequate; that is, although two geometries may have the same Q value, their near crack tip fields might actually be quite different, probably due to the interference of the *global stresses* with the singular fields. Thus, any constraint study should be based on a detailed field-matching procedure, as has been carried out in the present study.

For the sake of completeness, the generated constraint values for the cracked pipelines are compared here to those of SENT specimens[2]. The SENT specimen geometry considered here conforms to DNV recommendations [9]. Specimen's thickness is $W = 22$ mm, which represents the pipe thickness (t), less the minimum machining necessary to achieve a rectangular specimen. Specimen width is taken as $2B = 2W$, and the specimen length is $10W$. Figure 7.18 shows a schematic of the SENT specimen in relation to the actual flawed pipe section. The quarter symmetric FE model of the SENT specimen with the relevant boundary conditions is also shown. The crack tip

[2]SENT specimens loaded in fixed grip displacement control.

mesh characteristics are similar to those of the cracked pipeline model. Six models, corresponding to different combinations of $a = 2$, 4, 6 mm and $n = 10$, 25, were analyzed. The axial displacement applied at the end of the specimen was taken such to create an approximately equal value of $J/(\sigma_y \times a)$ to that of the corresponding cracked pipeline models. Comparison of the Q parameter between SENT and pipeline models are presented in Figure 7.18 for the material with $n = 10$. Indeed, the J-Q trajectories from both the SENT specimens and the pipelines share the same trends. Also, the values of Q in the SENT specimen are slightly higher than those of the corresponding pipeline models throughout the loading history (except at very low load levels as seen in Figure 7.18c, which would not have any practical applications). This is indeed in favor of conservatism, as higher constraint geometries would present lower toughness. Based on the constraint similarity between the SENT specimen and pipeline models, and also in consideration of the fact that the J-Q approach can effectively characterize the near tip fields in both SENT specimens and the cracked pipeline, the suitability of SENT specimens for integrity assessment of pipelines subject to extreme plastic bending is justified.

7.4.4 The J-$CTOD$ Relationship in Cracked Pipelines

As a finale to this study, the J-$CTOD$ relationship under extreme plastic bending is discussed. Here, we incorporate the usual definition of $CTOD$ [33]; that is, the opening of the crack flanks with intersection of 45° rays emanating from the crack tip in the deformed configuration. An example of the deformed crack tip and the $CTOD$'s schematics are shown in Figure 7.20 for Model#6, along with the contours of normalized Mises stress (σ_e/σ_y), which showcase the very high stress gradients in near the crack tip region.

While d in Equation (7.6) showed strong dependence on negative values of Q, as evident in Figure 7.4b, the same does not hold true for the case of cracked pipelines. A plot of d as a function of ε_g is presented in Figure 7.21 for all the 12 cases outlined in Table 7.1. The main factor controlling d is the strain hardening index, n, while the variations in d caused by the crack geometric factors a and $2c$ are only minimal and with no clear trend, as manifested by the close scatter of data for a specific n.

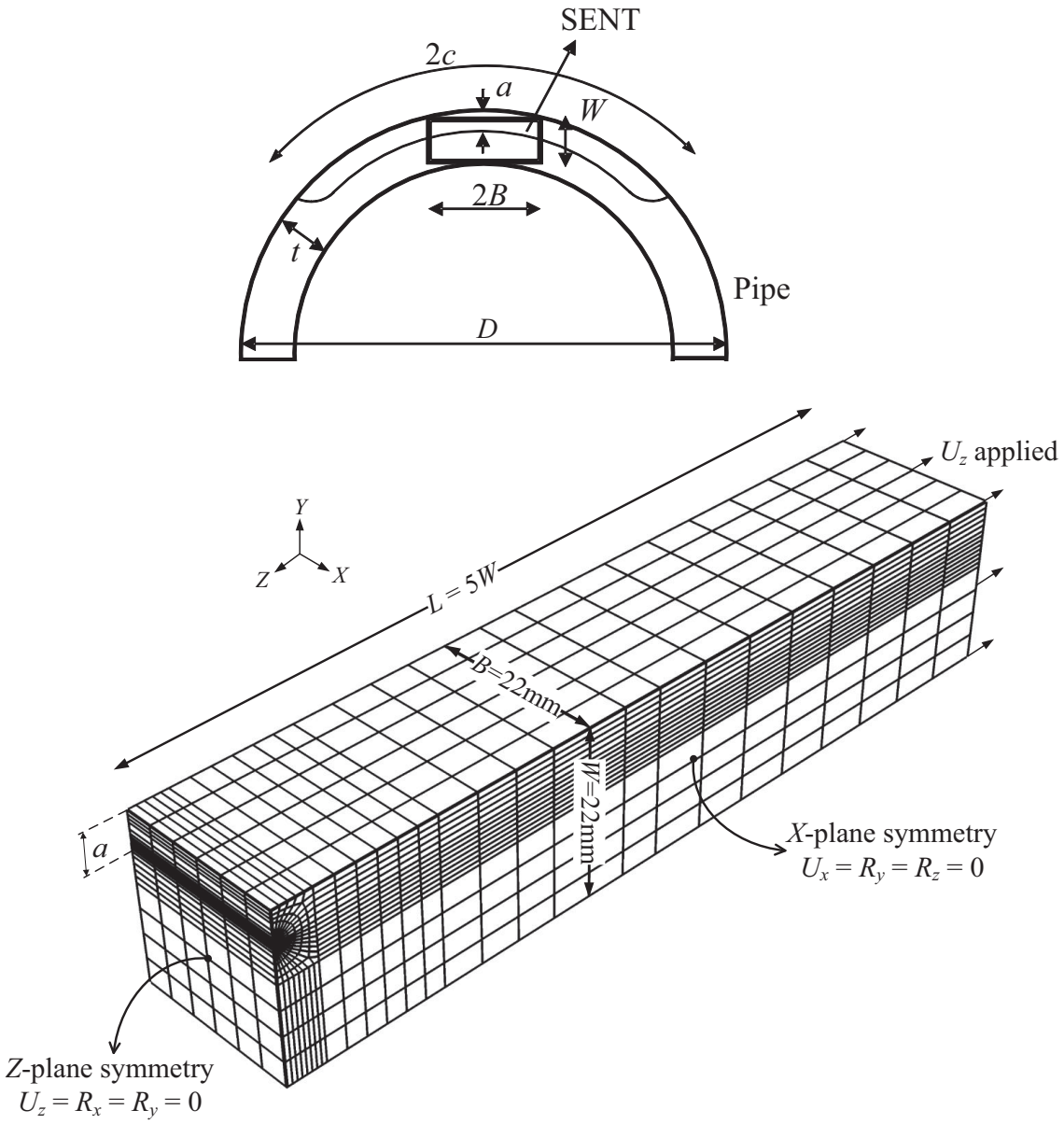

Figure 7.18. Schematic representation of the SENT specimen in relation to the cracked pipeline as per DNV guidelines [9] **(Top)** and quarter symmetric FE model of the SENT specimen **(Bottom)**.

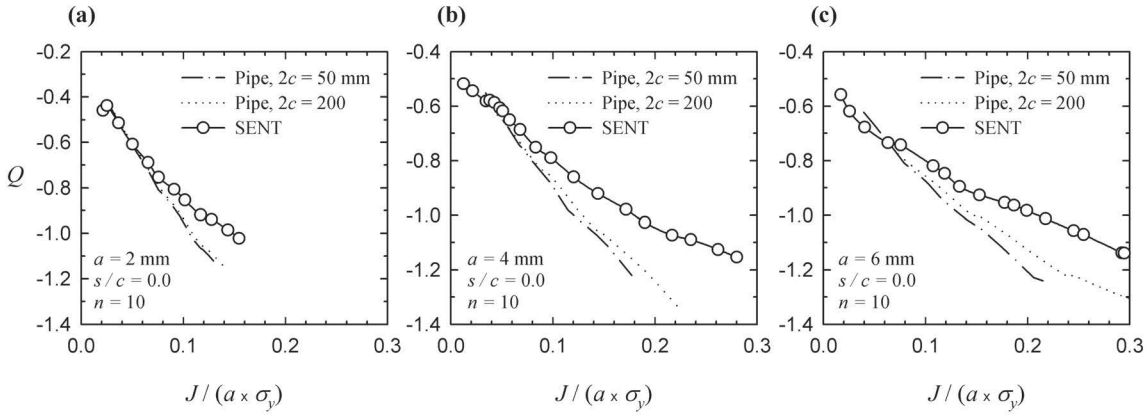

Figure 7.19. Comparison of the Q in the SENT specimen and cracked pipeline models for material with $n = 10$; **(a)** $a = 2$ mm, **(b)** $a = 4$ mm and **(c)** $a = 6$ mm.

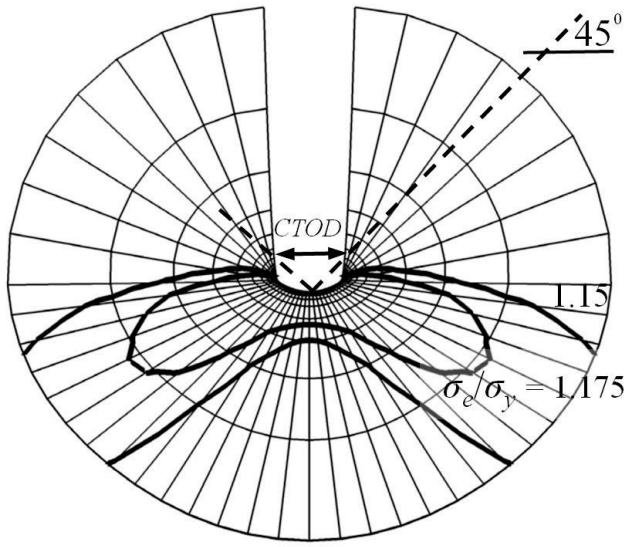

Figure 7.20. Plot of the near crack tip deformation and contours of the normalized Mises stress (σ_e/σ_y) for pipeline Model#6 at a global strain of $\varepsilon_g = 2\%$ (crack center, $s/c = 0$). $CTOD = 0.327$ mm, $J/\sigma_y = 0.482$ mm, $d = 0.67$ (the undeformed radius of annular zone is $3.24 \times J/\sigma_y$).

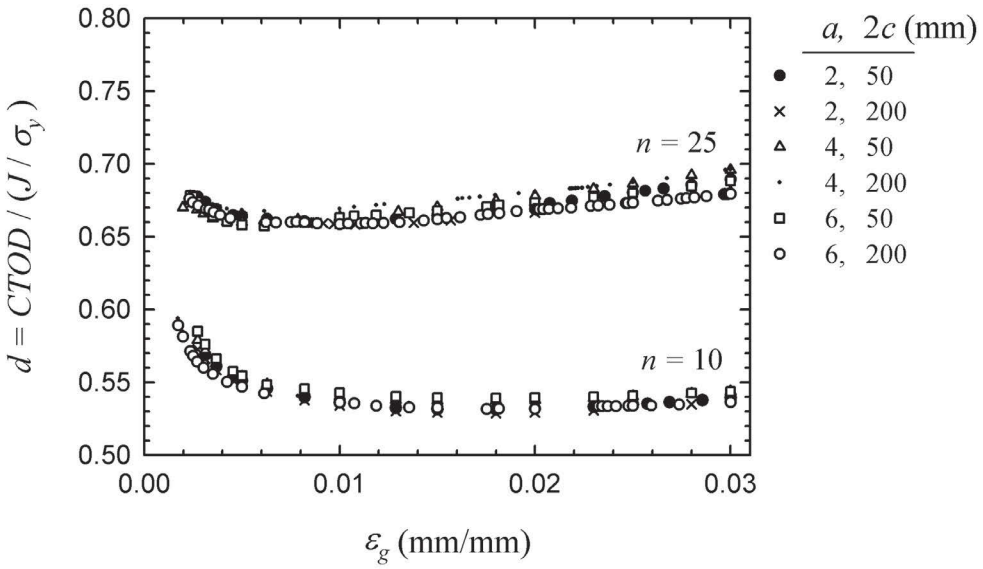

Figure 7.21. Crack tip coefficient, d, as a function of ε_g for all cracked pipeline models.

furthermore, after the initial elastic loading is surpassed, d becomes rather constant and independent of ε_g. It should be noted that a very slight increase of d with ε_g, more evident for $n = 25$ data is observed. However, the variation is much milder to be associated with the loss of constraint due to loading increase.

It is recommended that for practical applications and in the strain range of interest (i.e. $1\% < \varepsilon_g < 3\%$), an average value, independent of loading and crack size, could be considered, namely, $d = 0.54$ and 0.68 for the material with $n = 10$ and 25, respectively (theoretically, $d = 0.50$ for the idealized HRR plane strain case [33]). Moreover, representation of d as a function of Q enables a consistent comparison of the results with those of the MBL, as presented in Figure 7.22. In both the MBL models with $n = 10$ and 25, d increases very rapidly as Q decreases (and load increases), while the same does not hold true for actual pipelines. Actually, this is not an unexpected outcome; it should be noted that the J-Q theory characterizes an annular near tip zone bounded by $|\theta| < \pi/2$, while, $CTOD$ and thus d, are related to the crack flank deformations (i.e. at $\theta = \pm\pi$), which are not described by the J-Q formulation. In summary, while Q decreases rapidly with increased loading in cracked pipelines, this constraint loss does not significantly amplify d.

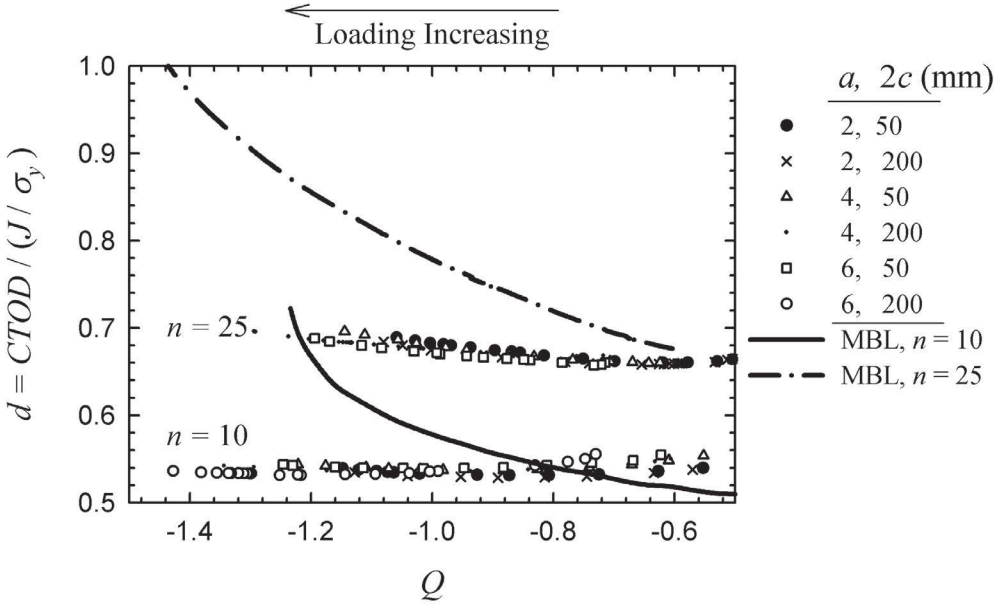

Figure 7.22. Comparison of crack tip coefficient, d, as a function of Q for cracked pipelines and MBL models.

7.5 Concluding Remarks

Using a series of fully nonlinear 3D Finite Element models, the fracture mechanics characteristics of a range of cracked pipelines with different geometric features and material properties relevant to oil and gas pipeline practice were investigated. Utilizing the framework of the two parameter J-Q fracture theory, it was revealed that the near tip stress and strain fields in such pipelines are analogous to those generated with the MBL model, up to severe bending moments causing a global strain as high as 3%, which is usually experienced by pipeline during reeling operations. This analogy was seen to exist between various stress and strain tensor components, both qualitatively and quantitatively. Based on the observed near tip field-matching between the cracked pipeline and the MBL model, it is concluded that the J-Q theory could be effectively and confidently incorporated for integrity assessment of such pipelines.

The near tip constraint of cracked pipelines, in terms of Q, was generated based on the computational results. Moreover, a simplified equation, representing the parameter Q as a linear function of the global bending strain, was developed and proposed.

Our observations indicated that Q in such pipelines could vary between –0.4 to -1.4. Thus flawed pipelined under extreme inelastic bending could be categorized amongst *low constraint* geometries. Furthermore, similarity of the crack tip constraint between cracked pipelines under bending and that of SENT specimen was demonstrated. Finally, the *J-CTOD* relationship for cracked pipelines was examined. The dependence of the opening coefficient, d, to constraint was observed to be marginal, thus verifying that a constant value of d could be used in such pipelines during the plastic bending regime. It is believed that the presented research results provide confidence and justification for the application of constraint corrected ECA procedures for pipelines subject to extreme plastic bending in which LSY conditions prevail throughout the pipeline.

Acknowledgements

The financial support of the Atlantic Innovation Fund is gratefully appreciated.

Chapter 8

Ductile Crack Growth & Constraint in Pipelines Subject to Combined Loadings

Nikzad Nourpanah and Farid Taheri

Department of Civil and Resource Engineering, Dalhousie University, Halifax, Nova Scotia, Canada, B3J 1Z1.

Accepted for publication in Journal of Engineering Fracture Mechanics.

8.1 Abstract

An important failure mode of offshore pipelines is ductile fracture of the pipe wall triggered by a hypothetical welding defect. In this study, pipelines having various sizes of external part-through semi-circumferential cracks, subject to combined internal pressure and inelastic bending are considered. This is done to assess the response of pipelines during both their installation and operational conditions. Detailed 3D nonlinear finite element (FE) models of pipelines are developed. A row of elements ahead of the initial crack front are modeled using a voided plasticity material model, which enables simulation of crack growth and the subsequent fracture failure mode (denoted by the critical curvature, κ_{crit}). After discussing the typical response characteristics of such pipelines, the FE model is used to parametrically investigate the effect of varying pipe and crack dimensions and also the internal pressure levels on κ_{crit}. In the second part of this paper, the crack tip constraint ahead of a growing crack in such pipes is evaluated and systematically compared to the crack tip constraint of both the traditionally used deeply cracked Single Edge Notch Bend (SENB) specimens and the constraint-matched Single Edge Notch Tensile (SENT) specimens. This is achieved by comparing the crack resistance curves (R-curves) along with stress triaxiality and equivalent plastic strain fields evaluated ahead of a growing crack of the three systems. The results present grounds for justification of usage of SENT

specimens in fracture assessment of such pipes as an alternative to the traditional overly conservative SENB specimens.

Keywords: Pipelines, Fracture failure mode, Combined Loading, Ductile Crack Growth, Crack Tip Constraint

8.2 Introduction

Currently, the design philosophy of offshore oil and gas pipelines as manifested in major design codes is based on the limit state approach [2, 3]. In this approach, each potential failure mode of the pipeline (such as bursting, local and global buckling, ovalization, fracture and etc.) are investigated separately. A pipeline could be frequently subjected to bending (both during the installation and operation), often combined with internal pressure, in turn causing a biaxial stress state in pipe's wall. A great number of these loading conditions are categorized as *displacement controlled*, thus providing the grounds for safely utilizing the plastic deformation capacity of the pipeline, as has been foreseen within the so-called Strain Based Design (SBD) approach [13].

The classical approach to assess a pipeline against the fracture failure mode (triggered by a welding flaw, and generally termed a crack), consists of two stages. First, the crack driving force in the structure (in terms of J or $CTOD$ for elastic-plastic regime relevant to SBD) is estimated. Subsequently, this value is compared with the materials fracture toughness (J_c or $CTOD_c$). A more detailed approach would involve a ductile tearing analysis in which the R-curve (describing the variation in fracture toughness of the material as a function of crack growth) is utilized to demonstrate the amount of stable crack growth.

The DNV offshore standard [2], and also the DNV guidelines on fracture assessment of reeled pipelines [9], both refer mainly to BS 7910 [8] for assessment of the fracture failure mode. The main crack driving force equation of BS 7910 [8] is based on the reference stress approach of Ainsworth [36] and the further improvements proposed by Milne et al. [40]. Note that the reference stress approach itself is an extension and simplification of the Electric Power Research Institute method [35].

Recent advancement of the topic includes the alternative assessment schemes developed by Østby [50], Tkaczyk et al. [51] and Nourpanah and Taheri [125] among the others. For combined loading scenarios, Jayadevan et al. [120], Østby et al. [47] and Gordon et al. [128] have shown that the addition of internal pressure to the primary tensile or bending load could substantially increases the crack driving force.

As an alternative to the above mentioned crack driving force estimation schemes, which mostly consider a stationary crack, it is possible to explicitly model the crack growth using detailed FE models. In such an approach, the critical or failure state of the pipeline would be manifested as a rapid loss of load bearing capacity of the structure. A well established numerical methodology to model the ductile crack propagation phenomena in a structure is to incorporate the voided plasticity material model often referred to as the Gurson-Tvergaard-Needleman (GTN) material model, due to Gurson [84], who originally developed the model, and also Tvergaard and Needleman [89], who later modified it. Several researchers [91, 96–99] have demonstrated the applicability and robustness of such a computational model for predicting the response of laboratory-size specimens undergoing ductile crack growth. In the context of pipelines subject to large plastic deformations, recent research by Sandvik et al. [100] and Dybwad et al. [101] both presented comparison of full scale test results on pipelines to predictions of nonlinear FE models (utilizing the GTN material model to accommodate ductile crack growth), showing satisfactory agreement. In the first part of the present paper, such a FE model is incorporated to systematically investigate the effect of a variety of different parameters, including the crack size and pipeline geometrics along with biaxial loading effects on the critical curvature of the pipeline.

The fracture assessment route also involves determination of material's fracture toughness and/or R-curve from laboratory-size specimens. Traditionally, high constraint laboratory specimens such as the Compact Tension (CT) or Single Edge Notch Bend (SENB) with deep cracks ($a/W \leq 0.5$) were recommended [75]. These configurations result in the lower bound fracture toughness of the material, with the uncracked ligament undergoing brittle fracture. The choice of high constraint laboratory specimens is irrespective of the actual constraint of the flawed structure under assessment.

Recently there has been an increased interest to provide the grounds for use of the so-called *constraint matched* specimens (i.e. a specimen with the same crack depth as in the actual structure) for the assessment and thus minimizing the excessive conservatism, as recommended in ref. [9]. For instance, the two-parameter J-Q fracture theory of O'Dowd and Shih [67, 68] has been incorporated in a number of studies on stationary cracks, and it has been successfully demonstrated that the constraint-matched Single Edge Notch Tensile (SENT) specimen can provide similar constraint to pipelines having a circumferential crack subject to bending (and internal pressure) up to extreme plastic deformation levels [78, 103, 126].

However, to the best of our knowledge, no generally accepted constraint theory exists for characterizing the near tip stress and deformation fields ahead of a propagating crack. Thus, the constraint match proved for stationary cracks can only be heuristically argued to hold for growing cracks. In contrast, a more direct approach can be incorporated as an alternative. The above mentioned FE model, which could effectively capture ductile crack growth by utilizing the GTN material model, could be used to determine the R-curves of the cracked pipeline and that of the corresponding constraint-matched SENT specimen along with the traditionally used deeply cracked SENB specimen. A comparison of the respective R-curves of these geometries would demonstrate the constraint similarity/match, and the suitable laboratory specimen for fracture toughness testing could be determined. Such an approach has been undertaken by Cravero et al. [103], who compared the R-curves of constraint matched SENT specimens with plates subject to biaxial loading (as a simplification of a pipe subject to combined loading). Xu et al. [104] also considered 2D SENT specimens and pipelines subject to tension and internal pressure with a full circumferential crack (thus enabling the use of 2D axisymmetric FE models), and again demonstrated the suitability of the constraint matched SENT specimen.

In the second part of this paper, 3D FE models of pipelines with realistic crack shapes and dimensions, subject to relevant loading scenarios are analyzed, and the suitability of the constraint matched SENT specimens are discussed via the R-curve approach.

8.3 Background and Numerical Procedures

8.3.1 The GTN Voided Plasticity Material Model

The ductile crack growth phenomenon is a result of void nucleation, growth and coalescence. McClintock [81], and Rice and Tracey [82] showed that the growth rate of a single void in an infinite continuum is an exponential function of the stress triaxiality, σ_m/σ_e. Gurson [84] considered a continuum (matrix) which contained an initial void. Using an upper bound approach, he showed that the yield potential of such a material could be approximated by the following function:

$$\Phi(\sigma_e, \sigma_m, \sigma_f, f) = \left(\frac{\sigma_e}{\sigma_f}\right)^2 + 2q_1 f \cosh\left(\frac{3q_2\sigma_m}{2\sigma_f}\right) - \left(1 + q_3 f^2\right) = 0 \qquad (8.1)$$

The first term on the RHS of Equation (8.1) is the usual J_2-plasticity yield loci, while the second and third terms introduce the effect of voids and their growth due to the mean stress σ_m. For a non-porous material (i.e. $f = 0$), the function capitulates to the J_2-plasticity yield potential. In this study, the uniaxial stress–strain curve of the matrix material has been assumed to follow a piecewise power-law, described mathematically by:

$$\varepsilon = \begin{cases} \sigma/E & \text{for } \sigma \leqslant \sigma_y, \\ \varepsilon_y \left(\sigma/\sigma_y\right)^n & \text{for } \sigma > \sigma_y. \end{cases} \qquad (8.2)$$

In Gurson's original analysis [84], it was assumed that $q_1 = q_2 = q_3 = 1$, while Tvergaard [85] showed that by setting $q_1 = 1.5$, $q_2 = 1.0$ and $q_3 = q_1^2$, a better fit to the experimental data could be achieved. These values have been widely used in the literature when using the GTN model. However, more recently, Faleskog et al. [86] showed that the value of q_1 and q_2 would depend on both n and σ_y/E and presented tabulated values of the q_1 and q_2 coefficients accordingly.

Upon the application of load, the void volume fraction, f, would increase, both due to enlargement of the existing voids, and also, to a lesser extent, due to nucleation of new voids. Thus the rate of void volume fraction increasing would be:

$$\mathrm{d}f = \mathrm{d}f_{gr} + \mathrm{d}f_{nucl} \qquad (8.3)$$

In reference to the incompressible plastic flow of the matrix material in the GTN model, the growth rate of the existing voids would read:

$$\mathrm{d}f_{gr} = (1 - f)\ \mathrm{d}\varepsilon^{p}_{ii} \tag{8.4}$$

Needleman and Rice [87] have proposed an empirical equation to approximate the void growth rate caused by nucleation of new voids as a function of mean and flow stress rates and equivalent plastic strain rate[1]:

$$\mathrm{d}f_{nucl} = A_1\,\mathrm{d}\varepsilon_p + A_2(\,\mathrm{d}\sigma_f + \,\mathrm{d}\sigma_m) \tag{8.5}$$

Assuming a normal distribution for the rate of void nucleation intensity, Chu and Needleman [88] expressed A_1, for strain controlled nucleation (i.e. when $A_2 = 0$), as:

$$A_1 = \frac{f_n}{s_n\sqrt{2\pi}} \exp\left[-\frac{1}{2}\left(\frac{\varepsilon_p - \varepsilon_n}{s_n}\right)^2\right] \tag{8.6}$$

while for stress controlled nucleation (where $A_1 = 0$), A_2 would read:

$$A_2 = \frac{f_n}{s_n\sqrt{2\pi}} \exp\left[-\frac{1}{2}\left(\frac{\sigma_f + \sigma_m - \sigma_n}{s_n}\right)^2\right] \tag{8.7}$$

where ε_n and σ_n are the mean nucleation strain and stress, respectively, and s_n is the standard deviation.

A material whose plastic flow could be described by Equation (8.1), can be used to model ductile crack growth. However, the assumption that neighboring voids do not interact is implicit in such an approach. On the contrary, the final phase of an increment of ductile crack growth includes necking of the matrix between two neighboring voids, leading to the final coalescence. This last phase is marked by a rapid loss of stress carrying capacity of the element. To account for these effects, Tvergaard and Needleman [89] introduced a modification to the original Gurson yield potential. They suggested using f^* instead of f in Equation (8.1), defined as:

$$f^* = \begin{cases} f & \text{for } f \leqslant f_c, \\ f_c + \dfrac{f^*_F - f_c}{f_F - f_c}(f - f_c) & \text{for } f_c < f < f_F, \\ f^*_F & \text{for } f \geqslant f_F. \end{cases} \tag{8.8}$$

[1]Needleman and Rice [87] proposed Equation (8.5) for stress controlled situations, thus without the $A_1\,\mathrm{d}\varepsilon_p$ term. The presented form of Equation (8.5) can be found in Ref. [94]

where $f_F^* = (q_1 + \sqrt{q_1^2 - q_3})/q_3$ (keeping in mind that when $q_3 = q_1^2$, it is seen that $f_F^* = 1/q_1$). The void volume fraction at initiation of void coalescence is denoted by f_c, while f_F represents the void volume fraction at final fracture where the stress carrying capacity of the element vanishes.

8.3.2 The Cell Model Approach

One approach to simulate ductile crack using the GTN material model is to model the whole structure with such a material; as such, the crack propagation direction will also be governed by the model. However, in a series of papers, Xia and Shih [93–95] stated that a more feasible modeling approach could be achieved by using the GTN material definition to describe only the region corresponding the initial crack plane, ahead of the crack tip (the so-called row of voided cells), while using a conventional elasto-plastic material model to model the remainder of the body. This approach was supported by experimental data of ductile crack growth in most metals that exhibit a planar propagation path. They further stated that the size of the GTN elements (D_0) used to model the crack front should be in the micro-level order, thus roughly representing the average spacing between large inclusions (voids) in the material, ahead of a crack. In other words, each element ahead of the crack is assumed to contain a single void. With this modeling approach, the crack tip element would go extinct once its void volume fraction reaches f_F, thus the crack would grow an increment equal to D_0. This process would continue till the final failure stage.

Moreover, it was shown [94] that the contribution of void nucleation (due to the second phase particles) to the void volume fraction increase could be neglected, and $\mathrm{d}f$ could be assumed to be driven by the growth of the existing voids (i.e. $\mathrm{d}f = \mathrm{d}f_{gr}$ and $\mathrm{d}f_{nucl} = 0$, see Equation (8.3)). This simplification is extremely convenient, as the void growth rate due to nucleation (Equations (8.5), (8.6) and (8.7)) are still under debate. The *cell model* approach has been experimentally verified [97], and also Ruggieri et al. [96] extended the approach to model 3D cracks in different specimens. Their results showed good agreement with their experimental data. The *cell model* approach is therefore incorporated in the 3D FE analysis in the present study.

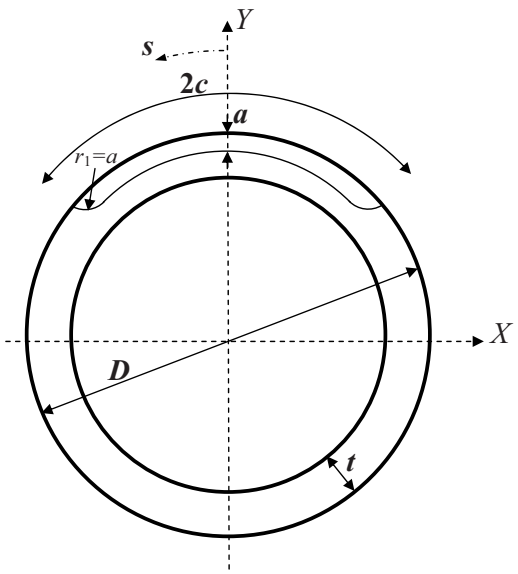

Figure 8.1. Schematic of the cracked pipeline cross section.

8.3.3 FE Modeling

The ABAQUS general FE software [10] was used in this study. 3D models of pipelines were constructed, having a semi-circumferential external part-through canoe shaped crack at their 12 O'clock position. Figure 8.1 shows the cross section of the pipe at the crack location and the canoe shape of the crack front, with its fillet radius equal to the crack depth. The considered crack shape is representative of real weld flaws observed in offshore pipelines [47, 120]. The pipeline is subjected to combined bending and internal pressure. The loading sequence consists of two steps, with the pipe undergoing internal pressure first, and bending in the second step, thus following a realistic loading scenario [47, 120].

In all models, the pipeline has a wall thickness of $t = 20$ mm. Pipelines with a D/t ratio of 10 to 60, a crack depth of $a = 2 \sim 6$ mm ($a/t = 0.1 \sim 0.3$) and crack length of $2c = 50 \sim 250$ mm have been considered. The considered crack depths cover the range of practical interest, as the weld pass height governs the flaw sizes in girth welded pipelines, which is typically $2 \sim 6$ mm in height [9]. Following the internal pressure-hoop stress relationship of $p(D/t - 1) = 2\sigma_h$, various magnitudes of internal pressure causing hoop stress of up to 75% of the yield stress ($\sigma_h/\sigma_y = 0.75$) were considered. Moreover a tensile force corresponding to the so-called end-cap effect

was applied to pipe's ends. The force was calculated by [2]: $T_{EndCap} = {}^1\!/\!_4\pi p(D-t)^2$. Application of the end-cap tension is necessary in a bending analysis involving large rotations; otherwise the extracted moment would be different at each location along the pipeline length [47].

A double symmetric FE model of the pipeline with a length of $L = 2D$ has been considered (see Figure 8.2[3]), which has been shown to be of sufficient length to capture the response discontinuity caused by the crack [125]. A single layer of elements containing the initial crack front profile have the GTN material definition with element size of ${}^1\!/\!_2 D_0$ (due to symmetry). D_0 was selected as $200\mu m$, as has been incorporated in similar studies by other researchers [97, 100, 101]. The rest of the model has the conventional elasto-plastic (i.e. no-damage) material definition. A mesh transition region shown in Figure 8.2 (Right) was included in the mesh to achieve the fine ${}^1\!/\!_2 D_0 \times {}^1\!/\!_2 D_0$ element mesh (in the Y-Z plane) of the voided (GTN) cells. A more descriptive view of the initially sharp crack tip and the arrangement of the GTN elements is illustrated in Figure 8.5a. Xia et al. [97] showed that both the initially sharp and blunt crack tips produce very similar R-curves after the first few increments of crack growth has taken place. Depending on the specific crack and pipe geometrics, the FE mesh consisted of 43,000-55,000 C3D8R elements (a 3D continuum element with 8 nodes, reduced integration and hour-glass control features [10]).

The pipe-end cross-section rotation was controlled by a master node, such that the cross section was constrained to remain plane (Euler bending), but free to ovalize. A Multi-Point Constraint was used to enforce such conditions, with the following relationship:

$$\tan R_x = \frac{z_j - z_{\text{mn}}}{y_j - y_{\text{mn}}} \tag{8.9}$$

where y_j and z_j are the coordinates of the j^{th} node located on the pipe-end cross-section and y_{mn} and z_{mn} are the coordinates of the master node (see Figure 8.2), following the deformed pipe configuration. It is understood that as the plastic deformation increases, the Euler assumption would not strictly hold; however, the resulting error has known to be insignificant [119]. The application of bending was done

[2]Regarding the doubly-symmetric pipeline FE model as will be discussed later, half of this value of T_{EndCap} is applied to the model.

[3]The presented Figure 8.2 is slightly more detailed than that submitted to the journal.

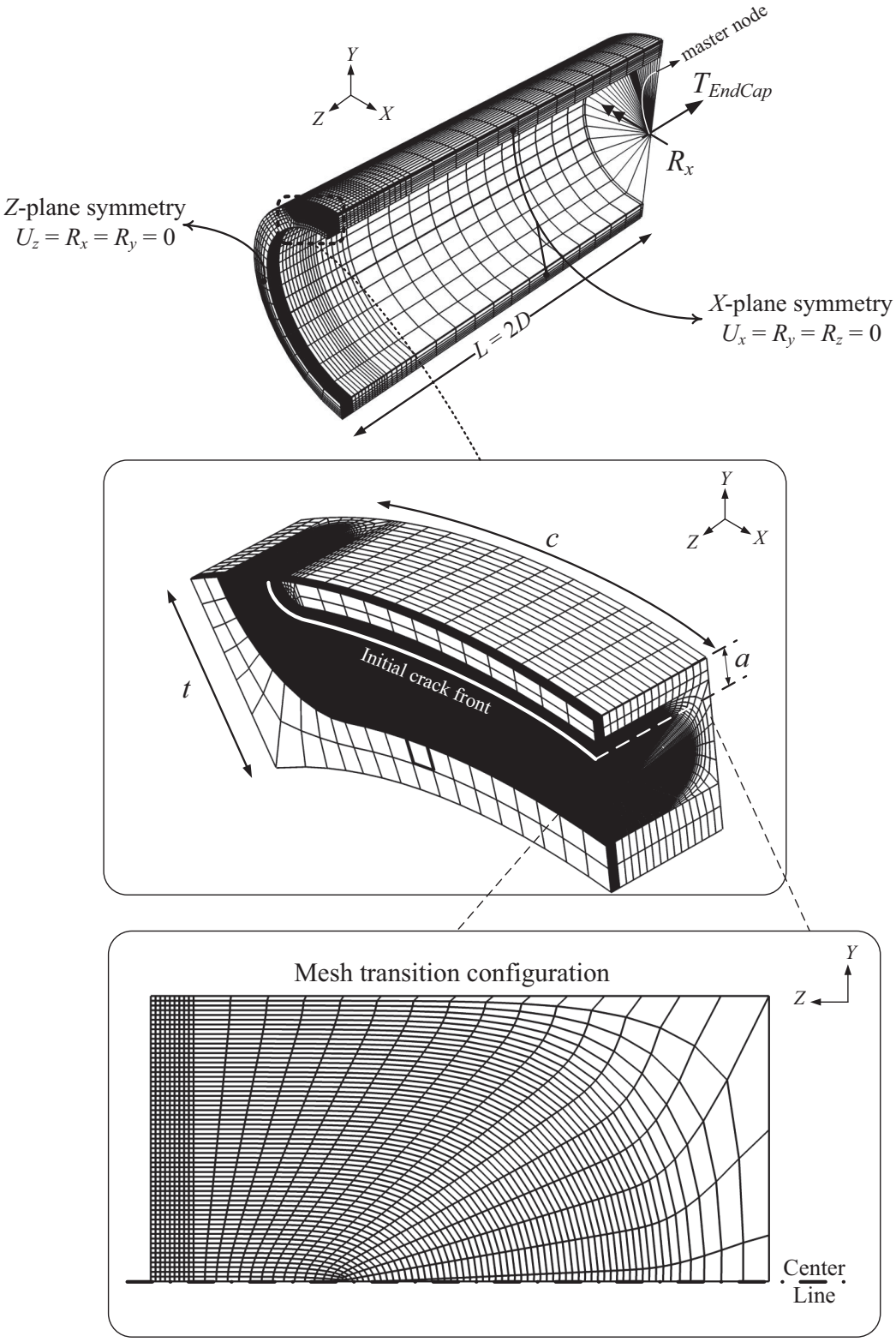

Figure 8.2. FE mesh of the pipeline and close-ups of the cracked region and the mesh transition arrangement.

by increasing the rotation of the master node in each model until a decline in the moment-curvature (M-κ) curve was observed, indicating the fracture failure. All the pre-processing tasks, including generation of the complicated mesh were performed with in-house developed Python scripts, which significantly expedited the parametric study[4].

The nonlinear geometric effect (NLG) was accounted for in all models in order to accurately model the blunting of the crack tip, the severe plastic deformation of the voided GTN elements ahead of the crack tip, and also the large rotation imposed on the pipeline through the master node. For modeling the response of the background material (the undamaged elasto-plastic media) and also the matrix of the GTN material, the rate-independent associated J_2 incremental plasticity theory with a Mises plastic potential and isotropic strain hardening features was considered. The material model followed the uniaxial true stress–strain relationship described by Equation (8.2). The ABAQUS formulates the equilibrium equations in an incremental form based on an updated Lagrangian framework. For treatment of elasto-plastic continua undergoing NLG, the rate of deformation is selected by ABAQUS as the strain measure, while the Jaumann rate of the Kirchhoff stress is employed as the suitable stress measure [10]. However, the Cauchy (true) stress and Logarithmic strains are reported as the output for convenience.

8.3.4 The Explicit Solution Procedure

The ABAQUS/Explicit [10] solver was used in this study. While the explicit solvers were initially developed for dynamic and impact problems, they can also be utilized to efficiently simulate quasi-static response. The ABAQUS/Explicit solver uses a central difference time integration scheme with 2^{nd} order accuracy, which is only conditionally stable. Therefore, very small time increments are required to satisfy the stability condition. Nonetheless, the explicit solution technique becomes advantageous by noting that each increment is computationally relatively *cheap*, as it does not require solution to a set of simultaneous equations and iterations (unlike the implicit solvers

[4]Detailed presentation and explanation of the Python scripts used in this chapter can be found in Appendix A.

such as the ABAQUS/Standard [10]). Furthermore, only the ABAQUS/Explicit has the capability to incorporate the failure criteria used in conjunction with the GTN material model. That is, the code considers the conditions set by Equation (8.8) and removes the voided element form the mesh when $f = f_F$ at the integration point of the element. Therefore, the incremental element removal explicitly models ductile crack growth.

The critical time increment (Δt_c) satisfying the central difference stability criterion is related to the maximum eigenfrequency of the system ($\omega_{\max}$), which by neglecting damping follows [129]:

$$\Delta t_c = 2/\omega_{\max} \tag{8.10}$$

Furthermore, it can be shown that $\omega_{\max} \leqslant \omega^e_{\max}$ [129], where $\omega^e_{\max}$ is the maximum eigenfreguency of an element in the system, thus

$$\Delta t_c \cong L_{\min}/c_d \tag{8.11}$$

in which $L_{\min}$ is the smallest element dimension in the mesh and cd is the dilatational wave speed across that length. The ABAQUS/Explicit assumes a hypoelastic material response and calculates c_d based on the effective Lamé constants [10]:

$$c_d = \sqrt{\frac{\hat{\lambda} + 2\hat{\mu}}{\rho}} \tag{8.12}$$

where $\hat{\lambda}$ and $\hat{\mu}$ are the first and second *effective* Lamé constants and ρ is material's density.

Considering Equation (8.11), it can be seen that for meshes involving very small element sizes (such as those customarily used for fracture mechanics modeling), Δt_c becomes very small and hence the computational cost might become prohibitive. To overcome this, one can artificially decrease the loading event time to achieve a shorter overall simulation period; however, the inertia effects have to be monitored to be minimal. The ABAQUS/Explicit offers a more robust and effective approach entitled *mass scaling*, which increases the material density ρ to achieve a larger Δt_c (see Equations (8.11) and (8.12)). Variable levels of mass scaling can be carried out for each element in the mesh (depending on their size) to achieve a uniform Δt_c (thus

the smallest elements would have the largest increase in their ρ and vice versa). In the present study, the variable mass scaling technique has been incorporated such that each loading step is solved with 200,000 increments (each step being 1 sec long), which resulted in a quasi-static response and lowered overall runtimes. Furthermore, the smooth amplitude function of the ABAQUS was used in each step to impose the loading (displacement) onto the structure. The amplitude function is represented by [10]:

$$amp = \xi^3(10 - 15\xi + 6\xi^2) \tag{8.13}$$

where ξ is the normalized step time (i.e. $\xi = 0$ at the beginning of each step and $\xi = 1$ at the end of the step). That is, at each instant in time (ξ_i) a fraction of $amp(\xi_i)$ of the load (i.e., R_x) is applied onto the pipe's end.

To verify the explicit scheme and assess its computational efficiency, a typical pipeline model was solved with both the ABAQUS/Explicit and ABAQUS/Standard solvers. The ABAQUS/Standard solver uses an implicit solution algorithm which is common for static simulations. The implicit model did not have the element removal feature and the rapid deterioration modification of Equation (8.8). The resulting M-κ curves are shown in Figure 8.3. The close agreement of the two solutions up to the critical point showcases that the dynamic effects in the explicit solution are minimal and the captured response can be deemed as quasi-static, thus justifying it for further use. The explicit solution runtime was approximately three times faster than the implicit one.

8.3.5 Material Properties

The background elasto-plastic (i.e. no damage) material model is defined by four parameters, namely E, ν, σ_y and n. On the other hand, the voided plasticity GTN material within the cell model (i.e., the damaged material) requires seven more parameters, which are: f_0, f_c, f_F, q_1, q_2, q_3, D_0 (these are in addition to the former four parameters, which describe the response of the matrix of the GTN material). Generally, the first three parameters of the GTN model are determined by fitting the characteristic load-displacement curve of a laboratory specimen to those obtained from FE simulations by a trial error approach (essentially, selecting various values

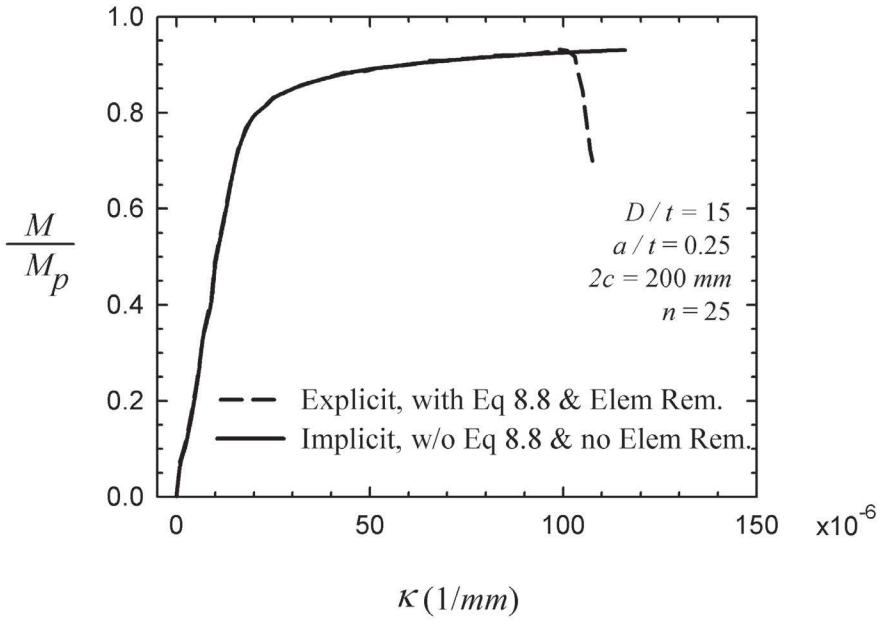

Figure 8.3. Comparison of the ABAQUS/Explicit and ABAQUS/Standard solutions ($\sigma_h/\sigma_y = 0$).

Table 8.1. Parameters describing the elasto-plastic and GTN material models.

E (GPa)	ν	σ_y (MPa)	n	f_0	f_c	f_F	q_1	q_2	q_3	$D_0(\mu m)$
200	0.3	400	25	0.0002	0.013	0.1504	1.678	0.975	q_1^2	200

of f_0, f_c and f_F, until the best match between the computational and experimental results is obtained [91]). In this research, the quantities obtained for the pipeline steels as reported in the literature are used [100, 101, 130]. Note that the assumption of $f_F = 0.15 + 2f_0$ used by Sandvik et al. [130] is in accord with the experimental observations of f_F as cited by Tvergaard and Needleman [89]. Furthermore, the data of Faleskog et al. [86] is used for determination of q_1 and q_2 (using $\sigma_y/E = 0.002$ and $n = 25$). All the material properties used in our study are reported in Table 8.1, which are believed to be descriptive of the response of a typical high strength offshore pipeline steel.

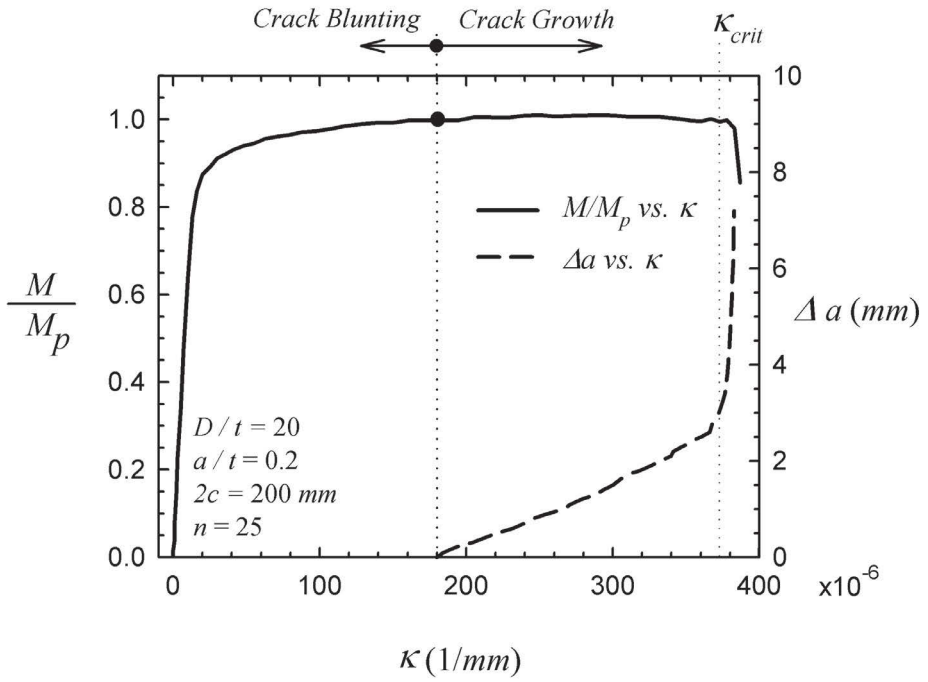

Figure 8.4. Typical M-κ and Δa-κ response of a cracked pipeline ($\sigma_h/\sigma_y = 0$).

8.4 Critical Curvature (κ_{crit}) of a Cracked Pipeline

8.4.1 Typical Response Characteristics

Figure 8.4 shows the typical M-κ response of a flawed pipe (solid line). Upon application of bending, the initially sharp crack tip starts to blunt, and at $\kappa_i \cong 180 \times 10^{-6}$ (1/mm), the first voided element at the crack tip reaches a void volume fraction of $f_F = 0.1504$ and is removed from the mesh, thus simulating the initiation of crack growth. At $\kappa_{crit} \cong 360 \times 10^{-6}$ (1/mm) a sudden drop in M is observed, which is due to the crack growing to an extent that the cross section loses its moment bearing capacity. Indeed, the dashed lines in Figure 8.4 (showing Δa as a function of κ on the right vertical axis), confirms the above mentioned postulation. As shown in the figure, $\Delta a = 0$ at κ_i and increases linearly as a function of κ and reaches approximately 2.5 mm at κ_{crit}, and subsequently a very rapid increase in Δa occurs, indicating the occurence of fracture failure. Furthermore, it is observed that $\kappa_{crit}/\kappa_i \cong 2$, indicating that crack growth influences the response through nearly half of the loading history.

Figure 8.5a shows the crack plane at the crack center ($s/c = 0$), at the unloaded situation, followed by extreme blunting prior to crack growth (Figure 8.5b), the initial ductile tearing (Figure 8.5c) and finally, accommodating a large amount of crack growth leading to failure of the pipe (Figure 8.5d). Figure 8.5e illustrates a 3D view of Figure 8.5d. It is observed from the figure that Δa is approximately constant along the crack front (s-coordinate). This feature is observed in other pipeline models too, and thus, the values of Δa at $s/c = 0$ is extracted and discussed hereafter.

Common FE meshes used to study stationary cracks would usually have a focused spider web pattern around the crack tip, which also facilitates the J-integral extraction. However, the FE meshes often used in modeling crack growth (e.g. Figure 8.2b and 8.5a), do not follow the mentioned meshing approach, and thus the extraction of the J-integral would lead to erroneous quantities. Therefore, in this study, the equally applicable $CTOD$ has been selected as the crack-tip characterization parameter (note that the $CTOD$ values are extracted from the node at a distance of D_0 from the initial crack tip node, as illustrated in Figure 8.5d). All the R-curves presented in the study thus describe the variation of $CTOD$ as a function of Δa. Figure 8.6 shows a typical R-curve, in which the raw FE data (dashed line) increases in a stepwise manner due to the fact that the smallest increment of crack advance is $\frac{1}{2}D_0$. However, once the raw data is smoothed, it follows a linear trend. This *smoothened* R-curve is further examined and discussed hereafter.

The void volume fraction ahead of the (current) crack tip for three values of Δa is shown in Figure 8.7 (the r-coordinate is shown in Figure 8.5e). At the *current* crack tip, $f/f_F = 1$ for all the three profiles and then it decreases very rapidly to f_0 over a few multiples of D_0. Thus, it can be argued that the fracture process zone in which the void growth mechanism is active spans only over a distance of $(2 \sim 3) \times D_0$, in accord with the observations made by other researchers [93]. Furthermore, the f/f_F profiles at all three levels of crack growth ($\Delta a = 0.2$, 1, 2 mm) are very similar, thus indicating the attainment of a steady state situation.

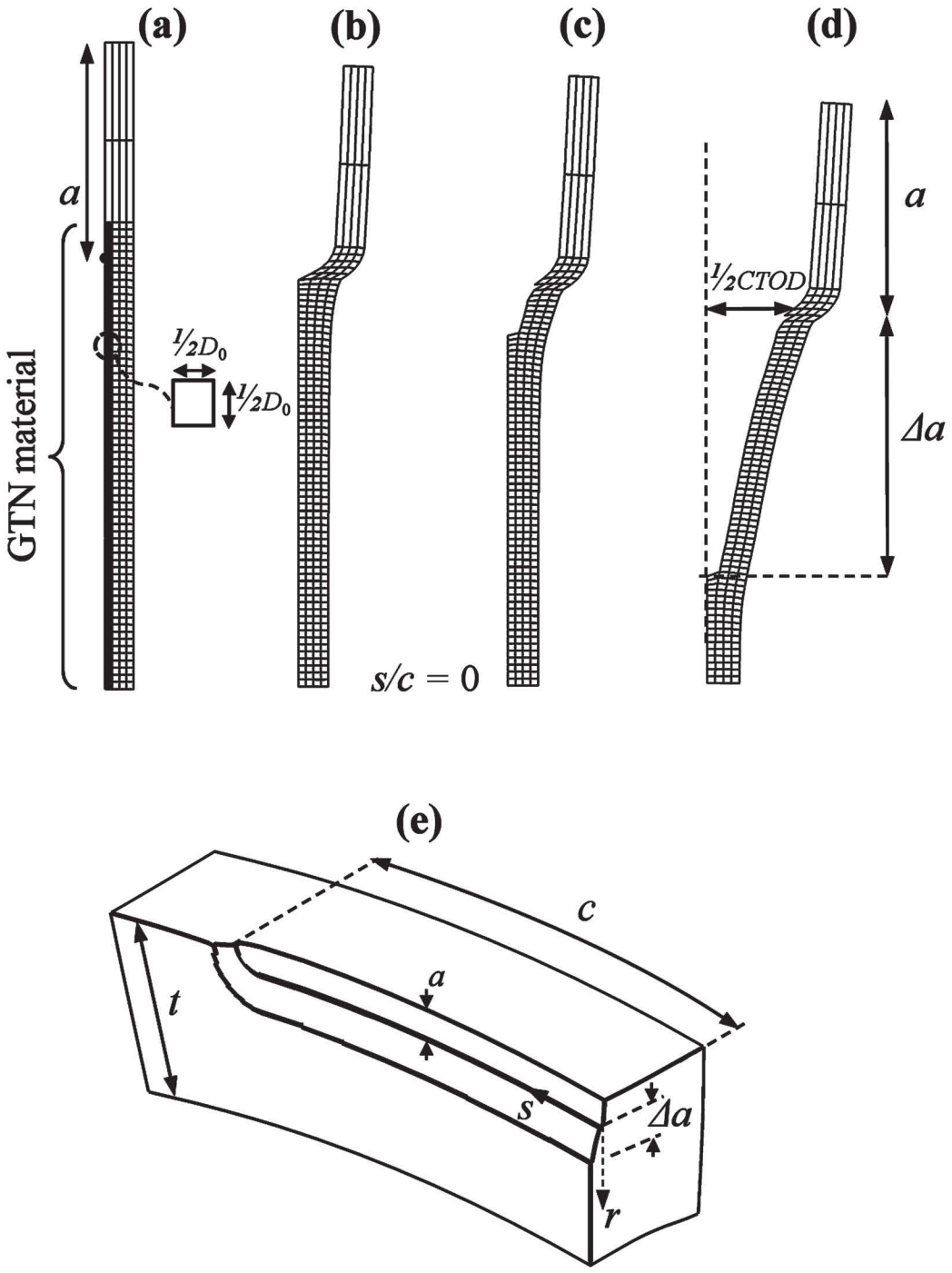

Figure 8.5. The crack plane ($s/c = 0$) at various levels of loading and crack growth **(a-d)**, and the 3D view of the cracked region **(e)**.

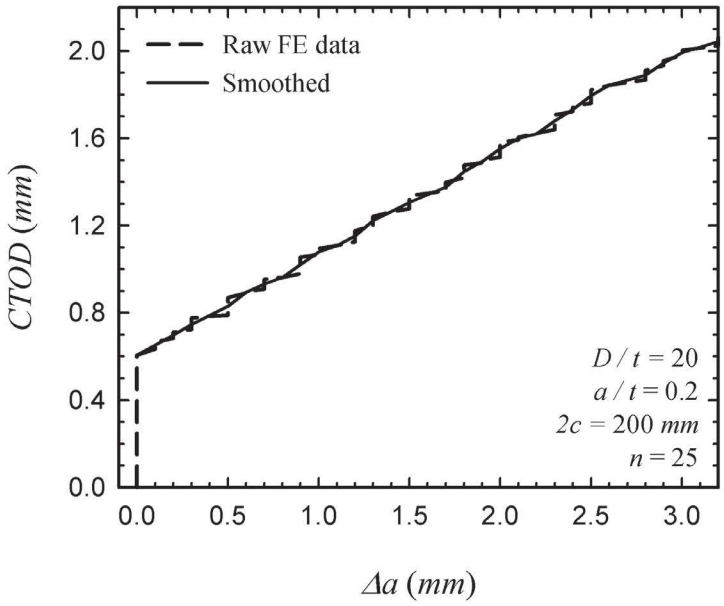

Figure 8.6. Typical R-curve of a cracked pipeline ($\sigma_h/\sigma_y = 0$).

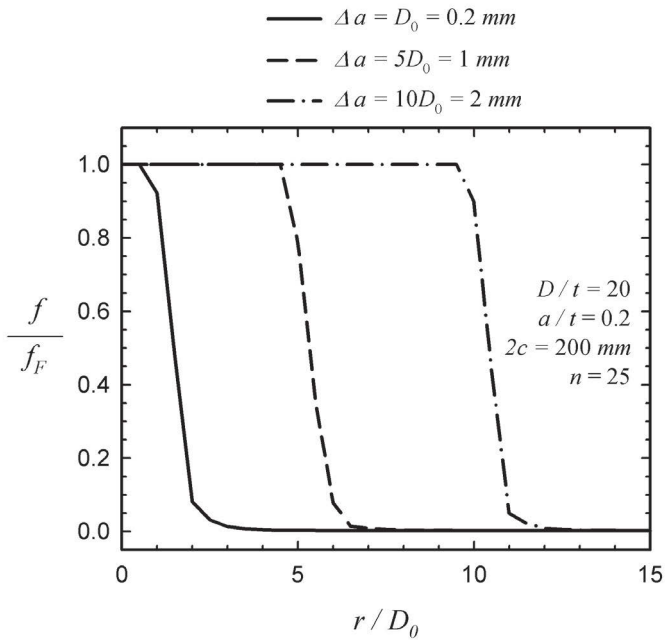

Figure 8.7. Typical distributions of f ahead of the growing crack at $s/c = 0$ in pipe ($\sigma_h/\sigma_y = 0$).

8.4.2 Parametric Study on the Critical Curvature (κ_{crit})

It is commonly agreed that for an unflawed pipeline subject to bending and internal pressure, the increase in σ_h/σ_y would decrease the moment capacity of the pipe, while the pipe could undergo larger curvatures prior to its local buckling failure [2, 3]. For a cracked pipeline, the larger values of σ_h/σ_y would increase the crack driving force [47, 128], thus it can be inferred that the fracture failure mode would also be promoted.

The M-κ curves for various values of σ_h/σ_y of a typical pipeline, are shown in Figure 8.8. The four solid curves for $\sigma_h/\sigma_y \geqslant 0.25$ correspond to the typical failure characteristics due to ductile crack growth and the subsequent fracture (e.g. sudden decrease in the moment capacity at the critical stage). For these four curves, increasing σ_h/σ_y would indeed reduce the maximum elastic attainable moment capacity, and more importantly, drastically reduce the value of κ_{crit}. For instance, for the $\sigma_h/\sigma_y = 0.25$ case, κ_{crit} is nearly three times larger than that for the $\sigma_h/\sigma_y = 0.75$ case. The same figure, illustrates that the two M-κ curves (dashed) corresponding to $\sigma_h/\sigma_y = 0$ and 0.125 do not exhibit the typical fracture failure characteristics. In those cases, the moment capacity decreases very gradually and the definition of a critical curvature becomes even rather ambiguous. It is believed that these two curves represent failure due to local buckling (i.e. excessive ovalization at the cracked cross section). A closer look at these two classes of responses, reveals that at their critical point, the pipes subject to $\sigma_h/\sigma_y \geqslant 0.25$ would have undergone large amounts of crack growth ($\Delta a \geqslant 4$ mm), while their ovalization would be relatively small ($\Delta D/D < 0.04$). On the other hand, the cases suspect to local buckling (which are subject to $\sigma_h/\sigma_y < 0.25$) undergo relatively small amounts of crack growth ($\Delta a \leqslant 0.4$ mm), while their ovalization is relatively more severe ($\Delta D/D > 0.07$). Furthermore, the local buckling failure cases manifest the expected effect of internal pressure. For example, the $\sigma_h/\sigma_y = 0.125$ case exhibits a larger κ_{crit} than the pipe undergoing pure bending ($\sigma_h/\sigma_y = 0$). The discussed transitional effect of the internal pressure on the failure mode is in agreement with the observed response of full scale experiments [131]. It should however be noted that no imperfection was introduced in the FE models, and the crack itself served as an imperfection to trigger the ovalization of the pipe at that location.

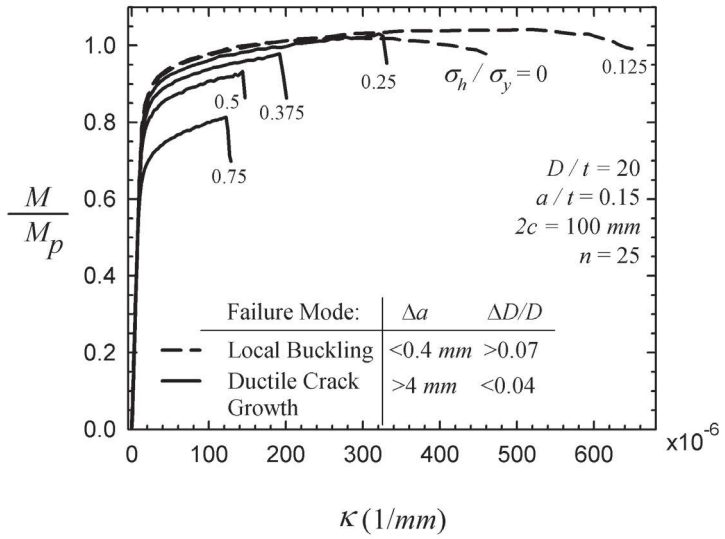

Figure 8.8. M-κ curves of pipelines subject to combined loading with various values of internal pressure (σ_h/σ_y).

While Figure 8.8 presented the response of pipes with $D/t = 20$, the same analysis was carried out to investigate the response of pipes with various D/t values, ranging from 10 to 60 (i.e. covering thick-wall pipelines usual for reeling applications as well as large diameter ones used as trunk lines). The results are presented in Figure 8.9, showing the variation of κ_{crit} as a function of σ_h/σ_y for a family of D/t values. The open symbols indicate that the failure mode was due to ductile fracture, while the solid symbols indicate a local buckling/ovalization failure mode. As for the fracture failure mode, it can be observed that κ_{crit} decreases steadily as σ_h/σ_y increases, however an asymptotic behavior is observed for $\sigma_h/\sigma_y > 0.375$. As observed in Figure 8.8, for lower values of σ_h/σ_y (< 0.25), ovalization governs the failure mode. A maxima is observable in each curve, which indicates the threshold value of σ_h/σ_y, which distinguishes the fracture and ovalization behavioral regimes. The threshold value seems to be a weak function of D/t. For the considered crack size ($a = 3$ mm, $2c = 100$ mm) the threshold value is determined to be at approximately $\sigma_h/\sigma_y \approxeq 0.125$. Furthermore, the effect of σ_h/σ_y on κ_{crit} is seen to be more pronounced for thick-wall pipelines ($D/t = 10$, 15, 20).

The M-κ curves for a family of crack depths are presented for two different values of

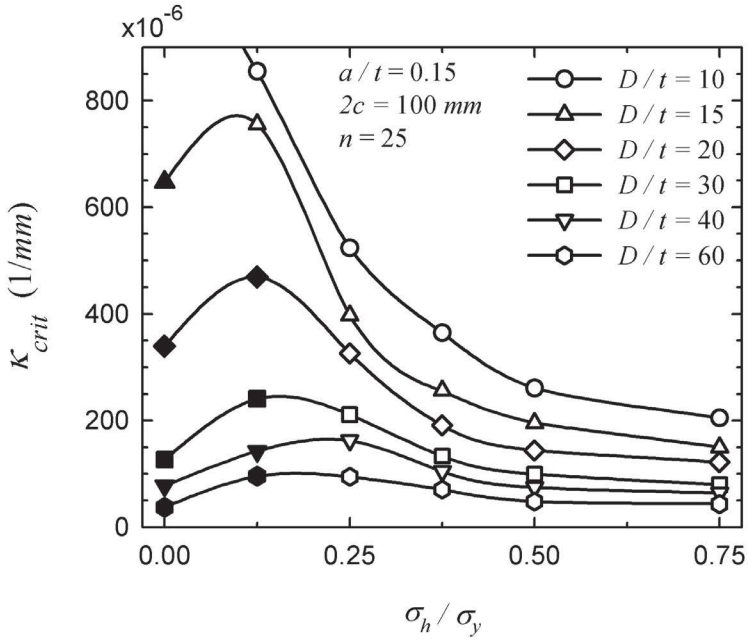

Figure 8.9. The effect of σ_h/σ_y on κ_{crit} for a family of D/t values (open symbols indicate a fracture failure mode and solid symbols indicate a local buckling failure mode).

internal pressure in Figure 8.10. For the $\sigma_h/\sigma_y = 0.25$ family of curves, the shallowest crack considered ($a/t = 0.1$) does not trigger the fracture failure mode, and the ovalization of the cross section governs the response. However, for larger crack depths ($a/t \geqslant 0.15$) the characteristic sudden drop in moment capacity due to excessive crack growth is observed. For both levels of σ_h/σ_y shown, the pipes with the largest crack ($a/t = 0.3$) exhibit very limited plastic deformation capacity and the fracture failure occurs very soon after the elastic regime is finished. The effect of σ_h/σ_y is also evident on decreasing both the proportional limit moment and also κ_{crit} (note that the critical curvature of the pipe with $a/t = 0.15$ decreases by 50% when σ_h/σ_y increases from 0.25 to 0.75).

The same parametric study was carried out for a wider range of σ_h/σ_y and the resulting κ_{crit} values as a function of a/t are summarized in Figure 8.11. As seen, κ_{crit} decreases very rapidly as a function of a/t. However, the curves start converging to an asymptote for $a/t \geqslant 0.2$. Furthermore, the variation in κ_{crit} seem to become independent of the internal pressure level for $\sigma_h/\sigma_y \geqslant 0.5$ and $a/t \geqslant 0.2$. The critical curvature for all levels of internal pressure is nearly identical for the pipelines with

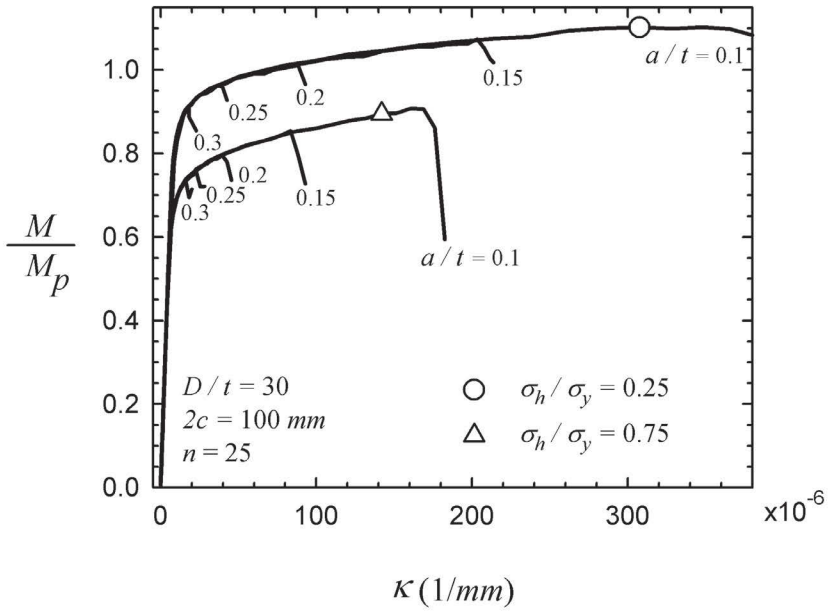

Figure 8.10. M-κ curves for a family of a/t values and at two levels of σ_h/σ_y.

the deepest crack ($a/t = 0.3$).

Figure 8.12a shows M-κ curves corresponding to different (initial) crack lengths, ranging from $2c = 50$ mm to 250 mm for an internal pressure level of $\sigma_h/\sigma_y = 0.25$, while Figure 8.12b is for $\sigma_h/\sigma_y = 0.75$. For both cases, the negative effect of longer cracks on decreasing the critical curvature is observed. Figure 8.12c shows κ_{crit} as a function of $2c$. While increasing the crack length from $2c = 50$ mm to 100 mm decreases κ_{crit} by a third, the effect is less pronounced for larger values of $2c$. That is, κ_{crit} changes very mildly for $2c \geqslant 150$ mm.

8.5 Constraint Match in Ductile Crack Growth

In this section, the similarity in crack tip constraint of the three systems is investigated, which are:

(i) Pipelines subject to a combined internal pressure and bending,

(ii) SENT specimens[5] with the same crack depth as the pipeline (i.e. constraint

[5]SENT specimens loaded in fixed grip displacement control.

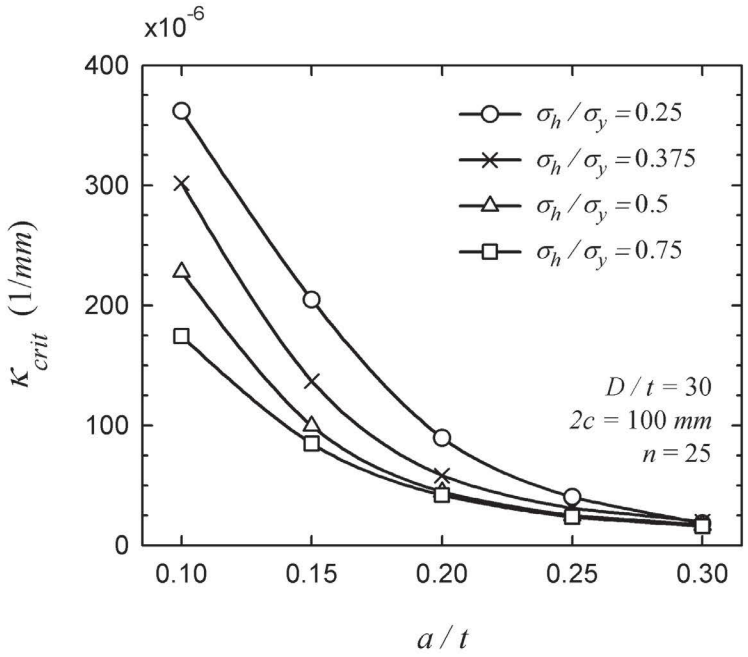

Figure 8.11. κ_{crit} as a function of a/t for different values of σ_h/σ_y.

matched); and

(iii) Traditionally used deeply cracked SENB specimen with $a/W = 0.5$.

Due to the lack of a generally accepted constraint theory for growing cracks, constraint similarity is studied via comparison of the R-curves and also comparison of the near-tip equivalent plastic strain (ε_p) and stress triaxiality fields (σ_m/σ_e) at various levels of crack growth.

The FE model for the SENT and SENB specimens consisted of ∼30,000 and ∼35,000 C3D8R elements respectively, while the rest of the modeling and solution details are very similar to those of the pipeline discussed earlier in Section 8.3.3 (with the arrangement of the GTN voided elements ahead of the crack tip also shown in Figure 8.5a). Figure 8.13a shows a double-symmetric model of the SENT specimen with relevant dimensions (in accordance with DNV's recommendations [9]) and boundary conditions (BC). The deformed crack region undergoing ductile crack growth is shown on Figure 8.13b.

The deeply cracked SENB model ($a/W = 0.5$) with dimensions as per ASTM-E1820 standard [75] is presented in Figure 8.14a. The two rollers, one for the support

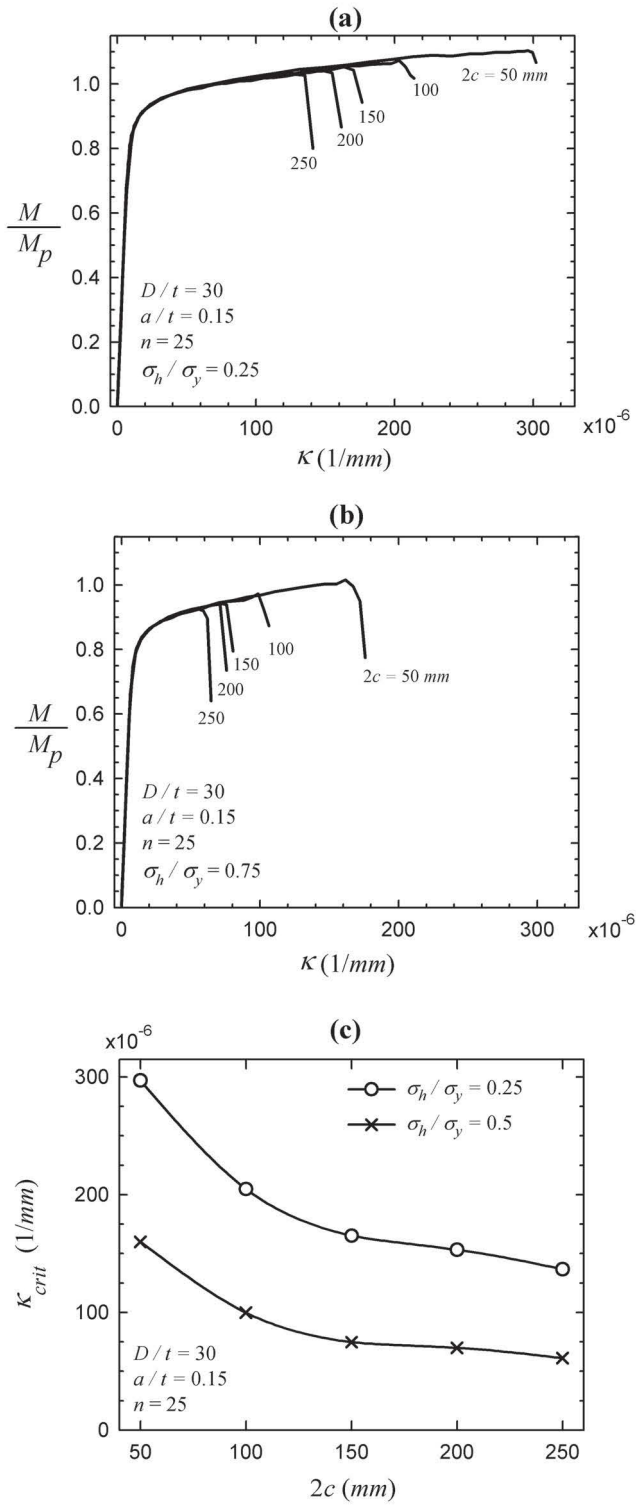

Figure 8.12. M-κ curves for a family of $2c$ values for **(a)** $\sigma_h/\sigma_y = 0.25$ and **(b)** $\sigma_h/\sigma_y = 0.75$. **(c)** κ_{crit} as a function of $2c$.

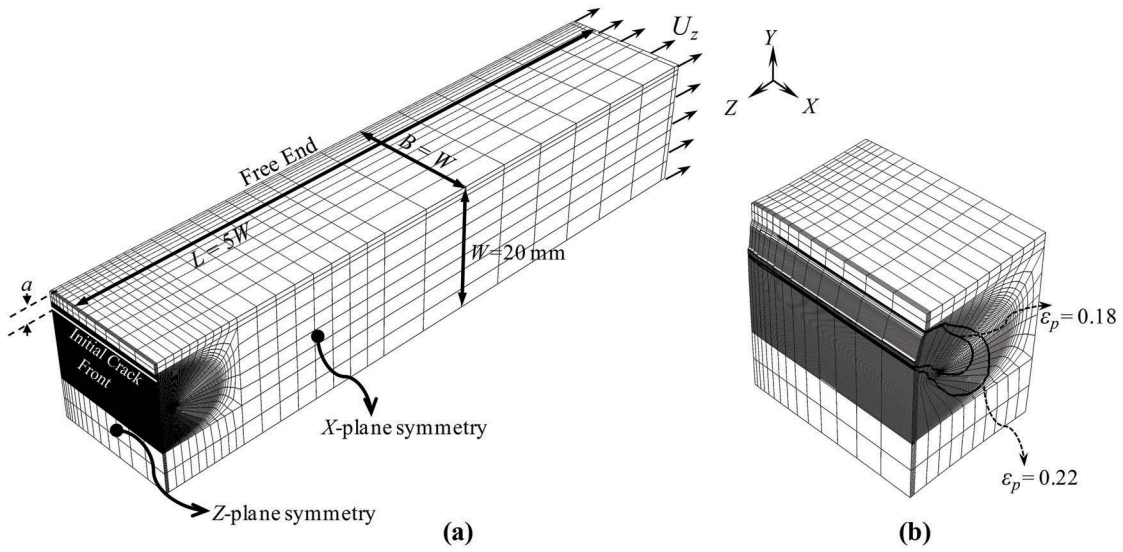

Figure 8.13. (a) a typical FE model of the SENT specimen ($a/W = 0.1$) and **(b)** the deformed crack region showing crack growth and contours of ε_p.

with radius of $^1/_4W$ and one for loading application with radius of $^1/_8W$ [75] are also shown. These rollers are modeled as analytical rigid surfaces, interacting with the specimen through a frictionless contact definition. The X and Z-plane symmetry BC's of the SENB specimen are similar to those of the SENT. Figure 8.14b shows the cracked region after some amount of crack growth. Both Figure 8.13b and 8.14b demonstrate that the initially horizontal crack front grows to a curvilinear shape (i.e. Δa at the *free end* is smaller than Δa at the symmetry plane), hence explaining the necessity of a biased mesh towards the free end (as seen in Figures 8.13a and 8.14a). The same steel material as used for modeling the pipeline (see Table 8.1 for material parameters) was used for the SENT and SENB as well.

8.5.1 *R*-curve Comparisons

In the subsequent discussion, the R-curves (representing the variation of $CTOD$ as a function of crack growth, Δa) are presented for the first 2 mm of crack growth (up to $\Delta a = 10 \times D_0$). Also, the R-curves of the specimens are highlighted with a solid line, while those of the pipeline are represented by the scattered data symbols. Figure 8.15a–c shows the R-curves for three crack depths, $a/t = 0.1$, 0.2, 0.3, compared to both the SENT and SENB specimens. In all cases, the SENT specimen results (with

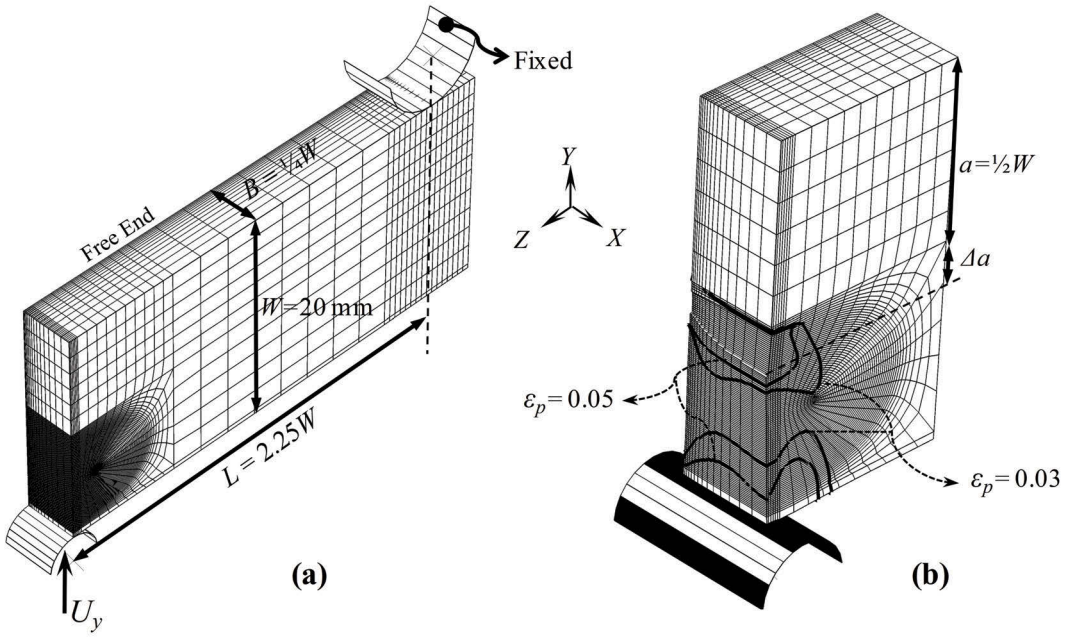

Figure 8.14. **(a)** The deeply cracked SENB specimen model ($a/W = 0.5$) and **(b)** the deformed crack region showing crack growth and contours of equivalent plastic strain, ε_p.

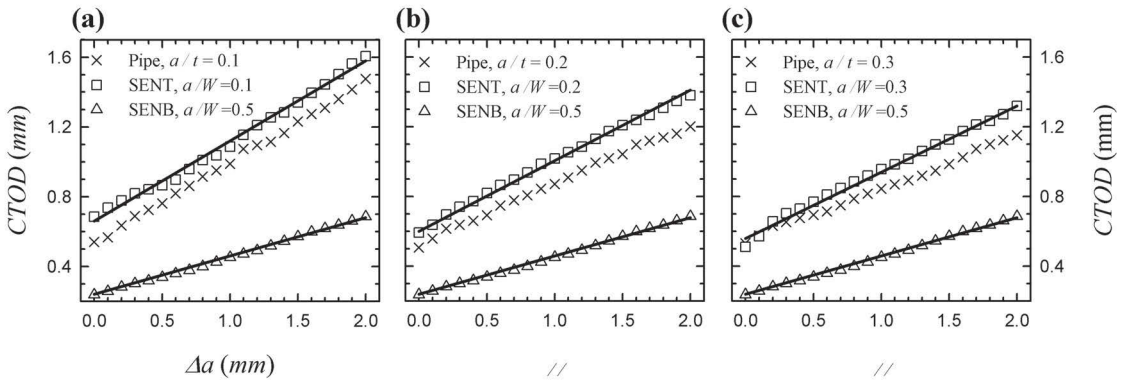

Figure 8.15. R-curves of pipes ($D/t = 30$, $2c = 100$ mm, $\sigma_h/\sigma_y = 0.25$) with crack depths of **(a)** $a/t = 0.1$, **(b)** $a/t = 0.2$, **(c)** $a/t = 0.3$ compared to those of SENT and SENB specimens.

same crack depth as the pipe) correlate much better to those of the pipe. The SENT specimen results provide an upper envelope to the $CTOD$ of the pipe, while the R-curve of the deeply cracked SENB predicts substantially lower values in comparison to the pipe.

In Figure 8.16, the R-curves of pipes with different crack lengths from $2c = 50$ mm

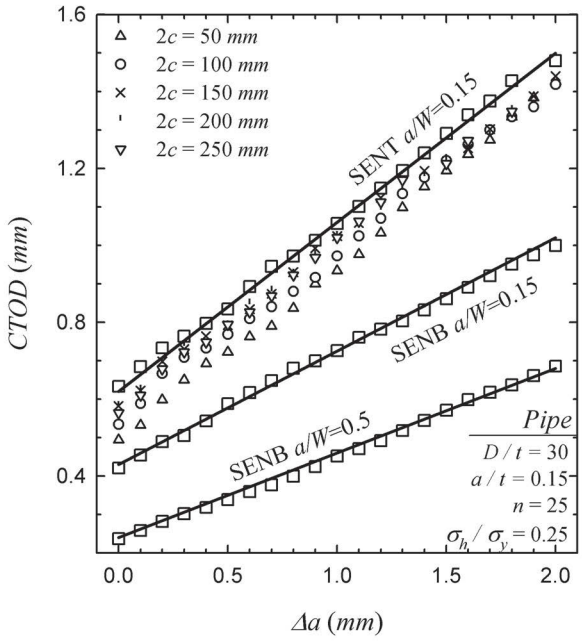

Figure 8.16. *R*-curves of pipes with various crack lengths compared to those of SENT and SENB specimens.

to 250 mm are shown in conjunction with those obtained from the SENT and SENB specimens (both deeply cracked, $a/W = 0.5$, and same crack size SENB, $a/W = 0.15$, specimens). All pipes tend to exhibit R-curves similar to the SENT specimen, with the R-curve of the SENT, again providing an upper envelope to the pipe. Interestingly, even the SENB specimen with $a/W = 0.15$ cannot provide an accurate estimation of the pipe's R-curve when $\Delta a > 1$ mm, while on the other hand, good agreement between the pipe and SENT R-curves holds, even as the crack grows. Although a clear-cut trend for the influence of $2c$ on the R-curve of pipes cannot be established, however, the pipe with the longest crack ($2c = 250$ mm) shows the best agreement with the SENT specimen.

The R-curves of the two pipes with $D/t = 10$ and 40 are shown in Figure refdcg17 along with those of the SENT and SENB specimens. The R-curve of the pipe with $D/t = 10$ perfectly matches to that of the SENT specimen up to $\Delta a = 1.2$ mm, while the R-curve of the $D/t = 40$ pipeline has less conformity with that of the SENT throughout the crack growth range. Still, it is clearly evident that the deeply cracked

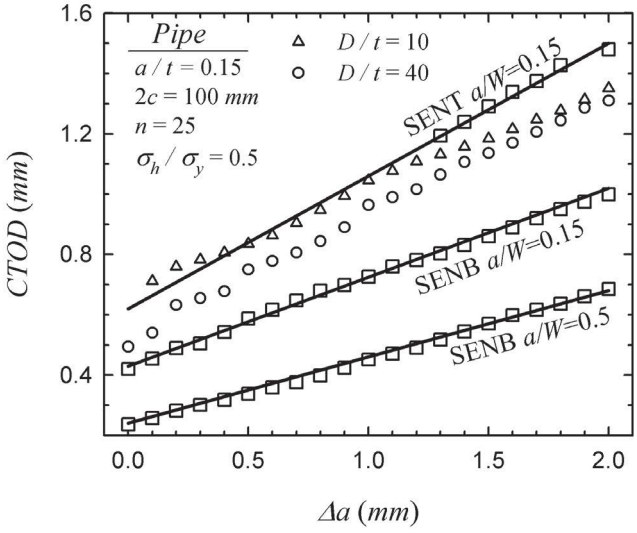

Figure 8.17. R-curves of the two pipes with $D/t = 10$ and 40 compared to those of the SENT and SENB specimens.

SENB specimen cannot provide a R-curve similar to that of the pipeline[6].

The effect of the internal pressure on the R-curve is illustrated in Figure 8.18 , which shows pipes' response subject to $\sigma_h/\sigma_y = 0.25$, 0.375 and 0.75. It is observed that as the internal pressure level is increased, the R-curves fall a little below the R-curve of the SENT specimen. However, no agreement is evident between the pipe and that of the deeply cracked SENB specimen. It should be noted that the increasing values of σ_h/σ_y would promote ductile fracture failure and hence, the global plastic deformation at failure in the pipe with $\sigma_h/\sigma_y = 0.75$ would be much lower than the pipe with $\sigma_h/\sigma_y = 0.25$. This explains the sequential drop of pipe R-curves as a function of increasing σ_h/σ_y.

Based on the detailed R-curve parametric comparison given above, it is believed that the SENT specimen with the same crack size as in the pipeline could provide very similar R-curves as that of cracked pipelines with a variety of geometric features and loading conditions. The traditional deeply cracked SENB specimen with $a/W = 0.5$ is found to be too conservative for characterizing the R-curve of a cracked pipe.

[6]Pipes with other values of D/t were also investegated but the results are not shown in Figure 8.17 for clarity. The drawn conclusions does hold true for them too.

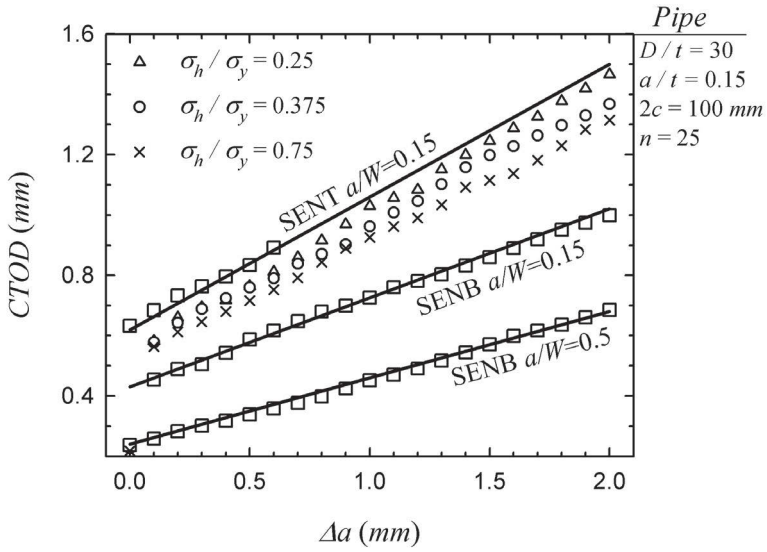

Figure 8.18. *R*-curves of pipes subjected to various levels internal pressure compared to those of SENT and SENB specimens.

8.5.2 Comparisons of the Stress Triaxiality and Equivalent Plastic Strain Ahead of the Growing Crack

To further investigate the constraint similarity of the SENT specimens with cracked pipelines, a detailed comparison on the equivalent plastic strain (ε_p) and stress triaxiality (σ_m/σ_e) fields are presented here. Both these quantities are prominent factors affecting the ductile crack growth process. The stress triaxiality, σ_m/σ_e, governs the void growth process (see Equation (8.1)), while the final failure of the matrix material between two enlarged voids (causing coalescence) occurs due to the necking or slipping mechanism, both controlled by the equivalent plastic strain (ε_p).

For comparison, σ_m/σ_e and ε_p fields are extracted at three successive values of crack growth: $\Delta a/D_0 = 1$, 5 and 10 (corresponding to $\Delta a = 0.2$, 1 and 2 mm) from the pipe, SENT and the deeply cracked SENB models. The r-s coordinate system for the pipe is shown in Figures 8.1 and 8.5e. For the SENT and SENB specimens the s-coordinate runs along the initial straight crack front (i.e., $s/B = 0$ at specimen's center and $s/B = 1$ at specimen's free end; see Figure 8.13 and refdcg14), while the r-coordinate emanates at the *initial* crack tip toward the uncracked ligament, similar to that in the pipeline.

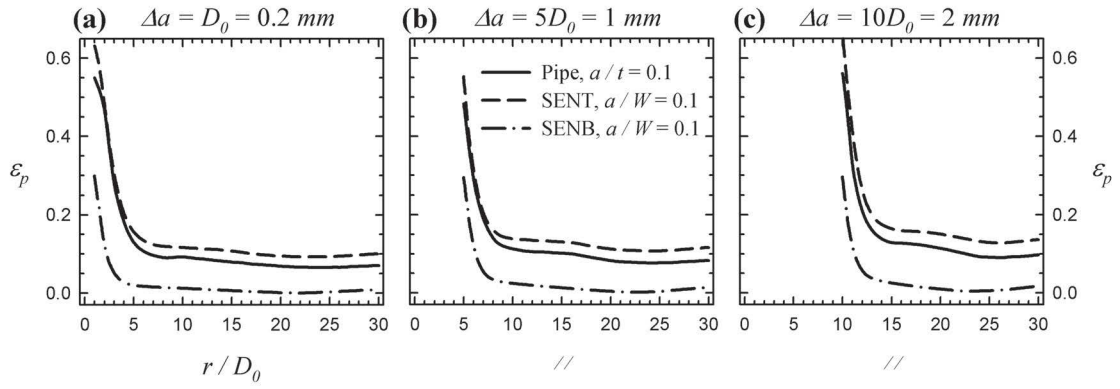

Figure 8.19. Distribution of ε_p ahead of the initial crack tip at the crack center ($s/c = s/B = 0$), for the pipe, the SENT and deeply crack SENB specimens (pipe specs: $D/t = 30$, $2c = 100$ mm and $\sigma_h/\sigma_y = 0.25$).

Figure 8.19 shows ε_p profiles ahead of the growing crack at the crack center ($s/c = s/B = 0$). In all the three sub-figures, ε_p attains maximum at the *current* crack tip and decreases precipitously to a very lower level over a distance $2 \sim 3 \times D_0$, and remaining constant thereafter. The size of these *singular zones* is comparable to the active void growth zone (refer to Figure 8.7 and its explanations). For all values of Δa it is observed that the ε_p distribution in the pipe tends to be more similar to the SENT specimen. The agreement is especially best in the singular zone, where the ε_p profiles of the pipe and the SENT specimen are almost identical. Further away from the *current* crack tip, the two profiles diverge slightly, with the SENT providing an upper envelope to the pipe. However, the ε_p profile of the deeply cracked SENB is considerably lower than both the pipe and also the SENT specimen in both the singular zone and the non-singular zone (which is governed by the global response.)

The ε_p distribution along the s-coordinate extracted at a distance of $5 \times D_0$ (1 mm) ahead of the *current* crack tip is shown in Figure 8.20 (for three values of crack growth). A relatively good agreement between the pipe and SENT specimen along the whole length of the crack front is evident. For all levels of crack growth, ε_p is approximately 2∼3% along the whole crack front for the deeply cracked SENB specimen. This strain level is much smaller than those observed for both the pipe and SENT (i.e. $\varepsilon_p \geqslant 10\%$ along the crack front for all three levels of Δa considered.)

The distribution of σ_m/σ_e along the uncracked ligament is shown in Figure 8.21 for

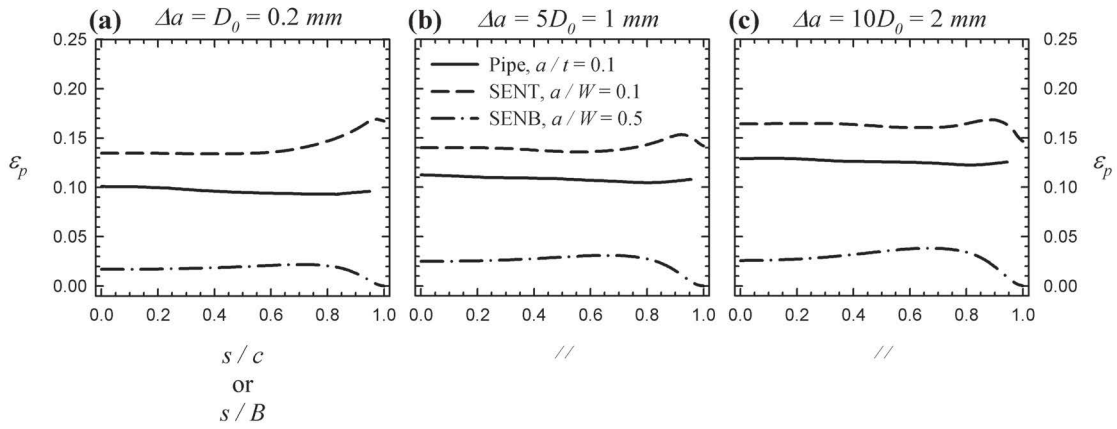

Figure 8.20. Distribution of ε_p along the s-coordinate in the pipe, SENT and SENB specimens, extracted at $5 \times D_0$ (1 mm) ahead of the *current* crack tip (pipe specs: $D/t = 30$, $2c = 100$ mm and $\sigma_h/\sigma_y = 0.25$).

the pipe, SENT and SENB specimens, extracted at the crack center ($s/c = s/B = 0$) at three levels of Δa. For the the pipe and SENT specimen, $(\sigma_m/\sigma_e)_{\max} \approxeq 1.5$ at all three levels of Δa, while the SENB specimen exhibits a substantially higher peak of $(\sigma_m/\sigma_e)_{\max} \approxeq 2.5$. Furthermore, the σ_m/σ_e profile for the SENB specimen reduces to negative values at some distance ahead of the initial crack tip. The σ_m/σ_e distribution of the pipe follows that of the SENT specimen very closely, while that of the SENB specimen is over-predictive at the near vicinity of the current crack tip, and then it is under-predictive at farther distances. The sign-change of the σ_m/σ_e profile in the SENB specimen is actually caused by a fundamental difference in comparison with the SENT specimen and also the pipe: the uncracked ligament in the SENB undergoes a compressive stress state at some distance ahead of the crack tip to accommodate the global bending moment, while the uncracked ligament in both the SENT specimen and pipeline is only subject to a tensile stress state.

The stress triaxiality (σ_m/σ_e) distribution along the s-coordinate, extracted at a distance of $5\times D_0$ (1 mm) ahead of the *current* crack tip center, is shown in Figure 8.22. For the initial crack growth increment (i.e. $\Delta a = 0.2$ mm, Figure 8.22a), the σ_m/σ_e values of the pipe and SENT are in perfect agreement up to $s/c = s/B \approxeq 0.4$. For the larger values of Δa (Figure 8.22b and c), the agreement is slightly less. Nonetheless, the general trends are very similar between the pipe and the SENT specimen, while

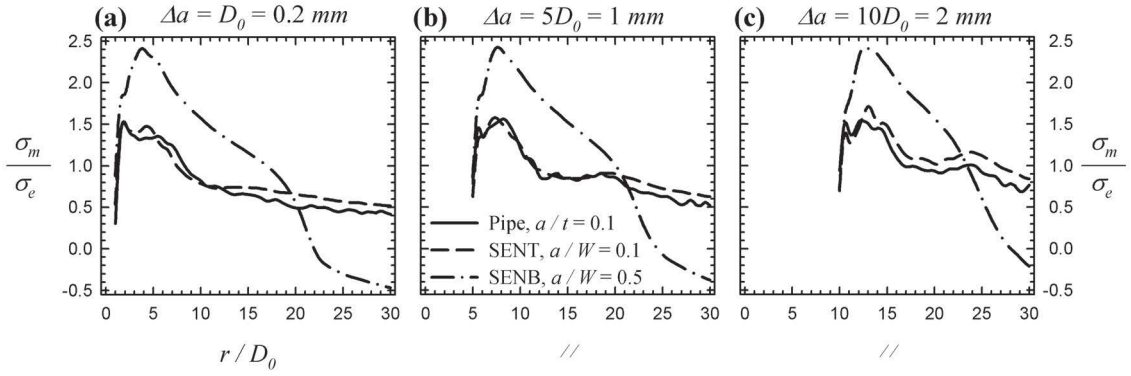

Figure 8.21. Distribution of σ_m/σ_e ahead of the initial crack tip for the pipe along with SENT and deeply crack SENB specimens at the crack center ($s/c = s/B = 0$). Typical pipe with $D/t = 30$, $2c = 100$ mm and $\sigma_h/\sigma_y = 0.25$

.

the SENB specimen results show a distinctly different distribution, across the entire crack front. For the SENB specimen, $(\sigma_m/\sigma_e)_{\max} \approxeq 2.15$, and also a very strong gradient is observed across the crack front (i.e. $\sigma_m/\sigma_e > 2$ at the mid-plane (at $s/B = 0$), and it decreases to approximately 0.5 at the free end (i.e. at $s/B = 1$). On the other hand, both the pipe and SENT specimens exhibit a more constant level of σ_m/σ_e along more than half the crack front length, and the decline in the distribution starts near the free end.

The presented σ_m/σ_e and ε_p fields ahead of the growing cracks in the three systems clearly indicate the similarity of these fields in the SENT and pipe models, both in quantity and general characteristics of the fields. Furthermore, the general trends observed (such as the high values of ε_p and low levels of σ_m/σ_e in the pipe and SENT models, versus the low ε_p and high σ_m/σ_e for the SENB model) are indicative of a brittle-type failure in the SENB and ductile fracture in the latter two models, both responses having been well documented elsewhere [78].

Based on the detailed comparisons of the R-curves, the near-tip triaxiality and equivalent plastic strain fields presented above, it is believed that a SENT specimen with the same crack depth as that in a pipeline of interest could provide fracture toughness data similar to that of the pipeline, regardless of pipe's geometric features and its loading condition. Thus, the excessive conservatism of the traditional deeply

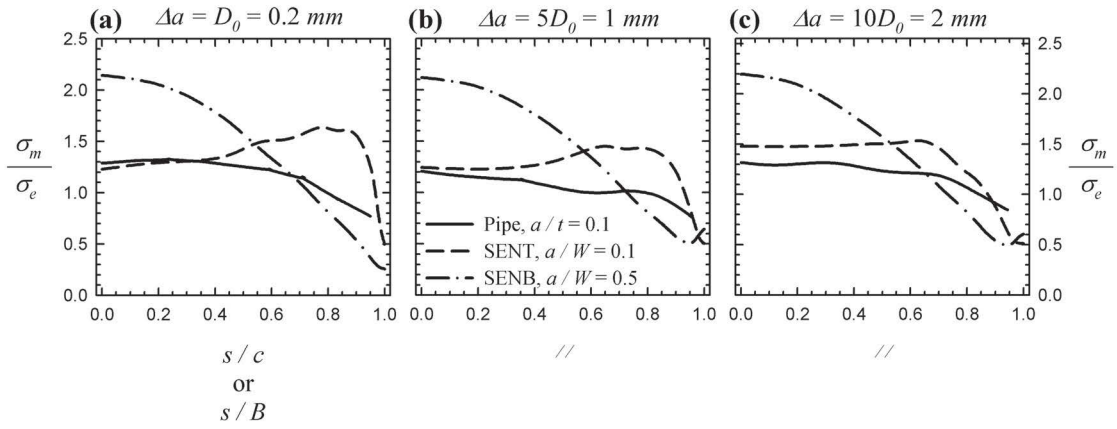

Figure 8.22. Distribution of σ_m/σ_e along the s-coordinate in the pipe, SENT and SENB specimens, extracted at $5 \times D_0$ (1mm) ahead of the *current* crack tip. Typical pipe with $D/t = 30$, $2c = 100$ mm and $\sigma_h/\sigma_y = 0.25$.

crack SENB specimen ($a/W = 0.5$) can be avoided with confidence, thereby generating more economic pipeline designs.

8.6 Concluding Remarks

A 3D detailed FE model of a cracked pipeline subject to internal pressure and bending was constructed to model ductile crack growth by utilizing the GTN voided plasticity material model. In the first part of the paper, the model was employed to study the critical curvature (κ_{crit}) of the pipe and the influence of various important parameters on κ_{crit}. The internal pressure (expressed through σ_h/σ_y) was found to significantly promote the ductile fracture failure mode, to the extent that some models reached their failure state shortly after the elastic regime was bypassed. Thick-wall pipelines with low D/t were able to sustain higher curvatures; in some cases, the local buckling/ovalization response dominated and caused their failure, rather than failure due to ductile crack growth. However, at higher values of σ_h/σ_y, the fracture failure mode would govern the pipes' response. Increase in both crack depth (a/t) and crack length ($2c$) decreased κ_{crit} significantly; however, an asymptotic response was observed (i.e. only minor changes in κ_{crit} were observed for $a/t \geqslant 0.2$ and $2c \geqslant 150$ mm.)

In consideration of the dependency of fracture toughness on crack-tip constraint

(from the perspectives of both the critical value and also the R-curve), the above discussed pipe models were used to generate the so-called R-curves ($CTOD$ as a function of crack growth, Δa). Also, the stress triaxiality and equivalent plastic strain fields ahead of the growing cracks were extracted. The same procedure was carried out for SENT specimens having the same crack depth as in the pipeline (constraint matched), as well as for the traditionally used deeply cracked SENB specimens ($a/W = 0.5$) recommended by the codes of practice [75]. Detailed comparisons revealed that the SENT specimen could exhibit very similar fracture characteristics to the pipe. The agreement was seen to exist for cracked pipes with various dimensions and internal pressure levels. Therefore, it is believed that the usage of SENT specimens, instead of the overly conservative deeply cracked SENB specimen is completely justified.

Acknowledgements

The financial support of the Atlantic Innovation Fund is gratefully appreciated.

Chapter 9

Conclusion

9.1 Summary

In this thesis, the integrity and fracture response of offshore pipelines undergoing large plastic strains was investigated using detailed nonlinear FE analysis. The investigation addressed the response, and potential fracture on the tensile side of a pipeline undergoing (predominantly) inelastic bending. The research was carried out in three main parts. While these parts may be precieved as distinct at first sight, they do form a complimentary body of work, providing better understanding of the fracture response and integrity of such pipes. The background and review presented in Chapter 2 clearly established the connection of these parts and their relevance to the issue of fracture and integrity assessment. This three-part investigation considered the following:

(i) Investigation of strain concentration in concrete coated pipelines, including parametric FE studies and design equation development (Chapters 3 and 4).

(ii) Development and calibration of a new crack driving force estimation scheme based on the reference strain method for pipelines subject to extreme plastic bending (Chapter 5).

(iii) Study of crack-tip constraint in pipelines undergoing large plastic strains, both under pure bending and also combined bending and internal pressure (Chapters 7 and 8).

Noting the general fracture integrity criterion (crack driving force $<$ fracture toughness), parts (ii) and (iii) compliment each other in the sense that part (ii) provides a new alternative formulation for crack driving force estimation, while part (iii) provides extensive justifications in support of the use of low-constraint (high toughness) specimens for establishing the fracture toughness data. Part (i) also provides

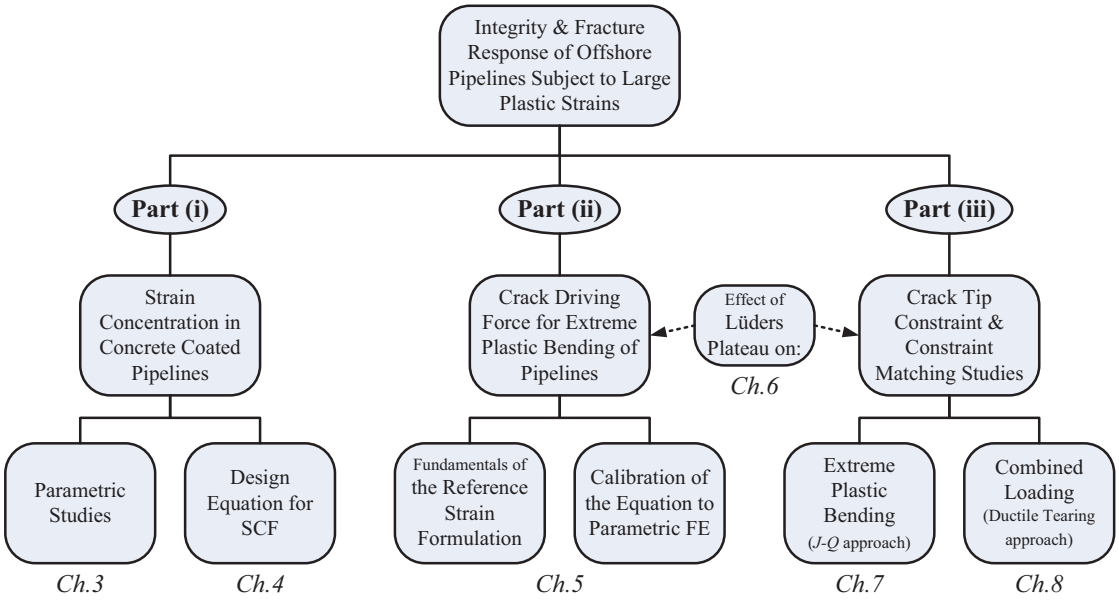

Figure 9.1. Hierarchy of the different parts and chapters of the thesis.

formulations for the accurate prediction of bending strain in a class of widely used offshore pipelines (concrete coated pipelines). This would itself be useful in crack driving force prediction for such pipelines. The general hierarchy of the thesis including the three constitutive parts are summarized and presented in Figure 9.1. With reference to Figure 9.1, Chapter 6 compliments both parts (ii) and (iii) by investigating the effect of Lüders plateau on the themes considered in those parts. It is believed that the methodologies and justifications presented in this thesis would help to diminish some of the excessive and unnecessary conservatism currently included in ECA procedures of pipelines. Contributions of the research noteworthy to mention are the proposed J-estimation scheme, and also the comprehensive justification provided to use low-constraint SENT specimens for ECA of such pipelines.

9.2 Conclusions

While the conclusions of each chapter are given at the end of the respective chapter separatley, only the most salient conclusions reached during the course of this research are outlined below:

(i) Based on a series of parametric FE analysis, a design equation for prediction of

SCF in the widely used X65 pipeline steel grade was developed. This equation can satisfactorily predict the SCF with an accuracy of ±20%. Additionally, it was observed that a *coating parameter*, $\lambda = Dt/(\varepsilon_g t_c^2)$, could be used to characterize the severity of strain concentration in the field joint. A *critical* value of this parameter could be established (λ_{crit}), for which the SCF shows an asymptotic behavior when $\lambda > \lambda_{crit}$, while configurations with $\lambda < \lambda_{crit}$ would undergo severe strain concentration in their FJ, and should be avoided in practice. For the specific steel grade $\lambda_{crit} \cong 8$.

(ii) A J-estimation scheme was proposed by upgrading the reference strain method with the addition of two plasticity functions (f_1 and f_2). A series of 300 FE analysis were used to calibrate f_1 and f_2 for a wide variety of pipe and crack dimensions and material properties. The equation took advantage of simplifying assumptions inherent to the problem, namely, displacement-controlled loading and LSY of the pipeline. The J-integral is predicted as a linear function of uncracked bending strain, $J/(\sigma_y t) = f_1 \varepsilon_{unc} + f_2$, with a ±2% accuracy with respect to FE results. The proposed equation does not require limit load definitions, thus providing extra convenience in its use.

(iii) The mere presence of a Lüders plateau was observed to significantly alter both the moment-strain curve, as well as the J-integral crack driving force curve. Higher values of the Lüders strain decrease the spatially-averaged constraint parameter Q_{ave}. Furthermore, the crack-opening stress profiles after the blunting zone ($J/\sigma_y < r < 5 \times J/\sigma_y$) decrease sequentially for increasing values of the Lüders strain. A micro-mechanic damage integral analysis also revealed that the Lüders plateau would adversely affect the fracture toughness of the material, especially for high hardening materials.

(iv) By incorporation of the J-Q fracture theory, the near-tip stress and strain fields of cracked pipeline bended up to LSY (ε_g up to 3%) were investigated. A comprehensive field-matching study with respect to the near-tip fields extracted from a standard MBL two term K-T model was performed. The observed similarity provided sufficient proof that the phenomenological fracture parameter J along

with the Q constraint parameter could successfully continue to characterize the near-tip stress and strain fields of cracked pipelines bended up to LSY levels. Additionally, the evolution of crack-tip constraint in the pipelines were observed to be a linear function of bending strain, which provided grounds for proposing the equation $Q = -0.25\varepsilon_g - b_1$. Furthermore, a close investigation of the J-Q trajectories among cracked pipelines and SENT specimens (with the same crack size) revealed the crack-tip similarity of these two systems. The various crack dimensions and material properties considered, provide confidence in using the SENT specimens for fracture assessment of such pipelines.

(v) Constraint studies on pipelines under combined loadings (biaxial stress state), constraint-matched SENT specimens, and also deeply cracked SENB specimens were performed. 3D FE models with the GTN voided plasticity material model, able to explicitly simulate ductile crack growth were utilized for this study. A comprehensive comparison on R-curves showed that for a cracked pipeline with a variety of geometries and internal pressure levels, the SENT specimen provides a very similar fracture resistance curve. Moreover, detailed comparisons on plastic strain and stress triaxiality fields ahead of the propagating crack among the three systems, again verified the similarity of fracture response of SENT specimens and pipelines. The fracture resistance of deeply-cracked SENB specimens is therefore deemed as too conservative with respect to the cracked pipeline. Based on the observed results, usage of SENT specimens for ECA of cracked pipelines subject to combined loadings and undergoing LSY, can be recommended with confidence.

9.3 Recommendations for Future Work

A comprehensive body of work, including new methodologies, justifications and also enhancements on application of fracture mechanics principles for assessment of off-shore pipelines subject to large plastic strains was presented herein. However, the following complimentary research issues would be a suitable follow up to this work:

(i) Strain concentration design equations based on elastic-plastic FE analysis (such

as that presented in Chapter 4 for concrete coated pipelines) are very rare in the literature. Development of such equations for other important causes of strain concentration, such as misalignment in adjoining pipes, weld mismatch, pipe wall thickness mismatch, to mention a few, would surely be useful in integrity assessment of offshore pipelines. Currently, the codes of practice mostly recommend approximate methods for determination of these concentration factors.

(ii) A general simplification incorporated in all parts of the investigation carried out in this thesis was neglecting the girth weld. This was based on the fact the codes require the girth weld to be always *over-matched*[1] with respect to the parent steel material. Hence, ignoring its presence would be in favor of conservatism. Furthermore, semi-empirical approaches used for accounting for the weld residual stress and strains are well established (see e.g. BS7910 [8]). However, it would be interesting to explicitly investigate the effect of the girth weld on the fracture response. Of particular interest would be the investigation of its effect on crack tip constraint in pipelines.

(iii) The proposed reference strain J-estimation scheme in Chapter 5 is only for pure bending loads. The next practical step would be its enhancement to account for combined loading conditions (such as inclusion of the internal pressure and axial load effects). The results of such an investigation would be extremely useful, as the current code recommendations do not present a clear-cut approach for treatment of bending (or tension) combined with internal pressure which causes a biaxial stress state in the pipe wall.

(iv) Validity of some of the drawn conclusions can be significantly increased if accompanied by relevant experimental data. An experimental investigation on the effect of Lüders plateau on fracture toughness, and its comparison with the results of the micro-mechanic damage integral approach of Chapter 6 would greatly help the validity of the approach.

(v) The FE models of Chapter 8 satisfactorily predicted the fracture failure mode of

[1] A welded joint is dubbed as *over-matched* when the weld consumables have a higher strength than the joined components.

pipelines based on the explicit simulation of crack growth. The extension of such a methodology to account for low-cycle fatigue damage (such as that resulting from pipeline reeling) would provide a very sophisticated and informative tool for accurate analysis of such structures.

(vi) In lieu and as an alternative to the current ECA procedure which is based on a phenomenological fracture parameter (such as J or $CTOD$), it would be very useful to justify the use of local damage approaches (such as the FE models used in Chapter 8) for fracture integrity assessment of offshore pipelines. This justification would certainly require a vast body of experimental work (in addition to the ones presently available), showing that the pipeline FE models with material definition incorporating damage (such as the GTN material model) can satisfactorily predict the fracture failure mode and critical load/displacement.

Bibliography

[1] Bai, Y., 2001. *Pipelines and risers*. Elsevier Ltd.

[2] DNV-OS-F101, 2000. *Offshore standard – Submarine pipeline systems*. Det Norske Veritas, Høvik, Norway.

[3] API-RP-1111, 1999. *Design, construction, operation, and maintenance of offshore hydrocarbon pipelines (limit state design)*, third ed. American Petroleum Institute, Washington DC, USA.

[4] Kyriakides, S., and Corona, E., 2007. *Mechanics of Offshore Pipelines: Buckling and Collapse*, first ed. Elsevier Ltd.

[5] Nogueira, A. C., and Mckeehan, D. S., 2005. "Design and construction of offshore pipelines (chapter 11)". In *Handbook of Offshore Engineering*, S. Chakrabarti, ed. Elsevier Ltd.

[6] URL. `http://www.epmag.com/resources/images/archives/hpht-deepsea1.jpg`. Retrieved at 15^{th} March 2011.

[7] Mousselli, A., 1981. *Offshore pipeline design, analysis, and methods*. Penn Well Books, Tulsa, OK, USA.

[8] BS7910, 2005. *Guide to methods for assessing the acceptability of flaws in metallic structures*. British Standards Institution, London.

[9] DNV-RP-F108, 2006. *Recommended Practice - Fracture control for pipeline installation methods introducing cyclic plastic strain*. Det Norske Veritas, Høvik, Norway.

[10] ABAQUS, 2008. *Abaqus ver. 6.8 users and theory manual*. Dassault Systèmes Simulia Corp., Providence, RI, USA.

[11] Mohr, W., 2003. *Strain-Based Design of Pipelines, Report Project No. 45892GTH*. U.S. Department of Interior, Minerals Management Service, Herndon (VA, USA).

[12] Mohr, W., Gordon, R., and Smith, R., 2004. "Strain-based design guidelines for pipeline girth welds". In International Offshore and Polar Engineering Conference (ISOPE), Vol. 1, Toulon, France, pp. 10–17.

[13] Vitali, L., Torselletti, E., Marchesani, F., and Bruschi, R., 1996. "Use (and abuse) of strain based criteria in offshore pipeline technology". In Aspect'96: Advances in Subsea Pipeline Engineering and Technology, Aberdeen, UK.

[14] Palmer, A. C., and King, R. A., 2008. *Subsea pipeline engineering*, second ed. PennWell Books.

[15] Bræstrup, M. W., and Andersen, J. B., 2005. *Design and installation of marine pipelines*. Wiley-Blackwell, Oxford, United Kingdom.

[16] Anderson, T. L., 2005. *Fracture mechanics: fundamentals and applications*, third ed. CRC.

[17] Bruschi, R., Torselletti, E., Vitali, L., Hauge, M., and Levold, E., 2005. "Fracture control–offshore pipelines: Current status of fracture assessment for pipelines, limitations and the need for development". In International Conference on Offshore Mechanics and Arctic Engineering (OMAE), Halkidiki, Greece, pp. 659–668.

[18] Archer, G., and Adams, A., 1983. "The behavior of concrete over thin film epoxy coatings on offshore pipelines". In Proceedings of the Offshore Technology Conference (OTC), Vol. 1, OTC paper no. 4453, Houston, TX, USA, pp. 85–94.

[19] Akten, H., Lund, S., and Miller, D., 1985. "On the design and construction of statpipe pipeline system". In Proceedings of the Offshore Technology Conference (OTC), OTC paper no. 4922, Houston, TX, USA.

[20] Verley, R., and Ness, O. B., 1995. "Strain concentrations in pipelines with concrete coating: Full scale bending tests and analytical calculations". In International Conference on Offshore Mechanics and Arctic Engineering (OMAE), Vol. 5, Copenhagen, Denmark, pp. 499–506.

[21] Ness, O. B., Hjartholm, G., Verley, R. L. P., and Thorsen, O. G., 1996. "Zeepipe IIA pipeline: Strains measured during laying and predictions". In International Offshore and Polar Engineering Conference (ISOPE), Vol. 2, Los Angeles, CA, USA, pp. 35–40.

[22] Lund, S., Bruschi, R., Montesi, M., and Sintini, L., 1993. "Laying criteria versus strain concentrations at field joints for heavily coated pipelines". In International Conference on Offshore Mechanics and Arctic Engineering (OMAE), Vol. 5, Glasgow, UK, pp. 41–56.

[23] Ness, O. B., and Verley, R., 1995. "Strain concentrations in pipelines with concrete coating an analytical model". In International Conference on Offshore Mechanics and Arctic Engineering (OMAE), Vol. 5, pp. 507–512.

[24] Endal, G., 1994. "Extreme bending of concrete coated offshore pipelines: A numerical study". In International DIANA Conference on Computational Mechanics, Delft, Netherlands.

[25] Sævik, S., Storheim, M., and Levold, E., 2008. "Efficient finite element for evaluation of strain concentrations in concrete coated pipelines". In International Conference on Offshore Mechanics and Arctic Engineering (OMAE), Estoril, Portugal.

[26] Williams, M. L., 1997. "On the stress distribution at the base of a stationary crack". *ASME J. Appl. Mech.,* **24**, pp. 111–114.

[27] Hutchinson, J. W., 1983. "Fundamentals of the phenomenological theory of nonlinear fracture mechanics". *ASME J. Appl. Mech.,* **50**, pp. 1042–1051.

[28] Rice, J. R., 1968. "A path independent integral and the approximate analysis of strain concentration by notches and cracks". *ASME J. Appl. Mech.,* **35**(2), pp. 379–386.

[29] Hutchinson, J. W., 1968. "Singular behaviour at the end of a tensile crack in a hardening material". *J. Mech. Phys. Solids,* **16**(1), pp. 13–31.

[30] Rice, J. R., and Rosengren, G. F., 1968. "Plane strain deformation near a crack tip in a power-law hardening material". *J. Mech. Phys. Solids,* **16**(1), pp. 1–12.

[31] Shih, C. F., 1983. *Tables of Hutchinson–Rice–Rosengren singular field quantities. MRL E-147.* Materials Research Laboratory, Brown University.

[32] Wells, A. A., 1961. "Unstable crack propagation in metals: Cleavage and fast fracture". In Proceedings of the Crack Propagation Symposium, Paper 84, Cranfield, UK.

[33] Shih, C. F., 1981. "Relationships between the J-integral and the crack opening displacement for stationary and extending cracks". *J. Mech. Phys. Solids,* **29**(4), pp. 305–326.

[34] API-5L, 2000. *Specification for Line Pipe*, 42nd ed. American Petroleum Institute, Washington DC, USA.

[35] Kumar, V., German, M. D., and Shih, C. F., 1981. *Engineering approach for elastic-plastic fracture analysis, EPRI Report NP-1931.* Electric Power Research Institute, Palo Alto (CA, USA).

[36] Ainsworth, R. A., 1984. "The assessment of defects in structures of strain hardening material". *Engng. Fract. Mech.,* **19**(4), pp. 633–642.

[37] Linkens, D., Formby, C. L., and Ainsworth, R. A., 2000. "A strain-based approach to fracture assessment – example applications". In Proceedings of the Fifth International Conference on Engineering Structural Integrity Management EMAS, pp. 45–52.

[38] Kumar, V., and Shih, C. F., 1980. "Fully plastic crack solutions, estimation scheme, and stability analyses for the compact specimen". In *ASTM STP 700: Fracture mechanics.* American Society for Testing Materials, Philadelphia, pp. 406–438.

[39] Miller, A. G., and Ainsworth, R. A., 1989. "Consistency of numerical results for power-law hardening materials and the accuracy of the reference stress approximation for J". *Engng. Fract. Mech.,* **32**(2), pp. 233–247.

[40] Milne, I., Ainsworth, R. A., Dowling, A. R., and Stewart, A. T., 1988. "Background to, and validation of, CEGB report R/H/R6 revision 3". *Int. J. Press. Ves. Pip.,* **32**, pp. 105–196.

[41] Kastner, W., Röhrich, E., Schmitt, W., and Steinbuch, R., 1981. "Critical crack sizes in ductile piping". *Int. J. Press. Ves. Pip.,* **9**(3), pp. 197–219.

[42] Neuber, H., 1961. "Theory of stress concentration for shear-strained prismatical bodies with arbitrary nonlinear stress-strain law". *ASME J. Appl. Mech.,* **28**(4), pp. 544–550.

[43] Miller, A. G., 1988. "Review of limit loads of structures containing defects". *Int. J. Press. Ves. Pip.,* **32**, pp. 197–327.

[44] Ainsworth, R. A., 1989. "Approximate non-linear fracture mechanics calculations using reference stress techniques". In International Conference on Pressure Vessel and Piping (PVP), pp. 13–19.

[45] Zerbst, U., Ainsworth, R. A., and Schwalbe, K. H., 2000. "Basic principles of analytical flaw assessment methods". *Int. J. Press. Ves. Pip.,* **77**(14-15), pp. 855–867.

[46] Pisarski, H. G., Phaal, R., Hadley, I., and Francis, R., 1994. "Integrity of steel pipe during reeling". In International Conference on Offshore Mechanics and Arctic Engineering (OMAE), Vol. 5, Houston, TX, USA, pp. 189–198.

[47] Østby, E., Jayadevan, K., and Thaulow, C., 2005. "Fracture response of pipelines subject to large plastic deformation under bending". *Int. J. Press. Ves. Pip.,* **82**(3), pp. 201–215.

[48] Pisarski, H. G., Smith, S., and Xu, G., 2006. "Fracture mechanics assessment of flaws in pipeline girth welds". *Cutting and Welding,* **5**(5), pp. 24–28.

[49] Tkaczyk, T., O'Dowd, N. P., and Howard, B. P., 2007. "Comparison of crack driving force estimation schemes for weld defects in reeled pipelines". In International Offshore and Polar Engineering Conference (ISOPE), Lisbon, Portugal, pp. 3141–3149.

[50] Østby, E., 2005. "Fracture control–offshore pipelines: New strain-based fracture mechanics equations including the effects of biaxial loading, mismatch, and misalignment". In International Conference on Offshore Mechanics and Arctic Engineering (OMAE), Halkidiki, Greece, pp. 649–658.

[51] Tkaczyk, T., O'Dowd, N. P., and Nikbin, K., 2009. "Fracture assessment procedures for steel pipelines using a modified reference stress solution". *ASME J. Press. Vess. Technol.,* **131**.

[52] Kim, Y. J., and Budden, P. J., 2002. "Reference stress approximations for J and COD of circumferential through-wall cracked pipes". *Int. J. Fract.,* **116**(3), pp. 195–218.

[53] McClintock, F. A., 1971. "Plasticity aspects of fracture". In *Fracture: an advanced treatise, Vol. 3*, H. Leibowitz, ed. Academic Press, New York, pp. 47–225.

[54] Begley, J. A., and Landes, J. D., 1976. "Serendipity and the J integral". *Int. J. Fract.,* **12**, pp. 764–766.

[55] Hancock, J. W., and Cowling, M. J., 1980. "Role of state of stress in crack-tip failure processes". *Metal Science,* **8**(9), pp. 293–304.

[56] Parks, D. M., 1992. "Advances in characterization of elastic–plastic crack–tip fields". In Topics in Fracture and Fatigue, A. S. Argon, ed., Springer-Verlag, pp. 59–98.

[57] Yuan, H., and Brocks, W., 1998. "Quantification of constraint effects in elastic-plastic crack front fields". *J. Mech. Phys. Solids,* **46**(2), pp. 219–241.

[58] Brocks, W., and Schmitt, W., 1995. "The second parameter in J-R curves: constraint or triaxiality?". In *ASTM STP 1244: Constraint effects in fracture, theory and applications: second volume*, M. Kirk and A. Bakker, eds. American Society for Testing Materials, Philadelphia, pp. 209–231.

[59] McMeeking, R. M., and Parks, D. M., 1979. "On criteria for J-Dominance of crack-tip fields in large-scale yielding". In *ASTM STP 668: Elastic-plastic fracture*, J. D. Landes, J. A. Begley, and G. A. Clarke, eds. American Society for Testing Materials, Philadelphia, pp. 175–194.

[60] Shih, C. F., and German, M. D., 1981. "Requirements for a one parameter characterization of crack tip fields by the HRR singularity". *Int. J. Fract.,* **17**(1), pp. 27–43.

[61] Betegon, C., and Hancock, J. W., 1991. "Two-parameter characterization of elastic-plastic crack-tip fields". *ASME J. Appl. Mech.,* **58**, pp. 104–110.

[62] Al-Ani, A. M., and Hancock, J. W., 1991. "J-Dominance of short cracks in tension and bending". *J. Mech. Phys. Solids,* **39**(1), pp. 23–43.

[63] Hancock, J. W., Reuter, W. G., and Parks, D. M., 1993. "Constraint and toughness parameterized by T". In *ASTM STP 1171: Constraint effects in fracture*, E. M. Hackett, K. H. Schwalbe, and R. H. Dodds, eds. American Society for Testing Materials, Philadelphia, pp. 21–40.

[64] Yang, S., Chao, Y. J., and Sutton, M. A., 1993. "Higher order asymptotic crack tip fields in a power-law hardening material". *Engng. Fract. Mech.,* **45**(1), pp. 1–20.

[65] Chao, Y. J., Yang, S., and Sutton, M. A., 1994. "On the fracture of solids characterized by one or two parameters: theory and practice". *J. Mech. Phys. Solids,* **42**(4), pp. 629–647.

[66] Chao, Y. J., and Zhu, X. K., 1998. "J-A_2 characterization of crack-tip fields: extent of J-A_2 dominance and size requirements". *Int. J. Fract.,* **89**(3), pp. 285–307.

[67] O'Dowd, N. P., and Shih, C. F., 1991. "Family of crack-tip fields characterized by a triaxiality parameter–I. Structure of fields". *J. Mech. Phys. Solids,* **39**(8), pp. 989–1015.

[68] O'Dowd, N. P., and Shih, C. F., 1992. "Family of crack-tip fields characterized by a triaxiality parameter–II. Fracture applications". *J. Mech. Phys. Solids,* **40**(5), pp. 939–963.

[69] Shih, C. F., O'Dowd, N. P., and Kirk, M. T., 1993. "A framework for quantifying crack tip constraint". In *ASTM STP 1171: Constraint effects in fracture*, E. M. Hackett, K. H. Schwalbe, and R. H. Dodds, eds. American Society for Testing Materials, Philadelphia, pp. 2–20.

[70] O'Dowd, N. P., and Shih, C. F., 1994. "Two-parameter fracture mechanics: theory and applications". In *ASTM STP 1207: Fracture Mechanics, 24th Volume*, J. D. Landes, D. E. McCabe, and J. A. M. Boulet, eds. American Society for Testing Materials, Philadelphia, pp. 21–47.

[71] O'Dowd, N. P., 1995. "Applications of two parameter approaches in elastic-plastic fracture mechanics". *Engng. Fract. Mech.,* **52**(3), pp. 445–465.

[72] Joyce, J. A., and Link, R. E., 1997. "Application of two parameter elastic-plastic fracture mechanics to analysis of structures". *Engng. Fract. Mech.,* **57**(4), pp. 431–446.

[73] Zhu, X. K., and Leis, B. N., 2006. "Application of constraint corrected J-R curves to fracture analysis of pipelines". *ASME J. Press. Vess. Technol.,* **128**, pp. 581–589.

[74] Faleskog, J., 1995. "Effects of local constraint along three-dimensional crack fronts–a numerical and experimental investigation". *J. Mech. Phys. Solids,* **43**(3), pp. 447–465.

[75] ASTM-E1820, 2009. *Standard test method for measurement of fracture toughness.* American Society for Testing and Materials.

[76] Chiesa, M., Nyhus, B., Skallerud, B., and Thaulow, C., 2001. "Efficient fracture assessment of pipelines. A constraint-corrected SENT specimen approach". *Engng. Fract. Mech.,* **68**(5), pp. 527–547.

[77] Pisarski, H. G., and Wignall, C. M., 2002. "Fracture toughness estimation for pipeline girth welds". In International Pipeline Conference (IPC), Calgary, Canada, pp. 1607–1611.

[78] Nyhus, B., Polanco, M. L., and Ørjasæther, O., 2003. "SENT specimens an alternative to SENB specimens for fracture mechanics testing of pipelines". In International Conference on Offshore Mechanics and Arctic Engineering (OMAE), Cancun, Mexico, pp. 259–266.

[79] Cravero, S., and Ruggieri, C., 2005. "Correlation of fracture behavior in high pressure pipelines with axial flaws using constraint designed test specimens–Part I: Plane-strain analyses". *Engng. Fract. Mech.,* **72**(9), pp. 1344–1360.

[80] Silva, L. A. L., Cravero, S., and Ruggieri, C., 2006. "Correlation of fracture behavior in high pressure pipelines with axial flaws using constraint designed test specimens. Part II: 3-D effects on constraint". *Engng. Fract. Mech.,* **73**(15), pp. 2123–2138.

[81] McClintock, F. A., 1968. "A criterion for ductile fracture by the growth of holes". *ASME J. Appl. Mech.,* **35**, pp. 363–371.

[82] Rice, J. R., and Tracey, D. M., 1969. "On the ductile enlargement of voids in triaxial stress fields". *J. Mech. Phys. Solids,* **17**(3), pp. 201–217.

[83] Anderson, T. L., Vanaparthy, N. M. R., and Dodds, R. H., 1993. "Predictions of specimen size dependence on fracture toughness for cleavage and ductile tearing". In *ASTM STP 1171: Constraint effects in fracture*, E. M. Hackett, K. H. Schwalbe, and R. H. Dodds, eds. American Society for Testing Materials, Philadelphia, pp. 473–491.

[84] Gurson, A. L., 1977. "Continuum theory of ductile rupture by void nucleation and growth: Part I-Yield criteria and flow rules for porous ductile media". *ASME J. Eng. Mater. Technol.,* **99**(1), pp. 2–15.

[85] Tvergaard, V., 1981. "Influence of voids on shear band instabilities under plane strain conditions". *Int. J. Fract.,* **17**(4), pp. 389–407.

[86] Faleskog, J., Gao, X., and Shih, C. F., 1998. "Cell model for nonlinear fracture analysis–I. Micromechanics calibration". *Int. J. Fract.,* **89**(4), pp. 355–373.

[87] Needleman, A., and Rice, J. R., 1978. "Limits to ductility set by plastic flow localization". In *Mechanics of Sheet Metal Forming*, D. P. Koistnen and N. M. Wang, eds. Plenum Publishing Corporation, New York, pp. 237–256.

[88] Chu, C. C., and Needleman, A., 1980. "Void nucleation effects in biaxially stretched sheets". *ASME J. Eng. Mater. Technol.,* **102**, pp. 249–256.

[89] Tvergaard, V., and Needleman, A., 1984. "Analysis of the cup-cone fracture in a round tensile bar". *Acta Metall.,* **32**(1), pp. 157–169.

[90] Zhang, Z. L., Thaulow, C., and Ødegård, J., 2000. "A complete Gurson model approach for ductile fracture". *Engng. Fract. Mech.,* **67**(2), pp. 155–168.

[91] Brocks, W., Klingbeil, D., Kiinecke, G., and Sun, D. Z., 1995. "Application of the Gurson model to ductile tearing resistance". In *ASTM STP 1244: Constraint effects in fracture, theory and applications: second volume*, M. Kirk and A. Bakker, eds. American Society for Testing Materials, Philadelphia, pp. 232–252.

[92] Thomason, P. F., 1990. *Ductile fracture of metals.* Pergamon Press, Oxford, UK.

[93] Xia, L., and Shih, C. F., 1995. "Ductile crack growth-I. A numerical study using computational cells with microstructurally-based length scales". *J. Mech. Phys. Solids,* **43**(2), pp. 233–259.

[94] Xia, L., and Shih, C. F., 1995. "Ductile crack growth–II. Void nucleation and geometry effects on macroscopic fracture behavior". *J. Mech. Phys. Solids,* **43**(12), pp. 1953–1981.

[95] Xia, L., and Shih, C. F., 1996. "Ductile crack growth–III. Transition to cleavage fracture incorporating statistics". *J. Mech. Phys. Solids,* **44**(4), pp. 603–615.

[96] Ruggieri, C., Panontin, T. L., and Dodds, R. H., 1996. "Numerical modeling of ductile crack growth in 3-D using computational cell elements". *Int. J. Fract.,* **82**(1), pp. 67–95.

[97] Xia, L., Shih, C. F., and Hutchinson, J. W., 1995. "A computational approach to ductile crack growth under large scale yielding conditions". *J. Mech. Phys. Solids,* **43**(3), pp. 389–413.

[98] Chen, Y., and Lambert, S., 2003. "Analysis of ductile tearing of pipeline-steel in single edge notch tension specimens". *Int. J. Fract.,* **124**(3), pp. 179–199.

[99] Chen, Y., and Lambert, S., 2005. "Numerical modeling of ductile tearing for semi-elliptical surface cracks in wide plates". *Int. J. Press. Ves. Pip.,* **82**(5), pp. 417–426.

[100] Sandvik, A., Østby, E., and Thaulow, C., 2008. "Fracture control – offshore pipelines JIP, Use of Abaqus/Explicit to simulate ductile tearing in pipes with defects loaded beyond yielding". In International Offshore and Polar Engineering Conference (ISOPE), Vancouver, BC, Canada, pp. 72–78.

[101] Dybwad, J., Törnqvist, R., Østby, E., and Thaulow, C., 2009. "Simulations of ductile tearing at large strains of biaxially loaded pipes". In International Conference on Offshore Mechanics and Arctic Engineering (OMAE), Honolulu, Hawaii, USA, pp. 115–122.

[102] O'Dowd, N. P., Shih, C. F., and Dodds, R. H., 1995. "The role of geometry and crack growth on constraint and implications for ductile/brittle fracture". In *ASTM STP 1244: Constraint effects in fracture, theory and applications: second volume*, M. Kirk and A. Bakker, eds. American Society for Testing Materials, Philadelphia, pp. 134–159.

[103] Cravero, S., Bravo, R. E., and Ernst, H. A., 2008. "Constraint evaluation and effects on J-R resistance curves for pipes under combined load conditions". In International Offshore and Polar Engineering Conference (ISOPE), Vancouver, BC, Canada, pp. 149–156.

[104] Xu, J., Zhang, Z. L., Østby, E., Nyhus, B., and Sun, D. B., 2010. "Constraint effect on the ductile crack growth resistance of circumferentially cracked pipes". *Engng. Fract. Mech.,* **77**(4), pp. 671–684.

[105] Tkaczyk, T., ODowd, N., Nikbin, K., and Howard, B. P., 2009. "The Effect of Pre-Strain on Ductile Fracture Toughness of Reeled Pipeline Steels". In International Conference on Pressure Vessel and Piping (PVP), Vol. 6, Prague, Czech Republic, pp. 1203–1212.

[106] Ness, O. B., and Verley, R., 1996. "Strain concentrations in pipelines with concrete coating". *ASME J. Offshore Mech. Arct. Eng.,* **118**, pp. 225–231.

[107] Bruschi, R., Malacari, L., Torselletti, E., and Vitali, L., 1995. "Concrete coated submarine pipelines: Further advances in strain concentration at field joints and relevant implications on strain based design". In Proceedings of the Offshore Technology Conference (OTC), OTC paper no. 7858, Houston, TX, USA.

[108] Nourpanah, N., and Taheri, F., 2009. "A design equation for evaluation of strain concentration factor in concrete coated X65 pipelines". *Mar. struct.,* **22**, pp. 758–769.

[109] Statoil TR1221, 2003. *External coating for linepipe – Fusion Bonded Epoxy (FBE) and FBE/ Polypropylene (PP) multilayer systems.* Statoil, Stavanger, Norway.

[110] URL. `http://allanedwards.com/pipeline_concrete_coating.php`. Retrieved at 23^{rd} June 2010.

[111] Igland, R. T., and Moan, T., 2000. "Reliability analysis of pipelines during laying, considering ultimate strength under combined loads". *ASME J. Offshore Mech. Arct. Eng.,* **122**, pp. 40–46.

[112] Murphy, C. E., and Langner, C. G., 1985. "Ultimate pipe strength under bending, collapse, and fatigue". In International Conference on Offshore Mechanics and Arctic Engineering (OMAE), Dallas, TX, USA, pp. 467–477.

[113] ACI318–05, 2005. *Building code requirements for structural concrete.* American Concrete Institute, MI, USA.

[114] MacGregor, J. G., 1992. *Reinforced concrete: mechanics and design.* Prentice Hall, NJ, USA.

[115] Nourpanah, N., and Taheri, F., 2009. "Finite element analysis of strain concentration in field joint of concrete coated pipelines". In International Conference on Offshore Mechanics and Arctic Engineering (OMAE), Vol. 3, Honolulu, Hawaii, pp. 35–40.

[116] Nourpanah, N., and Taheri, F., 2009. "A parametric study on strain concentration in field joint of concrete coated pipelines". In International Conference on Pressure Vessel and Piping (PVP), Vol. 3, Prague, Czech Republic, pp. 117–123.

[117] Cheaitani, M. J., 2007. "Case studies on ECA-based flaw acceptance criteria for pipe girth welds using BS 7910: 2005". In International Conference on Offshore Mechanics and Arctic Engineering (OMAE), Vol. 4, pp. 175–83.

[118] Seber, G. A. F., and Wild, C. J., 2003. *Nonlinear regression.* John Wiley and Sons Ltd.

[119] Pisarski, H. G., and Cheaitani, M. J., 2008. "Development of girth weld flaw assessment procedures for pipelines subjected to plastic straining". *Int. J. Offshore Polar Eng.,* **18**(3), pp. 183–187.

[120] K. R. Jayadevan, E. Østby, C. T., 2004. "Fracture response of pipelines subjected to large plastic deformation under tension". *Int. J. Press. Ves. Pip.,* **81**(9), pp. 771–783.

[121] Raju, I. S., and Newman, J. C., 1982. "Stress-intensity factors for internal and external surface cracks in cylindrical vessels". *ASME J. Press. Vess. Technol.,* **104**(4), pp. 293–298.

[122] Parks, D. M., 1977. "The virtual crack extension method for nonlinear material behavior". *Comput. Methods Appl. Mech. Engng.,* **12**(3), pp. 353–364.

[123] Kyriakides, S., Ok, A., and Corona, E., 2008. "Localization and propagation of curvature under pure bending in steel tubes with Lüders bands". *Int. J. Solids Struct.,* **45**(10), pp. 3074–3087.

[124] Parks, D. M., and Wang, Y. Y., 1988. "Elastic–plastic analysis of part-through surface cracks". In *ASME applied mechanics division, AMD, analytical, numerical, and experimental aspects of three dimensional fracture processes*. pp. 19–32.

[125] Nourpanah, N., and Taheri, F., 2010. "Development of a reference strain approach for assessment of fracture response of reeled pipelines". *Engng. Fract. Mech.,* **77**, pp. 2337–2353.

[126] Nourpanah, N., and Taheri, F., 2011. "A numerical study on the crack tip constraint of pipelines subject to extreme plastic bending". *to appear in Journal of Engineering Fracture Mechanics*.

[127] Ainsworth, R. A., and O'Dowd, N. P., 1995. "Constraint in the failure assessment diagram approach for fracture assessment". *ASME J. Press. Vess. Technol.,* **117**, pp. 260–267.

[128] Gordon, J. R., Zettlemoyer, N., and Mohr, W. C., 2007. "Crack driving force in pipelines subjected to large strain and biaxial stress conditions". In International Offshore and Polar Engineering Conference (ISOPE), Lisbon, Portugal, pp. 3129–3140.

[129] Crisfield, M., 1997. *Nonlinear finite element analysis of solids and structures. Volume 2: Advanced topics*. John Wiley and Sons Ltd.

[130] Sandvik, A., Østby, E., and Thaulow, C., 2008. "A probabilistic fracture mechanics model including 3d ductile tearing of bi-axially loaded pipes with surface cracks". *Engng. Fract. Mech.,* **75**(1), pp. 76–96.

[131] Østby, E., and Hellesvik, A. O., 2008. "Large-scale experimental investigation of the effect of biaxial loading on the deformation capacity of pipes with defects". *Int. J. Press. Ves. Pip.,* **85**(11), pp. 814–824.

Appendices

Appendix A

Python Scripts Developed for Parametric FE Studies

As noted in Chapters 3 to 8, all the complicated pre-processing tasks of the FE simulations were automatically performed using in-house developed Python scripts for the ABAQUS/CAE environment. Regarding the large volume of FE simulations reported in this work, and also the general complexity of the FE meshes required for 3D cracks, the presented research in this thesis would have been rendered impossible without the use of the developed Python scripts. In this appendix, the Python scripts developed specifically for the pipeline models in Chapter 8 are presented and discussed. Copies of these developed Python scripts can be freely obtained from the author (`n.nourpanah@dal.ca`).

A.1 General Hierarchy of the Scripts

In order to generate FE models required for a parametric study, a *main* script is used to describe the variation of the parameters of interest (such as D, t, a, c, etc.). The file `main.py` performs this task. For each specific combination of parameters, the *main* script calls and executes a *master* script (`pipeDCG.py`) which produces an ABAQUS input file. The ABAQUS input file contains the FE model definition of a pipeline with a set of specific parameters. For example, if one wants to investigate pipes with $D = 200$, 300, 400 mm and $a = 2$, 4, 6 mm, this would lead to 9 different combinations, and thus, execution of `main.py` would call and execute `pipeDCG.py` nine times, resulting in nine ABAQUS input files (e.g. `DCG_1.inp` to `DCG_9.inp`). After this, the *run* script, `RunAll.py`, should be executed, which sequentially passes these input files to the ABAQUS/EXPLICIT solver for their solution. As described, in the process of a FE parametric study, the user only executes two scripts, namely `main.py` and `RunAll.py`, and the script `pipeDCG.py` is called by `main.py` during its execution.

Within the ABAQUS environment, the Python scripts can be conveniently executed by two methods. First is within the ABAQUS/CAE graphical user interface (GUI). This can be done by going to the *File* menu and selecting *Run Script*, which opens a window that the required script can be selected from. Alternatively, the script can be run from the Command Line Interface (CLI) of the GUI of ABAQUS/CAE. This is done by the following command (which executes the `main.py` script):

```
execfile('C://FileDirectory//main.py')
```

In the second method, the script is executed from a terminal window and the GUI of ABAQUS/CAE is

```
abaqus cae noGUI="c:\FileDirectory\main.py"
```

A.2 The *Main* Script

The (typical) `main.py` Python script presented below constructs four FE models based on various combinations of $D/t = 10.0$, 15.0 and $a/t = 0.2$, 0.3. All four models have $2c = 100$ mm and $n = 25.0$. The four models are subject to a bending strain of $\varepsilon_g = 0.05$, 0.04, 0.045, 0.035 respectively. After execution, the four ABAQUS input files, namely `DCG_1.inp` to `DCG_4.inp` would be made.

```
import os
os.chdir(r'g://Nikzad//PipeDCG')
DirPath = 'g://Nikzad//PipeDCG//'
from abaqus import *
import testUtils
import cmath
testUtils.setBackwardCompatibility()
from abaqusConstants import *
import sketch
import part
import mesh
import material
import assembly
import regionToolset
import interaction
import job
```

```
myFile = open('summaryOfCasesFS.txt', 'w')
t = 20.0
E=200.0e3
sy=400.0
el=sy/E
egAll=(0.05, 0.04, 0.045, 0.035)
p1Range=(10.0, 15.0)
p2Range = (0.2, 0.3)
p3Range = (100.0, )
p4Range = (25.0, )
p5Range = (0.0,)
cnt1 = 0
cnt2 = 1
p1loop = 1
for p1 in p1Range:
    D = t * p1
    R = D / 2.0
    cnt1 = cnt1 + 1
    p2loop = 1
    for p2 in p2Range:
        a0 = p2 * t
        p3loop = 1
        for p3 in p3Range:
            c=p3/2.0
            p4loop = 1
            for p4 in p4Range:
                ndp = p4
                p5loop = 1
                for p5 in p5Range:
                    epsilonGlobal=egAll[p5loop-1]
                    #el = p5
                    pFactor=p5
                    codeName = str(p1loop) + str(p2loop) +
                        str(p3loop) + str(p4loop)
                    fileName = str(cnt2) + '_' + codeName
                    myFile.write('Case#' + str(cnt2).rjust(3) + ' Code#'
                        + str(codeName).ljust(4) + ' D= ' + str(D).ljust(6) +
                        ' t= ' + str(t).ljust(6) + ' D/t= ' + str(D/t).ljust(6)
```

```
                        + ' a/t= ' + str(a0/t).ljust(6) + ' beta/pi= ' +
                        str(p3).ljust(6) + ' n= ' + str(p4).ljust(6) +
                        ' sy/su= ' + str(p4RangeR[p4loop-1]).ljust(6) + '\n')
                    tempFile = open('infoTemp.txt', 'w')
                    tempFile.write(str(cnt2)+'\n')
                    tempFile.write(str(D)+'\n')
                    tempFile.write(str(t)+'\n')
                    tempFile.write(str(a0)+'\n')
                    tempFile.write(str(c)+'\n')
                    tempFile.write(str(ndp)+'\n')
                    tempFile.write(str(el)+'\n')
                    tempFile.write(str(pFactor)+'\n')
                    tempFile.write(str(E)+'\n')
                    tempFile.write(str(sy)+'\n')
                    tempFile.write(str(epsilonGlobal)+'\n')
                    tempFile.close()
                    execfile(DirPath + 'PipeDCG.py')
                    cnt2 = cnt2 + 1
                    p5loop = p5loop + 1
                p4loop = p4loop + 1
            p3loop = p3loop + 1
        p2loop = p2loop + 1
    p1loop = p1loop + 1
myFile.close()
```

A.3 The *Run* Script

The (typical) `RunAll.py` Python script presented sequentially passes the files `DCG_1.inp` to `DCG_20.inp` to the ABAQUS/EXPLICIT solver for solution. 16 cpus and 90% of the physical memory are used for each analysis.

```
import os
os.chdir(r'g:\\Nikzad\\PipeDCG')
DirPath = "g:\\Nikzad\\PipeDCG\\"
from abaqus import *
import time
Output = DirPath + 'RunTimes.txt'
File = open(Output, 'a')
```

```
File.write('----------------------------------------\n')
imin = 1
imax = 20
for i in range(imin, imax+1, 1):
    fileName = 'DCG_' + str(i) + '.inp'
    jobName = 'DCG_' + str(i)
    myJob = mdb.JobFromInputFile(name=jobName, inputFileName=fileName, type=ANALYSIS,
        explicitPrecision=SINGLE, nodalOutputPrecision=SINGLE,
        parallelizationMethodExplicit=DOMAIN, multiprocessingMode=DEFAULT,
        numDomains=16, userSubroutine='', numCpus=16, memory=90,
        memoryUnits=PERCENTAGE, scratch='')
    startTime=time.clock()
    myJob.submit()
    myJob.waitForCompletion()
    finishTime=time.clock()
    File.write(str(i).ljust(6)+str((finishTime-startTime)/60.0).ljust(20)+'min\n')
File.close()
```

A.4 The *Master* Script

The `pipeDCG.py` Python script constructs an FE model with a specific combination of parameters (as passed to it from the `main.py` script) and writes the corresponding ABAQUS input file. Various variables are used which define the geometric features of the pipeline, crack, and most importantly, the characteristics of the FE mesh. The most important of these variables are schematically illustrated in Figure A.1 and Figure A.2 (The coarse mesh depicted in these figures are used for clarity of the illustration). The `pipeDCG.py` script is as follows[1]:

[1]Python regards lines starting with # as a *comment*.

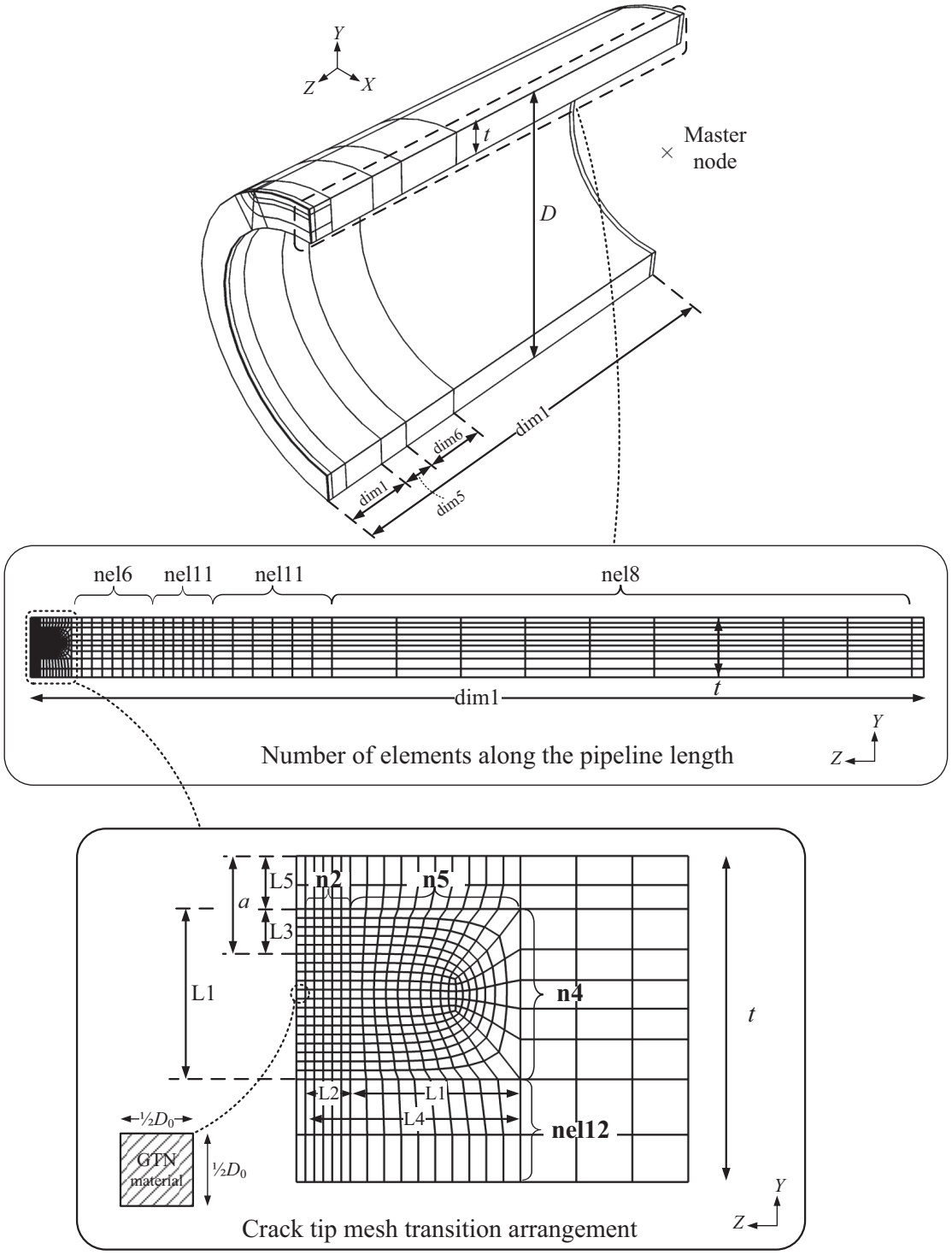

Figure A.1. Schematic of the pipeline dimensions and mesh characteristics as used in the *master* script.

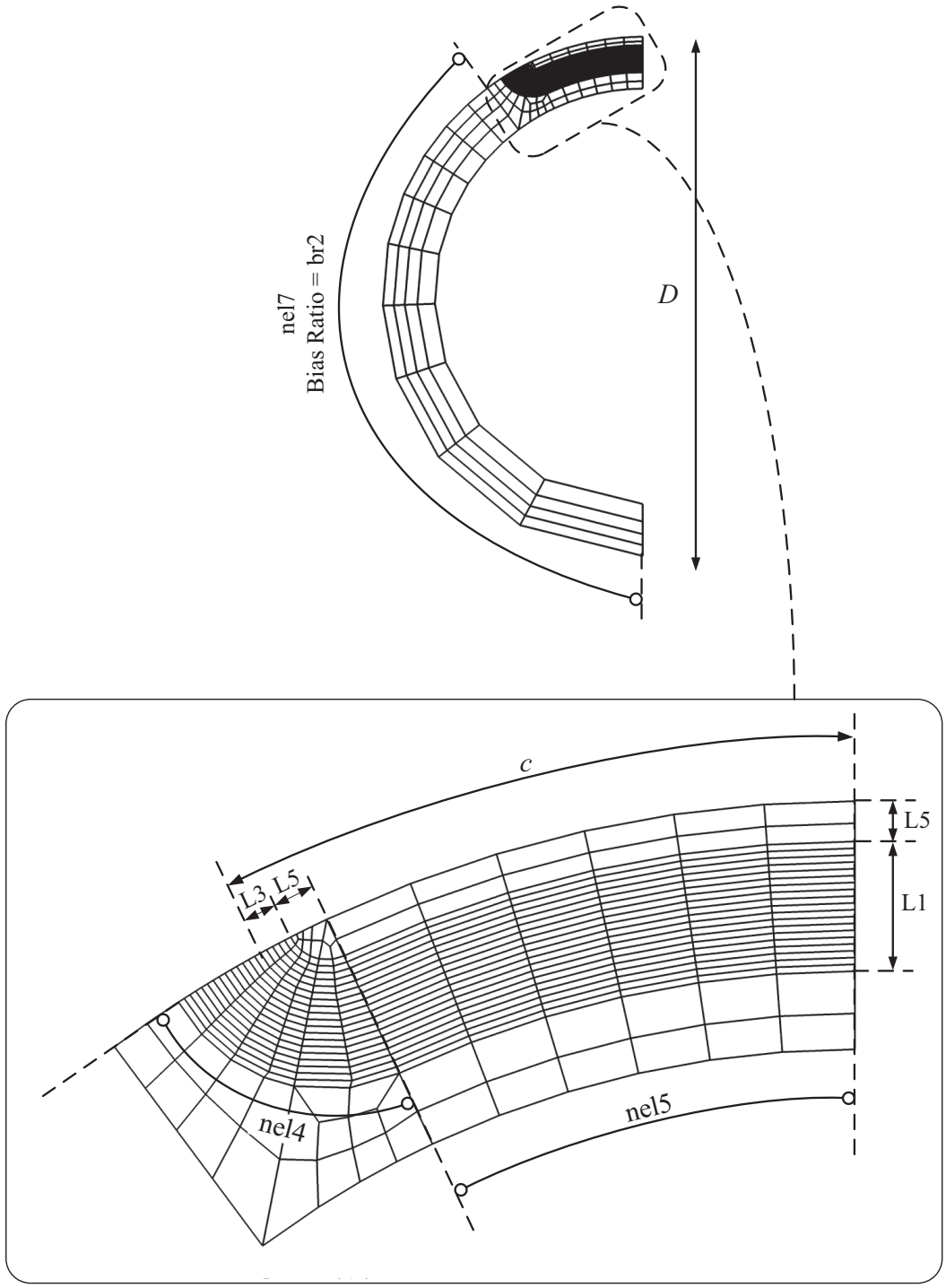

Figure A.2. Schematic of the cracked cross section of the pipeline showing dimensions and mesh characteristics as used in the *master* script.

```
"""
this script constructs a quarter symmetric model of a pipe
containing a part-through circumferential crack
Mesh for study of Ductile Crack Growth (DCG)
Nikzad Nourpanah, July 2010
"""
from abaqus import *
import testUtils
import cmath
testUtils.setBackwardCompatibility()
from abaqusConstants import *
import sketch
import part
import mesh
import material
import assembly
import regionToolset
import interaction
import job
import step
session.journalOptions.setValues(replayGeometry = COORDINATE)
tolr = 1e-4
tempFile = open('infoTemp.txt', 'r')
allLines = tempFile.readlines()
cnt2 = float(allLines[0][0:10])
cnt2 = int(cnt2)
D = float(allLines[1][0:10])
t = float(allLines[2][0:10])
a0 = float(allLines[3][0:10])
c = float(allLines[4][0:10])
ndp = float(allLines[5][0:10])
el = float(allLines[6][0:10])
pFactor = float(allLines[7][0:10])
E = float(allLines[8][0:10])
sy = float(allLines[9][0:10])
epsilonGlobal = float(allLines[10][0:10])
tempFile.close()
nu = 0.3
```

```
infoFileName = 'DCG_info_' + str(cnt2) + '.txt'
myFile6 = open(infoFileName, 'w')
##############################################################################################
################################### GENERAL SOLUTION ###########################
##############################################################################################
timePerBend=timePerPressure=1.0
numInt1=400
numInt2=4
numCpus1 = 16
numDomains1 = numCpus1
NumIncBend=2*100000
TimeIncBend=float(timePerBend/NumIncBend)
NumIncPressure=2*100000
TimeIncPressure=float(timePerPressure/NumIncPressure)
dens1=7850.0e-12
##############################################################################################
######################################### ELEMENT ##################################
##############################################################################################
elem1 = C3D8R
elem2 = C3D6
elem3 = C3D4
##############################################################################################
######################################### GEOMETRY ##################################
##############################################################################################
a=a0
dim3=3.0*R
beta = c/R
beta1 = (c-a)/R
ff = 1.0
alpha0=epsilonGlobal*dim3/R
##############################################################################################
###################################### GTN MATERIAL ##############################
##############################################################################################

D0 = 1.1
f0GTN = 0.0002
fr = 4.0
fcritical = 0.013
```

```
fextinct = 0.1504
if ndp==10.0:
    q1GTN = 1.46
    q2GTN = 0.931

if ndp==25.0:
    q1GTN = 1.678
    q2GTN = 0.975
##############################################################################################
#################################### SEEDING ##################################################
##############################################################################################
nel4=6
nel5=6
nel7=10
nel8=10
nel11=6
nel12=2

n1 = 19
n2 = 5
n3 = 5
n4 = 5
n5 = 10
nel6 = 8

L1 = float(n1)*D0/2.0
L2 = float(n2)*D0/2.0
L3 = float(n3)*D0/2.0
L4 = 0.5*D0+L2+L1
L5 = a-L3
beta3 = (c-L5)/R
dim2 = 2.0*(L1-L3)
if R-a-dim2>R-t:
    beta2=(c+dim2)/R
else:
    beta2=(c+t-a)/R

dim1 = 3.0*L4
```

```
dim5 = 1.0*t
dim6 = 2.0*t
br2=5.0
globalSeedSize = 4.0
################################################################################
############################## WRITING TEXT FILE ###############################
################################################################################
myFile6.write('timePer1'.ljust(25) + '|' + str(timePerBend).ljust(25) + '\n')
myFile6.write('numInt1'.ljust(25) + '|' +str(numInt1).ljust(25) + '\n')
myFile6.write('numCpus1'.ljust(25) + '|' +str(numCpus1).ljust(25) + '\n')
myFile6.write('NumIncBend'.ljust(25) + '|' +str(NumIncBend).ljust(25) + '\n')
myFile6.write('elem1'.ljust(25) + '|' +str(elem1).ljust(25) + '\n')
myFile6.write('elem2'.ljust(25) + '|' +str(elem2).ljust(25) + '\n')
myFile6.write('elem3'.ljust(25) + '|' +str(elem3).ljust(25) + '\n')
myFile6.write('Density'.ljust(25) + '|' + str(dens1).ljust(25) + '\n')
myFile6.write('E'.ljust(25) + '|' + str(E).ljust(25) + '\n')
myFile6.write('nu'.ljust(25) + '|' + str(nu).ljust(25) + '\n')
myFile6.write('sy'.ljust(25) + '|' + str(sy).ljust(25) + '\n')
myFile6.write('n'.ljust(25) + '|' + str(ndp).ljust(25) + '\n')
myFile6.write('D0'.ljust(25) + '|' + str(D0).ljust(25) + '\n')
myFile6.write('f0'.ljust(25) + '|' + str(f0GTN).ljust(25) + '\n')
myFile6.write('fc'.ljust(25) + '|' + str(fcritical).ljust(25) + '\n')
myFile6.write('fe'.ljust(25) + '|' + str(fextinct).ljust(25) + '\n')
myFile6.write('q1'.ljust(25) + '|' + str(q1GTN).ljust(25) + '\n')
myFile6.write('q2'.ljust(25) + '|' + str(q2GTN).ljust(25) + '\n')
myFile6.write('D'.ljust(25) + '|' + str(D).ljust(25) + '\n')
myFile6.write('t'.ljust(25) + '|' + str(t).ljust(25) + '\n')
myFile6.write('a0'.ljust(25) + '|' + str(a0).ljust(25) + '\n')
myFile6.write('c'.ljust(25) + '|' + str(c).ljust(25) + '\n')
myFile6.write('epsilonGlobal'.ljust(25) + '|' +
    str(epsilonGlobal).ljust(25) + '\n')
myFile6.write('dim1'.ljust(25) + '|' + str(dim1).ljust(25) + '\n')
myFile6.write('dim2'.ljust(25) + '|' + str(dim2).ljust(25) + '\n')
myFile6.write('dim3'.ljust(25) + '|' + str(dim3).ljust(25) + '\n')
myFile6.write('dim5'.ljust(25) + '|' + str(dim5).ljust(25) + '\n')
myFile6.write('dim6'.ljust(25) + '|' + str(dim6).ljust(25) + '\n')
myFile6.write('n1'.ljust(25) + '|' + str(n1).ljust(25) + '\n')
myFile6.write('n2'.ljust(25) + '|' + str(n2).ljust(25) + '\n')
```

```
myFile6.write('n3'.ljust(25) + '|' + str(n3).ljust(25) + '\n')
myFile6.write('n4'.ljust(25) + '|' + str(n4).ljust(25) + '\n')
myFile6.write('n5'.ljust(25) + '|' + str(n5).ljust(25) + '\n')
myFile6.write('nel6'.ljust(25) + '|' + str(nel6).ljust(25) + '\n')
myFile6.write('nel4'.ljust(25) + '|' + str(nel4).ljust(25) + '\n')
myFile6.write('nel5'.ljust(25) + '|' + str(nel5).ljust(25) + '\n')
myFile6.write('nel7'.ljust(25) + '|' + str(nel7).ljust(25) + '\n')
myFile6.write('nel8'.ljust(25) + '|' + str(nel8).ljust(25) + '\n')
myFile6.write('nel10'.ljust(25) + '|' + str(nel10).ljust(25) + '\n')
myFile6.write('nel11'.ljust(25) + '|' + str(nel11).ljust(25) + '\n')
myFile6.write('nel12'.ljust(25) + '|' + str(nel12).ljust(25) + '\n')
myFile6.write('CircumBiasRatio'.ljust(25) + '|' + str(br2).ljust(25) + '\n')
myFile6.write('globalSeedSize'.ljust(25) + '|'
    + str(globalSeedSize).ljust(25) + '\n')
myFile6.write('LudersTerminationStrain'.ljust(25) + '|'
    + str(el).ljust(25) + '\n')
myFile6.write('InternalPressureFactor'.ljust(25) + '|'
    + str(pFactor).ljust(25) + '\n')
##############################################################################
############################### MODEL CONSTRUCTION ###########################
##############################################################################
ModelName = 'DCG_' + str(cnt2)
myModel = mdb.Model(name=ModelName)
mySketch = myModel.ConstrainedSketch(name='Sketch pipe', sheetSize=2*R)

xyCoords = ((0.0, 0.0),
    (0.0, R-t), (0.0, R),
    (-R*sin(pi/ff), R*cos(pi/ff)),
    (-(R-t)*sin(pi/ff), (R-t)*cos(pi/ff)))

mySketch.ArcByCenterEnds(center=xyCoords[0],
    point1=xyCoords[1],
    point2=xyCoords[3])

mySketch.ArcByCenterEnds(center=xyCoords[0],
    point1=xyCoords[2],
    point2=xyCoords[4])
```

```
mySketch.Line(point1=xyCoords[1],
    point2=xyCoords[2])

mySketch.Line(point1=xyCoords[3],
    point2=xyCoords[4])

solidPart = myModel.Part(name='CrackPiece',
    dimensionality=THREE_D,
    type=DEFORMABLE_BODY)

solidPart.BaseSolidExtrude(sketch=mySketch, depth=dim3)
#############################################################################
sketch0 = myModel.ConstrainedSketch(name='canoe crack sketch - centerline',
    sheetSize=3*R,
    transform = (1,0,0,0,1,0,0,0,1,0,0,dim3))
crackTipSketch2 = myModel.ConstrainedSketch(
    name='canoe crack sketch - second offset',
    sheetSize=3*R,
    transform = (1,0,0,0,1,0,0,0,1,0,0,dim3))
crackTipSketch3 = myModel.ConstrainedSketch(
    name='canoe crack sketch - first offset',
    sheetSize=3*R,
    transform = (1,0,0,0,1,0,0,0,1,0,0,dim3))
#############################################################################
sketch0.ArcByCenterEnds(center=(0.0, 0.0),
    point1=(0.0, R-a+L3),
    point2=(-(R-L5)*sin(beta1), (R-L5)*cos(beta1)))
sketch0.ArcByCenterEnds(center=(-R*sin(beta1), R*cos(beta1)),
    point1=(-(R+L5)*sin(beta1), (R+L5)*cos(beta1)),
    point2=(-(R-L5)*sin(beta1), (R-L5)*cos(beta1)))
faceTemp = solidPart.faces.findAt((-(R-t/2)*sin(0.5*pi/ff),
    (R-t/2)*cos(0.5*pi/ff), dim3))
solidPart.PartitionFaceBySketch(faces = faceTemp, sketch = sketch0)
#############################################################################
transformProfile=(0.0, 0.0, -1.0, 0.0, 1.0, 0.0, 1.0, 0.0, 0.0, 0.0, 0.0, dim3)
sketch8 = myModel.ConstrainedSketch(name='sketch8',
    sheetSize=R, transform=transformProfile)
sketch8.Line(point1=(0.0, R-a+L3-L1), point2=(L4, R-a+L3-L1))
```

```
sketch8.Line(point1=(L4, R-a+L3-L1), point2=(L4, R-a+L3))
sketch8.Line(point1=(L4, R-a+L3), point2=(0.0, R-a+L3))
face1=solidPart.faces.findAt((0.0, R-t/2.0, dim3/2.0))
solidPart.PartitionFaceBySketch(faces=face1, sketch=sketch8)
##############################################################################
ed1=solidPart.edges.findAt((0.0, R-a+0.5*L3, dim3))
ed2=solidPart.edges.findAt((0.0, R-L5-L1, dim3-0.5*L4))
ed3=solidPart.edges.findAt((0.0, R-L5-0.5*L1, dim3-L4))
ed4=solidPart.edges.findAt((0.0, R-L5, dim3-0.5*L4))
ed5=[ed1, ed2, ed3, ed4]
ed6=solidPart.edges.findAt((-(R-L5)*sin(0.5*beta1), (R-L5)*cos(0.5*beta1), dim3))
solidPart.PartitionCellBySweepEdge(cells=solidPart.cells,
    edges=ed5, sweepPath=ed6)
##############################################################################
ed7=[]
for ed in solidPart.edges:
    x=ed.pointOn[0][0]
    if x==0.0: x=0.0001
    y=ed.pointOn[0][1]
    z=ed.pointOn[0][2]
    t1=abs(x)/y
    if abs(t1-tan(beta1))<tolr:
        ed7 += [ed]

x1=-R*sin(beta1)-L5*sin(pi/3.0-beta1)
y1=R*cos(beta1)-L5*cos(pi/3.0-beta1)
z1=dim3
ed8=solidPart.edges.findAt((x1,y1,z1))
solidPart.PartitionCellBySweepEdge(cells=solidPart.cells,
    edges=ed7, sweepPath=ed8)
##############################################################################
sketch7 = myModel.ConstrainedSketch(name='canoe crack sketch - crack front',
    sheetSize=3*R,
    transform = (1,0,0,0,1,0,0,0,1,0,0,dim3))
sketch7.ArcByCenterEnds(center=(0.0, 0.0),
    point1=(0.0, R-a),
    point2=(-(R-a)*sin(beta1), (R-a)*cos(beta1)))
sketch7.ArcByCenterEnds(center=(-R*sin(beta1), R*cos(beta1)),
```

```
    point1=(-(R+a)*sin(beta1), (R+a)*cos(beta1)),
    point2=(-(R-a)*sin(beta1), (R-a)*cos(beta1)))
face1 = solidPart.faces.findAt((-(R-a)*sin(0.5*beta1),
    (R-a)*cos(0.5*beta1), dim3))
solidPart.PartitionFaceBySketch(faces=face1, sketch=sketch7)

xt1 = -R*sin(beta1)-a*sin(pi/3.0-beta1)
yt1 = R*cos(beta1)-a*cos(pi/3.0-beta1)
face2 = solidPart.faces.findAt((xt1, yt1, dim3))
solidPart.PartitionFaceBySketch(faces=face2, sketch=sketch7)
##############################################################################
sketch9 = myModel.ConstrainedSketch(name='sketch9',
    sheetSize=3*R,
    transform = (1,0,0,0,1,0,0,0,1,0,0,dim3))
sketch9.ArcByCenterEnds(center=(0.0, 0.0),
    point1=(0.0, R-a-dim2),
    point2=(0.0, -(R-a-dim2)) )

face1 = solidPart.faces.findAt((-0.99*R, 0.0, dim3))
if(R-a-dim2>R-t):
    solidPart.PartitionFaceBySketch(faces=face1, sketch=sketch9)
##############################################################################
#DATUM OBJECT NUMBER 0 (for solidPart)
solidPart.DatumPlaneByPrincipalPlane(principalPlane=YZPLANE, offset=0)
##############################################################################
#DATUM OBJECT NUMBER 1 (for solidPart)
solidPart.DatumAxisByPrincipalAxis(principalAxis=ZAXIS)
allDatums = solidPart.datums
datumIDs = allDatums.keys()
##############################################################################
#DATUM OBJECT NUMBER 2 (for solidPart)
solidPart.DatumPlaneByRotation(plane=allDatums[datumIDs[0]],
    axis=allDatums[datumIDs[1]], angle=beta1*180.0/pi)
allDatums = solidPart.datums
datumIDs = allDatums.keys()
solidPart.PartitionCellByDatumPlane(cells = solidPart.cells,
    datumPlane = allDatums[datumIDs[2]])
##############################################################################
```

```
#DATUM OBJECT NUMBER 3 (for solidPart)
solidPart.DatumPlaneByRotation(plane=allDatums[datumIDs[0]],
    axis=allDatums[datumIDs[1]], angle=beta2*180/pi)
allDatums = solidPart.datums
datumIDs = allDatums.keys()
solidPart.PartitionCellByDatumPlane(cells = solidPart.cells,
    datumPlane = allDatums[datumIDs[3]])
##############################################################################
#DATUM OBJECT NUMBER 4
solidPart.DatumPlaneByPrincipalPlane(principalPlane=XYPLANE, offset=dim3-dim1)
allDatums = solidPart.datums
datumIDs = allDatums.keys()
solidPart.PartitionCellByDatumPlane(cells = solidPart.cells,
    datumPlane = allDatums[datumIDs[4]])
##############################################################################
#DATUM OBJECT NUMBER 5
solidPart.DatumPlaneByPrincipalPlane(principalPlane=XYPLANE,
    offset=dim3-dim1-dim5)
allDatums = solidPart.datums
datumIDs = allDatums.keys()
solidPart.PartitionCellByDatumPlane(cells = solidPart.cells,
    datumPlane = allDatums[datumIDs[5]])
##############################################################################
#DATUM OBJECT NUMBER 6
solidPart.DatumPlaneByPrincipalPlane(principalPlane=XYPLANE,
    offset=dim3-dim1-dim5-dim6)
allDatums = solidPart.datums
datumIDs = allDatums.keys()
solidPart.PartitionCellByDatumPlane(cells = solidPart.cells,
    datumPlane = allDatums[datumIDs[6]])
##############################################################################
#DATUM OBJECT NUMBER 7
solidPart.DatumPlaneByPrincipalPlane(principalPlane=XYPLANE, offset=dim3-0.5*D0)
allDatums = solidPart.datums
datumIDs = allDatums.keys()
solidPart.PartitionCellByDatumPlane(cells = solidPart.cells,
    datumPlane = allDatums[datumIDs[7]])
##############################################################################
```

```
#DATUM OBJECT NUMBER 8
solidPart.DatumPlaneByPrincipalPlane(principalPlane=XYPLANE,
    offset=dim3-0.5*D0-L2)
allDatums = solidPart.datums
datumIDs = allDatums.keys()
solidPart.PartitionCellByDatumPlane(cells = solidPart.cells,
    datumPlane = allDatums[datumIDs[8]])
##############################################################################
#DATUM OBJECT NUMBER 9
solidPart.DatumPlaneByPrincipalPlane(principalPlane=XYPLANE, offset=dim3-L4)
allDatums = solidPart.datums
datumIDs = allDatums.keys()
solidPart.PartitionCellByDatumPlane(cells = solidPart.cells,
    datumPlane = allDatums[datumIDs[9]])
##############################################################################
##############################################################################
cl1=[]
for cl in solidPart.cells:
    z=cl.pointOn[0][2]
    if (z>=dim3-L4):
        cl1 += [cl]

if(R-a-dim2>R-t):
    ed9=solidPart.edges.findAt((-(R-a-dim2), 0.0, dim3))
    ed91=solidPart.edges.findAt((-(R-a-dim2)*sin(0.5*beta1),
        (R-a-dim2)*cos(0.5*beta1), dim3))
    ed92=solidPart.edges.findAt((-(R-a-dim2)*sin(0.5*(beta1+beta2)),
        (R-a-dim2)*cos(0.5*(beta1+beta2)), dim3))
    ed99=solidPart.edges.findAt((0.0, R-t, dim3-0.25*D0))
    solidPart.PartitionCellByExtrudeEdge(line=ed99, cells=cl1,
        edges=[ed9,ed91,ed92], sense=REVERSE)
##############################################################################
##############################################################################
ey = sy/E
delE = el-ey
if abs(el-ey)<1.0e-5:
    PowerLawPlasticityTable = ((sy, 0.0), )
else:
```

```
    PowerLawPlasticityTable = ((sy, 0.0), (sy, el-ey), )

for i in range(1, 4000, 1):
    e = el + float(i)*0.001
    sigma = sy*( pow((e-delE)/ey, 1.0/ndp) )
    ep = e - sigma/E
    PowerLawPlasticityTable = PowerLawPlasticityTable + ((sigma, ep), )

##############################################################################
############################### FOR PERFECT PLASTICITY ########################
#PowerLawPlasticityTable = ((sy, 0.0), (sy, 0.7), )
##############################################################################
steelMat=myModel.Material(name = 'steel')
steelMat.Density(table=((dens1,), ))
steelMat.Elastic(table=((E, nu), ))
steelMat.Plastic(table=PowerLawPlasticityTable)
solidSection = myModel.HomogeneousSolidSection(name='Solid Section',
    material='steel')
##############################################################################
pSteelMat=myModel.Material(name ='porous steel')
pSteelMat.Density(table=((dens1,), ))
pSteelMat.Elastic(table=((E, nu), ))
pSteelMat.Plastic(table=PowerLawPlasticityTable)
pSteelMat.PorousMetalPlasticity(table=((q1GTN, q2GTN, q1GTN*q1GTN), ),
    relativeDensity=1.0-f0GTN)
pSteelMat.porousMetalPlasticity.PorousFailureCriteria(fraction=fextinct,
    criticalFraction=fcritical)
PorousSection = myModel.HomogeneousSolidSection(name='Porous Section',
    material='porous steel')
##############################################################################
solidSet = solidPart.Set(name = 'Solid Set', cells = solidPart.cells)
solidPart.SectionAssignment(region = solidSet, sectionName='Solid Section')
##############################################################################
x1=-(R-L5-0.9*L1)*sin(0.5*beta1)
y1=(R-L5-0.9*L1)*cos(0.5*beta1)
x2=-(R-L5-0.9*L1)*sin(1.01*beta1)
y2=(R-L5-0.9*L1)*cos(1.01*beta1)
```

```
cl1=solidPart.cells.findAt(
    [(x1, y1, dim3-0.25*D0), ],
    [(x2, y2, dim3-0.25*D0), ] )

porousSet = solidPart.Set(name='Porous Set', cells=cl1)
solidPart.SectionAssignment(region=porousSet, sectionName='Porous Section')
##############################################################################
edgeTemp1 = solidPart.edges.findAt((-R*sin(0.95*pi/ff), R*cos(0.95*pi/ff), 0))
center = solidPart.InterestingPoint(edge = edgeTemp1, rule = CENTER)
pnt1 = solidPart.vertices.findAt((0, R, 0))
pnt2 = solidPart.InterestingPoint(edge = edgeTemp1, rule = MIDDLE)
#DATUM OBJECT NUMBER 10 (for solidPart)
solidPart.DatumCsysByThreePoints(coordSysType = CYLINDRICAL,
    origin = center, point1 = pnt1, point2 = pnt2)
allDatums = solidPart.datums
datumIDs = allDatums.keys()
solidPart.MaterialOrientation(region = solidSet,
    localCsys = allDatums[datumIDs[10]], axis = AXIS_2, angle = 90.0)
##############################################################################
##############################################################################
myAssembly = myModel.rootAssembly
solidInstance = myAssembly.Instance(name = 'Solid Instance',
    part = solidPart, autoOffset = OFF, dependent = OFF)
myAssembly.translate(instanceList = ('Solid Instance', ), vector = (0, 0, -dim3))
##############################################################################
##############################################################################
elemType1 = mesh.ElemType(elemCode=elem1,
    elemLibrary=EXPLICIT, hourglassControl=ENHANCED)
elemType2 = mesh.ElemType(elemCode=elem2,
    elemLibrary=EXPLICIT, hourglassControl=ENHANCED)
elemType3 = mesh.ElemType(elemCode=elem3,
    elemLibrary=EXPLICIT, hourglassControl=ENHANCED)
myAssembly.setElementType(regions=(solidInstance.cells, ),
    elemTypes=(elemType1, elemType2, elemType3))

##############################################################################
##################################### SWEEP ##################################
##############################################################################
```

```
xt1 = -(R-a)*sin(0.5*beta1)
yt1 = (R-a)*cos(0.5*beta1)
xt2 = -R*sin(beta1)-a*sin(pi/3.0-beta1)
yt2 = R*cos(beta1)-a*cos(pi/3.0-beta1)

cl1 = solidInstance.cells.findAt((xt1, yt1, -0.5*0.5*D0))
cl2 = solidInstance.cells.findAt((xt1, yt1, -0.5*D0-0.5*L2))
cl3 = solidInstance.cells.findAt((xt1, yt1, -0.5*D0-L2-0.5*L1))
cl4 = solidInstance.cells.findAt((xt2, yt2, -0.5*0.5*D0))
cl5 = solidInstance.cells.findAt((xt2, yt2, -0.5*D0-0.5*L2))
cl6 = solidInstance.cells.findAt((xt2, yt2, -0.5*D0-L2-0.5*L1))

cl7 = [cl1, cl2, cl3, cl4, cl5, cl6]
myAssembly.setMeshControls(regions=cl7, elemShape=HEX,
    technique=SWEEP, algorithm=MEDIAL_AXIS, minTransition=OFF)
xt5 = -(R-L5)*sin(0.1*beta1)
yt5 = (R-L5)*cos(0.1*beta1)
edgeTemp1 = solidInstance.edges.findAt((xt5, yt5, -0.5*D0))
myAssembly.setSweepPath(region=(cl7[0]) , edge=edgeTemp1 , sense=REVERSE)
myAssembly.setSweepPath(region=(cl7[1]) , edge=edgeTemp1 , sense=REVERSE)
edgeTemp2 = solidInstance.edges.findAt((xt5, yt5, -L4))
myAssembly.setSweepPath(region=(cl7[2]) , edge=edgeTemp2 , sense=FORWARD)

xt6 = -R*sin(beta1)-L5*sin(pi/3.0-beta1)
yt6 = R*cos(beta1)-L5*cos(pi/3.0-beta1)
edgeTemp3 = solidInstance.edges.findAt((xt6, yt6, -0.5*D0))
myAssembly.setSweepPath(region=(cl7[3]) , edge=edgeTemp3 , sense=FORWARD)
myAssembly.setSweepPath(region=(cl7[4]) , edge=edgeTemp3 , sense=FORWARD)
edgeTemp4 = solidInstance.edges.findAt((xt6, yt6, -L4))
myAssembly.setSweepPath(region=(cl7[5]) , edge=edgeTemp4 , sense=FORWARD)
###############################################################################
################################### SEED ######################################
###############################################################################
e1=solidInstance.edges.findAt((0.0, R-L5-0.5*L3, 0.0))
myAssembly.seedEdgeByNumber(edges=(e1, ), number=n3, constraint = FIXED)

e1=solidInstance.edges.findAt((0.0, R-L5-0.5*(L3+L1), 0.0))
myAssembly.seedEdgeByNumber(edges=(e1, ), number=n1-n3, constraint = FIXED)
```

```
e1=solidInstance.edges.findAt((0.0, R-L5-0.5*L1, -0.5*D0))
myAssembly.seedEdgeByNumber(edges=(e1, ), number=n1, constraint = FIXED)

e1=solidInstance.edges.findAt((0.0, R-L5-0.5*L1, -0.5*D0-L2))
myAssembly.seedEdgeByNumber(edges=(e1, ), number=n1, constraint = FIXED)

e1=solidInstance.edges.findAt((0.0, R-L5-0.5*L1, -L4))
myAssembly.seedEdgeByNumber(edges=(e1, ), number=n4, constraint = FIXED)

e1=solidInstance.edges.findAt((0.0, R-L5, -0.5*0.5*D0))
myAssembly.seedEdgeByNumber(edges=(e1, ), number=1, constraint = FIXED)
e1=solidInstance.edges.findAt((0.0, R-L5-L1, -0.5*0.5*D0))
myAssembly.seedEdgeByNumber(edges=(e1, ), number=1, constraint = FIXED)

e1=solidInstance.edges.findAt((0.0, R-L5, -0.5*D0-0.5*L2))
myAssembly.seedEdgeByNumber(edges=(e1, ), number=n2, constraint = FIXED)
e1=solidInstance.edges.findAt((0.0, R-L5-L1, -0.5*D0-0.5*L2))
myAssembly.seedEdgeByNumber(edges=(e1, ), number=n2, constraint = FIXED)

e1=solidInstance.edges.findAt((0.0, R-L5, -0.5*D0-L2-0.5*L1))
myAssembly.seedEdgeByNumber(edges=(e1, ), number=n5, constraint = FIXED)
e1=solidInstance.edges.findAt((0.0, R-L5-L1, -0.5*D0-L2-0.5*L1))
myAssembly.seedEdgeByNumber(edges=(e1, ), number=n5, constraint = FIXED)
##############################################################################
################################### SEED NEL8 ################################
##############################################################################
ed1=[]
for ed in solidInstance.edges:
    x=ed.pointOn[0][0]
    z=ed.pointOn[0][2]
    if ((abs(x)<tolr) & (z<-dim1-dim5-dim6) & (z>-dim3)):
        ed1 += [ed]

myAssembly.seedEdgeByNumber(edges=ed1, number=nel8, constraint = FIXED)
##############################################################################
################################### SEED NEL11 ###############################
##############################################################################
```

```
ed1=[]
for ed in solidInstance.edges:
    x=ed.pointOn[0][0]
    z=ed.pointOn[0][2]
    if ((abs(x)<tolr) & (z<-dim1-dim5) & (z>-dim1-dim5-dim6)):
        ed1 += [ed]

myAssembly.seedEdgeByNumber(edges=ed1, number=nel11, constraint = FIXED)
##############################################################################
ed1=[]
for ed in solidInstance.edges:
    x=ed.pointOn[0][0]
    z=ed.pointOn[0][2]
    if ((abs(x)<tolr) & (z<-dim1) & (z>-dim1-dim5)):
        ed1 += [ed]

myAssembly.seedEdgeByNumber(edges=ed1, number=nel11, constraint = FIXED)
##############################################################################
################################### SEED NEL6 ################################
##############################################################################
ed1=[]
for ed in solidInstance.edges:
    x=ed.pointOn[0][0]
    z=ed.pointOn[0][2]
    if ((abs(x)<tolr) & (z<-L4) & (z>-0.99*dim1)):
        ed1 += [ed]

myAssembly.seedEdgeByNumber(edges=ed1, number=nel6, constraint = FIXED)
##############################################################################
################################### SEED NEL7 ################################
##############################################################################
e1=solidInstance.edges.findAt((-R,0.0,0.0))
myAssembly.seedEdgeByBias(end2Edges = (e1,), ratio = br2,
    number = nel7, constraint = FIXED)

e1=solidInstance.edges.findAt((-R,0.0,-0.5*D0))
myAssembly.seedEdgeByBias(end1Edges = (e1,), ratio = br2,
    number = nel7, constraint = FIXED)
```

```
e1=solidInstance.edges.findAt((-R,0.0,-0.5*D0-L2))
myAssembly.seedEdgeByBias(end1Edges = (e1,), ratio = br2,
    number = nel7, constraint = FIXED)

e1=solidInstance.edges.findAt((-R,0.0,-L4))
myAssembly.seedEdgeByBias(end1Edges = (e1,), ratio = br2,
    number = nel7, constraint = FIXED)

e1=solidInstance.edges.findAt((-R,0.0,-dim1))
myAssembly.seedEdgeByBias(end1Edges = (e1,), ratio = br2,
    number = nel7, constraint = FIXED)

e1=solidInstance.edges.findAt((-R,0.0,-dim1-dim5))
myAssembly.seedEdgeByBias(end1Edges = (e1,), ratio = br2,
    number = nel7, constraint = FIXED)

e1=solidInstance.edges.findAt((-R,0.0,-dim1-dim5-dim6))
myAssembly.seedEdgeByBias(end1Edges = (e1,), ratio = br2,
    number = nel7, constraint = FIXED)

e1=solidInstance.edges.findAt((-R,0.0,-dim3))
myAssembly.seedEdgeByBias(end1Edges = (e1,), ratio = br2,
    number = nel7, constraint = FIXED)
##############################################################################
e1=solidInstance.edges.findAt((-R+t,0.0,0.0))
myAssembly.seedEdgeByBias(end1Edges = (e1,), ratio = br2,
    number = nel7, constraint = FIXED)

e1=solidInstance.edges.findAt((-R+t,0.0,-0.5*D0))
myAssembly.seedEdgeByBias(end2Edges = (e1,), ratio = br2,
    number = nel7, constraint = FIXED)

e1=solidInstance.edges.findAt((-R+t,0.0,-0.5*D0-L2))
myAssembly.seedEdgeByBias(end2Edges = (e1,), ratio = br2,
    number = nel7, constraint = FIXED)

e1=solidInstance.edges.findAt((-R+t,0.0,-L4))
```

```
myAssembly.seedEdgeByBias(end2Edges = (e1,), ratio = br2,
    number = nel7, constraint = FIXED)

e1=solidInstance.edges.findAt((-R+t,0.0,-dim1))
myAssembly.seedEdgeByBias(end2Edges = (e1,), ratio = br2,
    number = nel7, constraint = FIXED)

e1=solidInstance.edges.findAt((-R+t,0.0,-dim1-dim5))
myAssembly.seedEdgeByBias(end2Edges = (e1,), ratio = br2,
    number = nel7, constraint = FIXED)

e1=solidInstance.edges.findAt((-R+t,0.0,-dim1-dim5-dim6))
myAssembly.seedEdgeByBias(end2Edges = (e1,), ratio = br2,
    number = nel7, constraint = FIXED)

e1=solidInstance.edges.findAt((-R+t,0.0,-dim3))
myAssembly.seedEdgeByBias(end1Edges = (e1,), ratio = br2,
    number = nel7, constraint = FIXED)
##############################################################################
if(R-a-dim2>R-t):
    e1=solidInstance.edges.findAt((-R+a+dim2,0.0,0.0))
    myAssembly.seedEdgeByBias(end1Edges = (e1,), ratio = br2,
        number = nel7, constraint = FIXED)

    e1=solidInstance.edges.findAt((-R+a+dim2,0.0,-0.5*D0))
    myAssembly.seedEdgeByBias(end2Edges = (e1,), ratio = br2,
        number = nel7, constraint = FIXED)

    e1=solidInstance.edges.findAt((-R+a+dim2,0.0,-0.5*D0-L2))
    myAssembly.seedEdgeByBias(end2Edges = (e1,), ratio = br2,
        number = nel7, constraint = FIXED)

    e1=solidInstance.edges.findAt((-R+a+dim2,0.0,-L4))
    myAssembly.seedEdgeByBias(end2Edges = (e1,), ratio = br2,
        number = nel7, constraint = FIXED)
##############################################################################
################################### SEED NEL12 ###############################
##############################################################################
```

```
e1=solidInstance.edges.findAt((0.0, R-L5-1.01*L1, 0.0))
myAssembly.seedEdgeByNumber(edges=(e1, ), number=nel12, constraint = FIXED)

e1=solidInstance.edges.findAt((0.0, R-L5-1.01*L1, -0.5*D0))
myAssembly.seedEdgeByNumber(edges=(e1, ), number=nel12, constraint = FIXED)

e1=solidInstance.edges.findAt((0.0, R-L5-1.01*L1, -0.5*D0-L2))
myAssembly.seedEdgeByNumber(edges=(e1, ), number=nel12, constraint = FIXED)

e1=solidInstance.edges.findAt((0.0, R-L5-1.01*L1, -L4))
myAssembly.seedEdgeByNumber(edges=(e1, ), number=nel12, constraint = FIXED)

e1=solidInstance.edges.findAt((-R*sin(0.99*beta2),R*cos(0.99*beta2),0.0))
myAssembly.seedEdgeByNumber(edges=(e1, ), number=nel12, constraint = FIXED)
###############################################################################
################################### SEED NEL5 #################################
###############################################################################
e1=solidInstance.edges.findAt((-(R-L5-L1)*sin(0.5*beta1),
    (R-L5-L1)*cos(0.5*beta1), 0.0))
myAssembly.seedEdgeByNumber(edges=(e1, ), number=nel5, constraint = FIXED)
###############################################################################
################################### SEED NEL4 #################################
###############################################################################
x6 = -R*sin(beta1)-(L5+L1)*sin(pi/3.0-beta1)
y6 = R*cos(beta1)-(L5+L1)*cos(pi/3.0-beta1)
e1=solidInstance.edges.findAt((x6, y6, 0.0))
myAssembly.seedEdgeByNumber(edges=(e1, ), number=nel4, constraint = FIXED)
###############################################################################
myAssembly.seedPartInstance(regions=(solidInstance, ), size=globalSeedSize)
###############################################################################
#DATUM OBJECT NUMBER 0 (for myAssembly)
myAssembly.DatumPlaneByPrincipalPlane(principalPlane=XYPLANE, offset=-dim3+0.2*t)
allDatums = myAssembly.datums
datumIDs = allDatums.keys()
myAssembly.PartitionCellByDatumPlane(cells=solidInstance.cells,
    datumPlane=allDatums[datumIDs[0]])
###############################################################################
rin = 0.5*D-t
```

```
sf=solidInstance.faces
i=0
for fc in sf:
    x=fc.pointOn[0][0]
    y=fc.pointOn[0][1]
    rrin = sqrt(x*x+y*y)
    if (abs(rrin-rin)<tolr):
        if i==0:
            fc100 = sf[fc.index:fc.index+1]
            i+=1
        else:
            fc100 += sf[fc.index:fc.index+1]

myAssembly.Surface(side1Faces=fc100, name='PipeInnerSurface')
##############################################################################
prevStep = 'Initial'
if pFactor!=0.0:
    pressureStep = myModel.ExplicitDynamicsStep(name='Pressure',
        previous=prevStep, timePeriod=timePerPressure, nlgeom=ON,
        maxIncrement=0.1, )
    prevStep = 'Pressure'

    pressureStep.setValues(massScaling=((SEMI_AUTOMATIC,
        MODEL, THROUGHOUT_STEP, 0.0, TimeIncPressure,
        BELOW_MIN, 0, 100, 0.0, 0.0, 0, None),) )

##############################################################################
bendingStep = myModel.ExplicitDynamicsStep(name='Bending', previous=prevStep,
    timePeriod=timePerBend, nlgeom=ON,
    maxIncrement=0.1, )

bendingStep.setValues(massScaling=((SEMI_AUTOMATIC,
    MODEL, THROUGHOUT_STEP, 0.0, TimeIncBend,
    BELOW_MIN, 0, 100, 0.0, 0.0, 0, None),) )
##############################################################################
################################### XSYMM BC #################################
##############################################################################
sf=solidInstance.faces
```

```
i=0
for fc in sf:
    x=fc.pointOn[0][0]
    z=fc.pointOn[0][2]
    if ((abs(x)<tolr) & (z>-dim3+0.2*t)):
        if i==0:
            fc99 = sf[fc.index:fc.index+1]
            i+=1
        else:
            fc99 += sf[fc.index:fc.index+1]

region3 = regionToolset.Region(faces = fc99)
myModel.XsymmBC(name='solid Xsymm BC', createStepName='Initial', region=region3)
##############################################################################################
################################### ZSYMM BC #################################################
##############################################################################################
x1=-(R-0.99*t)*sin(0.5*beta1)
y1=(R-0.99*t)*cos(0.5*beta1)
x2=-(R-0.99*t)*sin(0.5*(beta1+beta2))
y2=(R-0.99*t)*cos(0.5*(beta1+beta2))
x3=-(R-0.99*t)*sin(1.1*beta2)
y3=(R-0.99*t)*cos(1.1*beta2)
x4=-(R-L5-0.99*L1)*sin(0.5*beta1)
y4=(R-L5-0.99*L1)*cos(0.5*beta1)
x5=-(R-L5-0.9*L1)*sin(1.01*beta1)
y5=(R-L5-0.9*L1)*cos(1.01*beta1)

x11=-(R-a-0.99*dim2)*sin(0.5*beta1)
y11=(R-a-0.99*dim2)*cos(0.5*beta1)
x21=-(R-a-0.99*dim2)*sin(0.5*(beta1+beta2))
y21=(R-a-0.99*dim2)*cos(0.5*(beta1+beta2))
x31=-(R-a-0.99*dim2)*sin(1.1*beta2)
y31=(R-a-0.99*dim2)*cos(1.1*beta2)

if(R-a-dim2>R-t):
    faceTemp1 = solidInstance.faces.findAt(
        [(x1, y1, 0.0), ],
        [(x2, y2, 0.0), ],
```

```
        [(x3, y3, 0.0), ],
        [(x4, y4, 0.0), ],
        [(x5, y5, 0.0), ],
        [(x11, y11, 0.0), ],
        [(x21, y21, 0.0), ],
        [(x31, y31, 0.0), ] )

if(R-a-dim2<=R-t):
    faceTemp1 = solidInstance.faces.findAt(
        [(x1, y1, 0.0), ],
        [(x2, y2, 0.0), ],
        [(x3, y3, 0.0), ],
        [(x4, y4, 0.0), ],
        [(x5, y5, 0.0), ] )

region5 = regionToolset.Region(faces = faceTemp1)
myModel.ZsymmBC(name='solid Zsymm BC', createStepName='Initial', region=region5)
##############################################################################
################################ COUPLING MASTER POINT ########################
##############################################################################
edgeTemp1 = solidInstance.edges.findAt((-(R-t), 0.0, -dim3))
#REFERENCE POINT NUMBER 0 (for myAssembly)
pointTemp1 = solidInstance.InterestingPoint(edge = edgeTemp1, rule = CENTER)
myAssembly.ReferencePoint(point = pointTemp1)

allRefPoints = myAssembly.referencePoints
refPointIDs = allRefPoints.keys()
refPoint1 = (allRefPoints[refPointIDs[0]], )
region1 = regionToolset.Region(referencePoints = refPoint1)

faceTemp1 = solidInstance.faces.findAt(
    [(x1, y1, -dim3), ],
    [(x2, y2, -dim3), ],
    [(x3, y3, -dim3), ] )

region2 = regionToolset.Region(side1Faces=faceTemp1)
myModel.Coupling(name='Bending Constraint', controlPoint=region1, surface=region2,
    influenceRadius=WHOLE_SURFACE, couplingType=KINEMATIC,
```

```
    u1=OFF, u2=OFF, u3=ON, ur1=OFF, ur2=OFF, ur3=OFF)
##############################################################################
################################## OVALIZING BC ##############################
##############################################################################
region2 = regionToolset.Region(faces=faceTemp1)
myModel.DisplacementBC(name='Ovalizing BC', createStepName='Initial',
    region=region2,
    u1=UNSET, u2=UNSET, u3=UNSET,
    ur1=UNSET, ur2=0.0, ur3=0.0)
##############################################################################
##############################################################################
myModel.SmoothStepAmplitude(name='AmpPressure', data=((0.0,0.0),
    (timePerPressure, 1.0)), timeSpan=STEP)
myModel.SmoothStepAmplitude(name='AmpBend', data=((0.0,0.0),
    (timePerBend, 1.0)), timeSpan=STEP)
##############################################################################
################################## PRESSURE LOADING ##########################
##############################################################################
if pFactor!=0.0:
    presTemp = 2.0*t*pFactor*sy/(D-1.0*t)
    region3 = myAssembly.surfaces['PipeInnerSurface']
    myModel.Pressure(name='Pressurize', createStepName='Pressure',
        region=region3, distributionType=UNIFORM, field='', magnitude=presTemp,
        amplitude='AmpPressure')
    AxialForce = -pi*(D-t)*(D-t)*presTemp/4.0
    Asteel=(pi/4.0)*(D*D-(D-2.0*t)*(D-2.0*t))
    SigmaEndCap=AxialForce/Asteel

    myAssembly.Surface(side1Faces=faceTemp1, name='PipeEndSurface')
    region4 = myAssembly.surfaces['PipeEndSurface']

    myModel.Pressure(name='EndCapTension', createStepName='Pressure',
    region=region4, distributionType=UNIFORM, field='', magnitude=SigmaEndCap,
    amplitude='AmpPressure')

##############################################################################
################################## MASTER NODE BC ############################
##############################################################################
```

```
pointTemp3=solidInstance.vertices.findAt([(0.0, -R, -dim3),] )
region3=regionToolset.Region(vertices=pointTemp3)
myModel.DisplacementBC(name='Master Node BC', createStepName='Initial',
    region=region1,
    amplitude='AmpBend',
    u1=0.0, u2=UNSET, u3=UNSET,
    ur1=0.0, ur2=0.0, ur3=0.0)

myModel.boundaryConditions['Master Node BC'].setValuesInStep(stepName='Bending',
    u3=FREED, ur1=-alpha0)
##############################################################################################
############################## RigidBodyMotionPreventionBC ###################################
##############################################################################################
pointTemp3=solidInstance.vertices.findAt([(0.0, -R, 0.0),] )
region3=regionToolset.Region(vertices=pointTemp3)
myModel.DisplacementBC(name='RigidBodyMotionPreventionBC',
    createStepName='Initial',
    region=region3,
    amplitude='AmpBend',
    u2=0.0)
##############################################################################################
##############################################################################################
if(R-a-dim2>R-t):
    v11=solidInstance.vertices.findAt(coordinates=(-R*sin(beta1),
        R*cos(beta1), 0.0))
    v12=solidInstance.vertices.findAt(coordinates=(-R*sin(beta1),
        R*cos(beta1), -dim3))
    v13=solidInstance.vertices.findAt(coordinates=(-(R-a-dim2)*sin(beta2),
        (R-a-dim2)*cos(beta2), 0.0))

    sf=solidInstance.faces
    i=0
    for fc in sf:
        x=fc.pointOn[0][0]
        y=fc.pointOn[0][1]
        z=fc.pointOn[0][2]
        rr=sqrt(x*x+y*y)
        tet=abs(x)/y
```

```
        cn1=tet>tan(beta1)
        cn2=tet<tan(beta2)
        cn3=abs(z)<tolr
        cn4=rr>R-a-dim2
        if (cn1==True & cn2==True & cn3==True & cn4==True):
            if i==0:
                fc99 = sf[fc.index:fc.index+1]
                i+=1
            else:
                fc99 += sf[fc.index:fc.index+1]

    myAssembly.PartitionFaceByShortestPath(point1=v11, point2=v13, faces=fc99)

if(R-a-dim2<=R-t):
    v11=solidInstance.vertices.findAt(coordinates=(-R*sin(beta1),
        R*cos(beta1), 0.0))
    v12=solidInstance.vertices.findAt(coordinates=(-R*sin(beta1),
        R*cos(beta1), -dim3))
    v13=solidInstance.vertices.findAt(coordinates=(-(R-t)*sin(beta2),
        (R-t)*cos(beta2), 0.0))

    sf=solidInstance.faces
    i=0
    for fc in sf:
        x=fc.pointOn[0][0]
        y=fc.pointOn[0][1]
        z=fc.pointOn[0][2]
        rr=sqrt(x*x+y*y)
        tet=abs(x)/y
        cn1=tet>tan(beta1)
        cn2=tet<tan(beta2)
        cn3=abs(z)<tolr
        if (cn1==True & cn2==True & cn3==True):
            if i==0:
                fc99 = sf[fc.index:fc.index+1]
                i+=1
            else:
                fc99 += sf[fc.index:fc.index+1]
```

```
    myAssembly.PartitionFaceByShortestPath(point1=v11, point2=v13, faces=fc99)

##############################################################################
################################### SWEEP ####################################
##############################################################################
myAssembly.setMeshControls(regions=solidInstance.cells,
    elemShape=HEX, technique=SWEEP, algorithm=MEDIAL_AXIS, minTransition=OFF)
##############################################################################
################################### MESH #####################################
##############################################################################
myAssembly.generateMesh(regions=(solidInstance,), seedConstraintOverride=ON)
e1=solidInstance.edges.findAt([(-0.5*D, 0.0, -dim3), ])
dumSet=myAssembly.Set(name='dumSet',edges=e1)

for node in dumSet.nodes:
    x=node.coordinates[0]
    y=node.coordinates[1]
    cn1=abs(x)<tolr
    cn2=abs(y+0.5*D)<tolr
    if (cn1==True & cn2==True):
        label1=node.label

e2=solidInstance.edges.findAt(
    [(0.0, R-L5-0.5*L3, 0.0), ],
    [(0.0, R-0.5*L5, 0.0), ])
dumSet2=myAssembly.Set(name='dumSet2',edges=e2)

for node in dumSet2.nodes:
    y=node.coordinates[1]
    cn1=abs(y-(R-a+2*0.5*D0))<tolr
    cn2=abs(y-R)<tolr
    if (cn1==True):
        label2=node.label
    if (cn2==True):
        label3=node.label
##############################################################################
myFile6.write('ReferencePointNodeLabel'.ljust(25) + '|'
```

```
    + str(label1).ljust(25) + '\n')
myFile6.write('CTODNodeLabel'.ljust(25) + '|' + str(label2).ljust(25) + '\n')
myFile6.write('CMODNodeLabel'.ljust(25) + '|' + str(label3).ljust(25) + '\n')

e3=solidInstance.edges.findAt(
    [(-R*sin(0.5*beta1), R*cos(0.5*beta1), 0.0), ],
    [(-R*sin(0.5*beta1), -R*cos(0.5*beta1), 0.0), ])
dumSet3=myAssembly.Set(name='dumSet3',edges=e3)

xprev=0.0
for node in dumSet3.nodes:
    x=node.coordinates[0]
    y=node.coordinates[1]
    cn1=abs(x)<tolr
    cn3=abs(y+R)<tolr
    if (cn1==True & cn3==True):
        label5=node.label
    if x<xprev:
        xprev=x
        label6=node.label

myFile6.write('OvalityNodeBot'.ljust(25) + '|' + str(label5).ljust(25) + '\n')
myFile6.write('OvalityNodeLeft'.ljust(25) + '|' + str(label6).ljust(25) + '\n')

e4=solidInstance.edges.findAt(
    [(0.0, R-0.99*t, 0.0), ] )
dumSet4=myAssembly.Set(name='dumSet4',edges=e4)

for node in dumSet4.nodes:
    y=node.coordinates[1]
    cn1=abs(y-R+t)<tolr
    if cn1==True:
        label7=node.label

myFile6.write('OvalityNodeTopIn'.ljust(25) + '|' + str(label7).ljust(25) + '\n')
myFile6.write('#OutputIntervals'.ljust(25) + '|' + str(numInt1).ljust(25) + '\n')

numNodes=len(solidInstance.nodes)
```

```
numElements=len(solidInstance.elements)
myFile6.write('NumberOfNodes'.ljust(25) + '|' + str(numNodes).ljust(25) + '\n')
myFile6.write('NumberOfElements'.ljust(25) + '|'
    + str(numElements).ljust(25) + '\n')
myFile6.close()
##############################################################################
################################ HISTORY REQUEST ##############################
##############################################################################
if pFactor!=0.0:
    myModel.HistoryOutputRequest(name = 'Hist Out Req02',
        createStepName = 'Pressure', numIntervals=numInt2)

myModel.HistoryOutputRequest(name = 'Hist Out Req01',
    createStepName = 'Bending', numIntervals=numInt1)
##############################################################################
################################ FIELD REQUEST ################################
##############################################################################
if pFactor!=0.0:
    myModel.FieldOutputRequest(name='Field Out Req02', createStepName='Pressure',
        variables=('S', 'MISES', 'LE', 'PE', 'PEEQ',
        'U', 'RF', 'VVF', 'STATUS'), numIntervals=numInt2)
##############################################################################
myModel.FieldOutputRequest(name='Field Out Req01', createStepName='Bending',
    variables=('S', 'MISES', 'LE', 'PE', 'PEEQ',
    'U', 'RF', 'VVF', 'STATUS', 'EMSF'), numIntervals=numInt1)
del myModel.fieldOutputRequests['F-Output-1']
del myModel.historyOutputRequests['H-Output-1']
##############################################################################
################################ JOB DEFINITION ###############################
##############################################################################
myJob = mdb.Job(name=ModelName, model=myModel, type=ANALYSIS,
    explicitPrecision=SINGLE, nodalOutputPrecision=SINGLE, description='',
    parallelizationMethodExplicit=DOMAIN, multiprocessingMode=DEFAULT,
    numDomains=numDomains1, userSubroutine='', numCpus=numCpus1, memory=90,
    memoryUnits=PERCENTAGE, scratch='', echoPrint=OFF, modelPrint=OFF,
    contactPrint=OFF, historyPrint=OFF)
myJob.writeInput()
```

Appendix B

Copyright Agreement Forms

B.1 Copyright Agreement Form for Chapter 3

COPYRIGHT AGREEMENT (as of March 2010)

Publishing • Three Park Avenue • New York, NY 10016
Please email this form to journalcopyright@asme.org or fax to 212-591-7292

Before publication of your paper in a conference proceeding or in a journal, ASME must receive your signed Copyright Agreement Form. For conference papers, this form should be received by the deadline indicated by the Conference. Other forms may NOT be substituted for this form, nor may any wording on the form be changed. HANDWRITTEN SIGNATURES ONLY are acceptable.

PAPER NUMBER (for conference/journal papers): PVT-10-1142

TITLE: A Comprehensive Parametric Finite Element Study on the Development

AUTHOR(s): Nikzad Nourpanah, Farid Taheri

JOURNAL NAME: Journal of Pressure Vessel Technology

COPYRIGHT ASSIGNMENT
The following terms of copyright assignment refer to Sections 1, 2, and 3. Sections 4 and 5 may not be subject to copyright.

The undersigned hereby assigns irrevocably to ASME all worldwide rights under copyright in the Paper.

Authors retain all proprietary rights in any idea, process, procedure, or articles of manufacture described in the Paper, including the right to seek patent protection for them. Authors may perform, lecture, teach, conduct related research and display all or part of the Paper, in print or electronic format. Authors may reproduce and distribute the Paper for non-commercial purposes only. Non-commercial applies only to the sale of the paper per se. For all copies of the Paper made by Authors, Authors must acknowledge ASME as original publisher and include the names of all author(s), the publication title, and an appropriate copyright notice that identifies ASME as the copyright holder.

PLEASE READ THE TERMS AND CONDITIONS WHICH ARE FULLY INCORPORATED IN THIS AGREEMENT.

ASME requests that authors/copyright owners assign copyright to ASME in order for a conference or journal paper to be published by ASME. Authors exempt from this request are direct employees of the U.S. Government, whereby papers are not subject to copyright protection in the U.S., or non-U.S. government employees, whose governments hold the copyright to the paper. Otherwise, the author/ copyright owner(s) of the Paper should sign this form as instructed below. Please refer to the section below "Who Should Sign" and also to ASME's FAQs page for more information regarding copyright ownership and the copyright process.

WHO SHOULD SIGN

Only the copyright owner(s) of the Paper, or an authorized representative, can sign this form. If one of the following applies you may not own the copyright of the paper, or you may not be authorized to sign this agreement, and may need to have the appropriate copyright owner(s) or organization representative sign this Agreement:
(1) you created the Paper within the scope of your employment, and your employer is the copyright

owner
(2) you created the Paper under an independent contractor agreement**; or
(3) you received a grant that funded your Paper.

Please review your company policies regarding copyright, and if you are not authorized to sign this agreement, please forward to the appropriate organization representative. Please review applicable company, institutional, and grant policies and your employment/independent contractor agreement to determine who holds the rights to your Paper. For more information, please refer to the FAQs .

****Note to U.S. Government Contractors:** If you created the Paper under contract with the U.S. Government, e.g., U.S. Government labs, the paper may be subject to copyright, and you or your employer may own the copyright. Please review your company/institutional policies and your contractor agreement. Your Paper may require a footer acknowledging contract information and also the following statement:

"The United States Government retains, and by accepting the article for publication, the publisher acknowledges that the United States Government retains, a non-exclusive, paid-up, irrevocable, worldwide license to publish or reproduce the published form of this work, or allow others to do so, for United States Government purposes."

It is your responsibility to ensure that the final PDF version of the Paper you submit includes all necessary footers and statements required under your contract.

1. PAPERS OWNED BY ONE AUTHOR OR JOINT AUTHORS; DESIGNATED AUTHORS
(For jointly authored works, all authors should submit a signed Agreement, or one designated author (the lead author) may sign on behalf of the other authors, but ONLY IF the designated author has secured written authorization to do so from all other authors. The designated author must be able to produce such written authorization if requested.)

Designated authors, please sign below and list the names of the co-authors for whom you are signing. Please include full contact information for each author. Attach additional sheets if necessary.

Author(s)/co-author(s) not covered by the Designated author, please sign in the appropriate section below and provide full contact information. Attach additional sheets if necessary.

Author

Name : Nikzad Nourpanah Signature : _____ Date : March 9, 2011

Affiliation: Dalhousie U (Company or Institution) Job Title : PhD candidate

Address : c/o Dept. of Civil Engg, 1360 Barrington ST City : Halifax

State : NS Zip Code : B3J 1Z1 Country : Canada

Phone : 1-902-494-3821 Fax : 1-902-484-6635 Email : nk849925@Dal.Ca

Author

Name : Farid Taheri Signature : _____ Date : March 9, 2011

Affiliation: Ocean Research Centre-Atlantic, Dalhousie University (Company or Institution) Job Title : Professor and Director

Address : 1360 Barrington Street City : Halifax
State : NS Zip Code : B3J 1Z1 Country : Canada
Phone : 1-902-494-3935 Fax : 1-902-484-6635 Email : farid.taheri@dal.ca

Co-Author

Name : Nikzad Nourpanah Signature : Date :
Affiliation: Job Title :
(Company or Institution)
Address : City :
State : Zip Code : Country :
Phone : Fax : Email : n.nourpanah@dal.ca

Co-Author

Name : Signature : Date :
Affiliation: Job Title :
(Company or Institution)
Address : City :
State : Zip Code : Country :
Phone : Fax : Email :

Name : Signature : Date :
Affiliation: Title :
(Company or Institution)
Address : City :
State : Zip Code : Country :
Phone : Fax : Email :

Name : Signature : Date :
Affiliation: Title :
(Company or Institution)
Address : City :
State : Zip Code : Country :
Phone : Fax : Email :

---

2. **PAPERS OWNED BY EMPLOYER OF AUTHOR(s)** (Author may sign if so authorized; otherwise, an officer or other authorized agent of the employer should sign below.)

Name : Signature : Date :

Affiliation: _____ Job Title: _____
(Company or Institution)
Address : _____ City : _____
State : _____ Zip Code : _____ Country : _____
Phone: _____ Fax: _____ Email: _____

PAPERS NOT SUBJECT TO COPYRIGHT ASSIGNMENT

3. **PAPERS CREATED BY U.S. FEDERAL GOVERNMENT EMPLOYEES** (Please sign below if you created the Paper within your scope of your employment by the U.S. Federal Government, and you are authorized to sign on behalf of your agency or department; otherwise, an officer or authorized agent should sign. Please include the following footer on the final PDF version of the Paper you submit: "This material is declared a work of the U.S. Government and is not subject to copyright protection in the United States. Approved for public release; distribution is unlimited.")

Name: _____ Signature: _____ Date: _____
Affiliation: _____ Title: _____
(Company or Institution)
Address: _____ City : _____
State: _____ Zip Code : _____ Country : _____
Phone: _____ Fax: _____ Email: _____
Name(s) and affiliations of Author(s) (attach additional sheets if necessary): _____

---

4. **PAPERS CREATED BY U.S. FEDERAL OR STATE GOVERNMENT CONTRACTORS** (Please fill in and sign below if you created the Paper under contract with the U.S. Federal or State government (e.g., U.S. government labs) , and you are authorized to sign on behalf of your organization; otherwise, an officer or other authorized agent should sign. Please include any required footers on the final PDF version of your Paper.

Name: _____ Signature: _____ Date: _____
Affiliation: _____ Title: _____
(Company or Institution)
Address: _____ City : _____
State: _____ Zip Code : _____ Country : _____
Phone: _____ Fax: _____ Email: _____
Name(s) and affiliations of Author(s) (attach additional sheets if necessary): _____

---

5. **PAPERS CREATED BY NON-U.S. GOVERNMENT EMPLOYEES**
Please fill in and sign below if you created the Paper within the scope of your duties as an

officer or employee of a non-U.S. government, and you are authorized to sign on behalf of your government; otherwise, an officer or authorized agent should sign.
This work was prepared while under employment by the Government of _____ as part of the official duties of the author indicated below, and as such copyright is owned by that Government, which reserves its own copyright under national law. The copyright notice on the paper should read:
_____

Name: _____ Signature: _____ Date: _____

Affiliation: _____ Job Title: _____

(Company or Institution)

Address: _____ City : _____

State: _____ Zip Code : _____ Country : _____

Phone: _____ Fax: _____ Email: _____

ASME COPYRIGHT FORM TERMS AND CONDITIONS

The following terms and conditions are fully incorporated into the Copyright Form. Please read them carefully.

REPRESENTATIONS, OBLIGATIONS, ACKNOWLEDGEMENTS, AND INDEMNIFICATION

You represent and acknowledge that:

1. This Paper represents: either the first publication of material or the first publication of an original compilation of information from a number of sources as specifically noted by footnotes and/or bibliography.
2. You have the right to enter into this Copyright Form and to make the assignment of rights to ASME. If the Paper contains excerpts from other copyrighted material (including without limitation any diagrams, photographs, figures or text), you have acquired in writing all necessary rights from third parties to include those materials in the Paper, and have provided appropriate credit for that third-party material in footnotes or in a bibliography.
3. If you are signing this Form on behalf of any co-authors or other copyright holders, you have obtained express authorizations from all those authors and/or copyright holders to make this assignment of rights to ASME.
4. To the best of the author's knowledge, all statements contained in the Paper purporting to be facts are true or supported by reasonable scientific research, the Paper does not contain any defamatory or libelous material and does not infringe any third party's copyright, patent, trade secret, or other proprietary rights and does not violate the right of privacy or publicity of any third party or otherwise violate any other applicable law; furthermore that to the best of your ability, you are responsible for ensuring the accuracy of your research and the Paper's content.
5. If the Paper was produced in the course of an author's employment by, or contractual relationship with, the U.S. Federal or State Government and/or contains classified material, it has been appropriately cleared for public release and such is indicated in the paper.
6. The Paper is not subject to any prior claim, encumbrance or form and is not under consideration for publication elsewhere.
7. You have appropriately cited and acknowledged all third parties who have contributed significantly in the Paper's technical aspects.
8. ASME is not responsible for any misrepresentation, errors or omissions by those signing

this copyright form.

9. (I) All print and electronic copies of the Paper submitted to ASME become ASME's physical property regardless of whether or not ASME publishes the Paper, and that ASME is not obligated to publish your paper (see the Termination Section below if your paper is not published).
10. ASME is not responsible for any of your expenses incurred in connection with preparing the Paper or attending meetings to present it, nor will ASME pay you any financial compensation if it publishes your Paper.
11. Subject to and to the maximum extent permitted by law, you agree to indemnify and hold harmless ASME from any damage or expense related to a breach of any of the representations and warranties above.

TERMINATION

If ASME decides not to publish your Paper, this Form, including all of ASME's rights in your Paper, terminates and you are thereafter free to offer the Paper for publication elsewhere.

GENERAL PROVISIONS

This Copyright Form, the Terms & Conditions, and ASME Copyright Guidelines, constitutes the entire agreement between you and ASME, and supersedes all prior or current negotiations, understandings and representations, whether oral or written, between you and ASME concerning the Paper.

This Agreement is governed by, and should be construed in accordance with, the laws of the State of New York, United States of America, applicable to agreements made and performed there, except to the extent that your institution is prohibited by law from entering contracts governed by New York law, in which limited case this Agreement is governed by, and should be construed in accordance with, the laws of the jurisdiction in which your institution is located. Any claim, dispute, action or proceeding relating to this Agreement may be brought only in the applicable state and federal courts in the State and County of New York, and you expressly consent to personal jurisdiction and venue in any of those courts.

B.2 Copyright Agreement Form for Chapter 4

ELSEVIER LICENSE
TERMS AND CONDITIONS

Jan 04, 2011

This is a License Agreement between Nikzad Nourpanah ("You") and Elsevier ("Elsevier") provided by Copyright Clearance Center ("CCC"). The license consists of your order details, the terms and conditions provided by Elsevier, and the payment terms and conditions.

All payments must be made in full to CCC. For payment instructions, please see information listed at the bottom of this form.

Supplier	Elsevier Limited The Boulevard,Langford Lane Kidlington,Oxford,OX5 1GB,UK
Registered Company Number	1982084
Customer name	Nikzad Nourpanah
Customer address	5231 Kent Street, Apt# 56 Halifax, NS B3H 1P7
License number	2582041209308
License date	Jan 04, 2011
Licensed content publisher	Elsevier
Licensed content publication	Marine Structures
Licensed content title	A design equation for evaluation of strain concentration factor in concrete coated X65 pipelines
Licensed content author	Nikzad Nourpanah, Farid Taheri
Licensed content date	October 2009
Licensed content volume number	22
Licensed content issue number	4
Number of pages	12
Start Page	758
End Page	769
Type of Use	reuse in a thesis/dissertation
Intended publisher of new work	other
Portion	full article
Format	both print and electronic
Are you the author of this Elsevier article?	Yes
Will you be translating?	No
Order reference number	

Title of your thesis/dissertation	INTEGRITY AND FRACTURE RESPONSE OF OFFSHORE PIPELINES SUBJECT TO LARGE PLASTIC STRAINS
Expected completion date	Apr 2011
Estimated size (number of pages)	200
Elsevier VAT number	GB 494 6272 12
Permissions price	0.00 USD
Value added tax 0.0%	0.0 USD / 0.0 GBP
Total	0.00 USD
Terms and Conditions	

INTRODUCTION

1. The publisher for this copyrighted material is Elsevier. By clicking "accept" in connection with completing this licensing transaction, you agree that the following terms and conditions apply to this transaction (along with the Billing and Payment terms and conditions established by Copyright Clearance Center, Inc. ("CCC"), at the time that you opened your Rightslink account and that are available at any time at http://myaccount.copyright.com).

GENERAL TERMS

2. Elsevier hereby grants you permission to reproduce the aforementioned material subject to the terms and conditions indicated.

3. Acknowledgement: If any part of the material to be used (for example, figures) has appeared in our publication with credit or acknowledgement to another source, permission must also be sought from that source. If such permission is not obtained then that material may not be included in your publication/copies. Suitable acknowledgement to the source must be made, either as a footnote or in a reference list at the end of your publication, as follows:

"Reprinted from Publication title, Vol /edition number, Author(s), Title of article / title of chapter, Pages No., Copyright (Year), with permission from Elsevier [OR APPLICABLE SOCIETY COPYRIGHT OWNER]." Also Lancet special credit - "Reprinted from The Lancet, Vol. number, Author(s), Title of article, Pages No., Copyright (Year), with permission from Elsevier."

4. Reproduction of this material is confined to the purpose and/or media for which permission is hereby given.

5. Altering/Modifying Material: Not Permitted. However figures and illustrations may be altered/adapted minimally to serve your work. Any other abbreviations, additions, deletions and/or any other alterations shall be made only with prior written authorization of Elsevier Ltd. (Please contact Elsevier at permissions@elsevier.com)

6. If the permission fee for the requested use of our material is waived in this instance, please be advised that your future requests for Elsevier materials may attract a fee.

7. Reservation of Rights: Publisher reserves all rights not specifically granted in the combination of

(i) the license details provided by you and accepted in the course of this licensing transaction, (ii) these terms and conditions and (iii) CCC's Billing and Payment terms and conditions.

8. License Contingent Upon Payment: While you may exercise the rights licensed immediately upon issuance of the license at the end of the licensing process for the transaction, provided that you have disclosed complete and accurate details of your proposed use, no license is finally effective unless and until full payment is received from you (either by publisher or by CCC) as provided in CCC's Billing and Payment terms and conditions. If full payment is not received on a timely basis, then any license preliminarily granted shall be deemed automatically revoked and shall be void as if never granted. Further, in the event that you breach any of these terms and conditions or any of CCC's Billing and Payment terms and conditions, the license is automatically revoked and shall be void as if never granted. Use of materials as described in a revoked license, as well as any use of the materials beyond the scope of an unrevoked license, may constitute copyright infringement and publisher reserves the right to take any and all action to protect its copyright in the materials.

9. Warranties: Publisher makes no representations or warranties with respect to the licensed material.

10. Indemnity: You hereby indemnify and agree to hold harmless publisher and CCC, and their respective officers, directors, employees and agents, from and against any and all claims arising out of your use of the licensed material other than as specifically authorized pursuant to this license.

11. No Transfer of License: This license is personal to you and may not be sublicensed, assigned, or transferred by you to any other person without publisher's written permission.

12. No Amendment Except in Writing: This license may not be amended except in a writing signed by both parties (or, in the case of publisher, by CCC on publisher's behalf).

13. Objection to Contrary Terms: Publisher hereby objects to any terms contained in any purchase order, acknowledgment, check endorsement or other writing prepared by you, which terms are inconsistent with these terms and conditions or CCC's Billing and Payment terms and conditions. These terms and conditions, together with CCC's Billing and Payment terms and conditions (which are incorporated herein), comprise the entire agreement between you and publisher (and CCC) concerning this licensing transaction. In the event of any conflict between your obligations established by these terms and conditions and those established by CCC's Billing and Payment terms and conditions, these terms and conditions shall control.

14. Revocation: Elsevier or Copyright Clearance Center may deny the permissions described in this License at their sole discretion, for any reason or no reason, with a full refund payable to you. Notice of such denial will be made using the contact information provided by you. Failure to receive such notice will not alter or invalidate the denial. In no event will Elsevier or Copyright Clearance Center be responsible or liable for any costs, expenses or damage incurred by you as a result of a denial of your permission request, other than a refund of the amount(s) paid by you to Elsevier and/or Copyright Clearance Center for denied permissions.

LIMITED LICENSE

The following terms and conditions apply only to specific license types:

15. **Translation**: This permission is granted for non-exclusive world **English** rights only unless your license was granted for translation rights. If you licensed translation rights you may only translate this content into the languages you requested. A professional translator must perform all translations and reproduce the content word for word preserving the integrity of the article. If this license is to re-use 1 or 2 figures then permission is granted for non-exclusive world rights in all languages.

16. **Website**: The following terms and conditions apply to electronic reserve and author websites:
Electronic reserve: If licensed material is to be posted to website, the web site is to be password-protected and made available only to bona fide students registered on a relevant course if:
This license was made in connection with a course,
This permission is granted for 1 year only. You may obtain a license for future website posting,
All content posted to the web site must maintain the copyright information line on the bottom of each image,
A hyper-text must be included to the Homepage of the journal from which you are licensing at http://www.sciencedirect.com/science/journal/xxxxx or the Elsevier homepage for books at http://www.elsevier.com , and
Central Storage: This license does not include permission for a scanned version of the material to be stored in a central repository such as that provided by Heron/XanEdu.

17. **Author website** for journals with the following additional clauses:

All content posted to the web site must maintain the copyright information line on the bottom of each image, and
he permission granted is limited to the personal version of your paper. You are not allowed to download and post the published electronic version of your article (whether PDF or HTML, proof or final version), nor may you scan the printed edition to create an electronic version,
A hyper-text must be included to the Homepage of the journal from which you are licensing at http://www.sciencedirect.com/science/journal/xxxxx , As part of our normal production process, you will receive an e-mail notice when your article appears on Elsevier's online service ScienceDirect (www.sciencedirect.com). That e-mail will include the article's Digital Object Identifier (DOI). This number provides the electronic link to the published article and should be included in the posting of your personal version. We ask that you wait until you receive this e-mail and have the DOI to do any posting.
Central Storage: This license does not include permission for a scanned version of the material to be stored in a central repository such as that provided by Heron/XanEdu.

18. **Author website** for books with the following additional clauses:
Authors are permitted to place a brief summary of their work online only.
A hyper-text must be included to the Elsevier homepage at http://www.elsevier.com

All content posted to the web site must maintain the copyright information line on the bottom of each image
You are not allowed to download and post the published electronic version of your chapter, nor

may you scan the printed edition to create an electronic version.
Central Storage: This license does not include permission for a scanned version of the material to be stored in a central repository such as that provided by Heron/XanEdu.

19. **Website** (regular and for author): A hyper-text must be included to the Homepage of the journal from which you are licensing at http://www.sciencedirect.com/science/journal/xxxxx. or for books to the Elsevier homepage at http://www.elsevier.com

20. **Thesis/Dissertation**: If your license is for use in a thesis/dissertation your thesis may be submitted to your institution in either print or electronic form. Should your thesis be published commercially, please reapply for permission. These requirements include permission for the Library and Archives of Canada to supply single copies, on demand, of the complete thesis and include permission for UMI to supply single copies, on demand, of the complete thesis. Should your thesis be published commercially, please reapply for permission.

21. **Other Conditions**:

v1.6

Gratis licenses (referencing $0 in the Total field) are free. Please retain this printable license for your reference. No payment is required.

If you would like to pay for this license now, please remit this license along with your payment made payable to "COPYRIGHT CLEARANCE CENTER" otherwise you will be invoiced within 48 hours of the license date. Payment should be in the form of a check or money order referencing your account number and this invoice number RLNK10907947. Once you receive your invoice for this order, you may pay your invoice by credit card. Please follow instructions provided at that time.

Make Payment To:
Copyright Clearance Center
Dept 001
P.O. Box 843006
Boston, MA 02284-3006

If you find copyrighted material related to this license will not be used and wish to cancel, please contact us referencing this license number 2582041209308 and noting the reason for cancellation.

Questions? customercare@copyright.com or +1-877-622-5543 (toll free in the US) or +1-978-646-2777.

B.3 Copyright Agreement Form for Chapter 5

ELSEVIER LICENSE
TERMS AND CONDITIONS

Jan 04, 2011

This is a License Agreement between Nikzad Nourpanah ("You") and Elsevier ("Elsevier") provided by Copyright Clearance Center ("CCC"). The license consists of your order details, the terms and conditions provided by Elsevier, and the payment terms and conditions.

All payments must be made in full to CCC. For payment instructions, please see information listed at the bottom of this form.

Supplier	Elsevier Limited The Boulevard,Langford Lane Kidlington,Oxford,OX5 1GB,UK
Registered Company Number	1982084
Customer name	Nikzad Nourpanah
Customer address	5231 Kent Street, Apt# 56 Halifax, NS B3H 1P7
License number	2582040821342
License date	Jan 04, 2011
Licensed content publisher	Elsevier
Licensed content publication	Engineering Fracture Mechanics
Licensed content title	Development of a reference strain approach for assessment of fracture response of reeled pipelines
Licensed content author	Nikzad Nourpanah, Farid Taheri
Licensed content date	August 2010
Licensed content volume number	77
Licensed content issue number	12
Number of pages	17
Start Page	2337
End Page	2353
Type of Use	reuse in a thesis/dissertation
Portion	full article
Format	both print and electronic
Are you the author of this Elsevier article?	Yes
Will you be translating?	No
Order reference number	
Title of your thesis/dissertation	INTEGRITY AND FRACTURE RESPONSE OF OFFSHORE PIPELINES SUBJECT TO LARGE PLASTIC STRAINS

Expected completion date	Apr 2011
Estimated size (number of pages)	200
Elsevier VAT number	GB 494 6272 12
Permissions price	0.00 USD
Value added tax 0.0%	0.0 USD / 0.0 GBP
Total	0.00 USD
Terms and Conditions	

INTRODUCTION

1. The publisher for this copyrighted material is Elsevier. By clicking "accept" in connection with completing this licensing transaction, you agree that the following terms and conditions apply to this transaction (along with the Billing and Payment terms and conditions established by Copyright Clearance Center, Inc. ("CCC"), at the time that you opened your Rightslink account and that are available at any time at http://myaccount.copyright.com).

GENERAL TERMS

2. Elsevier hereby grants you permission to reproduce the aforementioned material subject to the terms and conditions indicated.

3. Acknowledgement: If any part of the material to be used (for example, figures) has appeared in our publication with credit or acknowledgement to another source, permission must also be sought from that source. If such permission is not obtained then that material may not be included in your publication/copies. Suitable acknowledgement to the source must be made, either as a footnote or in a reference list at the end of your publication, as follows:

"Reprinted from Publication title, Vol /edition number, Author(s), Title of article / title of chapter, Pages No., Copyright (Year), with permission from Elsevier [OR APPLICABLE SOCIETY COPYRIGHT OWNER]." Also Lancet special credit - "Reprinted from The Lancet, Vol. number, Author(s), Title of article, Pages No., Copyright (Year), with permission from Elsevier."

4. Reproduction of this material is confined to the purpose and/or media for which permission is hereby given.

5. Altering/Modifying Material: Not Permitted. However figures and illustrations may be altered/adapted minimally to serve your work. Any other abbreviations, additions, deletions and/or any other alterations shall be made only with prior written authorization of Elsevier Ltd. (Please contact Elsevier at permissions@elsevier.com)

6. If the permission fee for the requested use of our material is waived in this instance, please be advised that your future requests for Elsevier materials may attract a fee.

7. Reservation of Rights: Publisher reserves all rights not specifically granted in the combination of (i) the license details provided by you and accepted in the course of this licensing transaction, (ii) these terms and conditions and (iii) CCC's Billing and Payment terms and conditions.

8. License Contingent Upon Payment: While you may exercise the rights licensed immediately upon issuance of the license at the end of the licensing process for the transaction, provided that you have disclosed complete and accurate details of your proposed use, no license is finally effective unless and until full payment is received from you (either by publisher or by CCC) as provided in CCC's Billing and Payment terms and conditions. If full payment is not received on a timely basis, then any license preliminarily granted shall be deemed automatically revoked and shall be void as if never granted. Further, in the event that you breach any of these terms and conditions or any of CCC's Billing and Payment terms and conditions, the license is automatically revoked and shall be void as if never granted. Use of materials as described in a revoked license, as well as any use of the materials beyond the scope of an unrevoked license, may constitute copyright infringement and publisher reserves the right to take any and all action to protect its copyright in the materials.

9. Warranties: Publisher makes no representations or warranties with respect to the licensed material.

10. Indemnity: You hereby indemnify and agree to hold harmless publisher and CCC, and their respective officers, directors, employees and agents, from and against any and all claims arising out of your use of the licensed material other than as specifically authorized pursuant to this license.

11. No Transfer of License: This license is personal to you and may not be sublicensed, assigned, or transferred by you to any other person without publisher's written permission.

12. No Amendment Except in Writing: This license may not be amended except in a writing signed by both parties (or, in the case of publisher, by CCC on publisher's behalf).

13. Objection to Contrary Terms: Publisher hereby objects to any terms contained in any purchase order, acknowledgment, check endorsement or other writing prepared by you, which terms are inconsistent with these terms and conditions or CCC's Billing and Payment terms and conditions. These terms and conditions, together with CCC's Billing and Payment terms and conditions (which are incorporated herein), comprise the entire agreement between you and publisher (and CCC) concerning this licensing transaction. In the event of any conflict between your obligations established by these terms and conditions and those established by CCC's Billing and Payment terms and conditions, these terms and conditions shall control.

14. Revocation: Elsevier or Copyright Clearance Center may deny the permissions described in this License at their sole discretion, for any reason or no reason, with a full refund payable to you. Notice of such denial will be made using the contact information provided by you. Failure to receive such notice will not alter or invalidate the denial. In no event will Elsevier or Copyright Clearance Center be responsible or liable for any costs, expenses or damage incurred by you as a result of a denial of your permission request, other than a refund of the amount(s) paid by you to Elsevier and/or Copyright Clearance Center for denied permissions.

LIMITED LICENSE

The following terms and conditions apply only to specific license types:

15. **Translation**: This permission is granted for non-exclusive world **English** rights only unless

your license was granted for translation rights. If you licensed translation rights you may only translate this content into the languages you requested. A professional translator must perform all translations and reproduce the content word for word preserving the integrity of the article. If this license is to re-use 1 or 2 figures then permission is granted for non-exclusive world rights in all languages.

16. **Website**: The following terms and conditions apply to electronic reserve and author websites:
Electronic reserve: If licensed material is to be posted to website, the web site is to be password-protected and made available only to bona fide students registered on a relevant course if:
This license was made in connection with a course,
This permission is granted for 1 year only. You may obtain a license for future website posting,
All content posted to the web site must maintain the copyright information line on the bottom of each image,
A hyper-text must be included to the Homepage of the journal from which you are licensing at http://www.sciencedirect.com/science/journal/xxxxx or the Elsevier homepage for books at http://www.elsevier.com , and
Central Storage: This license does not include permission for a scanned version of the material to be stored in a central repository such as that provided by Heron/XanEdu.

17. **Author website** for journals with the following additional clauses:

All content posted to the web site must maintain the copyright information line on the bottom of each image, and
he permission granted is limited to the personal version of your paper. You are not allowed to download and post the published electronic version of your article (whether PDF or HTML, proof or final version), nor may you scan the printed edition to create an electronic version,
A hyper-text must be included to the Homepage of the journal from which you are licensing at http://www.sciencedirect.com/science/journal/xxxxx , As part of our normal production process, you will receive an e-mail notice when your article appears on Elsevier's online service ScienceDirect (www.sciencedirect.com). That e-mail will include the article's Digital Object Identifier (DOI). This number provides the electronic link to the published article and should be included in the posting of your personal version. We ask that you wait until you receive this e-mail and have the DOI to do any posting.
Central Storage: This license does not include permission for a scanned version of the material to be stored in a central repository such as that provided by Heron/XanEdu.

18. **Author website** for books with the following additional clauses:
Authors are permitted to place a brief summary of their work online only.
A hyper-text must be included to the Elsevier homepage at http://www.elsevier.com

All content posted to the web site must maintain the copyright information line on the bottom of each image
You are not allowed to download and post the published electronic version of your chapter, nor may you scan the printed edition to create an electronic version.
Central Storage: This license does not include permission for a scanned version of the material to be stored in a central repository such as that provided by Heron/XanEdu.

19. **Website** (regular and for author): A hyper-text must be included to the Homepage of the journal from which you are licensing at http://www.sciencedirect.com/science/journal/xxxxx. or for books to the Elsevier homepage at http://www.elsevier.com

20. **Thesis/Dissertation**: If your license is for use in a thesis/dissertation your thesis may be submitted to your institution in either print or electronic form. Should your thesis be published commercially, please reapply for permission. These requirements include permission for the Library and Archives of Canada to supply single copies, on demand, of the complete thesis and include permission for UMI to supply single copies, on demand, of the complete thesis. Should your thesis be published commercially, please reapply for permission.

21. **Other Conditions**:

v1.6

Gratis licenses (referencing $0 in the Total field) are free. Please retain this printable license for your reference. No payment is required.

If you would like to pay for this license now, please remit this license along with your payment made payable to "COPYRIGHT CLEARANCE CENTER" otherwise you will be invoiced within 48 hours of the license date. Payment should be in the form of a check or money order referencing your account number and this invoice number RLNK10907943. Once you receive your invoice for this order, you may pay your invoice by credit card. Please follow instructions provided at that time.

Make Payment To:
Copyright Clearance Center
Dept 001
P.O. Box 843006
Boston, MA 02284-3006

If you find copyrighted material related to this license will not be used and wish to cancel, please contact us referencing this license number 2582040821342 and noting the reason for cancellation.

Questions? customercare@copyright.com or +1-877-622-5543 (toll free in the US) or +1-978-646-2777.

B.4 Copyright Agreement Form for Chapter 6

COPYRIGHT AGREEMENT (as of December 2008)

ASME Publishing • Three Park Avenue • New York, NY 10016 ASME prefers that you return this form to: copyright@asme.org or fax the form to: FAX 212-591-7060 or 212-591-7292

Before publication of your paper in a conference proceeding or in a journal, ASME must receive your signed Copyright Agreement Form. For conference papers, this form should be received by the deadline indicated by the Conference. Other forms may NOT be substituted for this form, nor may any wording on the form be changed. HANDWRITTEN SIGNATURES ONLY are acceptable.

Please fill in the information requested below. The copyright owner(s) of the Paper should then sign this form as instructed below. Please refer to our FAQ page for more information regarding copyright ownership.

PAPER NUMBER (for conference papers): _____ *Multiple forms may be submitted.*

TITLE: Effect of Lüders Plateau on Fracture Response and Toughness of Pipelines Subject to Extreme Plastic Bending

AUTHOR(s): Nikzad Nourpanah and Farid Taheri

CONFERENCE NAME: _____

JOURNAL NAME: Journal of Pressure Vessel Technology

COPYRIGHT ASSIGNMENT

The undersigned hereby assigns irrevocably to ASME all worldwide rights under copyright in the Paper.

Authors retain all proprietary rights in any idea, process, procedure, or articles of manufacture described in the Paper, including the right to seek patent protection for them. Authors may perform, lecture, teach, conduct related research and display all or part of the Paper, in print or electronic format. Authors may reproduce and distribute the Paper for non-commercial purposes only. For all copies of the Paper made by Authors, Authors must acknowledge ASME as original publisher and include the names of all author(s), the publication title, and an appropriate copyright notice that identifies ASME as the copyright holder.

PLEASE READ THE TERMS AND CONDITIONS WHICH ARE FULLY INCORPORATED IN THIS AGREEMENT.

Who Should Sign:

Only the copyright owner(s) of the Paper can sign below. If one of the following applies you may not own the copyright of the paper and may need to have the appropriate copyright owner(s) sign this Agreement:
(1) you created the Paper within the scope of your employment, and your employer is the copyright owner;
(2) you created the Paper under an independent contractor agreement**; or
(3) you received a grant that funded your Paper.
Please review applicable company, institutional, and grant policies and your employment/independent contractor agreement to determine who holds the rights to your Paper. For more information, please refer to the FAQs

****Note to U.S. Government Contractors**: If you created the Paper under contract with the U.S. Government, it is not necessarily a public domain work. You or your employer may own the copyright. Please review your company/institutional policies and your contractor agreement. Your Paper may require a footer acknowledging contract information and also the following statement:

"The United States Government retains, and by accepting the article for publication, the publisher acknowledges that the United States Government retains, a non-exclusive, paid-up, irrevocable, worldwide license to publish or reproduce the published form of this work, or allow others to do so, for United States Government purposes."

Please be sure that the final PDF version of the Paper you submit includes all necessary footers and statements required under your contract.

owner
(2) you created the Paper under an independent contractor agreement**; or
(3) you received a grant that funded your Paper.

Please review your company policies regarding copyright, and if you are not authorized to sign this agreement, please forward to the appropriate organization representative. Please review applicable company, institutional, and grant policies and your employment/independent contractor agreement to determine who holds the rights to your Paper. For more information, please refer to the FAQs .

****Note to U.S. Government Contractors:** If you created the Paper under contract with the U.S. Government, e.g., U.S. Government labs, the paper may be subject to copyright, and you or your employer may own the copyright. Please review your company/institutional policies and your contractor agreement. Your Paper may require a footer acknowledging contract information and also the following statement:

"The United States Government retains, and by accepting the article for publication, the publisher acknowledges that the United States Government retains, a non-exclusive, paid-up, irrevocable, worldwide license to publish or reproduce the published form of this work, or allow others to do so, for United States Government purposes."

It is your responsibility to ensure that the final PDF version of the Paper you submit includes all necessary footers and statements required under your contract.

1. PAPERS OWNED BY ONE AUTHOR OR JOINT AUTHORS; DESIGNATED AUTHORS
(For jointly authored works, all authors should submit a signed Agreement, or one designated author (the lead author) may sign on behalf of the other authors, but ONLY IF the designated author has secured written authorization to do so from all other authors. The designated author must be able to produce such written authorization if requested.)

Designated authors, please sign below and list the names of the co-authors for whom you are signing. Please include full contact information for each author. Attach additional sheets if necessary.

Author(s)/co-author(s) not covered by the Designated author, please sign in the appropriate section below and provide full contact information. Attach additional sheets if necessary.

Author

Name : Nikzad Nourpanah Signature : _____ Date : March 9, 2011

Affiliation: Dalhousie U (Company or Institution) Job Title : PhD candidate

Address : c/o Dept. of Civil Engg, 1360 Barrington ST City : Halifax

State : NS Zip Code : B3J 1Z1 Country : Canada

Phone : 1-902-494-3821 Fax : 1-902-484-6635 Email : nk849925@Dal.Ca

Author

Name : Farid Taheri Signature : _____ Date : March 9, 2011

Affiliation: Ocean Research Centre-Atlantic, Dalhousie University (Company or Institution) Job Title : Professor and Director

B.5 Copyright Agreement Form for Chapter 7

ELSEVIER LICENSE
TERMS AND CONDITIONS

Feb 01, 2011

This is a License Agreement between Nikzad Nourpanah ("You") and Elsevier ("Elsevier") provided by Copyright Clearance Center ("CCC"). The license consists of your order details, the terms and conditions provided by Elsevier, and the payment terms and conditions.

All payments must be made in full to CCC. For payment instructions, please see information listed at the bottom of this form.

Supplier	Elsevier Limited The Boulevard,Langford Lane Kidlington,Oxford,OX5 1GB,UK
Registered Company Number	1982084
Customer name	Nikzad Nourpanah
Customer address	5231 Kent Street, Apt# 56 Halifax, NS B3H 1P7
License number	2600231162907
License date	Feb 01, 2011
Licensed content publisher	Elsevier
Licensed content publication	Engineering Fracture Mechanics
Licensed content title	A numerical study on the crack tip constraint of pipelines subject to extreme plastic bending
Licensed content author	N. Nourpanah, F. Taheri
Licensed content date	11 December 2010
Licensed content volume number	n/a
Licensed content issue number	n/a
Number of pages	1
Start Page	
End Page	
Type of Use	reuse in a thesis/dissertation
Intended publisher of new work	other
Portion	full article
Format	both print and electronic
Are you the author of this Elsevier article?	Yes
Will you be translating?	No
Order reference number	

Title of your thesis/dissertation	INTEGRITY AND FRACTURE RESPONSE OF OFFSHORE PIPELINES SUBJECT TO LARGE PLASTIC STRAINS
Expected completion date	Apr 2011
Estimated size (number of pages)	200
Elsevier VAT number	GB 494 6272 12
Permissions price	0.00 USD
Value added tax 0.0%	0.00 USD / GBP
Total	0.00 USD
Terms and Conditions	

INTRODUCTION

1. The publisher for this copyrighted material is Elsevier. By clicking "accept" in connection with completing this licensing transaction, you agree that the following terms and conditions apply to this transaction (along with the Billing and Payment terms and conditions established by Copyright Clearance Center, Inc. ("CCC"), at the time that you opened your Rightslink account and that are available at any time at http://myaccount.copyright.com).

GENERAL TERMS

2. Elsevier hereby grants you permission to reproduce the aforementioned material subject to the terms and conditions indicated.

3. Acknowledgement: If any part of the material to be used (for example, figures) has appeared in our publication with credit or acknowledgement to another source, permission must also be sought from that source. If such permission is not obtained then that material may not be included in your publication/copies. Suitable acknowledgement to the source must be made, either as a footnote or in a reference list at the end of your publication, as follows:

"Reprinted from Publication title, Vol /edition number, Author(s), Title of article / title of chapter, Pages No., Copyright (Year), with permission from Elsevier [OR APPLICABLE SOCIETY COPYRIGHT OWNER]." Also Lancet special credit - "Reprinted from The Lancet, Vol. number, Author(s), Title of article, Pages No., Copyright (Year), with permission from Elsevier."

4. Reproduction of this material is confined to the purpose and/or media for which permission is hereby given.

5. Altering/Modifying Material: Not Permitted. However figures and illustrations may be altered/adapted minimally to serve your work. Any other abbreviations, additions, deletions and/or any other alterations shall be made only with prior written authorization of Elsevier Ltd. (Please contact Elsevier at permissions@elsevier.com)

6. If the permission fee for the requested use of our material is waived in this instance, please be advised that your future requests for Elsevier materials may attract a fee.

7. Reservation of Rights: Publisher reserves all rights not specifically granted in the combination of

(i) the license details provided by you and accepted in the course of this licensing transaction, (ii) these terms and conditions and (iii) CCC's Billing and Payment terms and conditions.

8. License Contingent Upon Payment: While you may exercise the rights licensed immediately upon issuance of the license at the end of the licensing process for the transaction, provided that you have disclosed complete and accurate details of your proposed use, no license is finally effective unless and until full payment is received from you (either by publisher or by CCC) as provided in CCC's Billing and Payment terms and conditions. If full payment is not received on a timely basis, then any license preliminarily granted shall be deemed automatically revoked and shall be void as if never granted. Further, in the event that you breach any of these terms and conditions or any of CCC's Billing and Payment terms and conditions, the license is automatically revoked and shall be void as if never granted. Use of materials as described in a revoked license, as well as any use of the materials beyond the scope of an unrevoked license, may constitute copyright infringement and publisher reserves the right to take any and all action to protect its copyright in the materials.

9. Warranties: Publisher makes no representations or warranties with respect to the licensed material.

10. Indemnity: You hereby indemnify and agree to hold harmless publisher and CCC, and their respective officers, directors, employees and agents, from and against any and all claims arising out of your use of the licensed material other than as specifically authorized pursuant to this license.

11. No Transfer of License: This license is personal to you and may not be sublicensed, assigned, or transferred by you to any other person without publisher's written permission.

12. No Amendment Except in Writing: This license may not be amended except in a writing signed by both parties (or, in the case of publisher, by CCC on publisher's behalf).

13. Objection to Contrary Terms: Publisher hereby objects to any terms contained in any purchase order, acknowledgment, check endorsement or other writing prepared by you, which terms are inconsistent with these terms and conditions or CCC's Billing and Payment terms and conditions. These terms and conditions, together with CCC's Billing and Payment terms and conditions (which are incorporated herein), comprise the entire agreement between you and publisher (and CCC) concerning this licensing transaction. In the event of any conflict between your obligations established by these terms and conditions and those established by CCC's Billing and Payment terms and conditions, these terms and conditions shall control.

14. Revocation: Elsevier or Copyright Clearance Center may deny the permissions described in this License at their sole discretion, for any reason or no reason, with a full refund payable to you. Notice of such denial will be made using the contact information provided by you. Failure to receive such notice will not alter or invalidate the denial. In no event will Elsevier or Copyright Clearance Center be responsible or liable for any costs, expenses or damage incurred by you as a result of a denial of your permission request, other than a refund of the amount(s) paid by you to Elsevier and/or Copyright Clearance Center for denied permissions.

LIMITED LICENSE

The following terms and conditions apply only to specific license types:

15. **Translation**: This permission is granted for non-exclusive world **English** rights only unless your license was granted for translation rights. If you licensed translation rights you may only translate this content into the languages you requested. A professional translator must perform all translations and reproduce the content word for word preserving the integrity of the article. If this license is to re-use 1 or 2 figures then permission is granted for non-exclusive world rights in all languages.

16. **Website**: The following terms and conditions apply to electronic reserve and author websites:
Electronic reserve: If licensed material is to be posted to website, the web site is to be password-protected and made available only to bona fide students registered on a relevant course if:
This license was made in connection with a course,
This permission is granted for 1 year only. You may obtain a license for future website posting,
All content posted to the web site must maintain the copyright information line on the bottom of each image,
A hyper-text must be included to the Homepage of the journal from which you are licensing at http://www.sciencedirect.com/science/journal/xxxxx or the Elsevier homepage for books at http://www.elsevier.com , and
Central Storage: This license does not include permission for a scanned version of the material to be stored in a central repository such as that provided by Heron/XanEdu.

17. **Author website** for journals with the following additional clauses:

All content posted to the web site must maintain the copyright information line on the bottom of each image, and
he permission granted is limited to the personal version of your paper. You are not allowed to download and post the published electronic version of your article (whether PDF or HTML, proof or final version), nor may you scan the printed edition to create an electronic version,
A hyper-text must be included to the Homepage of the journal from which you are licensing at http://www.sciencedirect.com/science/journal/xxxxx , As part of our normal production process, you will receive an e-mail notice when your article appears on Elsevier's online service ScienceDirect (www.sciencedirect.com). That e-mail will include the article's Digital Object Identifier (DOI). This number provides the electronic link to the published article and should be included in the posting of your personal version. We ask that you wait until you receive this e-mail and have the DOI to do any posting.
Central Storage: This license does not include permission for a scanned version of the material to be stored in a central repository such as that provided by Heron/XanEdu.

18. **Author website** for books with the following additional clauses:
Authors are permitted to place a brief summary of their work online only.
A hyper-text must be included to the Elsevier homepage at http://www.elsevier.com

All content posted to the web site must maintain the copyright information line on the bottom of each image
You are not allowed to download and post the published electronic version of your chapter, nor

may you scan the printed edition to create an electronic version.
Central Storage: This license does not include permission for a scanned version of the material to be stored in a central repository such as that provided by Heron/XanEdu.

19. **Website** (regular and for author): A hyper-text must be included to the Homepage of the journal from which you are licensing at http://www.sciencedirect.com/science/journal/xxxxx. or for books to the Elsevier homepage at http://www.elsevier.com

20. **Thesis/Dissertation**: If your license is for use in a thesis/dissertation your thesis may be submitted to your institution in either print or electronic form. Should your thesis be published commercially, please reapply for permission. These requirements include permission for the Library and Archives of Canada to supply single copies, on demand, of the complete thesis and include permission for UMI to supply single copies, on demand, of the complete thesis. Should your thesis be published commercially, please reapply for permission.

21. **Other Conditions**:

v1.6

Gratis licenses (referencing $0 in the Total field) are free. Please retain this printable license for your reference. No payment is required.

If you would like to pay for this license now, please remit this license along with your payment made payable to "COPYRIGHT CLEARANCE CENTER" otherwise you will be invoiced within 48 hours of the license date. Payment should be in the form of a check or money order referencing your account number and this invoice number RLNK10923621. Once you receive your invoice for this order, you may pay your invoice by credit card. Please follow instructions provided at that time.

Make Payment To:
Copyright Clearance Center
Dept 001
P.O. Box 843006
Boston, MA 02284-3006

If you find copyrighted material related to this license will not be used and wish to cancel, please contact us referencing this license number 2600231162907 and noting the reason for cancellation.

Questions? customercare@copyright.com or +1-877-622-5543 (toll free in the US) or +1-978-646-2777.